LEABHARLANN CHOLÁISTE NA TRÍONÓIDE, BAILE ÁTHA CLIATH | TRINITY COLLEGE LIBRARY DUBLIN
Ollscoil Átha Cliath | The University of Dublin

Terms and Conditions of Use of Digitised Theses from Trinity College Library Dublin

Copyright statement

All material supplied by Trinity College Library is protected by copyright (under the Copyright and Related Rights Act, 2000 as amended) and other relevant Intellectual Property Rights. By accessing and using a Digitised Thesis from Trinity College Library you acknowledge that all Intellectual Property Rights in any Works supplied are the sole and exclusive property of the copyright and/or other IPR holder. Specific copyright holders may not be explicitly identified. Use of materials from other sources within a thesis should not be construed as a claim over them.

A non-exclusive, non-transferable licence is hereby granted to those using or reproducing, in whole or in part, the material for valid purposes, providing the copyright owners are acknowledged using the normal conventions. Where specific permission to use material is required, this is identified and such permission must be sought from the copyright holder or agency cited.

Liability statement

By using a Digitised Thesis, I accept that Trinity College Dublin bears no legal responsibility for the accuracy, legality or comprehensiveness of materials contained within the thesis, and that Trinity College Dublin accepts no liability for indirect, consequential, or incidental, damages or losses arising from use of the thesis for whatever reason. Information located in a thesis may be subject to specific use constraints, details of which may not be explicitly described. It is the responsibility of potential and actual users to be aware of such constraints and to abide by them. By making use of material from a digitised thesis, you accept these copyright and disclaimer provisions. Where it is brought to the attention of Trinity College Library that there may be a breach of copyright or other restraint, it is the policy to withdraw or take down access to a thesis while the issue is being resolved.

Access Agreement

By using a Digitised Thesis from Trinity College Library you are bound by the following Terms & Conditions. Please read them carefully.

I have read and I understand the following statement: All material supplied via a Digitised Thesis from Trinity College Library is protected by copyright and other intellectual property rights, and duplication or sale of all or part of any of a thesis is not permitted, except that material may be duplicated by you for your research use or for educational purposes in electronic or print form providing the copyright owners are acknowledged using the normal conventions. You must obtain permission for any other use. Electronic or print copies may not be offered, whether for sale or otherwise to anyone. This copy has been supplied on the understanding that it is copyright material and that no quotation from the thesis may be published without proper acknowledgement.

TRINITY COLLEGE DUBLIN
COLÁISTE NA TRÍONÓIDE
THE UNIVERSITY OF DUBLIN

Quantum Dot and Metal Nanoparticle based Composites for Biomedical Applications

Valérie Gérard

A thesis submitted to the University of Dublin, Trinity College for the degree of Doctor of Philosophy.

School of Chemistry and CRANN
Trinity College Dublin
Dublin 2
Ireland

2013

TRINITY COLLEGE
2 4 MAY 2013
LIBRARY DUBLIN

Thesis 10047

Declaration

This thesis is submitted by the undersigned to the University of Dublin, Trinity College for the examination of Doctorate of Philosophy. It has not been submitted as an exercise for a degree to this or any other university. Except as stated otherwise, the author carried out the work described herein alone. The author agrees that the University Library may lend or copy the thesis upon request. This permission covers only single copies made for study purposes, subject to Irish Copyright Legislation and Trinity College Library conditions of acknowledgement.

Summary

The main aim of this project is to develop a range of nanocomposite materials based on gold and silver nanostructures and semiconductor nanoparticles, or quantum dots (QDs). The work involves the synthesis, functionalisation and combination of anisotropic metal nanoparticles and CdTe QDs. The new nano-composites are to be characterised and their behaviour in biological media is to be investigated.

Chapter 1 provides a literature review and some background information on nanoscience and the materials which are studied in the project. It describes nanomaterials' properties and the state of the art for their synthesis and applications. The aims and objectives of the work are also detailed in this chapter.

Chapter 2 provides all experimental details relating to the work presented in the thesis. The characterisation techniques and instrumentation are also described.

A range of anisotropic silver and gold nanomaterials are investigated in chapter 3. Galvanic replacement reactions are used to produce hollow gold nanostructures using a silver template. The influence of various parameters is studied, and the entrapment of species inside these structures is attempted. Gold-coated silver nanowires are also synthesised and fully characterised, including by circular dichroism spectroscopy. Biological studies are conducted with these nanomaterials.

Chapter 4 deals with the preparation of biocompatible nanocomposites using gelatin. QDs are coated in gelatin and further functionalised to selectively target cancer cells. Various approaches are investigated to synthesised QD clusters embedded in gelatin. Silver and gold nanoparticles are also coated with gelatin. In addition, hybrid nanomaterials consisting of QDs and metal nanoparticles have been produced using gelatin and characterised by various instrumental techniques.

Chapter 5 describes the research on a series of metal nanoparticles and QDs, which are functionalised with DNA oligonucleotides. These are used to create assemblies of nanoparticles and to study their interactions. A new type of plasmon-induced circular dichroism is observed and investigated in oligonucleotide-functionalised gold nanoparticles. Assemblies of gold nanoparticles and QDs are prepared and characterised.

Fluorescent Resonant Energy Transfer (FRET) is recorded in assemblies of QDs and further investigated in *in vitro* cell cultures.

Chapter 6 provides the conclusions of this work and preliminary studies building on the results we obtained. The process developed in chapter 4 for preparing functionalised gelatinated QDs is employed for targeted drug delivery applications. Further investigation into the interactions of chiral nanoparticles with cells is performed *in vitro*. The pressure-dependence of plasmon-induced CD is studied. The plasmon resonance of hollow gold-silver nanostructures is investigated. Finally, metal nanoparticles are tested as potential contrast agents for a polymer catheter.

Overall, a range of nanocomposite materials based on gold and silver nanostructures and CdTe QDs have been designed, prepared and investigated. Preliminary biological studies have indicated their potential for biomedical applications such as diagnostics and targeted drug delivery. Other materials have introduced the possibility of chiral sensing. We believe that the work presented in this thesis may constitute a significant contribution to the fields of nanotechnology and nanomedicine.

Acknowledgements

First and foremost, I would like to express my sincere thanks to my supervisor, Prof. Yurii Gun'ko, for giving me the opportunity to work in such an exciting area of research, and for all the advice and support he has provided throughout my time in his research group. I could not have hoped for better guidance.

I would like to thank the School of Chemistry, through Prof. David Grayson and Prof. John Kelly, and Dublin Chemistry for funding my work. I would like to extend my gratitude to the School of Chemistry and CRANN for the use of the facilities. My thanks go to all the staff of the School of Chemistry and CRANN, especially to Manuel, Patsy, Mark and Fred who are always here to help. Thanks to Dr. Despina Bazou for the training in cell culture and biological experiments, Neal Leddy for TEM and SEM, and Gavin McManus for the use of the confocal microscope.

I wish to express my gratitude to all the people with whom I have had the chance to collaborate: Dr. Dania Movia and Dr. Adriele Prina-Mello in the Institute of Molecular Medicine, Trinity College Dublin, Prof. Alexander Govorov in the University of Ohio (USA), Prof. Eric Defrancq in the Université Joseph Fourier in Grenoble (France), Prof. Yury Rochev and his group in the National University of Ireland, Galway and Prof. Louise Bradley and her group in the School of Physics, Trinity College Dublin. All these have been very fruitful collaborations which have helped broaden the scope of my work considerably.

Thanks also to all members of the Gun'ko group, past and present. Special thanks to Gemma, Renata and Michele, my coffee buddies! Amanda, you may have been only briefly part of the group, but your friendship and positivity stayed here with me! Dr. Stephen Byrne and Dr. Damian Aherne, I cannot thank you enough for all your help in my early days. Thanks to the rest of the group for filling my days with absurd theories as much as serious scientific discussions, but mostly a lot of fun and good humour: Cormac, Shane, Finn, Lorcan, Sarah, Amro, Mícheál, Joe Govan, Joe Mc Carthy, Richie, Iftikhar and Arunas. Also, this work would not have been the same without the help of my students, Mattia, Ciaran, Mark and William.

Finally, I would like to express my warmest thanks to my family, for always pushing me to achieve the best. Maman, Papa, Caroline, Philippe and the whole Gérard clan: thanks for always asking about my work, and encouraging me. A huge thank you to my friends, especially those who helped proof-read this thesis: Gemma, Scanlon, Alex and Simone. And to Colin: thank you for being there.

Abbreviations

2D	Two-dimensional
3D	Three-dimensional
A	Adenine
a.u.	Arbitrary Units
Abs	Absorbance
AgNW	Silver nanowire
AuAgNB	Gold-silver nanobox
AuNP	Gold nanoparticle
AuNP-oligo	Gold nanoparticle-oligonucleotide conjugate
bp	base pair
C	Cytosine
Calcein AM	Calcein-Acetyoxymethyl
CD	Circular Dichroism
CdTe	Cadmium telluride
D-	Dextrorotary
DAPI	4',6'-diamidino-2-phenylindole
DCM	Dichloromethane
DLS	Dynamic Light Scattering
DNA	Deoxyribonucleic acid
DPBS	Dubelcco's modified Phosphate Buffered Saline
ds	double-stranded
EDC	1-Ethyl-3-(3-dimethylaminopropyl)carbodiimide
EDTA	Ethylenediaminetetraacetic acid
EDX	Energy Dispersive X-ray spectroscopy
Eg	Band Gap Energy
FA	Folic acid
FA-QD	Folic acid - Quantum Dot conjugate

FLIM	Fluorescence Lifetime Imaging Microscopy
FRET	Flurescent/Forster Resonant Energy Transfer
FWHM	Full Width at Half Maximum
G	Guanine
Hep-QD	Heparin-Quantum Dot conjugate
HRTEM	High Resolution Transmission Electron Microscopy
L-	Levorotary
M	molar
mM	millimolar
NB	Nanobox
NP	Nanoparticle
NR	Nanoring
NW	Nanowire
Oligo	Oligonucleotide
Opt	Optimal amount
OR	Ostwald Ripening
PB	Phosphate buffer
PBS	Phosphate Buffered Saline
PCTX	Paclitaxel
PEG	Polyethylene glycol
PEI	Poly-ethylene Imine
Pen	Penicillamine
PL	Photo-luminescence
PSSS	Poly (sodium-4-styrene) sulfonate
PVA	Ploy-vinyl Alcohol
PVP	Poly-vinylpyrrolidone
QD	Quantum dot
QD-Ab	QD-antibody conjugate
QD-Inh I	QD-caspase1 inhibitor I conjugate
QD-Inh II	QD-caspase1 inhibitor II conjugate

QD-oligo	QD-oligonucleotide conjugate
QY	Quantum yield
Rac-	Racemate
SEM	Scanning Electron Microscopy
SERS	Surface-Enhanced Raman Spectroscopy
SPR	Surface Plasmon Resonance
ss	single-stranded
STEM	Scanning Transmission Electron Microscopy
T	Thymine
TCSPC	Time-correlated single photon counting
TEM	Transmission Electron Microscopy
TGA	Thioglycolic acid
TGA	Thermogravimetric analysis
TGA-gel QD	Gelatine-coated TGA-capped Quantum Dot
TGA-QD	TGA-capped Quantum Dot
TSC	Tri-sodium citrate / Sodium citrate, tri-basic
UV-vis	Ultra violet - visible

Table of Contents

Chapter 1

Introduction **1**

1.1 Reaching the nanoscale 1

1.2 Semiconducting nanocrystals 2

1.2.1 Structure and properties 2

1.2.2 Aqueous growth of CdTe nanocrystals 5

1.2.3 Applications of QDs in biological imaging, diagnostics and therapeutics 8

1.2.4 Aspects of QD toxicity 10

1.3 Silver and gold nanostructures 12

1.3.1 Surface Plasmon Resonance (SPR) 13

1.3.2 Structure and properties of gold nanoparticles 15

1.3.3 Structure and properties of silver nanoparticles 15

1.3.4 Synthesis of anisotropic silver nanostructures 16

1.3.5 Growth of gold nanostructures on silver templates 19

1.4 Functionalisation and bio-conjugation of nanoparticles 19

1.4.1 Bio-conjugation of Quantum Dots for labelling and detection applications 19

1.4.2 Conjugation of oligonucleotides to metal nanoparticles 20

1.4.3 Gelatin-nanoparticle composites 21

1.5 Circular dichroism in nanostructures 22

1.5.1 Intrinsically chiral metal nanoparticles and QDs 24

1.5.2 Chiral assemblies of nanoparticles 30

1.6 Aims and objectives of the project 32

References 34

Chapter 2

Experimental **43**

2.1 Starting materials and general equipment 43

2.2 Experimental details for chapter 3 44

2.2.1 Synthesis of silver nanoprisms[1] 44

2.2.2 Synthesis of gold-coated silver nanoprisms[2] 44

2.2.3 Synthesis of gold nanorings 44
2.2.4 Synthesis of gold/silver nanoboxes[3] 45
2.2.5 Encapsulation of materials into gold/silver nanoboxes 45
2.2.6 Synthesis of penicillamine-stabilised gold nanoparticles 45
2.2.7 *In vitro* biological experiments 46
2.2.8 Gold-coating of silver nanowires 47
2.3 Experimental details for chapter 4 47
2.3.1 Synthesis of CdTe QDs 47
2.3.2 Synthesis of folic-acid modified QDs[5] 48
2.3.3 *In vitro* biological experiments 48
2.3.4 QD conjugates for caspase inhibition 49
2.3.5 Preparation of gelatin-mediated QD assemblies 50
2.3.6 Synthesis of gelatin nanoparticles w/o QD-loading 50
2.3.7 Synthesis of gelatin-coated silver nanoprisms 51
2.3.8 Synthesis of drug-loaded, FA-functionalised gelatin-coated Au-Ag nanoboxes 51
2.4 Experimental details for chapter 5 51
2.4.1 Synthesis of citrate-stabilised spherical gold nanoparticles 51
2.4.2 Conjugation of 3'-T6-phosphorothioate-modified oligonucleotides to metallic nanoparticles 52
2.4.3 Induced aggregation of gold nanoparticles 52
2.4.4 *In situ* synthesis of oligonucleotide-conjugated metal nanoparticles 52
2.4.5 Oligonucleotide-mediated assembly of metal nanoparticles 53
2.4.6 Conjugation of 5'amine-modified oligonucleotides to TGA-capped CdTe QDs 53
2.4.7 Oligonucleotide-mediated assembly of metal nanoparticles and QDs through the ds-oligonucleotide method 53
2.4.8 Oligonucleotide-mediated assembly of metal nanoparticles and QDs through the ss-oligonucleotide method 53
2.4.9 *In situ* Preparation of QD-oligo 54
2.4.10 FRET studies in oligonucleotide-mediated assemblies of QDs 54
2.4.11 Biological studies of oligonucleotide-mediated assemblies of QDs 54
2.5 Experimental details for chapter 6 55
2.5.1 QD-Heparin conjugates 55
2.5.2 Biological testing of CdS nanotetrapods 56

2.5.3 Preparation of samples for solid-state Circular Dichroism studies 56
2.5.4 Infiltration of polymer tubing with metal nanoparticles 57
2.6 Characterisation techniques 57
2.5.1 UV-Vis absorption spectroscopy 57
2.5.2 PL spectroscopy 57
2.5.3 Time-correlated single photon counting (TCSPC) spectrometry 57
2.5.4 Fluorescence Lifetime Imaging Microscopy (FLIM) 58
2.5.5 Circular Dichroism (CD) 58
2.5.6 Dynamic Light Scattering (DLS) 58
2.5.7 Gel Electrophoresis 60
2.5.8 Transmission Electron Micrsoscopy (TEM) 61
2.5.9 High Resolution TEM (HRTEM) / Scanning TEM (STEM) 61
2.5.10 Energy Dispersive X-ray spectroscopy (EDX) 61
2.5.11 Confocal microscopy 62
2.5.10 Epifluorescence microscopy 63
2.5.12 Thermogravimetric Analysis (TGA) 65
References 66

Chapter 3

Anisotropic Metal Nanostructures **67**

3.1 Introduction 67
3.2 Synthesis and characterisation of shape-controlled gold-silver nanostructures 68
3.2.1 Synthesis and characterisation of gold –coated silver nanoprisms 68
3.2.2 Synthesis and characterisation of gold nanorings 69
3.2.3 Synthesis and characterisation of gold-silver nanoboxes 74
3.3 *In vitro* cellular testing of metal nanoparticles 80
3.3.1 Chiral gold nanoparticles 81
3.3.2 Gold-silver Nanoboxes 84
3.4 Gold-coating and optical activity of silver nanowires 91
3.4.1 Preparation of gold-coated silver nanowires 91
3.4.2 Circular Dichroism of silver nanowires 101
3.5 Conclusions 103
References 104

Chapter 4

Nano-composites of Quantum Dots, Metal Nanoparticles and Gelatin **107**

4.1 Introduction 107

4.2 Synthesis, characterisation and *in vitro* study of CdTe QDs 108

4.2.1 Influence of reflux time 108

4.2.2 Importance of ligand choice 110

4.2.3 Synthesis and characterisation of gelatin-coated CdTe QDs 111

2.1.4 Cellular uptake of TGA-capped CdTe QDs 113

2.1.5 Cellular uptake of gelatin-coated TGA-capped (TGA-Gel) CdTe QDs 117

4.3 Folic acid-functionalised QDs 119

4.3.1 Characterisation of FA-modified QDs 122

4.3.2 Biological testing of FA-modified QDs 127

4.4 Caspase Inhibitor- and Antibody-modified QDs 133

4.5 Gelatin-mediated QD aggregates 137

4.4 QD-loaded gelatin nanoparticles 141

4.5.1 Optimisation of gelatin nanoparticles 141

4.5.2 Incorporation of QDs in gelatin nanoparticles 144

4.6 Gelatin-coated metal nanoparticles 148

4.6.1 Gelatin-coated silver nanoprisms 148

4.6.2 Drug-loaded, functionalised, gelatin-coated gold-silver nanoboxes 153

4.7 Conclusions 157

References 159

Chapter 5

Oligonucleotide-Nanoparticle Composites **163**

5.1 Introduction 163

5.2 Circular dichroism in oligonucleotide-metal nanoparticle conjugates 166

5.3 Oligonucleotide-mediated assemblies of nanoparticles 181

5.3.1 Oligonucleotide-mediated assembly of gold nanoparticles 181

5.3.2 Oligonucleotide-mediated assemblies of QDs and AuNPs 185

5.4 Oligonucleotide-mediated QD interactions 197

5.4.1 Synthesis of oligonucleotide-QD conjugates and evaluation of their hybridising ability 198

5.4.2 FRET studies 203

5.4.3 In vitro biological testing of Oligonucleotide-QD conjugates 207

5.5 Conclusions 212

References 213

Chapter 6

Conclusions and Future Work **217**

6.1 Conclusions 217

6.2 Preliminary studies and future work 218

6.2.1 Heparin-modified QDs 218

6.2.3 Biological testing of chiral CdS nanotetrapods 222

6.2.4 Solid-state CD 226

6.2.5 Infiltration of polymer tubing with gold metal nanoparticles 228

References 234

Appendices **237**

Appendix 1: HRTEM sizing data for CdTe QDs correlated to UV-visible absorption maxima (provided by Dr Yury Rakovich) 237

Appendix 2: Three plane projections of cells internalising QDs 238

Appendix 3: Localisation of internalised QDs and Golgi apparatus in live *in vitro* cell cultures 243

Publications **245**

Book Chapters 245

Journal Articles 245

Review Article 247

Presentations **248**

Oral Presentations 248

Poster Presentations 248

List of Figures and Tables

Chapter 1 *Introduction*

Figure 1.1 Examples of objects in the millimeter to sub-nanometer size range

Figure 1.2 Jablonski diagram representing the energy band gap structure in a semi-conductor material and the changes from bulk to nanostructure. Adapted from literature.[1]

Figure 1.3 Three stabilisers commonly used in aqueous CdTe QD synthesis

Figure 1.4 Schematic representation of the electrical double layer in the colloidal stability theory

Figure 1.5 Schematic representation of electronic cloud displacements in nanoparticles under the effect of an electromagnetic wave[2]

Figure 1.6 Absorption spectra of gold particles of various shapes and sizes[3]

Figure 1.7 A) Schematic illustration of a <110> oriented segment of a fcc crystal. The edges of crystal cut in this manner will have alternating pairs of <100> and <111> faces. B) Schematic of a nanoplate constructed from a single fcc crystal showing alternating pairs of <100> and <111> faces. C) Schematic of a nanoplate with a defect-induced hcp layer sandwiched between two fcc layers of unequal thicknesses. The block arrows indicate the directions of preferential growth.[4]

Figure 1.8 Schematic illustration of the mechanism proposed to account for the growth of silver nanowires with pentagonal cross sections: (A) Evolution of a nanorod from a multiply twinned nanoparticle of silver under the confinement of five twin planes and with the assistance of PVP. (B) Schematic model illustrating the diffusion of silver atoms toward the two ends of a nanorod, with the side surfaces completely passivated by PVP.[5]

Figure 1.9 Directional assembly of oligonucleotide-functionalised AuNPs into cat paws (A, B), satellites (C, D), and dendrimer-like structures (E, F).[6] Scale bar: 20 nm

Figure 1.10 Schematic representation of the structure of collagen, which may be broken down into gelatin

Figure 1.11 Schematic representation of (a) right-polarised light and (b) left-polarised light. The horizontal arrows represent the directions of propagation, and the arrows perpendicular to that denote the instantaneous spatial direction of the electric vector.[7]

Figure 1.12 The plasmonic CD band of Ag NPs assembled on DNA (left) and the geometry of the system including a TEM image of the Ag NP chain (right).[8]

Figure 1.13 Left: Schematic of a chiral penicillamine capped CdS nanoparticle. Right: CD spectra of L-penicillamine (green), D-penicillamine (blue) and racemic (red) CdS nanoparticles.[7]

Figure 1.14 Chiral memory of thiol-capped CdTe nanocrystals. QDs stabilized with chiral ligands retained their optical activity even after exchange with an achiral thiol[9]

Figure 1.15 Quantum dot models of two different chiral arrangements of cysteine and CdTe[10]

Figure 1.16 Chiral assemblies of gold nanoparticles using DNA scaffolds[11]

Table 1.1 Chiral ligands leading to chiral gold nanoparticles

Chapter 2 ***Experimental***

Figure 2.1 Schematic illustration of the electrical double layer and zeta potential[12] (Zetasizer Nano series technical note MRK654-01, Malvern Instruments)

Figure 2.2 Schematic representation of the confocal microscope principle[13]

Figure 2.3 Schematic representation of the light path in an epifluorescence microscope[14]

Figure 2.4 Schematic representation of the light path in dark-field microscopy

Chapter 3 *Anisotropic Metal Nanoparticles*

Figure 3.1 Schematic diagram of the synthetic routes to metallic nanostructures

Figure 3.2 TEM images of (a) silver nanoprisms and (b) gold-coated silver nanoprisms

Figure 3.3 TEM images of gold-coated silver nanoprisms formed (a) in presence and nanorings (b) in absence of TSC

Figure 3.4 TEM images of gold nanorings prepared using (a) 2250 μL, (b) 150 μL and (c) no ascorbic acid

Figure 3.5 TEM images of gold nanorings produced using increasing amounts of gold salt (a to d)

Figure 3.6 UV-Vis absorption spectra of silver nanoprisms, gold-coated silver nanoprisms and gold nanorings

Figure 3.7 TEM images of gold-silver nanoboxes

Figure 3.8 UV-Vis absorption spectra of silver nanoprisms and gold-silver nanoboxes and corresponding particle sizes as measured from TEM images

Figure 3.9 EDX scan of AuAg nanoboxes, showing gold as the dominant element

Figure 3.10 (A) SEM image of AuAgNB; (B) Schematic representation of the ridged morphology of AuAgNB

Figure 3.11 TEM images of AuAg nanoboxes formed in presence of CdTe QDs. From sideways, the dark spots appear to be bridges (right). Scale bars 5 nm

Figure 3.12 TEM images of AuAg nanoboxes formed in 100, 15 and 10 nmol/L PIC respectively (A,B,C); STEM image of AuAg nanoboxes formed in 10 nmol/L PIC.

Figure 3.13 UV-Visible absorption spectra of silver nanoprisms and subsequently formed gold/silver nanoboxes, with 100nM (top), 15 and 10nM (bottom) PIC

Figure 3.14 Plasmonic imaging of gold-silver nanoboxes

Figure 3.15 CD spectra of D- and L-penicillamine stabilised gold nanoparticles

Figure 3.16 (a, d, g, j) Brightfield, (b, e, h, k) epifluorescence and (c, f, i, l) merged images of J774 cells (d-l) with or (a-c) without L-Pen AuNPs. Examples of

single resonant metallic NPs, visible as lighter areas inside cells, are highlighted by arrows. Scale bars: 20 μm (100x magnification)

Figure 3.17 (a, d, g, j) Brightfield, (b, e, h, k) epifluorescence and (c, f, i, l) merged images of J774 cells (d-l) with or (a-c) without D-Pen AuNPs. Examples of single resonant metallic NPs, visible as lighter areas inside cells, are highlighted by arrows. Scale bars: 20 μm (100x magnification)

Figure 3.18 Size characterisation of AuAg nanoboxes. Top: TEM images of sample 1 and 2. Bottom: Size distribution of sample 1 and 2 as measured on TEM images.

Figure 3.19 (a, d, g) Brightfield, (b, e, h) epifluorescence and (c, f, i) plasmon resonance images of J774 cells incubated (d-i) with or (a-c) without AuAg Nanoboxes. (f, i) Examples of single resonant metallic Nanoboxes, visible as lighter dots, are clearly visible within cells. Scale bars: 20 μm (100× magnification)

Figure 3.20 Confocal microscopy images of J774 cells incubated with sample 1 (c,d) or sample 2 (e,f) of nanoboxes, and negative control without nanoboxes (a,b). Nuclei are stained in blue and the cell membrane is stained is red. Nanoboxes are visible as dark areas in bright field. 3D projection of Z-stacks (b,d,f) clearly show that nanoboxes are localised within the cells.

Figure 3.21 Epifluorescence images of 2D cell models of A549 cells incubated (a) without AuAg Nanoboxes or with (b) sample 1, (c) sample 2 AuAg nanoboxes. Nuclei are stained in blue, F-actin filaments in green while single resonant metallic AuAg Nanoboxes localized within the cells are here showed in pseudo-colour (red) for illustrative purposes. Scale bars: 20 μm (100× magnification).

Figure 3.22 Merged epifluorescence and plasmon resonance microscopy images of A549 cells in USWT. (A) Negative control without nanoboxes. (B) Cells treated with sample 1. (C) Cells treated with sample 2. F-actin stained in green, nuclei stained in blue, resonant metallic AuAg nanoboxes showed in pseudo-colour (red) for illustrative purposes. Scale bar 10 μm

Figure 3.23 Cellular response upon 24 hour-exposure to sample 1 and 2 of nanoboxes in various concentrations: effects on cell count, lysosomal mass and cell

membrane permeability. Negative control: untreated cell culture. Positive control: 40 mM doxorubicin. Stars indicate significant variations.

Figure 3.24 Live/Dead assay performed in 3D A549 cell aggregated in USWT. Live cells are stained with green-fluorescent Calcein AM. Dead cells are stained with red-fluorescent ethidium bromide

Figure 3.25 Citrullination: the chemical conversion of arginine to citrulline

Figure 3.26 Cytotoxicity indicators for A549 3D cell aggregates formed in USWT and treated with AuAg NBs. Negative control: untreated cells. AuAg NB sample 1 and 2 concentration: 10^{-8} mM. Carbon black concentration: 100 μg/mL.

Figure 3.27 TEM (top) and STEM (middle and bottom) images of original silver nanowires

Figure 3.28 TEM images of gold coated AgNW of various lengths. A: 3 μm; B: 5 μm; C: 10 μm; D: 14 μm; E, F: 28 μm

Figure 3.29 TEM images of (top) 5 and (bottom) 14 μm long gold-coated AgNW after washing with ammonia

Figure 3.30 TEM images of a single gold-coated AgNW. Close ups on the edge suggesting the presence of a shell.

Figure 3.31 STEM images of (top) 5 and (bottom) 14 μm long gold-coated silver nanowires

Figure 3.32 STEM image and corresponding EDX spectrum of whole gold-coated silver nanowires

Figure 3.33 STEM image and corresponding EDX spectrum of gold-coated AgNW and gold nanoparticles

Figure 3.34 TEM images of (top) 5 and (bottom) 14 μm long gold-coated silver nanowires after iron nitrate treatment

Figure 3.35 (A) Chemical structure of PVP. (B) CD spectrum of PVP.

Figure 3.36 CD spectra of 14 μm-long nanowires before and after gold-coating

Figure 3.37 CD spectra of 14um-long AuAgNW in absence (black) and presence (red) of added PVP

Table 3.1 Gold amount dependence of ring width

Table 3.2 Size characteristics of Sample 1 and 2 of AuAg nanoboxes

Chapter 4 ***Nano-composites of Quantum Dots, Metal Nanoparticles and Gelatin***

Figure 4.1 Influence of reflux time on the absorption spectrum of TGA-capped CdTe

Figure 4.2 Influence of reflux time on the emission spectrum of TGA-capped CdTe

Figure 4.3 Zeta potential graphs of TGA- (green) and Cysteamine- (red) stabilised CdTe QDs

Figure 4.4 Emission spectra of TGA-capped CdTe synthetised in presence of PEG, PEI, PVA and gelatin respectively

Figure 4.5 Chemical structures of PEG, PVA and PEI

Figure 4.6 Confocal microscope images of (A, B) Caco-2 cells and (C, D) HT-1080 cells incubated for four hours with TGA-capped CdTe QDs (red) and counter-stained with Calcein-AM (green). Overlay of red (excitation 543 nm) and green (excitation 488 nm) (A, D) and bright field (B,C) channels.

Figure 4.7 Three-plane projection of confocal microscopy slice by slice images of (left) Caco-2 and (right) HT-1080 cells treated with TGA-capped QDs (red) and counter-stained with calcein-AM. Overlay of red (excitation 543 nm) and green (excitation 488 nm) channels.

Figure 4.8 Bright field confocal microscope images of (A) Caco-2 cells control culture, (B,C) Caco-2 cells incubated with TGA-capped CdTe QDs, (D) HT1080 cells control culture and (E,F) HT-1080 cells incubated with TGA-capped CdTe QDs. (A, B, D, E) bright field images; (C, F) Overlay of red QD (excitation 543 nm) and green Calcein AM (excitation 488 nm) channels.

Figure 4.9 Confocal microscope images of (A,B) Caco-2 cells and (C,D) HT-1080 cells incubated with Gelatinated TGA-capped CdTe QDs (red) and counter-stained with Calcein-AM (green). Arrows indicate internalised QDs in wide field. Overlay of red (excitation 543 nm) and green (excitation 488 nm) (A, C) and bright field (B,D) channels

Figure 4.10 Confocal microscope images of HT-1080 cells incubated with (A) TGA-capped and (B) Gelatinated TGA-capped CdTe QDs (red) and counter-stained with Calcein-AM (green). Overlay of red (excitation 543 nm) and green (excitation 488 nm) channels.

Figure 4.11 Schematic of the EDC coupling reaction in the case of an oligonucleotide bearing a terminal amine group to be bound to carboxylic acid functionalised CdTe QD

Figure 4.12 Schematic representations of QD (A) - gelatine coated, (B) - with FA incorporated into the gelatine layer and (C) - with FA covalently bound to the surface

Figure 4.13 UV-visible absorption and PL emission spectra of selected samples of QD (A), (B) and (C). Excitation: 480 nm.

Figure 4.14 Luminescence decay curves obtained by TCSPC for QD(A), (B) and (C)

Figure 4.15 TEM images of QD (A), (B) and (C) as labelled

Figure 4.16 Comparison of core diameter as measured by TEM and hydrodynamic diameter from DLS for all three types of QDs

Figure 4.17 Confocal microscope images of Caco-2 cells treated with QD(A) (panel A), (B) (panel B) and (C) panel (C). Nuclei were stained with DAPI (blue), QDs emit in the red. Blue (excitation 405 nm) and red (excitation 543 nm) luminescence were merged with the bright field where cell membranes are visible.

Figure 4.18 Percentage of Caco-2 cells exhibiting internalised QDs (A, B or C respectively) in absence (blue) and presence (red) of free FA in the cell culture medium after four hours incubation

Figure 4.19 Confocal microscope images of HT-1080 cells treated with QD(A) (panel A), (B) (panel B) and (C) panel (C). Nuclei were stained with DAPI (blue), QDs emit in the red. Blue and red luminescence was merged with the bright field where cell membranes are visible.

Figure 4.20 Differential uptake of QD (A), (B) and (C) by HT1080 and Caco-2 cells. The respective uptakes of QD (A) are taken as a reference to show the relative increase for both cell lines

Figure 4.21 Structure of caspase1 inhibitor I (left) and II (right)

Figure 4.22 PL spectra of TGA-gel QDs before and after conjugation to Caspase1 Inhibitor I and II respectively

Figure 4.23 PL spectra of original TGA-gel QDs and QD-Ab conjugates

Figure 4.24 Concentration of released IL-1β upon activation with ATP and treatment with various concentrations of either Inhibitor I or II, anti-ASC antibody or their QD conjugates

Figure 4.25 PL emission spectra of TGA-gel QDs before (black) and after (red) heating at 70 °C for 3 min (excitation 480 nm)

Figure 4.26 PL spectra of TGA and TGA-gel QDs, and their mixture heated at 70 °C after 0, 1, 2 and 3 min.

Figure 4.27 DLS measurements of TGA QDs, TGA-gel QDs, TGA-gel QDs after heating at 70 °C for 3 min and a mixture of the two species heated at 70 °C for 3 min.

Figure 4.28 TEM (top) and STEM (bottom) images of TGA and TGA-gel QDs mixed in equal concentrations and heated at 70 °C for 3 min

Figure 4.29 TEM images of TGA-gel QDs after heating at 70 °C for 3 min

Figure 4.30 STEM images of gelatin nanoparticles synthesised using ultrasonic agitation (top). Size distribution of gelatin nanoparticles as measured on STEM images (bottom).

Figure 4.31 DLS measurements of four fractions successively obtained by size selective precipitation of gelatin nanoparticles synthesised using ultrasonic agitation. (Three measurements are displayed for each fraction)

Figure 4.32 UV-visible absoption (left) and PL emission spectra of initial QDs and QD-loaded gelatin nanoparticles. (Excitation: 330 nm)

Figure 4.33 Excitation spectrum of QD-loaded gelatin naoparticles at the maximum emission: 568 nm

Figure 4.34 STEM images of QD-loaded gelatin nanoparticles, where the gelatine shell can be observed as a sphere of ~300 nm diameter and the QDs are visible as very bright ~5 nm spots distributed within the gelatine sphere.

Figure 4.35 TEM images of QD-loaded gelatin nanoparticles, where only QDs are visible.

Figure 4.36 DLS measurements of QD-loaded gelatin nanoparticles

Figure 4.37 DLS measurements of silver nanoprisms (a) and gelatin-coated silver nanoprisms produced with (b) 0.01 g and (c) 0.05 g of gelatin. The top graph shows the size distribution by intensity and the bottom one shows the extrapolated distribution by number.

Figure 4.38 UV-visible absorption spectra measurements of silver nanoprisms (a) and gelatin-coated silver nanoprisms produced with (b) 0.01 g and (c) 0.05 g of gelatin.

Figure 4.39 DLS measurements of silver nanoprisms (red), gelatin-coated silver nanoprisms (blue) and QD-gelatin-coated silver nanoprisms (green)

Figure 4.40 TEM images of initial silver nanoprisms (a), gelatin-coated silver nanoprisms (b) and QD-gelatin-silver nanoprisms (c,d)

Figure 4.41 Chemical structures of paclitaxel and folic acid

Figure 4.42 Schematic representation of (A) AuAgNB-gel, (B) AuAgNB-gel-PCTX and (C) AuAgNB-gel-PCTX-FA

Figure 4.43 DLS measurements of AuAgNB, AuAgNB-gel, AuAgNB-gel-PCTX and AuAgNB-gel-PCTX-FA

Figure 4.44 HRTEM images of AuAgNB-gel. Arrows point to patches of gelatin.

Figure 4.45 STEM images of AuAgNB-gel

Figure 4.46 (A, C) TEM and (B, D) STEM images of (A, B) AuAgNB-gel-PCTX and (C, D) AuAgNB-gel-PCTX-FA

Table 4.1 Luminescence decay measurements. τ_1: shorter lifetime; τ_2: longer lifetime; B_1: relative contribution of T_1; B_2: relative contribution of T_2; χ^2: correlation factor

Table 4.2 Size of QDs as measured by TEM and DLS, and their zeta potential

Table 4.3 Cytotoxicity of FA modified QDs towards Caco-2 cells

Table 4.4 DLS and Zeta potential measurements of AuAgNB, AuAgNB-gel, AuAgNB-gel-PCTX and AuAgNB-gel-PCTX-FA

Chapter 5 *Oligonucleotide-Nanoparticle composites*

Figure 5.1 UV-visible absoprtion spectra of gold nanoparticles before and after oligonucleotide conjugation showing a 7 nm shift of the plasmon band

Figure 5.2 DLS measurements of bare and oligonucleotide-conjugated spherical gold nanoparticles

Figure 5.3 TEM images of bare (left) and oligonucleotide-conjugated (right) AuNPs

Figure 5.4 CD spectra of AuNPs incubated with oligonucleotides over time with increasing NaCl concentration, and after washing by centrifugation

Figure 5.5 UV-visible absoprtion spectra of gold nanorings before and after oligonucleotide conjugation showing a 12 nm shift of the plasmon band

Figure 5.6 TEM images of bare (left) and oligonucleotide-conjugated (right) gold nanorings

Figure 5.7 DLS measurements of bare and oligonucleotide-conjugated spherical gold nanorings

Figure 5.8 CD spectra of gold nanorings incubated with oligonucleotide over time with increasing concentrations of NaCl and after washing

Figure 5.9 UV-visible absoprtion spectra of gold nanoboxes before and after oligonucleotide conjugation showing an initial 5 nm shift of the plasmon band

Figure 5.10 TEM images of bare (left) and oligonucleotide-conjugated (right) Au-Ag nanoboxes

Figure 5.11 CD spectra of bare and oligonucleotide-conjugated Au nanoboxes, as well as after washing by centrifugation

Figure 5.12 Calculated averaged plasmonic enhancement factors for the plasmonic hot spot in the centre of an assembly of N_{Au} nanoparticles. Inset: Geometry of

one particular complex with N_{NP} = 6; the plasmonic hot spot is located in the centre of the system indicated as a blue sphere.[2]

Figure 5.13 Monitoring of the size of aggregates induced by increasing concentrations of NaCl, by UV-Vis absorption spectroscopy (top) and DLS (bottom)

Figure 5.14 CD response of aggregated spherical gold NPs

Figure 5.15 Effect of sonication and centrifugation on CD signal of oligonucleotide-AuNP conjugates

Figure 5.16 UV-Visible absorption (left) and CD (right) spectra of gold nanoparticles conjugated with ss- and ds-oligonucleotides, before after centrifugation-induced aggregation

Figure 5.17 UV-visible absorption and PL emission spectra of TGA-capped CdTe QDs before (black) and after (green) oligonucleotide conjugation

Figure 5.18 DLS measurements of bare (top) and oligonucleotide-conjugated (bottom) TGA-capped CdTe QDs

Figure 5.19 CD signal of TGA-capped CdTe QDs conjugated with oligonucleotides

Figure 5.20 UV-Visible absorption spectra of oligonucleotide-conjugated gold nanoparticles, assemblies and initial nanoparticles

Figure 5.21 DLS measurments of AuNP-oligo conjugates formed *in situ*

Figure 5.22 UV-Visible absorption spectra of gold nanoparticles conjugated with oligo 3.1, oligo 3.2 and oligo 3.1 pre-incubated with oligo 3.comp

Figure 5.23 DLS measurements of gold nanoparticles conjugated with oligo 3.1, oligo 3.2 and oligo 3.1 pre-incubated with oligo 3.comp

Figure 5.24 (A) Schematic of the duplex-induced assembly of a spherical gold nanoparticle and QDs. (B) TEM image of QDs (designated by arrows) bound to a gold nanoparticle through oligonucleotide duplex formation.

Figure 5.25 UV-visible absorption spectra of Au-oligo, QD-oligo, and mixtures of them in various ratios

Figure 5.26 TEM images of Au-oligo nanocomposites produced with (A) 1:12.5, (B) 1:25, (C) 1:62.5, and (D) 1:125 ratios of AuNP to QD. Aggregation decreased as the ratio increased.

Figure 5.27 HRTEM images of Au-oligo nanocomposites produced with a 1:125 ratio of AuNP to QD

Figure 5.28 PL emission spectra of original QDs, QD-oligo conjugates and Au-oligo nanocomposites (excitation 480 nm)

Figure 5.29 CD spectra of oligonucleotide-modified QD and subsequent ds-oligo mediated assembly of QD and AuNP

Figure 5.30 (A) Schematic of the direct assembly of a spherical gold nanoparticle and a QD through the ss-oligo method. (B) TEM image of a QD bound to a spherical nanoparticle through oligonucleotide conjugation.

Figure 5.31 UV-visible absorption spectra of AuNP-QD composites formed over time through single-stranded oligonucleotide binding

Figure 5.32 UV-visible absorption spectra of AuNP mixed with QD in absence of oligo

Figure 5.33 TEM images of AuNP-oligo-QD composites formed by the ss-oligo route

Figure 5.34 PL emission spectra of Au-QD nanocomposites formed through the ss-oligo method and mixture of AuNP and QD without oligo. (excitation 480 nm)

Figure 5.35 Schematic of the duplex-induced assembly of gold nanorings and QDs.

Figure 5.36 TEM images of QDs bound to gold nanorings through oligonucleotide duplex formation.

Figure 5.37 CD spectra of oligonucleotide-modified AuNR and subsequent assembly with QDs

Figure 5.38 UV-visible absorption (left) and PL emission (right) spectra of QDs treated with increasing amounts of EDC. PL emission spectra were normalised against concentration

Figure 5.39 PL emission spectra of QD on their own, QD treated with EDC, QD mixed with gold nanorings, QD and gold nanorings in presence of EDC (no oligo) and the final QD-gold nanoring conjugates.

Figure 5.40 CD spectra of QDs modified with complementary oligonucleotide sequences and their mixture in 1:1 ratio

Figure 5.41 DLS measurements of a 1:1 mixture of QDs modified with complementary oligonucleotide sequences and incubated for 0 to 55 min

Figure 5.42 DLS measurements of a 1:1 mixture of QDs modified with complementary sequences of oligonucleotides at increasing temperatures

Figure 5.43 HRTEM images of oligonucleotide-mediated assemblies of QDs. Some green-red QD dimers are highlighted as circled in green and red.

Figure 5.44 Gel electrophoresis of oligonucleotide-QD conjugates. Photograph of the gel (left) and intensity plot of the lanes (right). Lanes loaded as follows: 1) QD-oligo 1; 2) QD-oligo 2; 3) 1:1 mix of QD-oligo 1 and 2; 4) 2:1 mix of QD-oligo 1 and 2; 5) 3:1 mix of QD-oligo 1 and 2.

Figure 5.45 Left: Donor (a) and acceptor (a) UV-visible absorption and PL emission spectra. Right: Donor (a) quenching and acceptor (a) enhancement versus donor-to-acceptor ratio

Figure 5.46 Left: Donor (b) and acceptor (b) UV-visible absorption and PL emission spectra. Right: Donor (b) quenching and acceptor (b) enhancement versus donor-to-acceptor ratio

Figure 5.47 Left: Donor (c) and acceptor (c) UV-visible absorption and PL emission spectra. Right: Donor (c) quenching and acceptor (c) enhancement versus donor-to-acceptor ratio

Figure 5.48 Example of spectral bleed-through. Confocal microscope images of HT-1080 cells exhibiting internalised QDs. Top: donor (a). Bottom: acceptor (a). Left column: excitation 488 nm, emission 490-550 nm. Middle column: excitation 543 nm, emission above 560 nm. Right column: overlay of both channels with bright field.

Figure 5.49 Confocal microscope images of HT-1080 cells exhibiting internalised QDs. Top left: donor (a). Top right: acceptor (a). Bottom left: donor (a) and acceptor (a) added simultaneously. Bottom right: donor (a) and acceptor (a) with pre-incubation.

Figure 5.50 Confocal microscope images of HT-1080 cells exhibiting internalised QDs. First row: negative control; second row: donor (b); third row: acceptor (b); fourth row: donor (b) and acceptor (b) added simultaneously; fifth row: donor (b) and acceptor (b) with pre-incubation. First column: excitation 543 nm, emission 603 nm; second column: excitation 633 nm, emission 668 nm. Arrows indicate green QDs

Table 5.1 Zeta potential of gold nanoparticles, oligonucleotides and their conjugates

Table 5.2 Zeta potential measurements of TGA-capped CdTe QDs with and without conjugated oligonucleotides

Table 5.3 Zeta potential measurements of AuNP-oligo conjugates

Table 5.4 Characterisation of oligonucleotide-modified QDs

Chapter 6 ***Conclusions and Future Work***

Figure 6.1 Top: Pentasaccharide antithrombin binding site of heparin. A single saccharide unit is shown in red.[15] 3D representation of the structure of a small heparin chain.[16]

Figure 6.2 Confocal microscopy images of live THP-1 cells treated with (A) TGA-QDs, (B), TGA-gel QDs and (C) Hep-QDs. Nuclei are stained with Hoechst (blue)

Figure 6.3 Confocal microscopy images of live A549 cells treated with (A) TGA-QDs, (B), TGA-gel QDs and (C) Hep-QDs. Nuclei are stained with Hoechst (blue)

Figure 6.4 Confocal microscopy images of fixed permeabilised (A) THP-1, (B) A549 and (C) Caco-2 cells treated with Hep-QDs. Nuclei are stained with Hoechst (blue)

Figure 6.5 A wide field TEM images of D-Pen nano-tetrapods showing a number of tetrapods (A), a closer look of two tetrapods (B) and a high-resolution image of a single tetrapod (C). UV-VIS, PL (D) and CD (E) spectra of Pen stabilised CdS.[17]

Figure 6.6 Confocal images of HT-1080 cells treated with D-Pen (A), L-Pen (B) and Rac-Pen (C). Control, untreated HT-1080 cells (D). Bright field and green luminescence channels were merged.

Figure 6.7 Average integrated intensity generated by QDs in cells

Figure 6.8 Internalisation of D-, L- and Rac-Pen CdS tetrapods in absence and presence of free D-Pen in the cell culture medium

Figure 6.9 Solid-state CD spectra of (top) D-Pen AuNP and (bottom) Ag Nanoprisms in presence of DNA, and comparison with the same in solution.

Figure 6.10 Solid-state CD spectra of silver nanowires showing the pressure dependence

Figure 6.11 Schematic illustration of balloon dilatation catheter application.[18]

Figure 6.12 Photograph of a catheter bearing the X-ray opaque platinum markers indicated by the arrows

Figure 6.13 Chemical formula of Pebax. PA: polyamide block. PE: polyethylene block.

Figure 6.14 SEM images of AuNP-infiltrated polymer tube. Top: 1h ultrasonic agitation; Middle: 2h ultrasonic agitation; Bottom: 4h ultrasonic agitation.

Figure 6.15 TGA of pure polymer and AuNP-infiltrated polymer with 2h and 4 h reaction times.

Figure 6.16 Samples of AuNP-infiltrated tubes lined up (top) and X-Ray taken simultaneously (bottom). The black dots visible on X-ray are the gold markers on the catheters.

Table 6.1 Characteristics of selected TGA, TGA-gel and Heparin conjugated CdTe QDs

Appendices

Figure A.1 Experimental plot of CdTe QD core size against UV-Visible absorption maximum

Figure A.2 Three-plane projection of Caco-2 cells treated with red-emitting TGA-gel QDs (excitation 543 nm) and counter-stained with DAPI (excitation 405 nm)

Figure A.3 Three-plane projection of HT-1080 cells treated with red-emitting TGA-gel QDs (excitation 543 nm) and counter-stained with Calcein AM (excitation 488 nm)

Figure A.4 Three-plane projection of Caco-2 cells treated with red-emitting QD (B), FA incorporated into the gelatin shell, (excitation 543 nm) and counter-stained with DAPI (excitation 405 nm)

Figure A.5 Three-plane projection of Caco-2 cells treated with red-emitting QD (c), FA covalently bound, (excitation 543 nm) and counter-stained with DAPI (excitation 405 nm)

Figure A.6 Three-plane projection of HT-1080 cells treated with red-emitting QD (B), FA incorporated into the gelatin shell, (excitation 543 nm) and counter-stained with DAPI (excitation 405 nm)

Figure A.7 Three-plane projection of HT-1080 cells treated with red-emitting QD (c), FA covalently bound, (excitation 543 nm) and counter-stained with DAPI (excitation 405 nm)

Figure A.8 Three-plane projection of HT-1080 cells treated with QD-oligo donor (a) (excitation 488 nm, emission 520 nm)

Figure A.9 Three-plane projection of HT-1080 cells treated with QD-oligo acceptor (a) (excitation 543 nm, emission 612 nm)

Figure A.10 Three-plane projection of HT-1080 cells treated with QD-oligo donor and acceptor (a) (excitation 488 and 543 nm, emission 520 and 612 nm)

Figure A.11 Three-plane projection of HT-1080 cells treated with pre-mixed QD-oligo donor and acceptor (a) (excitation 488 and 543 nm, emission 520 and 612 nm)

Figure A.12 Confocal microscope images of Caco-2 cells treated with TGA-capped QDs and counter-stained with Organelle Lights CPF-PM and GPF-Golgi. Top row: Plasma membrane stained in blue (excitation 405 nm); Second row: Golgi apparatus stained in green (excitation 488 nm); Third row: red luminescent QDs (excitation 543 nm); Bottom row: overlay of the first three rows showing no co-localisation of QDs and Golgi apparati.

Figure A.13 Co-localisation plot of QDs and Golgi apparatus computed from confocal microscopy images

References

[1] A. L. Efros, *Soviet Physics Semiconductors-Ussr* **1982**, *16*, 772-775.

[2] A. Moores, F. Goettmann, *New Journal of Chemistry* **2006**, *30*, 1121-1132.

[3] M. Hanauer, S. Pierrat, I. Zins, A. Lotz, C. Sonnichsen, *Nano Letters* **2007**, *7*, 2881-2885.

[4] D. Aherne, D. M. Ledwith, M. Gara, J. M. Kelly, *Advanced Functional Materials* **2008**, *18*, 2005-2016.

[5] Y. Sun, B. Mayers, T. Herricks, Y. Xia, *Nano Letters* **2003**, *3*, 955-960.

[6] X. Xu, N. L. Rosi, Y. Wang, F. Huo, C. A. Mirkin, *Journal of the American Chemical Society* **2006**, *128*, 9286-9287.

[7] M. K. Johnson, in *Physical Methods in Bioinorganic Chemistry: Spectroscopy and Magnetism* (Ed.: L. Que), University Science Books, **2000**.

[8] G. Shemer, O. Krichevski, G. Markovich, T. Molotsky, I. Lubitz, A. B. Kotlyar, *Journal of the American Chemical Society* **2006**, *128*, 11006-11007.

[9] T. Nakashima, Y. Kobayashi, T. Kawai, *Journal of the American Chemical Society* **2009**, *131*, 10342-10343.

[10] Y. Zhou, M. Yang, K. Sun, Z. Tang, N. A. Kotov, *Journal of the American Chemical Society* **2010**, *132*, 6006-6013.

[11] A. J. Mastroianni, S. A. Claridge, A. P. Alivisatos, *Journal of the American Chemical Society* **2009**, *131*, 8455-8459.

[12] Malvern-Instruments, *Zetasizer Nano series technical note MRK654-01* **2005**.

[13] **2008**, http://www.scienceinyoureyes.com/index.php?id=71, Accessed 15/07/2012

[14] **2011**, http://www.fluorescence.com/tutorial/fm-optic.htm, Accessed 16/07/2012

[15] C. M. Lehman, E. L. Frank, *Lab Medicine* **2009**, *40*, 47-51.

[16] R. J. Linhardt, *Chemistry & Biology* **2004**, *11*, 420-422.

[17] J. E. Govan, E. Jan, A. Querejeta, N. A. Kotov, Y. K. Gun'ko, *Chemical Communications* **2010**, *46*, 6072-6074.

[18] Medtronic, Inc., **2012**, http://www.medtronic.com/for-healthcare-professionals/products-therapies/cardiovascular/catheters/balloon-dilatation-catheters/sprinter-otw-semicompliant-over-the-wire-balloon-dilatation-catheter/index.htm, Accessed 16/08/2012

Chapter 1

Introduction

1.1 Reaching the nanoscale

In recent years, materials science research has increasingly focused on reaching and exploring the nano-scale. Exciting nanostructures and their unique properties have opened new perspectives in all fields of science, and especially in biomedicine. Some direct interactions with living cells that used to be out of reach are now made possible by the reduced size of those new materials, and their physical properties have found applications for diagnosis or therapy. This chapter provides some background information about a variety of nanomaterials which are to be developed and investigated in this project.

Nanoscience is the area of research which deals with study of objects having at least one dimension in the 1-100 nm range. From the greek word *nanos*, meaning *dwarf*, the prefix nano- refers to one billionth of a unit. At this scale, physical and chemical properties of materials differ from the bulk, a fact which was exploited long before the existence of nanoparticles came to light. For example, in the Middle Ages, red-stained glass was produced using gold nanoparticles and widely used in church windows.

The discovery of nanoparticles was only made possible in the 1980s by the development of instruments capable of atomic resolution, such as the scanning tunnelling microscope (STM) which was invented in 1981 by Gerd Binnig and Heinrich Rohrer.[1] Nine years later, Eigler and Schweizer used that tool to produce their now famous "IBM" written in individual xenon atoms, thus demonstrating not only visualisation but also manipulation at the nano-scale.[2] The first nano-object, the carbon nanotube, was then discovered in 1991, but before that the discovery of fullerenes for which Robert Curl, Sir Harold Kroto, and Richard Smalley were awarded a Nobel Prize in chemistry in 1996 was a definite starting point for nanoscience research. Since then, many fields of science have been involved into the nanoscale research, from chemistry and physics to biology and engineering. Potential and actual applications have flourished and brought about the era of nanotechnology.

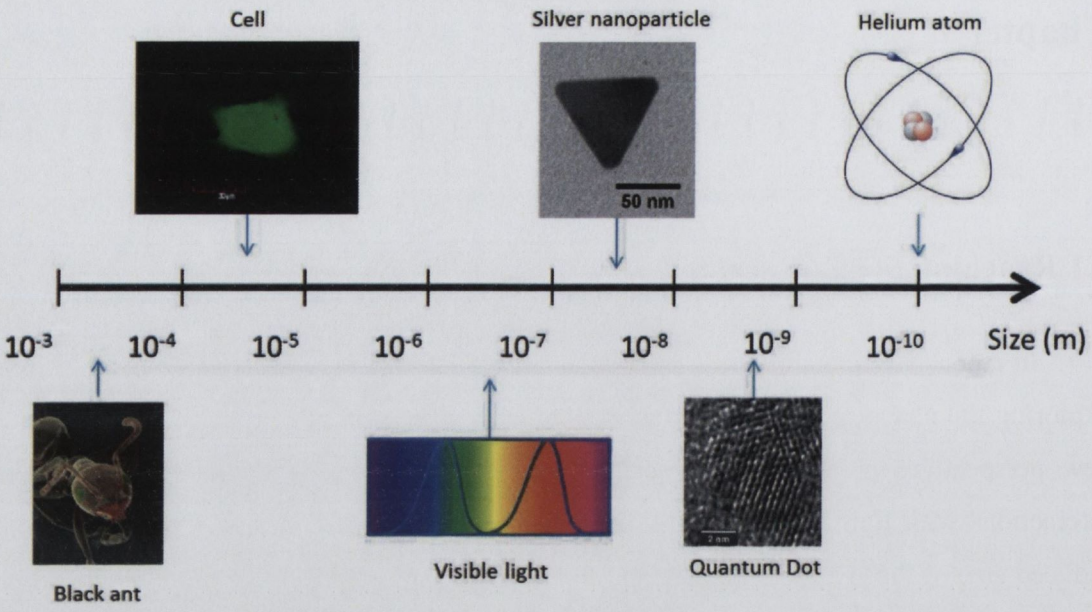

Figure 1.1 Examples of objects in the millimeter to sub-nanometer size range

The present work is focused on the study of semiconductor and metal nanoparticles for potential applications in biomedicine and sensing. As represented on Figure 1.1, nanoparticles dimensions support opportunities for interacting with living cells and visible light in ways that will be further described in this chapter.

1.2 Semiconducting nanocrystals

1.2.1 Structure and properties

In bulk semiconductor materials, the molecular orbitals (MO) of closely packed atoms overlap to form a valence band (VB) and a conduction band (CB), separated by an energy gap (Eg) corresponding to the energetic distance between the higher occupied molecular orbital (HOMO) and the lower unoccupied molecular orbital (LUMO). Consequently, electrons can move from VB to CB if provided with an amount of energy at least equal to Eg. When this occurs for instance at high temperatures, the semi-conductor material conduct electricity as electrons are able to move along the CB.[3] The excited electron leaves behind a "hole" (a positive charge carrier) in the VB; the electron-hole pair, or exciton, has a characteristic radius depending on the material called Bohr radius. In

semiconductor structures of much reduced size however, where the crystal size is smaller than the exciton Bohr radius, the carriers become independently confined, a phenomenon called quantum confinement. The electron-hole pair cannot spatially fit inside the particle to which it is linked and must enter a higher energy state in order to "fit" energetically.[4] It expresses itself in the reduction of the electronic band structure into discrete quantum levels; the smaller the particle the higher the confinement energy and the larger the band gap.[5] In other words, a semiconductor nanocrystal resembles more closely a molecule than a crystal in terms of electronic structure.

Such nanostructures can be two-dimensional (quantum wells or films), one-dimensional (quantum wires) or zero-dimensional which are designated as quantum dots (QDs). For the confinement effect to occur the particle radius should be smaller than either the Bohr radius of electrons, holes or excitons. Therefore, QDs are generally expected to be smaller than 10nm.[6] Quantisation of energy levels means that the particles can only absorb specific wavelengths of light that provide sufficient energy for electrons to overcome the band gap.

Since the band gap depends on the particle size, so does the range of absorption. The colour of nanocrystals is therefore directly linked to their size as larger particles will absorb lower energy i.e. longer wavelength light. When the charge carriers eventually recombine the exciton energy is lost as a photon, in the process of photoluminescence.

However, electrons and holes can also combine to various defects on the particle surface in a process that may or may not be radiative as schematically represented on Figure 1.2. Surface defects tend to be numerous on nanocrystals due to their high surface area to volume ratio, thus making bulk defects usually negligible. Defect related emission is characterised by a broad profile, a large Stokes shift and a longer decay as it was demonstrated for instance for CdS[7] or CdSe[8] whereas intrinsic luminescence is faster, with a narrow full width at half maximum (FWHM) and small Stokes shift (~40 nm). Even in the latter case defects may be present on the surface, which are manifested by a slight dissymmetry of the emission peak at higher wavelengths accounting for the lower energy defect emission.

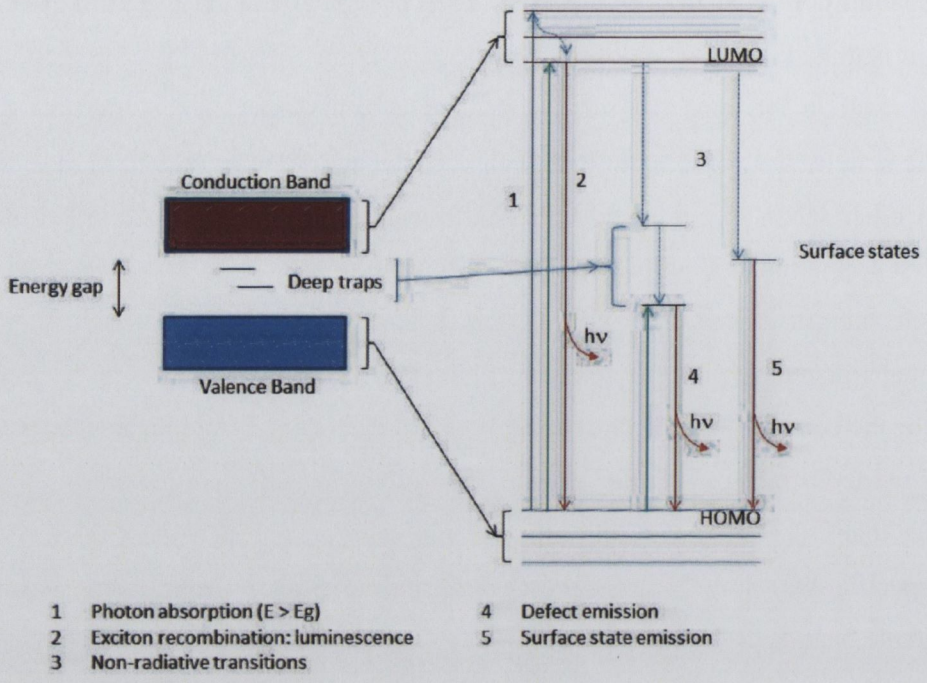

Figure 1.2 Jablonski diagram representing the energy band gap structure in a semi-conductor material and the changes from bulk to nanostructure. Adapted from literature.[4]

A variety of strategies have been developed in order to enhance QD emission efficiency, or quantum yield (QY). These approaches generally involve passivating the surface of the nanoparticles thus reducing surface defects that can lead to non-radiative recombination of the charge carriers.

The core/shell approach is a very common one, where the core QD is coated with a shell of a larger band-gap semiconductor. Typical systems include CdSe/ZnS,[9] CdSe/CdS,[10] CdSe/ZnSe[11] and CdTe/CdSe.[12] Successful passivation of the surface by a semiconductor shell relies on the choice of an appropriate material; the band gap must be wider than that of the core material and the lattice mismatch should be minimum.[11] Core-shell QDs can be either type I or type II. The former configuration arises when the valence band of the shell is lower than that of the core, and the conduction band of the shell is higher than that of the core, resulting in both the electron and hole being confined to the core; on the other hand, in a type II QD, both the valence and the conduction bands in the core are lower (or higher) than in the shell, therefore one carrier is mostly confined to the core while the other is mostly confined to the shell.[12]

Another approach is the use of a polymer coating, such as polyethylene glycol (PEG) or gelatin,[13] which presents the triple advantage of enhancing the luminescence, improving the biocompatibility[13-14] and facilitating further bio-conjugation.[15]

Fluorescence quenching in QDs may occur through two pathways: collisional or static. Collisional quenching involves a contact of the fluorophore, in our case the QD, with another molecule in the solution, which causes donation of an electron from the fluorophore in the excited state. Static quenching, on the other hand, relies on the formation of a complex between the fluorophore and the quencher. When the distance between a fluorophore and, for example, a plasmon active species (such as a gold nanoparticle) is shorter than 1 nm, quenching will occur through energy transfer[16] as non-radiative electron/hole recombination is facilitated. Static photoluminescence quenching may be useful as a detection method for sensing applications.[17]

A wide range of II-VI (group 12-group 16; CdS, CdSe, CdTe) and III-V (group 13-group 15; GaAs, InAs/InP, CdHgTe, HgTe) QDs can be produced using two main synthetic routes: an organometallic strategy based on the high temperature thermolysis of precursors in organic solvents; and an aqueous method, which was developed initially using thiols as stabilizing agents.[18] Our work will focus on the preparation and investigation of water soluble CdTe QDs.

1.2.2 Aqueous growth of CdTe nanocrystals

Semiconductor nanocrystals synthesis is usually a two-step mechanism as first described by La Mer.[19] In the first step, namely the nucleation step, the precursors react to form primary clusters. Then the actual growth occurs, where nanocrystals are formed and grow over time.[20]

The first semiconductor QDs were synthesised through the organometallic route, which is still predominantly used to produce QDs out of a wide range of semiconductor materials including CdS, CdSe, CdTe,[21] PbS,[22] PbSe[23] as well as core-shell CdSe-ZnS[9, 24] or CdSe-ZnSe[11] to name a few. Applications of these however are limited by the fact that they easily oxidise in air and thus lose their luminescence. Their water insolubility also makes them unsuitable for biological imaging. An aqueous synthetic route was then

developed based on the stabilisation with polyphosphates or thiols.[25] The method is limited to a small number of materials where the alignment of band energy levels is such that deep trap emission is inhibited by the electronic contribution of the thiol ligands. The resulting QDs, generally CdTe or CdSe, exhibit very good long-term stability and luminescence despite the absence of an inorganic shell. The binding of thiol groups to Cd atoms is believed to create a thin CdS shell passivating the surface.[25]

The main difference between the organic and aqueous synthetic approaches is that in the former, the nucleation occurs at very high temperature (300 °C) and is stopped by the injection of a ligand solution at room temperature, whereas in the aqueous synthesis, the nucleation step is conducted at low temperature, followed by a discontinuous and thermodynamically controlled growth as the temperature increases, and the actual QD formation takes place at the boiling point.

This essentially means that Ostwald Ripening (OR) is predominant in the aqueous synthesis as opposed to the organic-based one.[20] At higher temperature, the reaction is driven by thermodynamic forces that tend to lower the surface area to volume ratio, therefore inducing the dissolution of smaller crystals or their fusion into larger ones. This ultimately leads to a narrowing of size distribution.[26]

CdTe nanocrystals can be made water-soluble by using an appropriate thiol based organic stabilizer (e.g. thioglycolic acid – TGA). Cadmium ions being large, with filled *d*-orbitals, are classified as a "soft" acid and react well with "soft" bases containing large, easily polarisable atoms, such as thiol ligands. The stabilisation of CdTe nanocrystals relies on the ability of thiol groups to form strong complexes with cadmium ions.[27] Besides providing solubility, stability and surface functionality to the quantum dots, the thiol stabilizer allows for control of the synthesis kinetics and passivation of the surface dangling bonds.[28]

The choice of stabilizer molecule is very important. Its structure will affect the growth and stability of the QDs, as well as provide different properties and functionalisation opportunities. For instance, the effective charge of the particle may be varied, as well as the pH range of solubility, when the stabilizer bears an amine group instead of a carboxylic acid group. Figure 1.3 displays a few of the most commonly used thiol stabilizers.

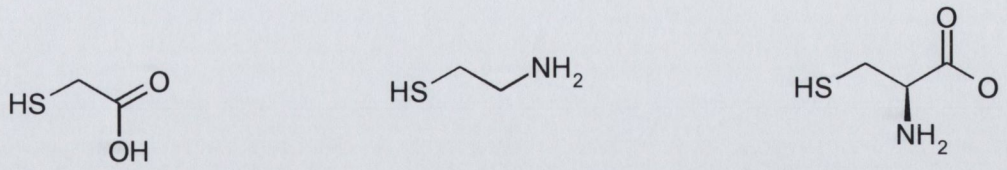

Thioglycolic acid (TGA) Cysteamine L-Cysteine

Figure 1.3 Three stabilisers commonly used in aqueous CdTe QD synthesis

Previous studies have shown that during the synthesis, a monothiocomplex is formed first, but a dithiocomplex eventually becomes dominant.[27] Thus, a cadmium:thiol ratio of 1:2 provides good stabilisation of the precursors leading to stable quantum dots colloidal suspensions. However, it was found that decreasing the ratio down to 1:1.5 allowed formation of QDs with a much higher quantum yield (around 30%), whilst maintaining stability. The reason for this phenomenon lies in the growth mechanism of QDs in aqueous solution.

The aqueous nanocrystal growth occurs through diffusion of monomers, either Cd-ligand complexes from the solution or from smaller clusters (OR), and coalescence with the existing nanocrystal. Electrostatic interactions therefore play a pivotal role. In the colloidal stability theory,[29] nanoparticles are kept stable in suspension thanks to repulsive electrostatic forces between similarly charged particles. The theory relies on the model of an electrical double-layer surrounding each particle and moving with it when subjected to an external field as represented in Figure 1.4. The nanoparticle can be viewed as composed of an inorganic core, a ligand shell, an adsorbed layer composed of contact counter-ions and representing the interface between the solid nanocrystal and the liquid environment, and a diffuse layer where the concentration of counter-ions exponentially decreases from the adsorbed layer to the solvent.[29]

A number of factors influence the nature and thickness of the electrical double layer, including pH, ionic strength and nature of counter ion. For a nanocrystal to grow, monomers must traverse through the diffuse layer and adsorb and coalesce with the nanocrystal in the adsorbed layer. A high precursor concentration in the form of Cd^{2+} ions comes to an increased ionic strength, so does a high pH which is obtained by addition of NaOH; a higher ionic strength means a diminution in the diffuse layer thickness and a lower surface charge, thus facilitating monomer diffusion. Consequently, such conditions

will lead to a faster growth rate. Increasing the ratio of Cd to Te will provide an excess of Cd-ligand complexes, and therefore increase the ionic strength and have the same effect as above.[30]

On the other hand, the same conditions give poor charge-selectivity of the diffuse layer. For instance, Cd(TGA), $Cd(TGA)_2^{2-}$ and $Cd(TGA)_3^{4-}$ are all able to reach the adsorbed layer; due to steric effects though, the coalescence of $Cd(TGA)_2^{2-}$ and $Cd(TGA)_3^{4-}$ with the nanocrystal creates more surface defects and eventually leads to a lower QY.[31] It is therefore crucial to maintain the ionic strength at an optimum level to ensure a decent QY.

Finally, both the growth rate and the QY are affected by the Cd:ligand ratio. Increasing this ratio leads to increasing the concentration of monothiocomplex and decrease that of di- and trithiocomplexes.[28] As monothiocomplexes have a lower charge, they diffuse more easily through the diffuse layer, and hence induce a faster growth, and their low spatial obstruction lowers surface defects and ensures a strong luminescence of the QDs.[30]

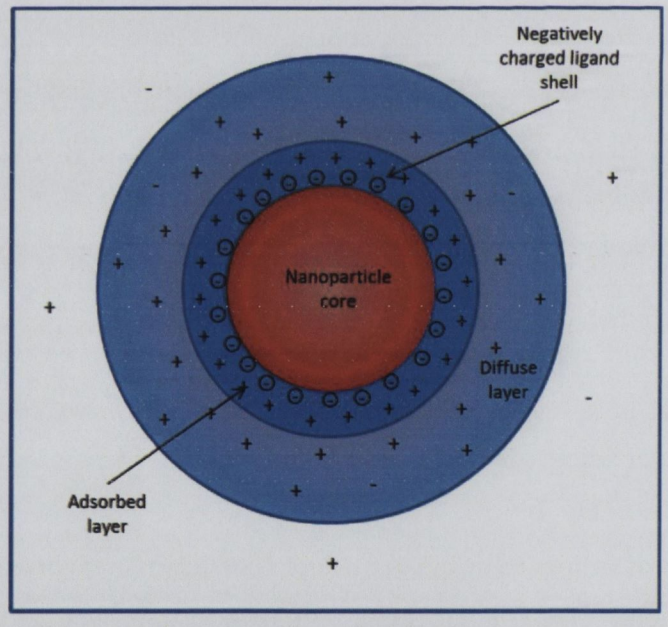

Figure 1.4 Schematic representation of the electrical double layer in the colloidal stability theory

1.2.3 Applications of QDs in biological imaging, diagnostics and therapeutics

QDs have been investigated for a wide range of applications, from solar cells and solar concentrators[32] to display technology.[33] The present work however focused on

exploiting the optical, physical and chemical properties of QDs for biomedical applications.

The most widespread use of QDs in biomedicine is for *in vitro* biological imaging which consists in illuminating the cell membrane, the cytoplasm or selected organelles using a fluorophore. Choosing an appropriate combination of staining agents enables one to elucidate cellular structures or mechanisms by visualising them with a fluorescence or confocal microscope.

In this area QDs have a number of advantages over organic dyes. They present a continuous absorption spectrum for wavelengths that are shorter than the emission wavelength, and a narrow and symmetrical emission which can be tuned to a particular wavelength. It is therefore possible to excite QDs of a number of colours with the same source and to spectrally resolve their emissions.[34] CdTe, CdSe and CdS are especially attractive as their quantum confinement region, and therefore emission, spans the entire visible spectrum where very few dyes provide a decent quantum yield. QDs are believed to be up to twenty times as bright and a hundred times as photostable as conventional fluorophores.[34] QDs also exhibit longer luminescence lifetimes (typically 10 to 100 ns) than organic dyes (under 10 ns) which allows for better discrimination from background luminescence caused by sample auto-fluorescence or scattered excitation light.

On the other hand, the bi- to multi-exponential decay of QD luminescence limits the possibility of species identification using time-resolved luminescence measurements.[35] Other drawbacks of QDs such as toxicity and poor stability have been tackled by surface modifications which also ensure high thermal and chemical stability.[34]

Building on the intrinsic toxicity of QDs, applications for therapeutics have also been explored and especially photodynamic therapy (PDT). In this technique, a dye molecule is used as a photo-sensitiser. Energy transfer between its excited state and the triplet ground state of molecular oxygen produces singlet oxygen which in turns causes apoptotic cell death. QDs may be used to increase excitation of the photo-sensitiser through energy transfer and therefore induce the production of more singlet oxygen for more efficient PDT.[36] QDs could also be used as photo-sensitisers themselves provided that energy transfer to molecular oxygen is sufficient.

All applications in therapeutics however rely on the capacity to preserve healthy tissue while treating targeted zones as well as the rapid clearance of QDs from the body which remains uncertain.[37] QD toxicity will be further discussed in the next section.

Biosensing is another family of application in the field of biomedicine. On-Off fluorescence sensors have been developed for the detection of glucose,[38] DNA[39] or biomarkers[40] to name a few. The most common approach is to use the initial binding of a quencher to the QDs which will be displaced by the analyte thus restoring the luminescence. A major issue with this approach however is the extreme susceptibility of QD luminescence to the environment which does not always allow for full restoration of the luminescence and thus for good sensitivity of the sensor.[41]

1.2.4 Aspects of QD toxicity

Many semiconductor QDs are made of intrinsically toxic components, both acutely and chronically, such as cadmium, tellurium or selenium, and their use in biological system naturally raises the question of QD toxicity. Extensive studies have been published on the effect of QD exposure on live cells,[42] with a focus on cancerous cells in order to use QD toxicity rather than vainly combat it. The mechanism and extent of QD cytotoxicity is dependent on a number of parameters such as core material,[43] surface coating,[13, 44] size[14, 45] and concentration[14] of QD, but also cell type.

One major cause of QD cytotoxicity is believed to be the leaking of Cd^{2+} ions from the core of the nanoparticles.[46] They are taken up into calcium membrane channels where they accumulate, thus disrupting the normal cell machinery. Cd also interacts with DNA, breaking up strands and mutating chromosomes, and inhibits the synthesis of DNA, RNA and proteins.[47] Cells possess defence mechanisms against metal poisoning which have been shown to be activated upon exposure to QDs.[48] For instance, the metallothioneins superfamily of proteins becomes over-expressed after short-term exposure to QDs.

Cd release from QDs is mainly due to oxidation of the surface; therefore a common strategy to reduce the leaking is to passivate the surface with a shell of inorganic (eg. ZnS) or polymer material.

The second suspected mechanism of toxicity however is less controllable and is not reduced by the presence of a shell; it consists in the production of reactive oxygen species

(ROS) due to resonance energy transfer from QD to molecular oxygen, especially upon photoactivation by UV light. The presence of high levels of ROS, such as singlet oxygen, superoxide anions, hydroxyl radicals or hydrogen peroxide, brings the cells in a state of oxidative stress which may eventually lead to cell death.[46] ROS interact with all biomolecules and affect the cell structure and functioning at various levels. By reacting with lipids they disrupt membranes, and if mitochondria or lysosomes membranes are ruptured this leads to apoptosis; reactions with peptides and proteins mean transmitters may be affected and so will be signalling mechanisms; they oxidise DNA bases which leads to strand breaking.[49]

Coating or ligands present on the surface of QDs also have an impact on cytotoxicity. First, the shell and ligands may modify the mode of uptake and localisation in the cells. Target-specific biomolecules such as peptides or antibodies can be attached to the surface of QDs which will determine the organelle where they will be brought.[50] This, in turn, has an impact on cytotoxicity as they interact with said organelle which can be a mitochondrion or a lysosome for instance. In the latter, the acidic environment will cause ligands to detach and QDs to decompose, leading to the release of a large amount of cadmium.[50] If the QDs are not functionalised, however, meaning that they do not bear any specific biomolecule, they will enter the cell through non-specific endocytosis and will be mostly found in the cytoplasm or in the nucleus for the smaller ones.[14, 50] The penetration of small QDs into the nuclei is believed to be the main reason for their higher cytotoxicity compared to their larger counterparts.[45]

Thiol-stabilised aqueous CdTe QDs have been used extensively for biological imaging and sensing applications even though the absence of an inorganic shell and the short length of thiol ligands make them likely to be oxidised and to release Cd^{2+} ions. They indeed exhibit a higher cytotoxicity upon long term exposure[51] but this can be counteracted by the addition of a layer of a biocompatible material such as gelatine[13-14] or polyethylene glycol (PEG)[52] to prevent leakage of Cd^{2+} ions.

For all types of QDs there have been signs of the concurring involvement of Cd poisoning and ROS production in cytotoxic effects. Exposed cells showed signs of apoptosis: plasma membrane blebbing, shrinkage and deformation of nucleus and condensation of chromatin on the short term, then swelling of mitochondria and lysosomes and their localisation in the perinuclear region.[45] Damage to lysosomes is known to be

induced by oxidative stress but also by metal poisoning. Cell death could be significantly reduced by the presence in the cell culture of an anti-oxidant which was evidence of the involvement of ROS.[45] On the other hand, concentration-dependent cell death was observed when CdTe QDs were embedded in polymer microcapsules which allowed release of Cd^{2+} but prevented other direct QD-cell interactions. Low concentrations resulted in adherent cells detaching from slow poisoning and apoptosis whereas higher concentrations induced a more rapid death, probably by necrosis, with dead cells still adhering to their substrate.[53]

QDs being inherently cytotoxic through a range of mechanisms, it is unlikely that they will ever be made safe to living organisms. They can however be exploited as potential anti-cancer agents since tumour cells are very resilient and require aggressive treatments as it is the case with current chemotherapy. For instance the generation of ROS is useful in photodynamic therapy. It is nonetheless crucial that QDs would affect as little as possible healthy tissues and they must therefore be target-specific as well as rapidly cleared from the system. *In vivo* animal studies are aimed at determining their distribution and clearance. They showed that QDs significantly accumulate in the liver, more so than in the spleen, and are also found in lymph nodes and bone marrow. Surface modifications strongly influence their aggregation within tissues and clearance from blood plasma. Studies have shown rather low *in vivo* toxicity but also low renal clearance which could be an issue on the long term.[54-55] Other studies however have demonstrated that QDs can induce epigenetic changes, which means that they could induce persistent modifications of gene expression with serious long-term effects.[56]

1.3 Silver and gold nanostructures

Silver and gold nanoparticles have been widely investigated for their peculiar optical and electronic properties enabling potential applications in biological sensing,[57-59] drug delivery[60] or optoelectronics[61] amongst others. Similarly to QDs, their small sizes confer them some degree of electronic confinement. Their metallic nature however results in very different effects than those observed in semiconductors. In bulk metals, the valence and conduction bands are not separated by any energy gap, a property responsible for their high conductivity but also for the appearance of surface plasmons.

1.3.1 Surface Plasmon Resonance (SPR)

Plasmons are the collective oscillation of electrons that occur in a metal subjected to an external electromagnetic field. At the interface of the metal with a dielectric medium, surface plasmons can arise from interaction with light and propagate as an evanescent wave, or polariton, along the surface until the energy is dissipated through absorption by the metal or radiation. In the case of nanoparticles the surface area is so large that all plasmons can be seen as polaritons as opposed to the free plasmons occurring in bulk metal.

With nanoparticles being much smaller than the wavelength of visible light, it can be considered that all the electrons confined in a given nanoparticle are subjected to the same field at any given time; this is referred to as the quasi-static hypothesis. Displacement of the electron cloud by the electric field results in the creation of surface charges as represented on Figure 1.5. The electrons can thus be assimilated to an oscillator which may be described by the Maxwell equations. Consequently, conditions may be found for which the electron cloud will resonate. Such conditions were calculated from the Maxwell equations, and the Mie solution is generally recognised as the most accurate.[62] The Mie solution considers the problem as a purely scattering one and determines the scattering cross section (C_{ext}) which is directly proportional to the intensity of scattering, as described by equation (1).

$$C_{ext} = \frac{24\pi^2 R^3 \varepsilon_m^{2/3}}{\lambda} \frac{\varepsilon_2}{(\varepsilon_1 + 2\varepsilon_m)^2 + \varepsilon_2^2} \qquad (1)$$

With R the radius of the particles, ε_m the dielectric constant of the medium and $\varepsilon(\omega) = \varepsilon_1(\omega) + i\,\varepsilon_2(\omega)$ the dielectric constant of the metal. Plasmon resonance corresponds to when the cross section is maximal.

Although not providing a physical explanation for the mathematical model, the Mie solution highlights however several parameters which influence the position of the plasmon resonance, such as the size, the environment and the composition of the nanoparticles. First of all, the diameter affects the dielectric constant of the metal and thus modifies the intensity, the position and the bandwith of resonance.

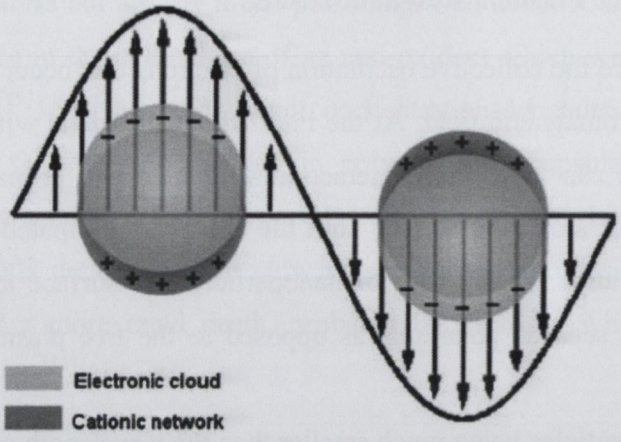

Figure 1.5 Schematic representation of electronic cloud displacements in nanoparticles under the effect of an electromagnetic wave[62]

Ligands or other functional molecules bound to the surface of nanoparticles also play a crucial role in the position of plasmon resonance. On the one hand they affect the dielectric constant of the surrounding medium and on the other hand they interact electronically with the metal core, partially oxidising or reducing it and therefore changing the electronic density; both parameters influence the resonant wavelength.[62] This property has been widely used in bio-detection and for monitoring chemical reactions.[63]

Practically, plasmon resonance results in both high scattering and absorption of light of that particular wavelength and therefore a high extinction coefficient.[64] A sharp peak is thus observed in the absorption spectrum of nanoparticles. The position of the resonant wavelength may be predicted using calculation of increasing complexity as the particle degree of anisotropy increases. There are however a number of rules that can be used to predict the absorption spectra of particles relative to each other:[65]

- Increasing diameter of spherical particles causes the resonance wavelength to shift to lower energy (red shift);

- Increasing diameter of spherical particles causes the resonance peak intensities to increase;

- The resonance frequencies for non-spherical particles redshift with increasing corner sharpness and particle anisotropy;

- The intensity of the resonance peak increases if charges separate with mirror symmetry;

- The number of resonance peaks increases with the number of ways that the particle can be polarized.

1.3.2 Structure and properties of gold nanoparticles

Bulk crystalline gold has a face-centred cubic (fcc) structure. X-Ray Diffraction (XRD) patterns revealed that nanoparticles have the same type of structure, only with a much higher local structural disorder. For particles around 3 nm in size, the fcc structure remains a good approximation, but computer simulations integrating extended structural defects and division of the particle into domains provided a better description.[66]

In general small particles (3 to 15 nm) are spherical in shape, whereas bigger ones tend to be faceted nanocrystals, as it can be observed in TEM images.[67]

The atomic disorder in gold nanoparticles accounts for the broadening of the electronic density of states which leads to a blue shift in optical absorption as the particle size decreases.[68] For instance, 10 nm-sized gold nanoparticles exhibit a plasmon peak at around 520 nm as illustrated by Figure 1.6.

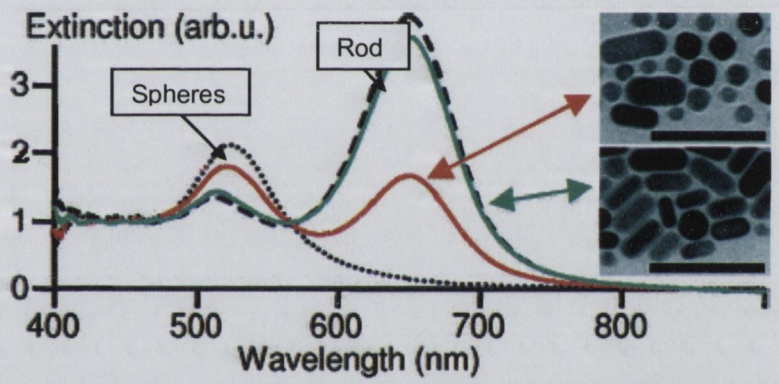

Figure 1.6 Absorption spectra of gold particles of various shapes and sizes[69]

1.3.3 Structure and properties of silver nanoparticles

Similarly to gold, silver nanoparticles mostly preserve the fcc structure of the bulk.[70] It was however reported that a small portion of silver nanoparticles prepared in water adopt the more unusual hcp structure. Furthermore, in the event of coalescence upon drying, which was observed by Fast Fourier Transform (FFT) High resolution (HR) TEM, the fcc-structured nanoparticles are converted into hcp to their contact, and form 3D dendritic microstructures bearing this crystal structure.[71] This peculiar crystal structure transformation is thought to be the basis for the anisotropic growth of silver nanostructures as will be discussed in the next paragraph.

1.3.4 Synthesis of anisotropic silver nanostructures

Silver nanoprisms are anisotropic nanomaterials that have the particularity to be grown in isotropic medium. The optical properties of metal nanoparticles, especially their surface plasmon resonance (SPR) being highly dependent on their size and shape, means such nanoprisms have attracted much attention in recent years. The two traditional routes of synthesis are: (i) photochemical,[72] which produces good quality particles but can be very time-consuming, and (ii) thermal,[73] a quicker way which often produces a range of shapes and sizes. An alternative method was developed for a rapid synthesis at room temperature, producing particles of a controlled size in a very reproducible way.[74]

Silver nanoparticles have been synthesised in various controlled shapes and sizes, such as nanorods, nanowires[75] or nanocubes.[76] These anisotropic shapes are usually obtained owing to the preferential binding of stabiliser molecules to the more stable <111> faces of the silver crystal, thus directing the growth in the <100> and <110> faces left open to the growth medium.[76]

In our research group, the aqueous synthesis of flat triangular silver nanoprisms have been developed and investigated for growth mechanism.[74] This particular type of anisotropic growth was found not to depend on the presence of tri-sodium citrate, the stabiliser, and therefore to arise from a different effect. HR-TEM and XRD analyses highlighted the presence of parallel stacking defects in the {111} direction in silver nanoprisms as well as in the seed particles.[77] The very large number of defects gives rise to a continuous portion of crystal exhibiting a hcp structure instead of the regular fcc structure and forming a lamellar region of approximately 1.5 nm thick.[74] This results in the hcp defect region being exposed to the growth medium on the edges of the particle. Not being the natural structure of the silver crystal, hcp is expected to be less stable than fcc and therefore sustain a faster growth from the edges.

Due to the hexagonal symmetry of both fcc and hcp structures however, one could expect equal growth from all edges resulting in flat hexagonal nanoprism. The triangular shape is explained by the position of the hcp layer in the fcc sandwich. As presented on Figure 1.7, a hexagonal nanoplate would be exposing alternating <100> and <111> faces on the edges; the assymetrical intercalation of the hcp layer would therefore produce three faces with a larger <111> than <100> and the remaining three with a larger <100> than

<111> face. The latter will be less stable and thus grow faster, which will ultimately result in the formation of flat triangles.[74]

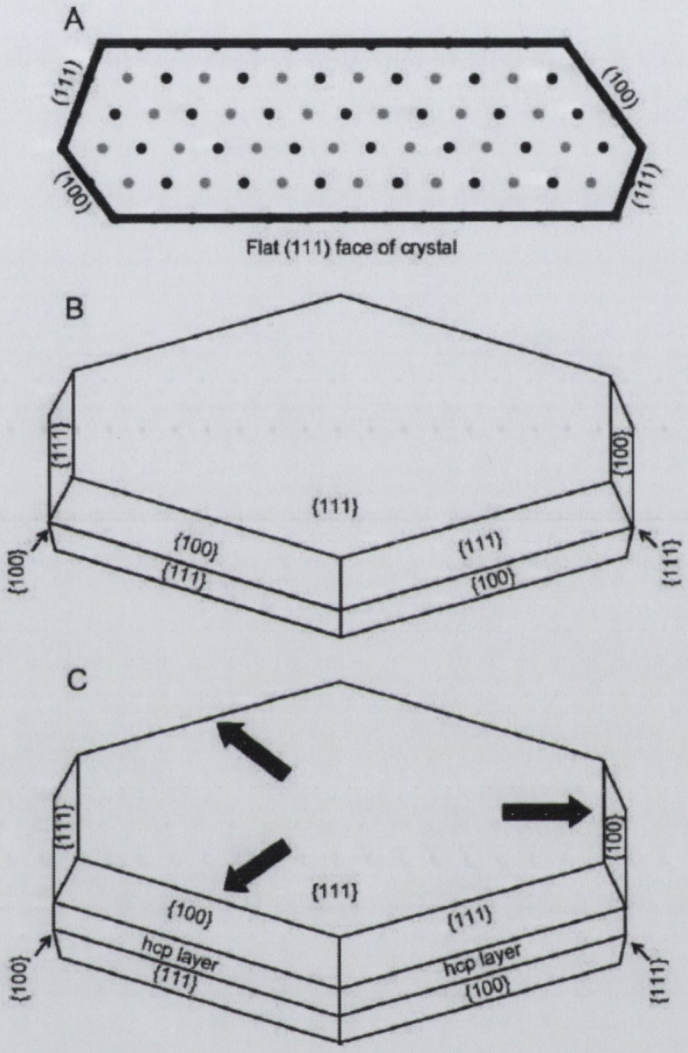

Figure 1.7 A) Schematic illustration of a <110> oriented segment of a fcc crystal. The edges of crystal cut in this manner will have alternating pairs of <100> and <111> faces. B) Schematic of a nanoplate constructed from a single fcc crystal showing alternating pairs of <100> and <111> faces. C) Schematic of a nanoplate with a defect-induced hcp layer sandwiched between two fcc layers of unequal thicknesses. The block arrows indicate the directions of preferential growth.[74]

Another type of anisotropic metal nanostructures are one-dimensional (1D) objects, exhibiting to distinct axes with an aspect ratio higher than 5. Such structures are typically referred to as nanorods if their aspect ratio is comprised between 5 and 25, and nanowires above 25. Many different methods have been developed in order to anisotropically confine the highly symmetrical fcc structure of gold and silver. Some consist in physical direction of growth on hard templates such as porous alumina.[78] Others employ the colloidal route,

a seed-mediated synthesis where the 1D growth is induced and maintained by surface-capping agents. Most common directing surfactants are Cetyl trimethylammonium bromide (CTAB)[79] and polyvinylpyrrolidone (PVP).[80]

In both cases investigations revealed a similar mechanism of nanowire growth. The synthesis starts the same way as that of silver nanoprisms with the formation of small seeds. These seeds are then grown into larger metal nanoparticles through Ostwald ripening. This is a crucial step as it allows for the seeds to adopt the crystal structure that is necessary for one-dimensional growth: beyond a critical size, around 8 nm, a multiply twinned structure becomes energetically more favourable as opposed to the mostly monocrystalline structure described above.[80] The resulting nanoparticles exhibit five twin plane boundaries, five triangular <111> faces at each end, and five <100> faces which will become the side faces of the nanowires[81] as illustrated on Figure 1.8. Appropriate stabilisers, CTAB or PVP, preferentially bind to the more reactive <100> faces and block the growth from those faces. Simultaneously, the exposed twin planes are the highest energy sites and therefore attract silver atoms which deposit on the seeds. Once the elongation has been initiated, the stabilisation of side faces allows for rapid growth of the nanowires.

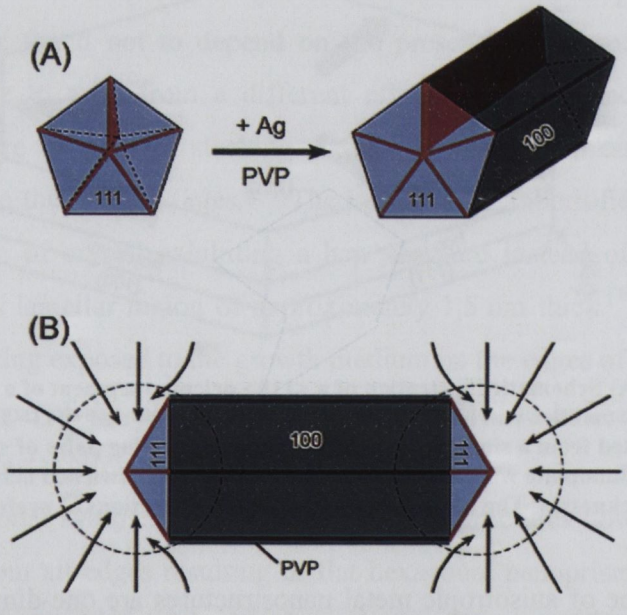

Figure 1.8 Schematic illustration of the mechanism proposed to account for the growth of silver nanowires with pentagonal cross sections: (A) Evolution of a nanorod from a multiply twinned nanoparticle of silver under the confinement of five twin planes and with the assistance of PVP. (B) Schematic model illustrating the diffusion of silver atoms toward the two ends of a nanorod, with the side surfaces completely passivated by PVP.[80]

1.3.5 Growth of gold nanostructures on silver templates

One major obstacle in exploiting silver nanoparticles is their susceptibility to etching agents such as NaCl. Gold on the other hand is very resistant to harsh conditions and present the other advantage of being biocompatible. Galvanic replacement has been exploited to deposit gold onto silver templates to produce either partial[82] or full coating, new hollow nanostructures[76, 83-84] or even nanorings or nanoframes.[85]

Deposition of a thin layer of gold around the edges of silver nanoprisms was found to prevent etching and ensure stability of the particles over time. Building on the previously described theory that <100> faces on the sides of the nanoplates are much more reactive than the large triangular <111> faces, it was observed that galvanic replacement occurs primarily on the former. When using a small amount of gold salt, not sufficient to oxidise all of the silver, a layer of gold around the edges of the nanoplates was thus obtained. The <111> faces were left exposed, but their low reactivity prevented them from being etched by chloride ions.[82]

When a large excess of gold salt is added to the silver nanoparticle suspension, complete galvanic replacement occurs and results in the full coating of the silver template and simultaneous oxidation and dissolution of silver. This leads to the formation of hollow structures, so-called nanoboxes,[84] composed of a gold-silver alloy. Partial coating and subsequent etching of silver was also used to create nanoframes or nanocages.[85]

In the same way, gold may also be reduced on silver nanowires to form either gold coated nanowires or hollow gold nanotubes.[86]

1.4 Functionalisation and bio-conjugation of nanoparticles

The unique optical and electronic properties of both metal and semi-conductor nanoparticles make them good candidates for labelling or detection applications. However, frequently for this purpose, some surface modification is required.

1.4.1 Bio-conjugation of Quantum Dots for labelling and detection applications

Thiol stabilised QDs are easily functionalised using a terminal carboxylic acid or amine group from the stabiliser. QDs have proved very useful for bio-imaging as they

display several advantages over organic dyes, such as narrow and symmetric emission spectra, broad absorption spectra and less susceptibility to photobleaching.[87] In addition QDs can be linked, for instance, to an antibody in order to detect a specific antigen *in vitro,*[88] or to a particular protein as a label allowing the tracing of cancerous cells *in vivo.*[89] QDs have also been used in DNA sensing based on fluorescence resonance energy transfer (FRET) to an organic dye.[90-91] Such conjugations generally involve EDC activation of the terminal acid carboxylic group of the ligand on the surface of the QDs,[92] although electrostatic interactions may also be used.[93-94]

1.4.2 Conjugation of oligonucleotides to metal nanoparticles

Oligonucleotide-conjugated metal nanoparticles can be used for various applications based on their plasmonic properties. Hybridisation and dehybridisation is easily observed by the shift in maximum absorption wavelength that occurs upon variation of the distance between particles. This has been widely used for biosensing, allowing the detection of a specific DNA sequence for example.[57, 95]

However, applications of those conjugates are found beyond the field of bio-diagnostics as their functionality may be triggered by an external stimulus. Upon excitation by a laser[96] or an electric field,[97] DNA dehybridisation can be remotely controlled, giving rise to selective heat transfer[97] or molecular release.[96] The latter was proved useful for drug delivery or gene therapy due to the increased stability of oligonucleotide-modified metal nanoparticles against enzymatic action[98] and their facilitated internalisation by the cells[99] compared to free oligonucleotides. Conjugates also exhibit significantly higher affinity constants with targets.[100]

Oligonucleotide-directed assemblies of metal nanoparticles which are reported in the literature include core-satellite silver-gold aggregates,[101] satellite structures composed of gold particles of different sizes,[102-103] shape-controlled groupings using branched DNA scaffolds[104] and one dimensional structures. Figure 1.9 displays examples of oligonucleotide-directed assemblies of gold nanoparticles both with a schematic representation and TEM images of the actual structures. In order to precisely control the shape and size of aggregates that are formed, particles bearing one, two or many oligonucleotides need to be parted from each other, which can often be achieved by electrophoresis.[101, 105-106]

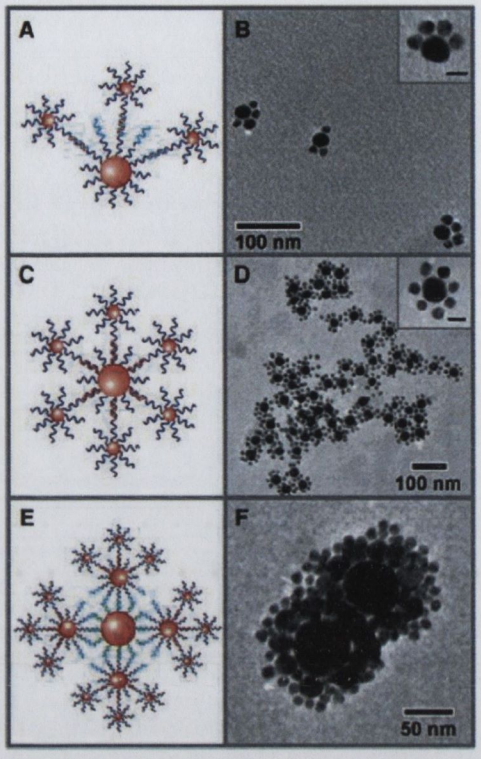

Figure 1.9 Directional assembly of oligonucleotide-functionalised AuNPs into cat paws (A, B), satellites (C, D), and dendrimer-like structures (E, F).[103] Scale bar: 20 nm

1.4.3 Gelatin-nanoparticle composites

Gelatin is a mixture of peptides extracted from collagen of animal sources. Collagen is the main component of the connective tissue matrix, such as of skin, bone and tendon. It is composed of a triple helical structure forming fibres which are arranged in bundles, or fibrils as represented in Figure 1.10. Alkali- or acid-based hydrolysis of collagen results in the breaking of covalent bonds between amino acids at random points. Gelatin refers to these random chain molecules. Gelatin, under its commercial name gelatine, is commonly used in the food industry for its gelling property. It forms a high viscosity solution in water which rapidly turns into a gel at room temperature. Its melting point being *circa* 35 °C, slightly below the body temperature, the gelling and melting properties are widely exploited for *in vivo* interactions. It is notably the principal ingredient of most drug capsules.

The chemical composition of gelatin is generally similar to that of the parent collagen[107] but their physical properties including melting point and gel strength may vary significantly depending on the preparation process.[108] When dissolved in hot water, the

triple helix is denatured by the breaking up of hydrogen and electrostatic bonds to form one, two or three random chain gelatin molecules. Upon cooling, triple helical zones are obtained through cross-linking as well as disordered zones. This phenomenon is responsible for the gelling property of gelatin.

Gelatin can be formed into nanoparticles and loaded with a drug[109-111] to serve as a **delivery vehicle, or a "nano-tablet"**. It has also been employed to coat CdTe QDs, thereby improving their biocompatibility[14, 112] but also their luminescence efficiency.[13] The work presented on this thesis will build on the promising results obtained with gelatinated CdTe QDs, so-**called "Jelly Dots", in order to develop drug delivery or diagnostics tools through** further functionalisation and use of different materials.

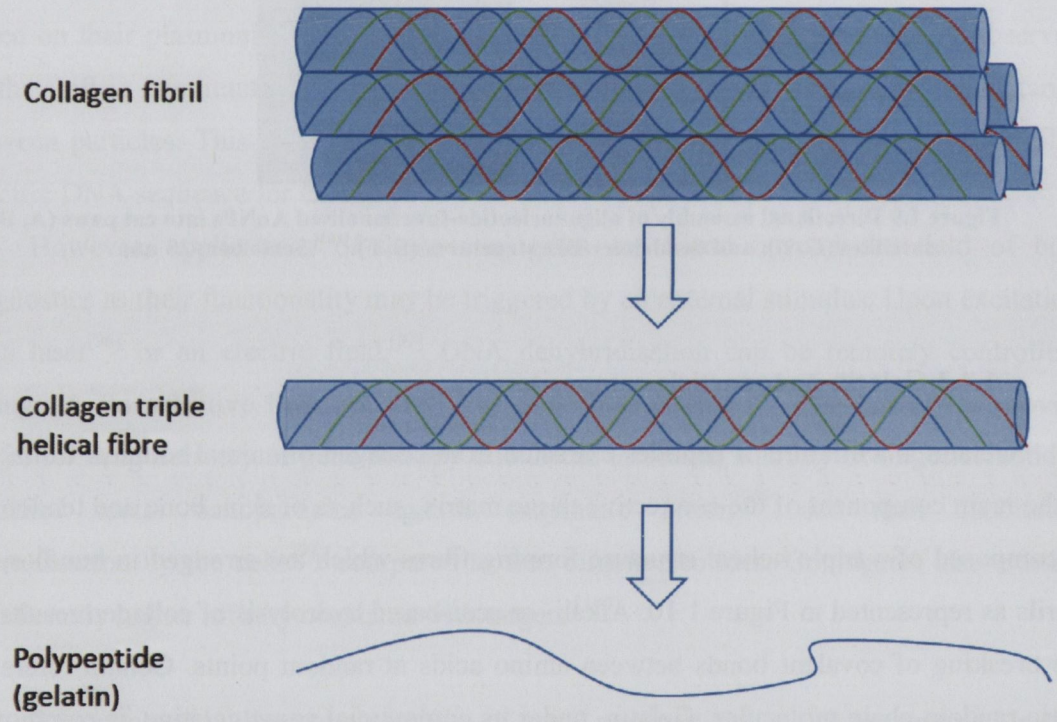

Figure 1.10 Schematic representation of the structure of collagen, which may be broken down into gelatin

1.5 Circular dichroism in nanostructures

In circularly polarised light, the electric field vector rotates uniformly about the direction of propagation, thus forming a helix in space while propagating as illustrated by Figure 1.11.

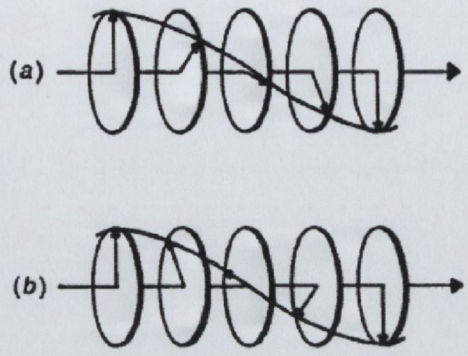

Figure 1.11 Schematic representation of (a) right-polarised light and (b) left-polarised light. The horizontal arrows represent the directions of propagation, and the arrows perpendicular to that denote the instantaneous spatial direction of the electric vector.[113]

Optical activity is the ability of a compound to rotate the plane of polarised light which results either in Circular Dichroism (CD), a phenomenon by which a substance absorbs right- and left-polarised light differently, or rotary dispersion depending on the wavelength.[114] A CD spectrum represents the wavelength-dependent differential absorption of the sample ($\Delta A=A_L-A_R$, the difference between the absorbance of left- and right-polarised light) which can be expressed as molar circular dichroism $\Delta\varepsilon= \Delta A/lc$, or molar ellipticity θ in degrees.[115] Such optical activity normally arises from chiral compounds which naturally present a dissymmetric structure.

Nanoparticles (NPs) do not usually demonstrate CD, even though they may be individually chiral, due to their inhomogeneous nature. They are random assemblies of atoms therefore each nanoparticle has a unique geometry. It is however possible to induce a degree of CD in metal NP systems using various molecules and strategies.

There are a few different mechanisms which can make metal nanoparticles (mainly Ag and Au) or semiconductor QDs exhibit CD. They can be divided into three groups depending on whether they lead to intrinsically chiral NPs, chiral assemblies of NPs or to a projection of the optical activity of a chiral molecule associated with the metal NPs through interference with the electronic transitions. Most strategies involve a chiral species interacting with the achiral nanoparticle.

The ways of generating CD in metal nanoparticles are very different depending on the metal due to their respective modes of interaction with chiral ligands.

1.5.1 Intrinsically chiral metal nanoparticles and QDs

1.5.1.a Intrinsically chiral gold nanoparticles

Gold nanoparticles are usually synthesised by the reduction of a gold salt in presence of a ligand which chelates to the gold ions and eventually acts as a stabiliser for the nanoparticles. Citrate is the most widely used stabiliser for gold NPs although thiols also make excellent ligands owing to the strong affinity of gold for sulphur. Among these are a number of chiral amino acids. The stabilisation of gold NPs with such molecules results in a new CD spectrum, with peaks appearing in the plasmon region. Table 1 provides a few examples of suitable chiral stabilising ligands found in the literature.

Table 1.1 Chiral ligands leading to chiral gold nanoparticles

L-glutathione[116]	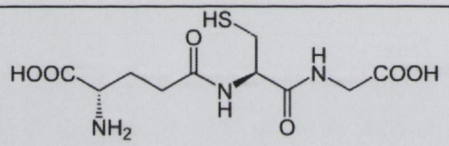
L/D-Penicillamine[116]	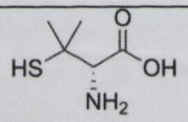
N-isobutyryl-D/L-cysteine[117]	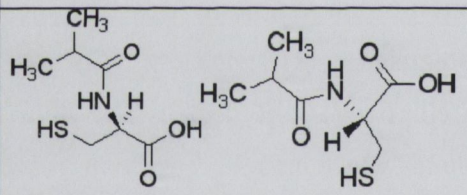
s(R)/(S) 2,2'-bis-(diphenylphosphino)-1,1'-binaphtyl (BINAP)[118]	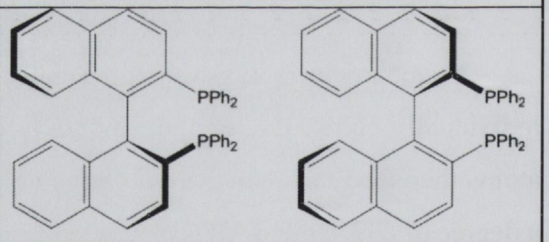 (S)-BINAP (R)-BINAP

The CD exhibited by these gold nanoparticles is not simply due to the presence of chiral ligands on their surface, as first comes to mind. Such a model relies on Metal-Based Electronic Transitions (MBET) being linked to a perturbation of the symmetrical core by a chiral field arising from a chiral adsorption pattern of ligands. It was disproved by the fact that the CD spectrum remains unchanged when excess ligand is added to the suspension.[116] Additionally, stabilisation by the same chiral thiols of pre-made citrate-stabilised nanoparticles *via* ligand exchange fails to produce any CD in the plasmon

region.[119] On the other hand, inversion of chirality can be obtained by exchanging the ligand for the same thiol of the opposite configuration,[116] which indicates that the core of the gold nanoparticles remains achiral. The postulated origin of CD is thus a local distortion of the crystal structure at the nanoparticle surface. The chelating ligand induces a specific helicity to the gold atoms during the nanocrystal formation, the direction of which is opposite for the L and D enantiomers.[120] The resulting crystal structure however is not stable enough to withstand ligand exchange.

The influence of AuNP's core diameter was investigated in the work of Schaaff and Whetten.[121] Small glutathione-stabilised nanoparticles (less than 2 nm) were synthesized, which can also be viewed as large clusters (20-40 atoms). Their UV-visible absorption spectra were very different from the usual plasmon peak at 520 nm that is observed for 10 nm AuNPs. Due to quantisation of the electronic transitions, they demonstrated a step-like structure ranging from red to near-IR. It also differed from smaller clusters which typically exhibit a strong blue absorption band. This peculiar electronic structure was also reflected in their CD spectra where several very intense bands and frequent changes of sign could be observed. They were further evidence for a series of distinct electronic transitions, but also strongly suggested that the core AuNPs were intrinsically chiral. Similarly to previously reported chiral fullerenes[122] and helicenes,[123] these large gold clusters are thought to assemble in a helical or generally low symmetry way.[121]

1.5.1.b Intrinsically chiral silver nanoparticles

Although the synthesis of silver NPs is based on the same reduction process in presence of a stabiliser as for gold nanoparticles, their interaction with chiral ligands is quite different. Chiral silver NPs have been prepared through ligand exchange of citrate for a chiral thiol such as cysteine,[119, 124] penicillamine or glutathione.[119] They produced a CD signal in the plasmon region (260-400 nm) which was not present in the free molecule spectra. In each case, both enantiomers of the ligand give a mirror image CD signal. Other chiral amino acids such as glutamine and lysine which do not possess a thiol group did not give any new CD, suggesting that chemisorption of the ligand onto the particle surface is essential.[119] The mechanism of generation of CD in that case is not fully understood however it is thought to be related to the formation of hydrogen bonds between ligands, through the amino and carboxylic acid groups.

Another way of producing chiral silver nanoparticles is to synthesise them on a DNA template.[125] Silver ions can bind to the DNA backbone through association with the heterocyclic bases. The interaction is especially strong with single-stranded DNA, and induces an inversion of the CD band of DNA at 260 nm, which indicates a conformational change of the helix. When silver (I) ions are complexed to 700 base pair poly(dG)-poly(dC) and subsequently reduced, a linear chain of silver nanoparticles is produced.[126] The formation of nanoparticles leads to the appearance of a new band at 425 nm which is the plasmon resonance frequency of the silver particles (Figure 1.12). They could be seen as chiral assemblies of nanoparticles but pre-made nanoparticles subsequently mixed with DNA do not give rise to that new CD. It may therefore be concluded that DNA directs the asymmetric growth of nanoparticles as opposed to an assembly of achiral particles on a chiral template.

Regarding Ag-based hybrids, it was postulated that the interactions of Ag^+ with DNA induces some conformational changes and that the modification of the bases arrangement relatively to the helical axis is responsible for the changes in CD. Silver nanoparticles in turn induce different alterations of the DNA conformation and consequently of the CD spectrum.[125]

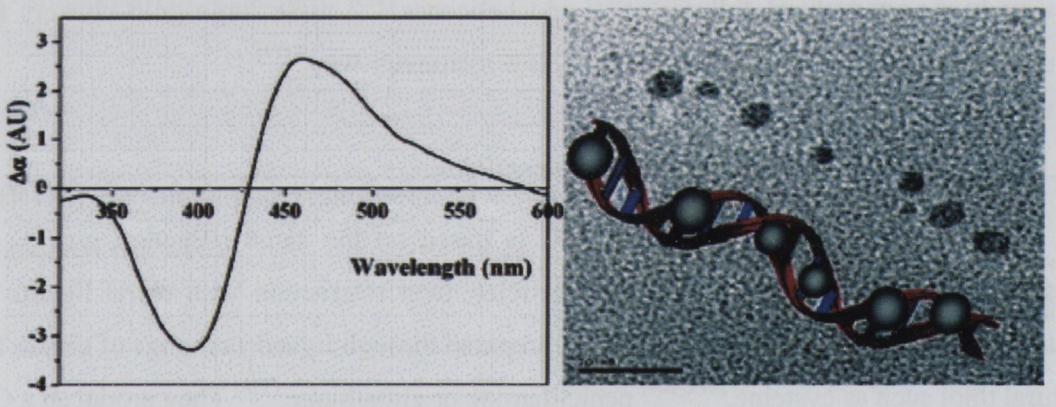

Figure 1.12 The plasmonic CD band of Ag NPs assembled on DNA (left) and the geometry of the system including a TEM image of the Ag NP chain (right). Reproduced from Shemer *et al.*[126]

1.5.1.d Intrinsically chiral QDs

Thiol group containing amino acids have proved to be excellent stabilizers, with *L*-cysteine becoming one of the most popular surface capping molecules for CdX (X = S, Se, Te) nanoparticles.[25, 127-133] Recently the use of stereospecific chiral stabilizing molecules opened another avenue of interest in the area of quantum dot research, as chirality is a key factor in

biological and biochemical interactions. There are however only a limited number of relatively recent reports dealing with chiral QDs.[7, 134-137]

Initially, chiral CdS QDs were prepared using microwave induced heating with the Racemic (*Rac*), *D*- and *L*- enantiomeric forms of penicillamine (Pen) as stabilizers as illustrated by Figure 1.13.[7] Circular dichroism (CD) studies of these QDs have shown that D- and L - penicillamine stabilized particles produced mirror image CD spectra (Figure 1.13) while the particles prepared with a Rac mixture showed only a weak signal. Because the particles are optically active from 200-360 nm, the chirality cannot be simply attributed to the penicillamine ligand and therefore the QDs themselves can be considered chiral. It was also demonstrated that all three types of CdS particles (*D*-, *L*-, and *Rac* penicillamine*)* exhibit very broad emission bands between 370 and 710 nm with the maximum emission wavelength in the range 485 - 505 nm due to defects or trap states on the surfaces of the crystals. DFT calculations of electronic states have demonstrated that the longer-wavelength circular dichroism is associated with near-surface Cd atoms that are enantiomerically distorted by the penicillamine ligands.[134] Models of the CdS QD surface show that the penicillamine ligand bonds *via* N and S to one surface Cd atom, and introduces chirality through additional bonding of carboxylate to a neighboring Cd atom. The interaction between ligand and cluster is strong, as are the interaction among ligands on the surface, compared to the weaker CdS surface structure. The ligands thus pack into helical bands on the surface and strongly distort the outermost Cd atoms of the QD, transmitting an enantiomeric structure to the surface layers. However, there is little distortion of the CdS geometry in the QD core, which remains achiral.

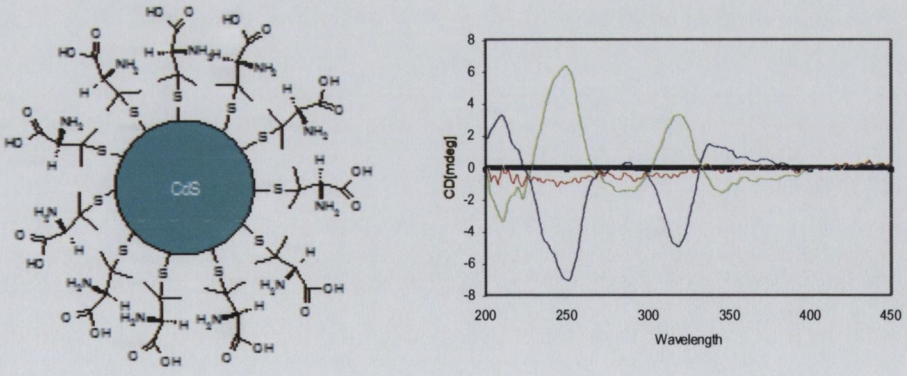

Figure 1.13 Left: Schematic of a chiral penicillamine capped CdS nanoparticle. Right: CD spectra of L-penicillamine (green), D-penicillamine (blue) and racemic (red) CdS nanoparticles.[7]

More recently, aqueous chiral CdSe quantum dots have also been synthesized

using microwave heating.[8] These nanoparticles similarly exhibited a very broad distribution of photoluminescence which originates from emissive defect states. According to time resolved photoluminescence spectroscopy studies, there is a range of defect states associated with each individual quantum dot as well as a shift of the emission band to longer wavelengths at longer times after excitation which suggests the existence of traps of varying depth.

The concept of chiral surface defects of QDs (distorted QD shell) was also confirmed by experiments with CdTe nanocrystals bearing chiral D- and L-cysteinemethylester hydrochloride ligands.[135] Interestingly, the chirality of the QD surface was maintained even after ligand exchange with an achiral thiol (Figure 1.14) and transfer of CdTe QDs into a different (organic) phase, a phenomenon referred to as "chiral memory".

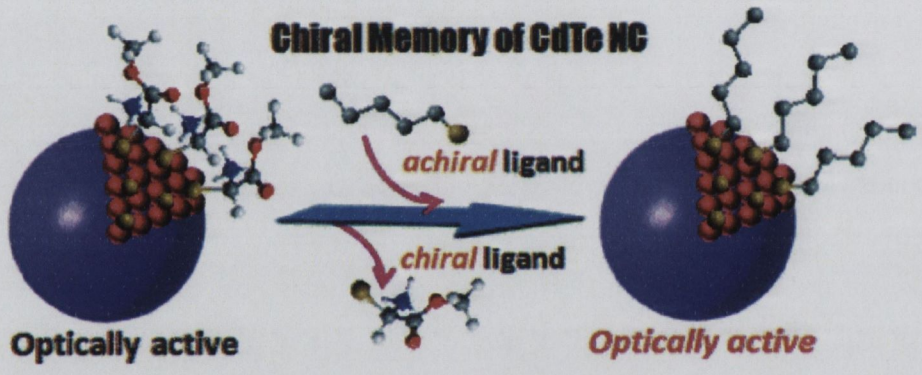

Figure 1.14 Chiral memory of thiol-capped CdTe nanocrystals. QDs stabilized with chiral ligands retained their optical activity even after exchange with an achiral thiol[135]

It was also demonstrated that the chirality of cysteine stabilizers has an effect on both the growth kinetics and the optical properties of CdTe nanocrystals.[137] This work suggested that the topological origin of chiral sites in nanocrystals is similar to that in organic compounds. Quantum mechanical calculations have shown that the thermodynamically preferred configuration of CdTe nanocrystals is *S* type when the stabilizer is *D*-cysteine and *R* type when *L*-cysteine is used as a stabilizer (Figure 1.15). These calculations correlated well with the experimental kinetics of particle growth.[137]

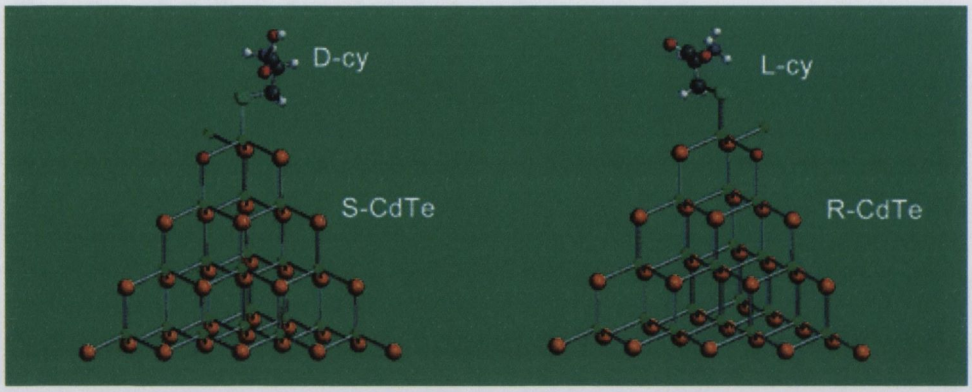

Figure 1.15 Quantum dot models of two different chiral arrangements of cysteine and CdTe[137]

In addition to QDs more complex chiral quantum nanostructures have been reported. Unusual chiral CdS nanotetrapods have been produced by heating of a basic aqueous solution of $CdCl_2$, thioacetamide and Racemic, *D*- or *L*- enantiomeric forms of penicillamine (Pen) under reflux.[138] These materials have also demonstrated a very broad emission band between 400 and 700 nm, which is indicative of defect emission. CD spectra of the D- and L- Pen stabilized samples showed clear CD responses within the band-edge region of the spectrum from 300-400 nm, while the Rac-Pen samples as expected showed no CD activity at all. It was found that further heating of the tetrapodal structures lead to the formation of chiral assemblies and their precipitation from solution. Preliminary biological testing showed that these materials have very low cytotoxicity, which could be potentially useful for *in vitro* cellular imaging and biological sensing.

Self-assembly of CdS nanocrystals on chiral nanofibers have also been recently reported.[139] The synthesis was achieved by growth of CdS on the surface of synthetic self-assembled helical or nonhelical nanofibers after the immobilization of a peptide capping agent. It was found that there are differences in shape, size, and photoluminescence properties of the CdS nanocrystals depending on the chiral nature of the nanofibers on which they were grown.

Finally very interesting chiral CdS QDs have been prepared in ferritin protein nanocage.[140] These QDs displayed left-handed circularly polarized luminescence from both direct transition and surface-trapping sites. The authors also demonstrated that the chiral luminescence can be modulated by laser photoetching. It was found that after photoetching the luminescent bands from surface trapping sites blue-shifted with a decrease in QD size, while bands from the direct transition band disappeared. Thus, chiral QDs demonstrate unique photophysical properties. It is expected that chiral QDs and their

assemblies will find a range of potential applications including chiroptical memory and circular polarized light emitting devices, and assays for biological and biochemical analysis. The use of chiral QDs for recognition and analysis of chiral mixtures of enantiomers,[136] amino- [141] and nucleic acids,[130] and for *in vitro* cellular testing[142] have already been demonstrated.

1.5.2 Chiral assemblies of nanoparticles

While controlling the position of every atom in a nanocrystal seems impossible, ordering a limited number of nanoparticles may be manageable and is a very intuitive way of forming chiral structures.

In principle, optical activity (local or macroscopic) may arise from random aggregation of nanoparticles, even without any chiral species in the vicinity, due to the fact that they gather with no centre or plane of symmetry and are therefore likely to exhibit local handedness. Large local optical activity was found in particular in fractal aggregates of plasmonic nanoparticles, while no macroscopic circular dichroism was observed. This phenomenon was explained by the formation of hot spots where the exciting electromagnetic field concentrates and may enhance optical activity.[143] Another possibility to create plasmonic CD would be the use of random aggregates of nanoparticles and chiral molecules. In such aggregates, plasmonic fields may be strongly enhanced in hot spots and, therefore, the interaction between plasmons and chiral molecules can be strongly amplified.[144-145] This phenomenon is referred to as plasmon-induced CD and will be further explored in the present work.

1.5.2.a Chiral assemblies of gold nanoparticles

The interaction of DNA with gold ions is of a very different nature from that of DNA with silver ions, and does not allow the formation of gold nanoparticles in the absence of a stronger stabiliser. Thiol-modified oligonucleotides however can be permanently bound to pre-formed citrate-stabilised gold nanoparticles.[105] One major attraction of synthetic oligonucleotides is that their hybridisation and denaturation are sequence specific and can be finely controlled. Oligonucleotide-conjugated gold nanoparticles can therefore be used as building blocks for higher geometry structures, such as dimmers, trimers or pyramids as

illustrated by Figure 1.16. By choosing four different sized gold nanoparticles and carefully designing the DNA sequences, such assemblies can be made chiral.[146] The most common strategy for DNA directed assembly is the modification of different batches of nanoparticles with complementary strands of single-stranded (ss)-DNA and subsequent hybridisation.[105, 146-147]

Other methods include the use of a linker sequence to hybridize the two ss-DNA strands immobilized on the nanoparticles [102, 148] but also formation of double-stranded (ds)-DNA prior to binding to nanoparticles on both ends. The latter strategy was proved very efficient for creating dimers.[147] However, it does not suit the formation of higher geometry assemblies. All of these nanostructures rely on the binding of thiol-modified DNA sequences to the gold. It has been shown that the chain length and sequence as well as the choice of thiol-spacer strongly influence the resulting assemblies.[148]

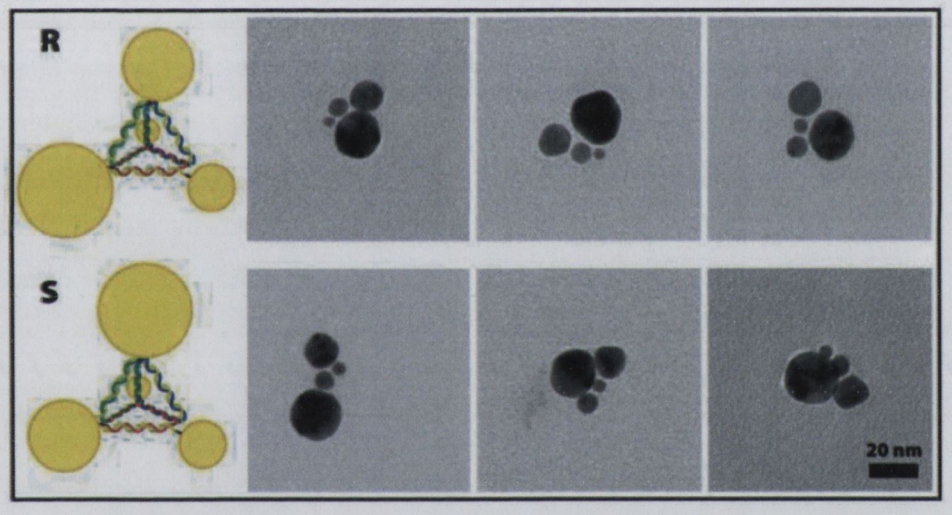

Figure 1.16 Chiral assemblies of gold nanoparticles using DNA scaffolds[146]

1.5.2.b Chiral assemblies of silver nanoparticles

There are substantially less reports on chiral assemblies of silver nanoparticles than of gold nanoparticles. DNA immobilisation on silver particles appears to be quite troublesome, partially due to the fact that unprotected silver nanoparticles are unstable under physiological conditions because of catalytic oxidation (etching) of the surface in the presence of chloride and other anions.[149-150] Therefore nucleic acids mediated assemblies are not a favoured route. Forming silver nanoparticles on a chiral template however has proved very successful. For example, they can be synthesised in the pores of a templated

silica thin film. Chirality is transferred to the silica through casting with a chiral nematic liquid crystal formed from nanocrystalline cellulose (NCC).[151] Three levels of chirality are present, from the molecular levels owing to the D-glucose building blocks of cellulose, to the screw-shaped morphology of individual nanocrystals and to the longer scale of nematic ordering of NCC. The resulting film is infiltrated with silver (I) ions which are subsequently reduced to form nanoparticles. The silver nanoparticle-infiltrated films demonstrate CD in the plasmon range, which is sensitively dependent on the interparticle distance (controlled by the initial silver ion concentration) and the environment.[152]

1.6 Aims and objectives of the project

Analysis of the literature highlights the fact that nanoparticles are a very versatile family of objects presenting fascinating physical, optical and chemical properties which can be selected and tuned according to the material, size and shape.

The main aim of the work presented in this thesis is to produce new nano-composites based on gold and silver nanoparticles and semiconductor QDs and to investigate their properties and explore their potential applications in biology, medicine and sensing.

Biomolecules and especially oligonucleotides and DNA present the double interest of interacting with either the plasmon or the exciton of nanoparticles, and to provide them with new functionalities.

In summary, the proposed research and technical objectives of the work are as follows:

- To produce and investigate a range of anisotropic gold and silver nanomaterials;
- To improve the biocompatibility and specificity of nanoparticles towards selected cells in order to produce imaging tools or sensing nanoprobes;
- To functionalise a range of metal nanoparticles with DNA oligonucleotides and to investigate any change in their optical properties;
- To prepare and investigate new chiral metal nanoparticles and their aggregates;
- To develop and investigate assemblies of nanoparticles. Coupling plasmons and excitons in various configurations are expected to give way to a number of energy transfer processes, leading to enhancement or quenching of luminescence.

- To study the behaviour of new nanocomposites in selected cell cultures and therefore to assess their potential for biological imaging, diagnostics or therapy. The work is mainly to be focused on interactions with cancer cells given the intrinsically toxic nature of cadmium based QDs.

References

[1] D. Baird, A. Shew, in *Discovering the nanoscale* (Eds.: J. Schummer, A. Nordmann, D. Baird), IOS Press, **2004**, pp. 145-150.

[2] D. M. Eigler, E. K. Schweizer, *Nature* **1990**, *344*, 524-526.

[3] R. Chang, *Chemistry*, 7 ed., James M. Smith, **2002**.

[4] A. L. Efros, *Soviet Physics Semiconductors-Ussr* **1982**, *16*, 772-775.

[5] D. Ramadurai, D. Geerpuram, D. Alexson, M. Dutta, N. A. Kotov, Z. Tang, M. A. Stroscio, *Superlattices and Microstructures* **2006**, *40*, 38-44.

[6] J. Drbohlavova, V. Adam, R. Kizek, J. Hubalek, *International Journal of Molecular Sciences* **2009**, *10*, 656-673.

[7] M. P. Moloney, Y. K. Gun'ko, J. M. Kelly, *Chemical Communications* **2007**, 3900-3902.

[8] S. A. Gallagher, M. P. Moloney, M. Wojdyla, S. J. Quinn, J. M. Kelly, Y. K. Gun'ko, *Journal of Materials Chemistry* **2010**, *20*, 8350-8355.

[9] B. O. Dabbousi, J. Rodriguez-Viejo, F. V. Mikulec, J. R. Heine, H. Mattoussi, R. Ober, K. F. Jensen, M. G. Bawendi, *The Journal of Physical Chemistry B* **1997**, *101*, 9463-9475.

[10] D.-W. Deng, Yu, J.-S., Pan, Y., *Journal of Colloid and Interface Science* **2006**, *299*, 225-232.

[11] P. Reiss, J. Bleuse, A. Pron, *Nano Letters* **2002**, *2*, 781-784.

[12] S. Kim, B. Fisher, H.-J. Eisler, M. Bawendi, *Journal of the American Chemical Society* **2003**, *125*, 11466-11467.

[13] S. J. Byrne, Y. Williams, A. Davies, S. A. Corr, A. Rakovich, Y. K. Gun'ko, Y. P. Rakovich, J. F. Donegan, Y. Volkov, *Small* **2007**, *3*, 1152-1156.

[14] B. Prasad, N. Nikolskaya, D. Connolly, T. Smith, S. Byrne, V. Gerard, Y. Gun'ko, Y. Rochev, *Journal of Nanobiotechnology* **2010**, *8*, 7.

[15] V. Gérard, C. Maguire, D. Bazou, Y. Gun'ko, *Journal of Nanobiotechnology* **2011**, *9*, 50.

[16] H. Krishna Kanta, P. Amitava, *Applied Physics Letters* **2009**, *95*, 063103.

[17] Y. Shan, J.-J. Xu, H.-Y. Chen, *Chemical Communications* **2010**, *46*, 5079-5081.

[18] N. Gaponik, D. V. Talapin, A. L. Rogach, K. Hoppe, E. V. Shevchenko, A. Kornowski, A. Eychmuller, H. Weller, *The Journal of Physical Chemistry B* **2002**, *106*, 7177-7185.

[19] V. K. LaMer, R. H. Dinegar, *Journal of the American Chemical Society* **1950**, *72*, 4847-4854.

[20] H. Zhang, D. Wang, B. Yang, H. Mohwald, *Journal of the American Chemical Society* **2006**, *128*, 10171-10180.

[21] C. B. Murray, D. J. Norris, M. G. Bawendi, *Journal of the American Chemical Society* **1993**, *115*, 8706-8715.

[22] M. A. Hines, G. D. Scholes, *Advanced Materials* **2003**, *15*, 1844-1849.

[23] T. T. Tan, S. T. Selvan, L. Zhao, S. Gao, J. Y. Ying, *Chemistry of Materials* **2007**, *19*, 3112-3117.

[24] M. A. Hines, P. Guyot-Sionnest, *The Journal of Physical Chemistry* **1996**, *100*, 468-471.

[25] N. Gaponik, D. V. Talapin, A. L. Rogach, K. Hoppe, E. V. Shevchenko, A. Kornowski, A. Eychmuller, H. Weller, *The Journal of Physical Chemistry B* **2002**, *106*, 7177-7185.

[26] T. Sugimoto, *Journal of Colloid And Interface Science* **1978**, *63*, 16-26.

[27] M. A. Vairavamurthy, W. S. Goldenberg, S. Ouyang, S. Khalid, *Marine Chemistry* **2000**, *70*, 181-189.

[28] A. L. Rogach, T. Franzl, T. A. Klar, J. Feldmann, N. Gaponik, V. Lesnyak, A. Shavel, A. Eychmuller, Y. P. Rakovich, J. F. Donegan, *The Journal of Physical Chemistry C* **2007**, *111*, 14628-14637.

[29] H. C. Hamaker, *Recueil des Travaux Chimiques des Pays-Bas* **1936**, *55*, 1015-1026.

[30] H. Zhang, Y. Liu, C. Wang, J. Zhang, H. Sun, M. Li, B. Yang, *ChemPhysChem* **2008**, *9*, 1309-1316.

[31] S. J. Byrne, S. A. Corr, T. Y. Rakovich, Y. K. Gun'ko, Y. P. Rakovich, J. F. Donegan, S. Mitchell, Y. Volkov, *Journal of Materials Chemistry* **2006**, *16*, 2896-2902.

[32] F. Purcell-Milton, Y. K. Gun'ko, *Journal of Materials Chemistry* **2012**.

[33] Q. Dai, C. E. Duty, M. Z. Hu, *Small* **2010**, *6*, 1577-1588.

[34] J. Drbohlavova, V. Adam, R. Kizek, J. Hubalek, *International Journal of Molecular Sciences* **2009**, *10*, 656-673.

[35] U. Resch-Genger, M. Grabolle, S. Cavaliere-Jaricot, R. Nitschke, T. Nann, *Nat Meth* **2008**, *5*, 763-775.

[36] A. Rakovich, D. Savateeva, T. Rakovich, J. F. Donegan, Y. P. Rakovich, V. Kelly, V. Lesnyak, A. Eychmller, *Nanoscale Research Letters* **2010**, *5*, 753-760.

[37] R. Bakalova, H. Ohba, Z. Zhelev, M. Ishikawa, Y. Baba, *Nat Biotech* **2004**, *22*, 1360-1361.

[38] B. Hu, L.-P. Zhang, M.-L. Chen, M.-L. Chen, J.-H. Wang, *Biosensors and Bioelectronics* **2012**, *32*, 82-88.

[39] X. Xiang, L. Chen, Q. G. Zhuang, X. H. Ji, Z. K. He, *Biosensors & Bioelectronics* **2012**, *32*, 43-49.

[40] Y. F. Li, L. L. Liu, X. L. Fang, J. C. Bao, M. Han, Z. H. Dai, *Electrochimica Acta* **2012**, *65*, 1-6.

[41] R. Nötzel, A. Urbańczyk, *Current Opinion in Solid State and Materials Science* **2012**, *16*, 59-63.

[42] M. Bottrill, M. Green, *Chemical Communications* **2011**, *47*, 7039-7050.

[43] S. J. Cho, D. Maysinger, M. Jain, B. Roder, S. Hackbarth, F. M. Winnik, *Langmuir* **2007**, *23*, 1974-1980.

[44] A. M. Derfus, W. C. W. Chan, S. N. Bhatia, *Advanced Materials* **2004**, *16*, 961-966.

[45] J. Lovrić, H. S. Bazzi, Y. Cuie, G. R. A. Fortin, F. M. Winnik, D. Maysinger, *Journal of Molecular Medicine* **2005**, *83*, 377-385.

[46] K. G. Li, J. T. Chen, S. S. Bai, X. Wen, S. Y. Song, Q. Yu, J. Li, Y. Q. Wang, *Toxicology in Vitro* **2009**, *23*, 1007-1013.

[47] J. C. Wataha, C. T. Hanks, R. G. Craig, *Journal of Biomedical Materials Research* **1994**, *28*, 427-433.

[48] B. R. Prasad, E. O'Connell, T. J. Smith, V. A. Gérard, Y. K. Gun'ko, Y. Rochev, *Vol. 906* (Ed.: M. Soloviev), Humana Press, **2012**, pp. 171-183.

[49] J. Boonstra, J. A. Post, *Gene* **2004**, *337*, 1-13.

[50] D. Maysinger, J. Lovrić, A. Eisenberg, R. Savić, *European Journal of Pharmaceutics and Biopharmaceutics* **2007**, *65*, 270-281.

[51] S. J. Cho, D. Maysinger, M. Jain, B. Röder, S. Hackbarth, F. M. Winnik, *Langmuir* **2007**, *23*, 1974-1980.

[52] K. Susumu, B. C. Mei, H. Mattoussi, *Nature Protocols* **2009**, *4*, 424-436.

[53] C. Kirchner, A. M. Javier, A. S. Susha, A. L. Rogach, O. Kreft, G. B. Sukhorukov, W. J. Parak, *Talanta* **2005**, *67*, 486-491.

[54] T. S. Hauck, R. E. Anderson, H. C. Fischer, S. Newbigging, W. C. W. Chan, *Small* **2010**, *6*, 138-144.

[55] J. A. J. Fitzpatrick, S. K. Andreko, L. A. Ernst, A. S. Waggoner, B. Ballou, M. P. Bruchez, *Nano Letters* **2009**, *9*, 2736-2741.

[56] A. Choi, S. Brown, M. Szyf, D. Maysinger, *Journal of Molecular Medicine* **2008**, *86*, 291-302.

[57] H. Zhong, X. Lei, X. Hun, S. S. Zhang, *Chemical Communications* **2009**, 6958-6960.

[58] Y.-w. Jun, S. Sheikholeslami, D. R. Hostetter, C. Tajon, C. S. Craik, A. P. Alivisatos, *Proceedings of the National Academy of Sciences* **2009**, *106*, 17735-17740.

[59] J. J. Storhoff, R. Elghanian, C. A. Mirkin, R. C. Mucic, R. L. Letsinger, *Journal of the American Chemical Society* **1998**, *120*, 1959-1964.

[60] P. Ghosh, G. Han, M. De, C. K. Kim, V. M. Rotello, *Advanced Drug Delivery Reviews* **2008**, *60*, 1307-1315.

[61] F. McKenzie, D. Graham, *Chemical Communications* **2009**, 5757-5759.

[62] A. Moores, F. Goettmann, *New Journal of Chemistry* **2006**, *30*, 1121-1132.

[63] J. Homola, *Analytical and Bioanalytical Chemistry* **2003**, *377*, 528-539.

[64] J. Yguerabide, E. E. Yguerabide, *Analytical Biochemistry* **1998**, *262*, 137-156.

[65] B. J. Wiley, S. H. Im, Z.-Y. Li, J. McLellan, A. Siekkinen, Y. Xia, *The Journal of Physical Chemistry B* **2006**, *110*, 15666-15675.

[66] V. Petkov, Y. Peng, G. Williams, B. Huang, D. Tomalia, Y. Ren, *Physical Review B* **2005**, *72*, 195402.

[67] T. K. Sau, A. Pal, N. R. Jana, Z. L. Wang, T. Pal, *Journal of Nanoparticle Research* **2001**, *3*, 257-261.

[68] B. Palpant, B. Prével, J. Lermé, E. Cottancin, M. Pellarin, M. Treilleux, A. Perez, J. L. Vialle, M. Broyer, *Physical Review B* **1998**, *57*, 1963.

[69] M. Hanauer, S. Pierrat, I. Zins, A. Lotz, C. Sonnichsen, *Nano Letters* **2007**, *7*, 2881-2885.

[70] J. Spreadborough, J. W. Christian, *Proceedings of the Physical Society* **1959**, *74*, 609.

[71] M. Grouchko, I. Popov, V. Uvarov, S. Magdassi, A. Kamyshny, *Langmuir* **2009**, *25*, 2501-2503.

[72] R. C. Jin, Y. W. Cao, C. A. Mirkin, K. L. Kelly, G. C. Schatz, J. G. Zheng, *Science* **2001**, *294*, 1901-1903.

[73] G. S. Métraux, C. A. Mirkin, *Advanced Materials* **2005**, *17*, 412-415.

[74] D. Aherne, D. M. Ledwith, M. Gara, J. M. Kelly, *Advanced Functional Materials* **2008**, *18*, 2005-2016.

[75] J. Q. Hu, Q. Chen, Z. X. Xie, G. B. Han, R. H. Wang, B. Ren, Y. Zhang, Z. L. Yang, Z. Q. Tian, *Advanced Functional Materials* **2004**, *14*, 183-189.

[76] Y. Sun, Y. Xia, *Science* **2002**, *298*, 2176-2179.

[77] T. C. R. Rocha, D. Zanchet, *The Journal of Physical Chemistry C* **2007**, *111*, 6989-6993.

[78] J. Choi, G. Sauer, K. Nielsch, R. B. Wehrspohn, U. Gösele, *Chemistry of Materials* **2003**, *15*, 776-779.

[79] C. J. Murphy, A. M. Gole, S. E. Hunyadi, C. J. Orendorff, *Inorganic Chemistry* **2006**, *45*, 7544-7554.

[80] Y. Sun, B. Mayers, T. Herricks, Y. Xia, *Nano Letters* **2003**, *3*, 955-960.

[81] C. J. Johnson, E. Dujardin, S. A. Davis, C. J. Murphy, S. Mann, *Journal of Materials Chemistry* **2002**, *12*, 1765-1770.

[82] D. Aherne, D. E. Charles, M. E. Brennan-Fournet, J. M. Kelly, Y. K. Gun'ko, *Langmuir* **2009**, *25*, 10165-10173.

[83] Y. Sun, B. T. Mayers, Y. Xia, *Nano Letters* **2002**, *2*, 481-485.

[84] D. Aherne, M. Gara, J. M. Kelly, Y. K. Gun'ko, *Advanced Functional Materials* **2010**, *20*, 1329-1338.

[85] X. M. Lu, L. Au, J. McLellan, Z. Y. Li, M. Marquez, Y. N. Xia, *Nano Letters* **2007**, *7*, 1764-1769.

[86] Y. Sun, Y. Xia, *Journal of the American Chemical Society* **2004**, *126*, 3892-3901.

[87] W. C. Schumacher, A. J. Phipps, P. K. Dutta, *Advanced Powder Technology* **2009**, *20*, 438-446.

[88] W. C. Chan, S. Nie, *Science* **1998**, *281*, 2016-2018.

[89] K.-T. Yong, I. Roy, M. T. Swihart, P. N. Prasad, *Journal of Materials Chemistry* **2009**, *19*, 4655-4672.

[90] W. R. Algar, U. J. Krull, *Analytica Chimica Acta* **2007**, *581*, 193-201.

[91] C.-Y. Zhang, H.-C. Yeh, M. T. Kuroki, T.-H. Wang, *Nat Mater* **2005**, *4*, 826-831.

[92] C. S. Wu, J. M. Cupps, X. D. Fan, *Nanotechnology* **2009**, *20*, 7.

[93] C. Gerhards, C. Schulz-Drost, V. Sgobba, D. M. Guldi, *The Journal of Physical Chemistry B* **2008**, *112*, 14482-14491.

[94] H. Mattoussi, J. M. Mauro, E. R. Goldman, G. P. Anderson, V. C. Sundar, F. V. Mikulec, M. G. Bawendi, *Journal of the American Chemical Society* **2000**, *122*, 12142-12150.

[95] M. Fischler, U. Simon, *Journal of Materials Chemistry* **2009**, *19*, 1518-1523.

[96] M. Reismann, J. C. Bretschneider, G. von Plessen, U. Simon, *Small* **2008**, *4*, 607-610.

[97] K. Hamad-Schifferli, J. J. Schwartz, A. T. Santos, S. Zhang, J. M. Jacobson, *Nature* **2002**, *415*, 152-155.

[98] D. S. Seferos, A. E. Prigodich, D. A. Giljohann, P. C. Patel, C. A. Mirkin, *Nano Letters* **2009**, *9*, 308-311.

[99] D. S. Seferos, D. A. Giljohann, H. D. Hill, A. E. Prigodich, C. A. Mirkin, *Journal of the American Chemical Society* **2007**, *129*, 15477-15479.

[100] J.-H. Kim, H. H. Jang, S.-M. Ryou, S. Kim, J. Bae, K. Lee, M. S. Han, *Chemical Communications* **2010**, *46*, 4151-4153.

[101] S. Pal, J. Sharma, H. Yan, Y. Liu, *Chemical Communications* **2009**, 6059-6061.

[102] R. C. Mucic, J. J. Storhoff, C. A. Mirkin, R. L. Letsinger, *Journal of the American Chemical Society* **1998**, *120*, 12674-12675.

[103] X. Xu, N. L. Rosi, Y. Wang, F. Huo, C. A. Mirkin, *Journal of the American Chemical Society* **2006**, *128*, 9286-9287.

[104] S. A. Claridge, S. L. Goh, J. M. J. Frechet, S. C. Williams, C. M. Micheel, A. P. Alivisatos, *Chemistry of Materials* **2005**, *17*, 1628-1635.

[105] D. Zanchet, C. M. Micheel, W. J. Parak, D. Gerion, A. P. Alivisatos, *Nano Letters* **2001**, *1*, 32-35.

[106] R. A. S. T. Pellegrino, A. P. Alivisatos, and W. J. Parak, *Journal of Biomedicine and Biotechnology* **2007**, *2007*, 9.

[107] J. E. Eastoe, *Biochem J.* **1955**, *61*, 589-600.

[108] F. Badii, N. K. Howell, *Food Hydrocolloids* **2006**, *20*, 630-640.

[109] K. L. C. J. Coester, H. Von Briesen, J. Kreuter, *Journal of Microencapsulation* **2000**, *17*, 187-193.

[110] K. Zwiorek, *Gelatin Nanoparticles as Delivery System for Nucleotide-Based Drugs*, Hut, **2006**.

[111] N. Adhirajan, N. Shanmugasundaram, M. Babu, *Journal of Microencapsulation* **2007**, *24*, 659-671.

[112] B. R. Prasad, G. Mullins, N. Nikolskaya, D. Connolly, T. J. Smith, V. A. Gérard, S. J. Byrne, G.-L. Davies, Y. K. Gun'ko, Y. Rochev, *Journal of Nanobiotechnology* **2012**, *10*, 4.

[113] M. K. Johnson, in *Physical Methods in Bioinorganic Chemistry: Spectroscopy and Magnetism* (Ed.: L. Que), University Science Books, **2000**.

[114] J. G. Foss, *Journal of Chemical Education* **1963**, *40*, 592.

[115] R. M. Pagni, *Journal of Chemical Education* **1998**, *75*, 1095.

[116] C. Gautier, T. Burgi, *Journal of the American Chemical Society* **2008**, *130*, 7077-7084.

[117] C. Gautier, T. Burgi, *Journal of the American Chemical Society* **2006**, *128*, 11079-11087.

[118] M. Tamura, H. Fujihara, *Journal of the American Chemical Society* **2003**, *125*, 15742-15743.

[119] L. Taihua, P. Hyun Gyu, L. Hee-Seung, C. Seong-Ho, *Nanotechnology* **2004**, *15*, S660.

[120] H. Yao, K. Miki, N. Nishida, A. Sasaki, K. Kimura, *Journal of the American Chemical Society* **2005**, *127*, 15536-15543.

[121] T. G. Schaaff, R. L. Whetten, *The Journal of Physical Chemistry B* **2000**, *104*, 2630-2641.

[122] C. Thilgen, A. Herrmann, F. Diederich, *Angewandte Chemie International Edition in English* **1997**, *36*, 2268-2280.

[123] K. Meurer, F. Vögtle, in *Organic Chemistry, Vol. 127*, Springer Berlin / Heidelberg, **1985**, pp. 1-76.

[124] P. Rezanka, K. Záruba, V. Král, *Colloids and Surfaces A: Physicochemical and Engineering Aspects* **2010**, *374*, 77-83.

[125] J. T. Petty, J. Zheng, N. V. Hud, R. M. Dickson, *Journal of the American Chemical Society* **2004**, *126*, 5207-5212.

[126] G. Shemer, O. Krichevski, G. Markovich, T. Molotsky, I. Lubitz, A. B. Kotlyar, *Journal of the American Chemical Society* **2006**, *128*, 11006-11007.

[127] J. Chen, Y. Gao, C. Guo, G. Wu, Y. Chen, B. Lin, *Spectrochimica Acta Part A: Molecular and Biomolecular Spectroscopy* **2008**, *69*, 572-579.

[128] Y. Chen, Z. Rosenzweig, *Analytical Chemistry* **2002**, *74*, 5132-5138.

[129] H. Bao, E. Wang, S. Dong, *Small* **2006**, *2*, 476-480.

[130] F. Huang, G. Chen, *Spectrochimica Acta Part A: Molecular and Biomolecular Spectroscopy* **2008**, *70*, 318-323.

[131] F.-C. Liu, T.-L. Cheng, C.-C. Shen, W.-L. Tseng, M. Y. Chiang, *Langmuir* **2008**, *24*, 2162-2167.

[132] W. Liu, H. S. Choi, J. P. Zimmer, E. Tanaka, J. V. Frangioni, M. Bawendi, *Journal of the American Chemical Society* **2007**, *129*, 14530-14531.

[133] Y.-h. Zhang, H.-s. Zhang, X.-f. Guo, H. Wang, *Microchemical Journal* **2008**, *89*, 142-147.

[134] S. D. Elliott, M. c. l. P. Moloney, Y. K. Gun'ko, *Nano Letters* **2008**, *8*, 2452-2457.

[135] T. Nakashima, Y. Kobayashi, T. Kawai, *Journal of the American Chemical Society* **2009**, *131*, 10342-10343.

[136] C. Carrillo-Carrión, S. Cárdenas, B. M. Simonet, M. Valcárcel, *Analytical Chemistry* **2009**, *81*, 4730-4733.

[137] Y. Zhou, M. Yang, K. Sun, Z. Tang, N. A. Kotov, *Journal of the American Chemical Society* **2010**, *132*, 6006-6013.

[138] J. E. Govan, E. Jan, A. Querejeta, N. A. Kotov, Y. K. Gun'ko, *Chemical Communications* **2010**, *46*, 6072-6074.

[139] P. P. Bose, A. Banerjee, *Journal of Nanoparticle Research*, *12*, 713-718.

[140] M. Naito, K. Iwahori, A. Miura, M. Yamane, I. Yamashita, *Angewandte Chemie-International Edition*, *49*, 7006-7009.

[141] C. P. Han, H. B. Li, *Small* **2008**, *4*, 1344-1350.

[142] V. V. Breus, C. D. Heyes, K. Tron, G. U. Nienhaus, *Acs Nano* **2009**, *3*, 2573-2580.

[143] V. P. Drachev, W. D. Bragg, V. A. Podolskiy, V. P. Safonov, W.-T. Kim, Z. C. Ying, R. L. Armstrong, V. M. Shalaev, *The Journal of the Optical Society of America B* **2001**, *18*, 1896-1903.

[144] A. O. Govorov, Z. Fan, P. Hernandez, J. M. Slocik, R. R. Naik, *Nano Letters* **2010**, *10*, 1374-1382.

[145] A. O. Govorov, *The Journal of Physical Chemistry C* **2011**, *115*, 7914-7923.

[146] A. J. Mastroianni, S. A. Claridge, A. P. Alivisatos, *Journal of the American Chemical Society* **2009**, *131*, 8455-8459.

[147] Y. Hui, Y. Changqing, T. Chi-Hung, Z. Jungie, Y. Megsu, *Nanotechnology* **2007**, *18*, 015102.

[148] S.-J. Park, A. A. Lazarides, J. J. Storhoff, L. Pesce, C. A. Mirkin, *The Journal of Physical Chemistry B* **2004**, *108*, 12375-12380.

[149] P. Mulvaney, T. Linnert, A. Henglein, *The Journal of Physical Chemistry* **1991**, *95*, 7843-7846.

[150] T. Pal, T. K. Sau, N. R. Jana, *Langmuir* **1997**, *13*, 1481-1485.

[151] K. E. Shopsowitz, H. Qi, W. Y. Hamad, M. J. MacLachlan, *Nature* **2010**, *468*, 422-425.

[152] H. Qi, K. E. Shopsowitz, W. Y. Hamad, M. J. MacLachlan, *Journal of the American Chemical Society* **2011**, *133*, 3728-3731.

Chapter 2

Experimental

2.1 Starting materials and general equipment

All chemicals were purchased from Sigma-Aldrich unless stated otherwise. Al_2Te_3 was purchased from Cerac Inc. The oligonucleotides were obtained from Prof. Defrancq (Ingénierie et Interactions BioMoléculaires (I2BM), Département de Chimie Moléculaire – UMR CNRS 5250, Université J. Fourier, Grenoble, France). Caco-2 and HT-1080 cells were purchased from the European Cell Culture Collection (ECCC) and provided by the department of pharmacy and pharmaceutical sciences, Trinity College Dublin. Materials for biological experiments were purchased from Invitrogen. Glass-bottomed Petri dishes and μ-slides were supplied by Ibidi.

Adherent mouse BALB/c macrophages (J774 cells) were obtained from the American Tissue Culture Collection (ATCC, USA).

Unless specified otherwise, all syntheses were carried out in water from a Millipore filtration system operating at 18 MΩ (referred to as Millipore water).

Two centrifuges were used throughout. A Hettich Zentrifugen Universal 32 was used for large volumes, namely for fractioning QDs and gelatin nanoparticles. For small volumes and higher speed required to wash metal nanoparticles, a Hermle Z233 M-2 was used.

For ultrasonic agitation, a Grant XB6 ultrasonic bath was operated at 5-60 Hz. A Model GEX-750 ultrasonic processor fitted with a Model CV33 tip with ¼ in. tapered tip was also used. It was operated at 20 % of maximum power.

All experimental errors and size distributions were expressed by the standard deviation of values from the mean. The standard deviation σ is defined by the expression:

$$\sigma = \sqrt{\frac{1}{N}\sum_{i=1}^{N}(x_i - \mu)^2} \qquad (1)$$

Where N is the number of discrete value in the population, x_i is the value number i, and μ is the mean value.

$$\mu = \frac{1}{N}\sum_{i=1}^{N} x_i \quad (2)$$

2.2 Experimental details for chapter 3

2.2.1 Synthesis of silver nanoprisms[1]

Silver seeds were produced by the addition of 5 mL of $AgNO_3$ (0.5 mM) at a rate of 2 mL/min to a solution containing 5 mL TSC (2.5 mM), 250 µL PSSS (500 mg/L) and 300 µL $NaBH_4$ (10 mM). 800 µL of these seeds were diluted in 40 mL of Millipore water to which were added 600 µL of ascorbic acid (10 mM) and 24 mL of $AgNO_3$ (0.5 mM) at a rate of 4 mL/min. Except if the nanoprisms were to be used as templates for nanoboxes, 20 mL of TSC (25 mM) were finally added. The solution was divided into eight batches (8.2 mL each).

2.2.2 Synthesis of gold-coated silver nanoprisms[2]

To one 8.2 mL batch of citrate-stabilised silver nanoprisms were added 150 µL of ascorbic acid (10 mM) and 100 to 450 µL of $HAuCl_4$ (0.5 mM) depending on the initial size of the nanoprisms as determined by the position of their plasmon band.

2.2.3 Synthesis of gold nanorings

To one 8.2 mL batch of citrate-stabilised silver nanoprisms were added variable volumes of ascorbic acid (10 mM) and $HAuCl_4$ (0.5 mM). The optimal volumes as determined owing to those variations were 150 µL of ascorbic acid and three times the volume of $HAuCl_4$ that would have been required to deposit a protective layer on the edge according to the initial size of the nanoprisms.[2] The excess ascorbic acid was washed out by centrifuging the sample for 30 min at 10000 rpm, removing the supernatant and resuspending the particles in the same volume of Millipore water. To 2 mL of the sample

were added 50 μL of $Fe(NO_3)_3$. It was centrifuged again (30 min, 10 000 rpm) to remove excess $Fe(NO_3)_3$.

2.2.4 Synthesis of gold/silver nanoboxes[3]

To one 8.2 mL batch of silver nanoprisms were added 675 μL of ascorbic acid (10 mM) and 8 mL of $HAuCl_4$ (0.5 mM) at the rate of 1 mL/min.

2.2.5 Encapsulation of materials into gold/silver nanoboxes

Silver nanoprisms were prepared as described before except 4 mL of suspension were mixed with either gelatinated QDs (10 μL, $7x10^{-5}$ M) or 1,1'-diethyl-2,2'-cyanine chloride (pseudoisocyanine chloride, PIC). The volume of PIC was varied in different experiments: 450 μL or 200 μL of 10^{-4} M, or 450 μL of 10^{-3} M solution. The rest of the nanoboxes preparation was carried out as normal with the addition of 500 μL of 10 mM ascorbic acid and 5 mL of 0.5 mM $HAuCl_4$ at 1 mL/hour. Excess QD or PIC was washed out by centrifuging the particles (10 000 rpm, 10 min) and replacing the supernatant with the same volume of water.

2.2.6 Synthesis of penicillamine-stabilised gold nanoparticles

Aqueous solutions of chloroauric acid (0.15 g in 12 mL) and of either D- or L-penicillamine (0.33 g in 12 mL) were prepared, mixed together and stirred for an hour at room temperature. A stock solution of sodium borohydride was prepared by dissolving 0.05 g in 5 mL of water. 700 μL of sodium borohydride solution were added to the penicillamine/chloroauric acid solution at a rate of 3 mL/h. The resulting nanoparticle suspension was stirred vigorously overnight. They were then purified by centrifugation at 10000 rpm for 10 min and replacement of the supernatant with Millipore water.

2.2.7 *In vitro* biological experiments

Biological experiments described in this section were carried out in close collaboration with Dr. Adriele Prina-Mello and Dr. Dania Movia, Institute of Molecular Medicine, and Dr. Anthony Davies, High Content Screening facility, Trinity College Dublin.

2.2.6.a Cell culture

J774 cells were cultured in modified RPMI 1640 media (supplemented with 2nM Glutamine 1% P/S and 10% FBS) and incubated at 37 °C and 5% CO_2. At 80% confluence, cells were diluted in modified RPMI 1640 media at concentrations appropriate for each experimental procedure.

2.2.6.b Cell exposure to Pen-AuNP and Au Nanoboxes

J774 cells were seeded in 8-well Millicell® EZ Slide (Millipore™, MA, USA) at a concentration of 10^6 cells/mL counted using a Countess™ Automated Cell Counter (Invitrogen, Oregon, USA). Adherent J774 cells were incubated for 24 h at 37 °C with or without D- or L-Pen AuNP, sample 1 or sample 2 Au Nanoboxes at an exposure concentration of circa 3×10^{-11} mol/L. The final volume of solution added (AuNPs dispersion and/or modified RPMI 1640 media) was 400 µL/well.

2.2.6.c Imaging of fixed cells

After 24 h in culture, supernatants were collected from each well and multiple washings with phosphate-buffered saline (PBS) were carried out in order to completely remove Au Nanoboxes from wells. Samples were stained with Hoechst for the nuclei (1 h, 37 °C) and Cell Mask Deep Red for the cell plasma membranes where appropriate, fixed with 8% paraformaldehyde (PFA), rinsed with PBS and subsequently mounted in transparent Vectashield® mounting medium prior to epifluorescence microscopy.

2.2.6.d Imaging of live cells

After 24 h in culture, live cells were imaged in brightfield view directly on the 8-wells chamber by an inverted microscope (OPTIKA) equipped with a CCD camera.

2.2.8 Gold-coating of silver nanowires

As-received samples of silver nanowires (40 mg/mL) were diluted in Millipore water down to 80 µg/mL, in a final volume of 5 mL. A 0.5 mM solution of cholorauric acid ($HAuCl_4$) was added at a rate of 1 mL/hour with vigorous stirring. The volume added depended on the length of nanowires as follows:

- 28 µm AgNW: 0.4 mL
- 14 µm AgNW: 0.3 mL
- 10 µm AgNW: 0.2 mL
- 5 µm AgNW: 0.15 mL
- 3 µm AgNW: 0.09 mL

After the end of the addition, the solution was stirred for another 30 min at room temperature. To each 5 mL sample, 3 mL of 35% ammonia was added to dissolve silver chloride aggregates. The nanowires were precipitated out by centrifugation (10 000 rpm, 10 min) and resuspended in water. The process was carried out twice for washing.

2.3 Experimental details for chapter 4

2.3.1 Synthesis of CdTe QDs

CdTe QDs were synthesised using our modification of the method previously published by Gaponik and co-workers.[4] $Cd(ClO_4)_2 \cdot 6H_2O$ and the relevant stabiliser (TGA or cysteamine) were added to 150 mL degassed Millipore water. The pH of the solution was adjusted to 11 by dropwise addition of a 2M NaOH solution. When appropriate, 0.3 g of gelatine, 0.5 g of PEG or PVA, or 0.25 g of PEI were added to the solution. To a known weight of Al_2Te_3 were added 15mL of H_2SO_4 to generate H_2Te gas which then bubbled through the Cd/thiol solution. The resulting non-luminescent solution was then heated under reflux. Once the QDs reached the desired size, the reflux was stopped and different fractions were obtained *via* size-selective precipitation using isopropanol. The final samples were further purified on a Sephadex-G25 column.

2.3.2 Synthesis of folic-acid modified QDs[5]

QD (A), (B) and (C) were synthesised using a modification of the procedure detailed in section 2.3.1 Synthesis of CdTe QDs. After preparation of gelatine-coated CdTe QDs and their heating under reflux for 2 hours, the solution was cooled to 80°C and divided into three flasks, A, B and C. Folic acid (0.01 moles, 0.28 g) was added directly to Flask B and the solution was stirred for 15 min. EDC (0.1 g) and DMAP (0.1 g) were added to flask C and the solution was stirred for 15 min to activate the QDs for conjugation. Folic acid (0.01 moles, 0.28 g) was then added, and the mixture was allowed to react for 15 min, while stirring. From each of the crude solutions A, B and C, different fractions were precipitated out using 2-isopropanol and centrifuging (3 000 rpm, 10 min). Unreacted materials were removed by purification on a Sephadex G25 column.

2.3.3 *In vitro* biological experiments

2.3.3.a Cell culture

Caco-2 and HT1080 cells were cultured in medium (500 mL Minimum Essential Medium (MEM) supplemented with 0.055 g of sodium pyruvate, 5 mL of a solution of penicillin (2 mM) and streptomycin (2 mM), 5mL of 1 mM gentamicin and 100 mL of Fetal Bovine Serum (FBS)) at 37°C and in a 5% CO_2 atmosphere.

2.3.3.b Cell exposure to QDs

80% confluent cell cultures were detached using Trypsin and re-suspended in cell culture medium to a final concentration of 5.10^4 cells/mL and seeded in 35 mm-diameter glass-bottomed Petri dishes (2 mL per dish) for a final 1.10^5 cells per dish. After 24h incubation allowing the cells to adhere to the substrate, half of the medium was removed from each dish and replaced by 1 mL of serum-free medium. The cells were incubated for a further 4h before the medium was aspirated out and replaced with 2 mL of QD suspension in Dubelcco's modified Phosphate Buffer Saline (DPBS) at a final concentration of 10^{-7} mol/L, or pure DPBS for control experiments. After four more hours, the QD containing solution was aspirated out of the dishes and the cells were washed three times with PBS.

2.3.3.c Live cell imaging

A cytoplasm-staining solution was prepared by dissolving 50 µg of Calcein AM in 50 µL of DMSO which was subsequently added to 6 mL of PBS. The solution was added to the cells (1 mL per dish) and left for 30 min at room temperature after which the cells were washed three times with PBS.

2.3.3.d Fixed cell imaging

Cells were grown on a coverslip at the bottom of the 35 mm Petri dish following the same procedure as before. They were then fixed with 90% ethanol for 10 min, and washed three times with PBS. The coverslips were mounted on glass slide with a drop of Vectashield® mounting media containing the nuclei-staining dye 4',6'-diamidino-2-phenylindole (DAPI).

2.3.4 QD conjugates for caspase inhibition

2.3.4.a Preparation of QD-Inhibitor conjugates

Caspase 1 inhibitors I and II were each dissolved in DMSO to a final 10^{-2} M concentration. In two separate sample tubes, TGA-gel QDs were diluted to 10^{-5} M in 2.2 mL of water, and 23.1 µL of either Caspase 1 inhibitor were added, to a final concentration of 10^{-4} M. the samples were wrapped in tin-foil and incubated overnight on a shaker at room temperature. Excess inhibitor was removed on a Sephadex G25 column.

2.3.4.b Preparation of QD-Antibody conjugate

In 850 µL of 25 mM PB solution were dissolved 20 mg of EDC. Subsequently, TGA-gel QDs 10^{-5}M and incubated for 15 min at room temperature. Anti-ASC antibody was in turn added to equal concentration and the solution was incubated for another 15 min. Unreacted antibody was removed on a Sephadex G25 column.

2.3.4.c Biological testing of QD conjugates

Biological testing of QD-inhibitors and antibody conjugates were performed in collaboration with Dr. Niamh Murphy and Prof. Marina Lynch, Trinity College Institute of

Neuroscience. Mixed glia, microglia and astrocytes from neonatal Wistar rats were cultured for 14 days at 37°C and 5% CO_2. Cultures were treated with ATP and inflammasome-targeting nanoparticles, control nanoparticles or inhibitors and antibodies alone at various concentrations. IL-1β and caspase 1 activity and cellular fluorescence were assessed.

2.3.5 Preparation of gelatin-mediated QD assemblies

TGA-gel QDs diluted in 10 mL of water to a final concentration of 10^{-6} M were submitted to 70°C for 3 min and immediately cooled down. The same treatment was applied to an equal concentration mixture of green-emitting TGA QD and red-emitting TGA-gel QD. UV-visible absorption and PL emission spectra were recorded.

2.3.6 Synthesis of gelatin nanoparticles w/o QD-loading

Gelatin nanoparticles were prepared using the two-step desolvation method.[6] The first step was aimed at narrowing the size distribution of gelatin molecules while the second step was the actual formation of nanoparticles. Gelatin powder (0.5 g) was dissolve in 10 mL of water at 50°C with vigorous stirring. To precipitate larger molecules, 12 mL of acetone were added out of the heat and with no stirring. The supernatant was discarded 2 min after addition and the volume of water was reconstituted. The pH was adjusted to 12 using 2 M NaOH. If appropriate, 25 µL of TGA-capped CdTe QDs ($3.3\ 10^{-5}$ M) were added at this stage. The flask was placed back over the magnetic stirrer, without heating, and 10 mL of acetone were added at a rate of 3 mL/min. At the end of the addition, 10 µL of 50% glutaraldehyde were injected and the turbid suspension was stirred overnight.

In attempts to produce smaller gelatin nanoparticles, the mode of agitation in the second step was varied. The slow addition of acetone was performed while maintaining the suspension in an ultrasonic bath. It was then either kept in the ultrasonic bath overnight, or further agitated with an ultrasonic tapered tip for 2 min before being returned to the bath and kept there overnight. Fractions were separated as described before.

2.3.7 Synthesis of gelatin-coated silver nanoprisms

Gelatine powder (0.01 g, 0.05 g or 0.1 g) was dissolved in 2 mL of water at 50°C. Freshly prepared silver nanoprisms were added to the solution with vigorous stirring. Where appropriate, 20 µL of gelatinated CdTe QDs (9.10^{-4} M) were also added. The mixture was cooled slowly to room temperature with constant stirring. The sample was divided into fractions by successive centrifugation cycles (10 000 rpm, 10min).

2.3.8 Synthesis of drug-loaded, FA-functionalised gelatin-coated Au-Ag nanoboxes

Gelatine powder (0.05 g) was dissolved in 4 mL of water at 50°C. Gold-silver nanoboxes (4 mL, 10^{-11} M) were added to the solution with vigorous stirring. Where appropriate, 8 µL of $5x10^{-3}$M paclitaxel were also added. The mixture was cooled slowly to room temperature with constant stirring. For FA functionalisation, 15 mg of EDC and 8 µL of 10^{-4} M FA were added to the reaction mixture and stirred for 30 min. Samples were washed of excess reagents by successive centrifugation cycles (10 000 rpm, 10min) and resuspended in Millipore water.

2.4 Experimental details for chapter 5

The oligonucleotide sequences used throughout the chapter were as follows:

- oligo 1: 5' NH2- A10 TAG GAA TAG TTA TCA (Tps6) 3'
- oligo 2: 5' NH2 – A10 TGA TAA CTA TTC CTA (Tps6) 3'
- oligo 3.1: 3'-Tps6-ACT.ATT.GAT.AAG.GATps6-5'
- oligo 3.2: Tps6-ACT.ATT.GAT.AAG.GAT-5'
- oligo 3.comp: 5'-TGA.TAA.CTA.TCC.CTA-3'

2.4.1 Synthesis of citrate-stabilised spherical gold nanoparticles

6 mL of a 1mM $HAuCl_4$ solution was brought to the boil. Trisodium citrate (TSC; 25mM; 1mL) was added at once. The solution was further heated for approximately 5 minutes until it turned ruby red. At this point the heat was removed and the solution was left to stir for half an hour.

2.4.2 Conjugation of 3'-T6-phosphorothioate-modified oligonucleotides to metallic nanoparticles

1.5 mL of particles (gold spherical, gold-coated silver nanoprisms or gold nanorings) brought to a concentration of 8 nM were mixed with 5 μL of either one of the thiolated oligonucleotides (oligo 1, 2, 3.1 or 3.2; 100 μM) and incubated for 24h at room temperature, in the dark and under gentle shaking. Using a 1 M NaCl solution, the concentration of NaCl was brought to 0.1 M. The next day, the NaCl concentration was brought up to 0.2 M; after one more day it was brought up to 0.3 M and left to incubate for a final 24h.

Unbound oligonucleotides were washed away by centrifugation at 10 000 rpm for 10 min which precipitated the nanoparticles out; the supernatant was discarded and replaced by the same the volume of water. This was repeated twice more to remove all unbound oligonucleotide.

2.4.3 Induced aggregation of gold nanoparticles

Citrate-stabilised spherical gold nanoparticles were dispersed in a total volume of 2 mL, in increasing concentrations of sodium chloride: 0, 0.025, 0.05, 0.1 and 0.2 M. Aggregation of nanoparticles was verified by UV-visible absorption spectroscopy and DLS.

2.4.4 *In situ* synthesis of oligonucleotide-conjugated metal nanoparticles

6 mL of a 1mM $HAuCl_4$ solution was brought to the boil. Oligo 1 or 2 was added (100 μM, 100 μL) was added followed by trisodium citrate (TSC; 25mM; 1mL). The solution was further heated for approximately 5 minutes until it turned ruby red. At this point the heat was removed and the solution was left to stir for half an hour. To remove any excess oligonucleotide the resulting particles were centrifuged at 10000rpm for 10 minutes. The supernatant was removed and the remaining concentrated liquid was redispersed in half the original volume of water.

2.4.5 Oligonucleotide-mediated assembly of metal nanoparticles

Metal nanoparticles conjugated to complementary sequences of oligonucleotide were mixed to the same final concentration. The resulting sample was wrapped in tin-foil and incubated on a shaker at room temperature for up to three days.

2.4.6 Conjugation of 5'amine-modified oligonucleotides to TGA-capped CdTe QDs

15 mg of EDC were dissolved in 400 µL of 25 mM Phosphate Buffer (PB), to which were added 200 µL of TGA-capped CdTe QDs (2.5×10^{-5} M); the solution was left at room temperature for 15 min before 100 µL of either oligo 1 or 2 (100 µM) were added. The solution was then incubated for 30 min at 30°C. The excess EDC and unbound oligonucleotides were separated from the QDs on a Sephadex-G25 column.

2.4.7 Oligonucleotide-mediated assembly of metal nanoparticles and QDs through the ds-oligonucleotide method

Metal nanoparticles and QDs conjugated to complementary sequences of oligonucleotide respectively were mixed in different ratios. AuNP-oligo1 (5.10^{-9} M, 80 µL) was mixed with (a) 10 µL, (b) 20 µL, (c) 50 µL and (d) 100 µL of QD-oligo2 (5.10^{-7} M) and the total volume was brought up to 2 mL with water. The four samples were wrapped in tin-foil and incubated on a shaker at room temperature for up to three days.

2.4.8 Oligonucleotide-mediated assembly of metal nanoparticles and QDs through the ss-oligonucleotide method

In an Eppendorf tube, 1 mg of 1-Ethyl-3-(3-dimethylaminopropyl)carbodiimide (EDC) was dissolved in 100 µL of 25 mM phosphate buffer (PB). TGA-capped CdTe QD (5 µL) was added to a final concentration of 1.2×10^{-6} M. After 15 min of incubation at room temperature, 800 µL of oligonucleotide-modified gold nanoparticles (AuNP-oligo1, 4.10^{-9} M) were added and the reaction was carried out at 30° C for up to one and a half hour. UV-visible absorption spectra of the mixture were recorded every half hour.

2.4.9 *In situ* Preparation of QD-oligo

QD-oligo were synthesised using our modification of the method published by Tikhomirov and co-workers.[7] $Cd(ClO_4)_2 \cdot 6H_2O$ and TGA were added to 150 mL degassed Millipore water. The pH of the solution was adjusted to 11 by dropwise addition of a 2M NaOH solution. Either oligo 1 or 2 (100 µM, 30 µL) was added to the solution. To a known weight of Al_2Te_3 were added 15 mL of H_2SO_4 to generate H_2Te gas which then bubbled through the Cd/thiol solution. The resulting non-luminescent solution was then heated under reflux. Once the QDs reached the desired size, the reflux was stopped and different fractions were obtained *via* size-selective precipitation using isopropanol. The final samples were further purified on a Sephadex-G25 column.

2.4.10 FRET studies in oligonucleotide-mediated assemblies of QDs

In a disposable fluorescence cuvette, the acceptor QD was diluted in 2 mL of water to a final concentration of 2.10^{-7} M. The acceptor QD was added by small increment of 2 to 3 µL to obtain a range of donor-to-acceptor ratios from 0.28:1 to 3.6:1. Between each addition of donor QD, the mixture was incubated for 30 min on a shaker at room temperature, wrapped in tin-foil. UV-visible absorption and PL emission spectra were then recorded for each ratio.

2.4.11 Biological studies of oligonucleotide-mediated assemblies of QDs

2.4.11.a Cell culture

HT1080 fibrosarcoma cells were cultured in medium (500 mL Minimum Essential Medium (MEM) supplemented with 0.055 g of sodium pyruvate, 5 mL of a solution of penicillin (2 mM) and streptomycin (2 mM), 5mL of 1 mM gentamicin and 100 mL of Fetal Bovine Serum (FBS)) at 37°C and in a 5% CO_2 atmosphere.

2.4.11.b Cell exposure to QDs

80% confluent cell cultures were detached using Trypsin and re-suspended in cell culture medium to a final concentration of 5.10^4 cells/mL and seeded in 35 mm-diameter glass-bottomed Petri dishes (2 mL per dish) for a final 1.10^5 cells per dish. After 24h incubation allowing the cells to adhere to the substrate, half of the medium was removed

from each dish and replaced by 1 mL of serum-free medium. The cells were incubated for a further 4h before the medium was aspirated out and replaced with 2 mL of QD suspension in Dubelcco's modified Phosphate Buffer Saline (DPBS) at a final concentration of 10^{-7} mol/L, or pure DPBS for control experiments. Cells were exposed to either Donor-QD, Acceptor QD, Donor+Acceptor QDs which were added one after the other, or pre-incubated Donor+Acceptor QDs. The latter was prepared by mixing Donor and Acceptor to a total QD concentration of 10^{-6} mol/L and incubating the suspension on a shaker, wrapped in tin-foil, for an hour. It was diluted down to 10^{-7} mol/L just before addition to the cell cultures. After four more hours, the QD containing solution was aspirated out of the dishes and the cells were washed three times with PBS.

2.5 Experimental details for chapter 6

2.5.1 QD-Heparin conjugates

2.5.1.a Preparation of QD-Heparin conjugates

Heparin conjugated CdTe-gelatine quantum dots were prepared using a modified, previously published procedure.[5] $Cd(ClO_4)_2 \cdot 6H_2O$ and TGA were added to 150 mL degassed Millipore water so the final molar ratio of Cd:Te:TGA was equal to 1:0.25:1.4. The pH of the solution was adjusted to 11 by dropwise addition of a 2M NaOH solution and 0.3 g of gelatine were added to the solution. To the known weight of Al_2Te_3 were added 15mL of H_2SO_4 to generate H_2Te gas which then bubbled through the Cd/thiol solution. The resulting non-luminescent solution was then heated under reflux for 24 h. EDC activated heparin was prepared by dissolving heparin (51 mg, $3x10^{-6}$ moles) in 10 ml EDC/DMAP solution ($3x10^{-3}$ M). The activated heparin was then added to one half of the quantum dot solution cooled to 80°C, while the other half was kept as TGA-gel QD reference. Different fractions were then obtained for both heparin-conjugated QDs and non-conjugated CdTe-gelatine quantum dots by size selective precipitation using 2-isopropanol and centrifugation.

2.5.1.b In vitro biological testing of QDs and conjugates

THP-1 cells (20,000 cells/well) were seeded on a Lab-Tek 8 well chambered borosilicate slide. To induce differentiation from monocytes to macrophages, cells were

cultured with 100 $ng.ml^{-1}$ PMA for 72 hours. A549 or Caco-2 cells (15,000 cells/well) were seeded on a Lab-Tek 8 well chambered borosilicate slide and allowed to adhere for 72 hours. Cells were washed and incubated with 5 μM solutions of the quantum dots for 2 hours at room temperature. The cells were then washed with media to remove unbound quantum dots and the nucleus counterstained using Hoescht 33342 (1.25 μg/ml) for 30 min at room temperature. Cells were washed twice with media and immediately imaged.

Cells were washed and fixed using 7.4% PFA for 20 min, washed with PBS and stored at 4 °C until required. Fixed cells were permeabilised with 0.5% Triton X-100 for 15 min. Cells were then washed and incubated with 5 μM solutions of the quantum dots for 1 hour at room temperature. The cells were then washed with PBS to remove unbound quantum dots and the nucleus counterstained using Hoescht 33342 (1.25 μg/ml) for 30 min at room temperature. Cells were washed with PBS and imaged.

2.5.2 Biological testing of CdS nanotetrapods

D-, L- and Rac-Pen CdS nanotetrapods were synthesised according to published procedure[8] and provided by Dr Joseph Govan. HT-1080 cells cultured to 80 % confluence were seeded in glass-bottomed 35 cm^2 petri dishes to the concentration of 10^5 cells/dish and incubated for 24 h at 37°C. Half of the culture medium was replaced with serum-free medium and the cells were incubated for another 4h. The cell culture medium was aspirated out of the dishes and CdS nanotetrapods were added to the cell cultures to a final 10^{-8} concentration in DPBS. To a control culture, only DPBS with no nanotetrapods was added. After 4h of incubation, the nanoparticle containing DPBS was removed and the cells were washed three times with DPBS to remove non-internalised nanotatrapods. Finally, cells were imaged by confocal microscopy.

2.5.3 Preparation of samples for solid-state Circular Dichroism studies

Aqueous solutions of metal nanoparticles, chiral molecules or other compounds to be analysed were deposited on a quartz slide and allowed to dry at room temperature. The slide was inserted in the CD spectropolarimeter in place of a cuvette. Pressure was induced by applying a second quartz slide against the specimen and tying it using plastic paraffin film. The variation in pressure was indirectly evaluated by measuring the outer distance between both slides.

2.5.4 Infiltration of polymer tubing with metal nanoparticles

A 5 cm piece of polymer tube was soaked in solvent for 1h. It was then transferred to a solution of gold nanoparticles (AuNP, 2 mL) in the same solvent, and the whole system was placed in an ultrasonic bath for 1h, 2h or 4h. Loading was studied by scanning electron microscopy (SEM) and thermogravimetric analysis (TGA).

2.6 Characterisation techniques

2.5.1 UV-Vis absorption spectroscopy

A Shimadzu UV-1601 UV - Visible Spectrophotometer was used to measure QD and metallic nanoparticles absorption. Most of the scans were carried in the 300-700 nm range although this was extended in some cases; larger silver nanoparticles required to scan up to 1100 nm while the presence of oligonucleotides was assessed by scanning down to 200 nm in order to measure the characteristic absorption peak at 260 nm.

2.5.2 PL spectroscopy

A Varian - Cary Eclipse Fluorescence Spectrophotometer was used to determine the fluorescence emission/photoluminescence (PL) spectra of QDs. The excitation wavelength was 480 nm and the emission was detected in the range 490-700 nm. The Quantum Yields (QY) were calculated from the PL spectra using Rhodamine 6G as a reference. The QD sample and the dye solutions were made up to the same absorbance at any wavelength between 470 and 480 nm where Rhodamine 6G has a QY of 95%. The wavelength of equal absorbances was used as the excitation wavelength. Both emission spectra of sample and dye were integrated between 490 and 700 nm. The sample's QY was then calculated using the formula: $QY = (sample\ integration/dye\ integration) \times 0.95$

2.5.3 Time-correlated single photon counting (TCSPC) spectrometry

Photo-luminescence lifetime measurements were performed using TCSPC on a Fluorolog 3 Horiba Jobin Ivon spectrometer. The QDs were excited at 458 nm using a

"Nanoled" semiconductor diode laser (Horiba Jobin Yvon) and the emitted photons were collected at the maximum emission wavelength to 10 000 counts.

2.5.4 Fluorescence Lifetime Imaging Microscopy (FLIM)

Based on the same principle as TCSPC spectrometry, FLIM couples fluorescence decay measurements with microscopy to generate a map of fluorescence lifetimes. Samples were analysed on a PicoQuant system composed of a MicroTime 200 inverse time-resolved fluorescent microscope, picosecond pulsed diode lasers exciting at 466 and 405 nm, a HydraHarp 400 multichannel picosecond event timer and TCSPC module and the SymphoTime imaging and analysis software. FLIM measurements were performed in the Materials Physics Centre in San Sebastian (Spain) with the help of Prof. Yury Rakovich.

2.5.5 Circular Dichroism (CD)

CD spectroscopy is a technique commonly used to identify chiral compounds. It is based on the differential interactions of enantiomers with circularly polarised light. Each enantiomer absorbs either right or left polarised light, and is accordingly qualified as dextro- or levogyre. More generally, species that exhibit CD are called optically active. A CD spectropolarimeter measures the absorption of both left and right polarised lights and the final signal is an average of those at each wavelength.

The CD spectra were recorded on a JASCO J-810 spectropolarimeter, using a scan rate of 200 nm/min and three to five accumulations per scan.

2.5.6 Dynamic Light Scattering (DLS)

Dynamic Light Scattering (DLS), also called Photon Correlation Spectroscopy (PCS) is a technique used to measure the hydrodynamic radius of proteins and nanoparticles. It is based on the difference in mobility of particles in suspension according to their size. When illuminated they generate a scattering pattern which varies at a speed that relates to the movement of particles. The instrument records the correlation function of the pattern and deduces the size distribution, taking into account the refractive index of the

material as well as the dispersant. Because of electrostatic and hydrogen bonding with the solvent molecules, the measured radius is not actually that of the nanoparticles, but also comprises the solvent shell which varies significantly with the surface composition and the solvent. The same machine can also measure the surface charge of nanoparticles, based on the electrostatic theory of colloidal stability. It describes nanoparticles as surrounded by an electrical double layer. The adsorbed layer is composed of counter-ions tightly packed around the surface, and the diffuse layer is a gradient of ions from the adsorbed layer to the suspension medium. The double layer is considered to be solidary with the particle. Zeta potential actually corresponds to the charge at the edge of the diffuse layer. That charge is responsible for the particles repulsing each other and therefore being stable in suspension. Figure 2.1 illustrates the electrical double layer theory.[9] Zeta potential is measured by applying an electric field across the dispersion in a specially designed cell fitted with electrodes. Particles within the dispersion will migrate toward the electrode of opposite charge with a velocity proportional to the magnitude of the zeta potential. This velocity is measured using the technique of laser Doppler anemometry. A laser beam is used to measure the mobility of the particles through the frequency shift or phase shift that they induce. The Smoluchowski or the Huckel theory, in polar or non-polar media respectively, is then used to convert the mobility into zeta potential.

Hydrodynamic radii and zeta potential of nanoparticles were measured on a Malvern Zetasizer Nano Series V5.10. The concentration of samples used for these measurements was typically corresponding to an absorbance around 0.2 in the plasmon band. Five measurements were usually taken for each sample, each made of 10 to 20 accumulations as optimised by the machine.

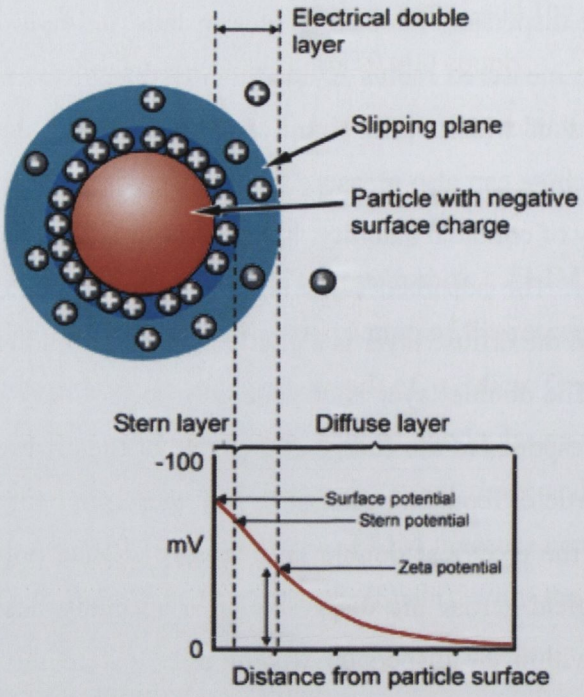

Figure 2.1 Schematic illustration of the electrical double layer and zeta potential[10] (Zetasizer Nano series technical note MRK654-01, Malvern Instruments)

2.5.7 Gel Electrophoresis

Electrophoresis is an analytical technique that separates species according to their mass and charge. In the present work, agarose gel electrophoresis was employed, where an electrical current is applied through the gel containing the nanoparticles to be analysed. The density of the gel determines the pore size and how nanoparticles are slowed down depending on their size, while the electrical current induces the migration according to their charge.

The running buffer was Tris-Borate-EDTA (TBE) and prepared as follows. In 700 mL of water, 5.45 g of Trizma base, 2.75 g of boric acid and 0.23 g of ethylenediaminetetraacetic acid (EDTA). The solution was stirred until complete dissolution of all powders and the volume was then brought up to 1 L. This made up the 1xTBE stock solution to be diluted by half for analyses.

A 0.2 % agarose gel was prepared in 0.5xTBE buffer. The agarose powder (0.2 g) was dissolved in 100 mL of buffer and brought to the boil. After complete dissolution the initial mass was reconstituted by adding water. The hot solution was casted into a cassette and left to settle for one and a half hour. The cassette was placed in a Sigma Aldrich mini

horizontal electrophoresis unit fitted with a 8-well comb and filled with 400 mL of 0.5xTBE and connected to a Consort EV231 power supply. The sample to be analysed were pipetted into the wells (40 µL each). A 100 V tension was applied to the gel for 30 min after which the gel was photographed and analysed using the ImageJ software.

2.5.8 Transmission Electron Micrsoscopy (TEM)

A Jeol 2100 Transmission Electron Microscope (TEM) was used to image metal nanoparticles. It was operated at an acceleration voltage of 200 kV with a Lanthanum Hexaborise emission source. The specimens were deposited on a formvar film on copper grids. Sizes of nanoparticles were calculated using ImageJ software.

2.5.9 High Resolution TEM (HRTEM) / Scanning TEM (STEM)

Imaging of QDs, high resolution of metal nanoparticles and elemental analyses were performed on a FEI TITAN field emission TEM operated at 300 kV. Specimens were preferentially deposited on lacey carbon films on copper grids. Switching from parallel to convergent beam (or nanoprobe) mode and using the High Angle Annular Dark Field (HAADF) detectors allowed performing STEM imaging with the same instrument.

2.5.10 Energy Dispersive X-ray spectroscopy (EDX)

EDX is an analytical technique that allows resolving the elemental composition of a sample. A beam of X-rays is focused onto the specimen and interacts with the atoms present. When doing so they may provide sufficient energy to eject an electron from the k shell, leaving a hole. When it recombines with an electron from a higher energy shell, excess energy is released in the form of x-rays which are collected. Since each element has a specific atomic structure and characteristic electronic energy levels, this allows to determine what elements are present.

EDX analyses were performed on the FEI TITAN TEM fitted with an EDAX-AMETEK Sapphire Li(Si) detecting unit. It comprises a retractable EDX detector with a 30 mm^2 crystal. Specimen were analysed with a 15° tilt towards the detector.

2.5.11 Confocal microscopy

Confocal microscopy is an optical imaging technique which, by opposition to conventional optical microscopy, provides an image of the focal plane only and eliminates out-of-focus light from the rest of the specimen. It uses point illumination with a laser source and a pinhole in an optically conjugated focal plane close to the detector to eliminate out-of-focus signal. Figure 2.2 illustrates the principle of the technique. Confocal microscopy has a double advantage. By eliminating most of the background it significantly improves the resolution and signal-to-noise ratio compared to conventional fluorescence microscopy. It also allows to independently image successive sections of the specimen, and ultimately to reconstruct a 3D image.

An Olympus FV1000 Point-Scanning Confocal Microscope was used to examine the cells after staining with QDs and counter-staining with Calcein AM or DAPI. The system was equipped with a multiline argon (453/488/515 nm) laser, and 405, 543 and 633 nm lasers. Sequential acquisition was used to acquire two to three channel images (two colours of fluorescence and brightfield) which were overlaid and analysed using the Olympus Fluoview version 7B software. Quantitative analyses were performed by either manually counting cells or integrating the luminescence intensity and averaging over at least 10 images.

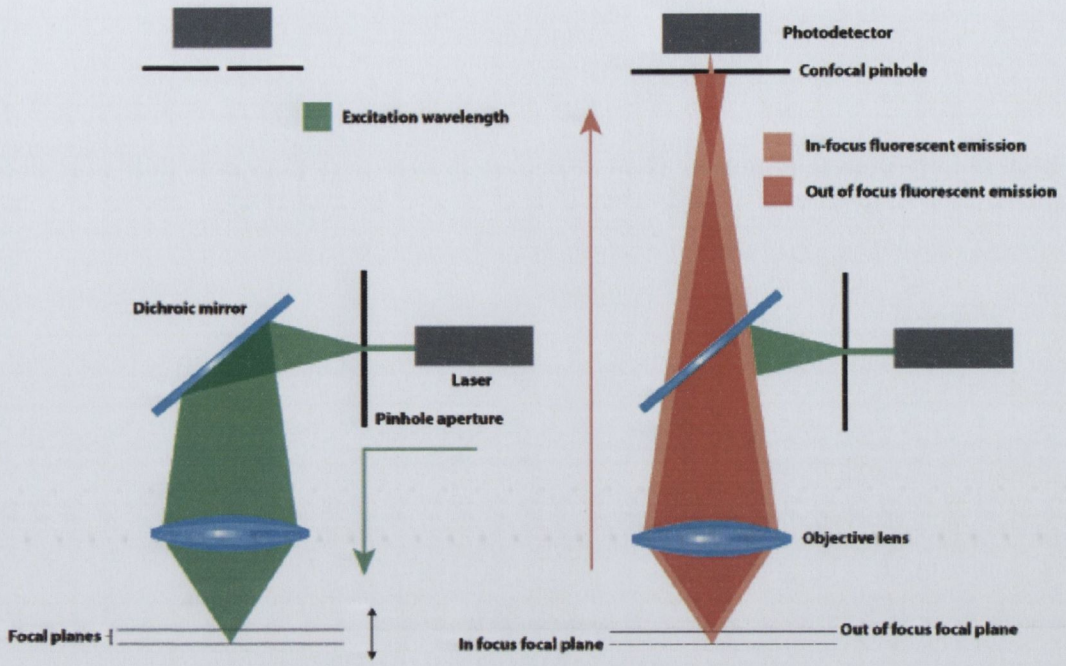

Figure 2.2 Schematic representation of the confocal microscope principle[11]

For imaging of cell cultures treated with Gold nanoboxes, specimens were analysed by a ZEISS 510 Meta confocal microscope equipped with a Zeiss LSM Image Browser. Two-channel (blue fluorescence and brightfield) qualitative confocal imaging was carried out by acquiring a series of Z-stack images. Pseudo-3D images of the nuclei staining were obtained by the function Pseudo-3D of the software Zeiss LSM Image Browser.

2.5.10 Epifluorescence microscopy

Metal nanoparticles in cell cultures could not be identified straight away in confocal microscopy as they are not luminescent. Epifluorescence microscopy was used to observe light reflected by the nanoparticles. The technique consists in passing the exciting light through the objective and the sample. All exciting light that is not absorbed or reflected by the specimen is transmitted through, and therefore do not reach the objective. The principle is illustrated by Figure 2.3. The final image is thus composed of emitted and reflected light with very little background. The microscope was also used in dark-field mode, based on the scattering ability of metal nanoparticles. Part of the exciting light is

blocked by a disk called "patch stop" to leave an outer ring of light (Figure 2.4). The condenser lens focuses the light onto the specimen, and only the scattered light reaches the objective while the directly transmitted light misses it.

Specimens were examined with a Nikon Eclipse TE300 **epifluorescence** microscope equipped with a high resolution CCD camera and the Q-Capture Pro image acquisition/processing software.

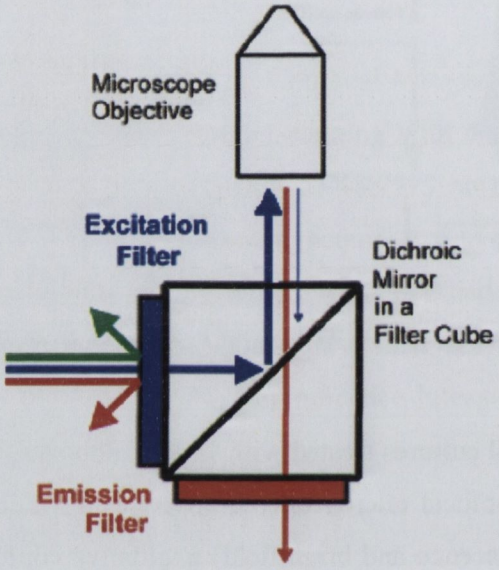

Figure 2.3 Schematic representation of the light path in an epifluorescence microscope[12]

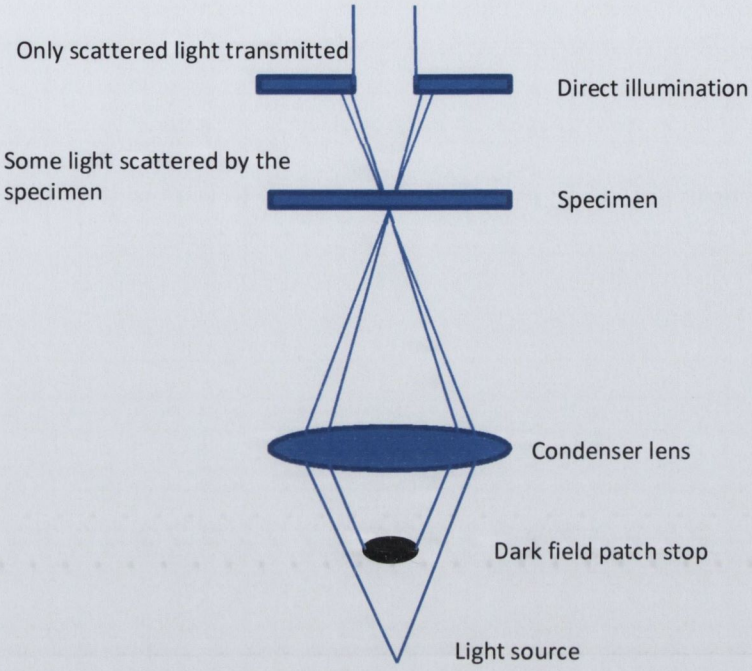

Figure 2.4 Schematic representation of the light path in dark-field microscopy

2.5.12 Thermogravimetric Analysis (TGA)

Thermogravimetric analysis is a technique which measures the weight-loss of a material according to the temperature. It allows to elucidate the quantitative composition of materials especially when they are made of components with very different pyrolysis temperatures, such as organic and inorganic elements.[13] The machine combines a micro-balance which continuously records the specimen's weight with a programmable furnace.

TGA measurements were carried out in air using a STA 1500 simultaneous thermal analyser from Rheometric Scientific with a temperature scan rate of 10°C min^{-1} from 20 to 900 °C.

References

[1] D. Aherne, D. M. Ledwith, M. Gara, J. M. Kelly, *Advanced Functional Materials* **2008**, *18*, 2005-2016.

[2] D. Aherne, D. E. Charles, M. E. Brennan-Fournet, J. M. Kelly, Y. K. Gun'ko, *Langmuir* **2009**, *25*, 10165-10173.

[3] D. Aherne, M. Gara, J. M. Kelly, Y. K. Gun'ko, *Advanced Functional Materials* **2010**, *20*, 1329-1338.

[4] N. Gaponik, D. V. Talapin, A. L. Rogach, K. Hoppe, E. V. Shevchenko, A. Kornowski, A. Eychmuller, H. Weller, *The Journal of Physical Chemistry B* **2002**, *106*, 7177-7185.

[5] V. Gérard, C. Maguire, D. Bazou, Y. Gun'ko, *Journal of Nanobiotechnology* **2011**, *9*, 50.

[6] K. L. C. J. Coester, H. Von Briesen, J. Kreuter, *Journal of Microencapsulation* **2000**, *17*, 187-193.

[7] G. Tikhomirov, S. Hoogland, P. E. Lee, A. Fischer, E. H. Sargent, S. O. Kelley, *Nature Nanotechnology* **2011**, *6*, 485-490.

[8] J. E. Govan, E. Jan, A. Querejeta, N. A. Kotov, Y. K. Gun'ko, *Chemical Communications* **2010**, *46*, 6072-6074.

[9] D. J. Shaw, *Introduction to Colloid and Surface Chemistry, Vol. 15*, Butterworth Heinman, UK, **1994**.

[10] Malvern-Instruments, *Zetasizer Nano series technical note MRK654-01* **2005**.

[11] http://www.scienceinyoureyes.com/index.php?id=71, *Bioimaging* (2008), accessed 15/07/2012

[12] http://www.fluorescence.com/tutorial/fm-optic.htm, *C&L Instruments Inc.* (2011), accessed 16/07/2012

[13] M. E. Brown, *Introduction to Thermal Analysis; Techniques and Applications*, Chapman and Hall, **1988**.

Chapter 3

Anisotropic Metal Nanostructures

3.1 Introduction

Metal nanoparticles, gold and silver in particular, have demonstrated good potential for a range of applications. Their main attraction resides in the surface plasmon resonance (SPR) phenomenon, which can be tuned both in wavelength and intensity by varying the size, shape and composition of metal nanoparticles. That collective oscillation of electrons creates a strong enhancement of the electromagnetic field in the vicinity of the nanoparticles upon photo-excitation. This in turn is the basis for many applications. It has been successfully employed to enhance Raman signals in Surface Enhanced Raman Spectroscopy (SERS). Raman spectroscopy is a characterisation technique based on the inelastic scattering of photons by certain molecules. The photon sets the material into vibration and is scattered with a different frequency, or energy, and that shift is measured. SERS arises from the presence of metal nanoparticles on the substrate. The SPR-induced enhancement of the electromagnetic field in the vicinity of the surface strongly enhances the vibrational modes. A charge-transfer complex may also be formed between the surface and the analyte molecule, with electronic transitions in the visible range. It should be noted that the SERS effect does not occur on smooth surfaces, but only on rough, nanoparticulate ones. Although initially developed with spherical nanoparticles, SERS has been proven to be influenced by the particle size and shape.[1-2] The optimal signal enhancement is obtained with the appropriate combination of analyte and nanoparticle.[3] Furthermore, there is a growing interest for gold nanoparticles in the fields of drug delivery and biological imaging. They are indeed a biologically inert material which also provides opportunities for functionalization as well as plasmonic imaging.[4] They can also be triggered by an external stimulus to release their cargo or produce heat.[5]

Silver nanoparticles, on the other hand, appear to be more easily synthesised in a controlled way in aqueous solution and at room temperature. Silver also exhibits stronger SPR intensities. The formation of binary gold-silver nanostructures would therefore

combine the advantages of versatility, strong SPR and biocompatibility. Anisotropy of materials is expected to influence the interactions with biological species.

The main aim of this part of our work is the synthesis of a variety of anisotropic metal nanostructures and the investigation of their properties for potential biomedical applications. Building on the optimised synthesis of silver triangular nanoplates, or nanoprisms, developed in our research group, we were able to produce gold nanorings. Complete coating of nanoprisms with gold led to the formation of hollow nanoboxes. These were studied for functionalisation and potential encapsulation of material.
In a similar way, silver nanowires were coated with gold and fully characterised in the prospect of *in vivo* studies.

3.2 Synthesis and characterisation of shape-controlled gold-silver nanostructures

A variety of anisotropic nanostructured materials were produced based on the reduction of silver and gold salts, in a rapid synthesis at room temperature. Figure 3.1 summarises the pathways used to obtain each of these shapes.

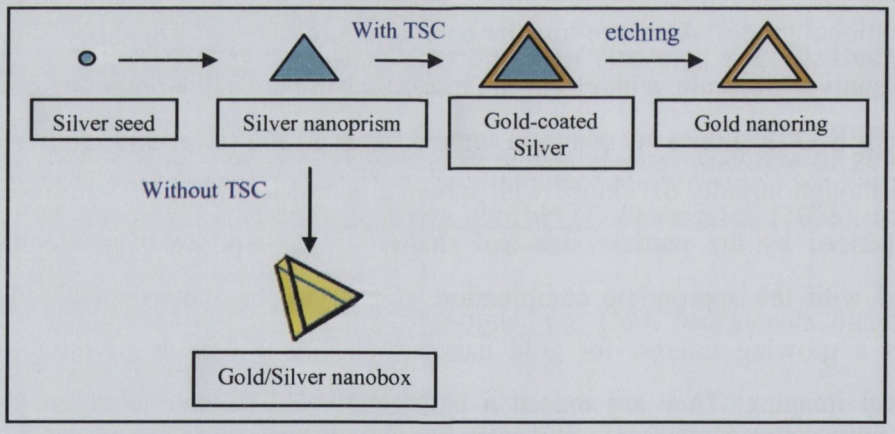

Figure 3.1 Schematic diagram of the synthetic routes to metallic nanostructures

3.2.1 Synthesis and characterisation of gold –coated silver nanoprisms

Silver nanoprisms were successfully synthesised and coated with a protective layer of gold according to published procedure[6] (Figure 3.1). Figure 3.2 below shows TEM images of those. A darker section around the edges could be observed on the gold–coated

sample. The average length of the triangle's sides was 31 nm (± 7 nm) for the silver nanoprisms and 34 nm (± 6 nm) for the gold-coated silver nanoprisms.

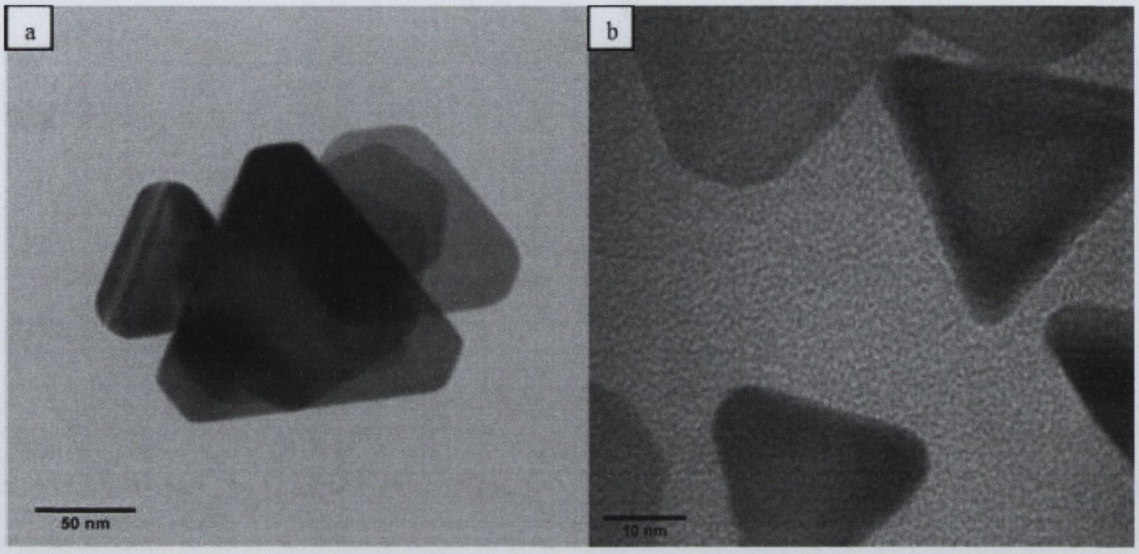

Figure 3.2 TEM images of (a) silver nanoprisms and (b) gold-coated silver nanoprisms

The protective effect of gold-coating was assessed by adding a highly concentrated solution of sodium chloride to both samples; a complete decolouration of the sample containing bare silver nanoprisms accounted for the degradation of the particles, while the samples coated with gold did not undergo any colour change. This was all consistent with published results.[7]

3.2.2 Synthesis and characterisation of gold nanorings

As-synthesised silver nanoprisms were used as templates to form gold nanorings[8] (Figure 3.1). This was achieved by depositing a layer of gold at the edges of silver nanoprisms and subsequently etching away the remaining silver. It resulted in the formation of closed shapes from triangles to circles, best described as toroidal polyhedra. In common parlance, a ring designates a band-like object with a vacant centre, usually of circular shape. By extension, the closed triangles may be viewed as degenerated rings with nanometric dimensions. For simplicity, such materials are referred to as nanorings.

The influence of several factors was explored in order to find the conditions that produced the most shape-controlled, uniform rings.

3.2.2.a Influence of TSC concentration

In previous work, the use of trisodium citrate (TSC) as a capping agent was proven to minimise the damage done to the silver nanoprisms through galvanic replacement during the coating process.[7] Therefore, it was expected that performing the coating in the absence of TSC might actually allow for the nanoprisms to be converted into rings without any additional etching step. As shown in Figure 3.3, the initial triangular shape of the silver nanoprisms was indeed lost, and galvanic replacement occurred, hence the formation of rings. The size distribution was preserved, with an average diameter of 32 nm (± 6 nm). However, the rings were fairly irregular in width and shape, with gold tending to grow towards the middle. For this reason, the method was abandoned. TSC was used in all subsequent experiments.

It is believed that the preferential deposition of gold around the nanoprism edges is due to the increased stabilisation of the <111> large triangular face by the presence of citrate molecules. In their absence, gold reacts faster with that face, resulting in deposition towards the middle of the particle.

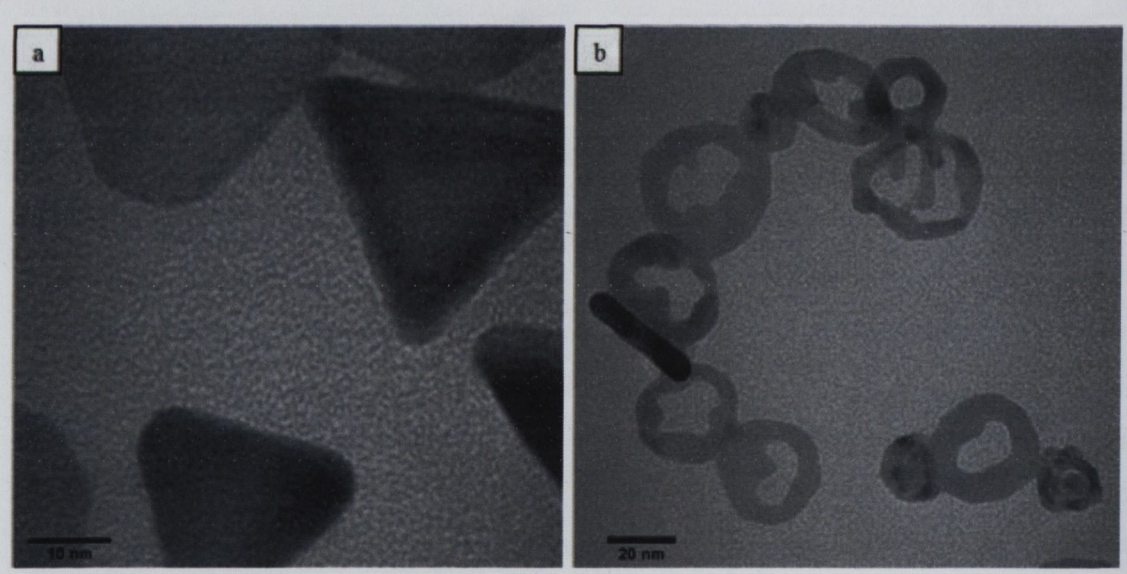

Figure 3.3 TEM images of gold-coated silver nanoprisms formed (a) in presence and nanorings (b) in absence of TSC

3.2.2.b Influence of ascorbic acid concentration

The straightforward addition of chloroauric acid solution to silver nanoprisms would result in the formation of rings through galvanic replacement due to the large

difference in reducing potential of the Ag^+/Ag pair (0.8V vs SHE) and the $AuCl_4^-/Au$ pair (0.99V vs SHE).[9] The gold (III) salt entirely oxidises silver, especially with the help of chloride ions forming silver chloride and thus driving the reducing potential of Ag^+/Ag further down. As noted before, gold preferentially deposits on the nanoprism edges. The presence of ascorbic acid, however, allows reducing $AuCl_4^-$ without oxidising the silver, thus preserving the integrity of the nanoprisms. Here it was decided to compare the direct formation of nanorings in absence of ascorbic acid with the controlled epitaxial deposition of gold and subsequent etching of silver using iron nitrate (a common etchant used by jewellers). Figure 3.4 shows TEM images of samples prepared using different amounts of ascorbic acid.

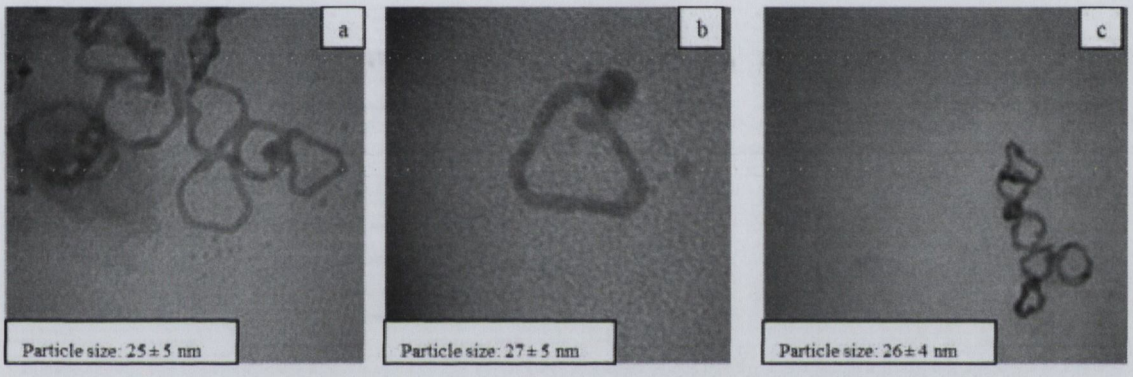

Figure 3.4 TEM images of gold nanorings prepared using (a) 2250 µL, (b) 150 µL and (c) no ascorbic acid

Rings formed in absence of ascorbic acid were very irregular compared to those produced in presence of ascorbic acid. When galvanic replacement was allowed to occur, the oxidation of silver from the whole nanoprism led to gold growing towards the middle in random branches. When the reduction of gold was achieved by adding ascorbic acid, however, the deposition remained controlled by the fact that the edge faces are least stable, and resulted in more even width of ring. While ascorbic acid was always added in excess compared to chloroauric acid, increasing the concentration might have increased the rate of reaction and altered the deposition. However, varying the amount did not make a significant difference in the shape or regularity of rings. Therefore, the minimum amount was used in all future experiments.

3.2.2.c Influence of gold amount

Aherne *et al.* previously determined the optimal amount of $HAuCl_4$ to provide a protective layer around the edges.[7] This amount depends on the size, and therefore plasmonic band, of the starting silver nanoprisms. At equal silver contents, smaller nanoprisms require a larger amount of gold due to the larger total surface area. The decrease in optimal Au/Ag ratio is non-linear with increasing plasmon resonance wavelength. In the following sections, the gold amount will be quantified with reference to that optimal ratio (Opt). For instance, Opt x3 means that three times the optimal amount was added.

Gold-coating of silver nanoprisms was performed using various amounts of gold with the prospect of increasing the width of the rings after etching of the silver. Figure 3.5 shows TEM images of the resulting samples.

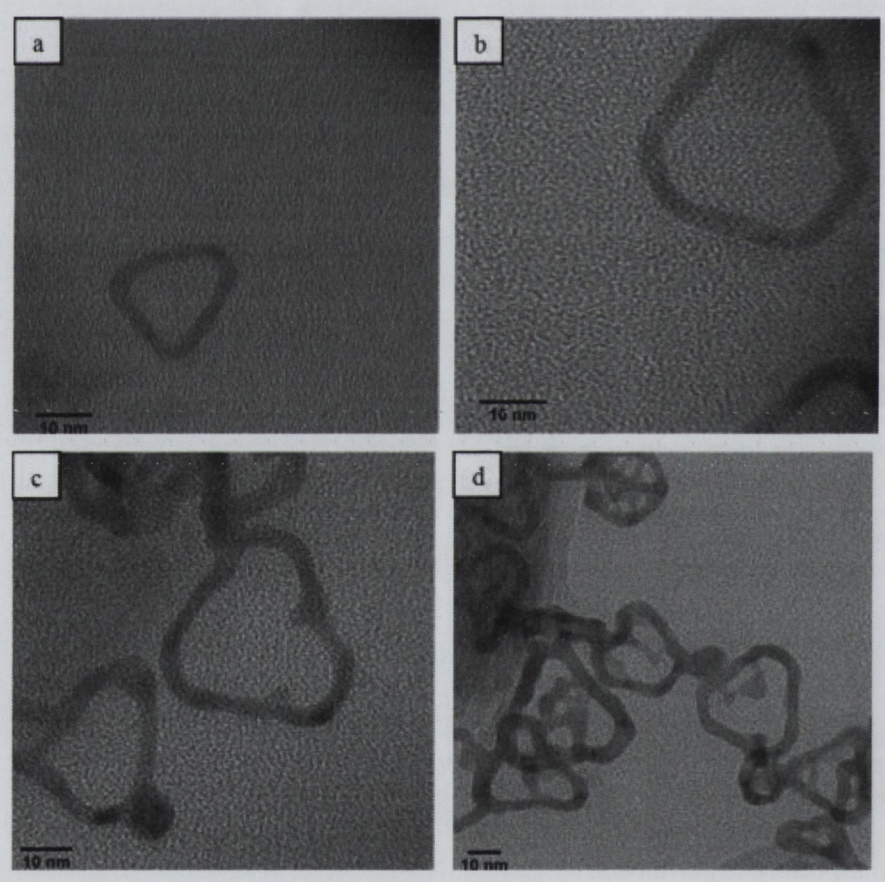

Figure 3.5 TEM images of gold nanorings produced using increasing amounts of gold salt (a to d)

A small increase in the width of the rings was observed with increasing amounts of gold as summarised in Figure 3.5 and in Table 3.1. However, the variation was not significant since it mostly remained in the error range. Large amounts of gold produced less regular, more globular rings. In the case of the largest amount being used, gold started to form bridges across the rings. When smaller quantities of gold were used, on the other hand, the gold layer was too thin to hold together as a ring after the etching step (picture not shown). It was thus concluded that the optimal amount was three times the one that was previously identified as providing an effective protective layer.

Table 3.1 Gold amount dependence of ring width

Sample	$HAuCl_4$ added	Ring width (nm)	Standard Deviation
a	Opt x3	3.0	0.9
b	Opt x4	3.4	0.5
c	Opt x5	3.6	0.9
d	Opt x10	4.0	0.9

The trend in variation of UV-Vis spectra for the different structures produced above is illustrated in Figure 3.6. The gold-coating of silver nanoprisms resulted in a red shift, which was accentuated in the case of ring formation.

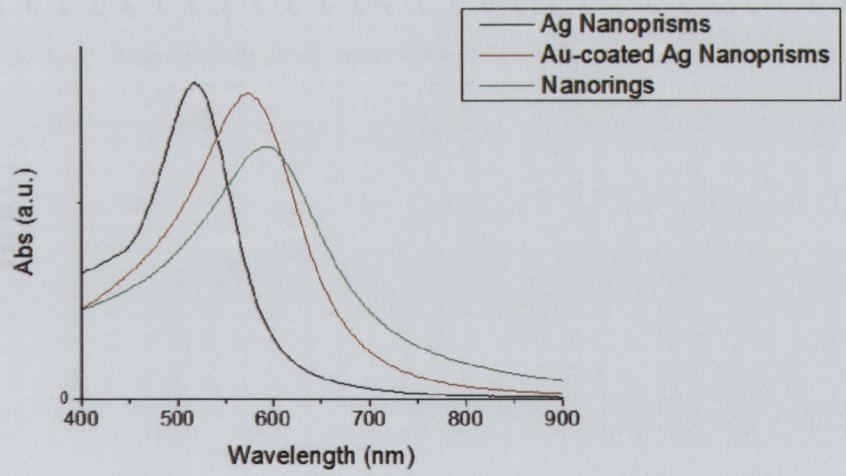

Figure 3.6 UV-Vis absorption spectra of silver nanoprisms, gold-coated silver nanoprisms and gold nanorings

3.2.3 Synthesis and characterisation of gold-silver nanoboxes

In the absence of TSC, gold was previously reported to grow towards the middle of the silver nanoprisms. Addition of a large amount of gold and ascorbic acid in excess thus showed the formation of a hollow triangular nanostructure which was designated as nanobox[10] (Figure 3.1). This result was successfully reproduced (see Figure 3.7, TEM images of nanoboxes).

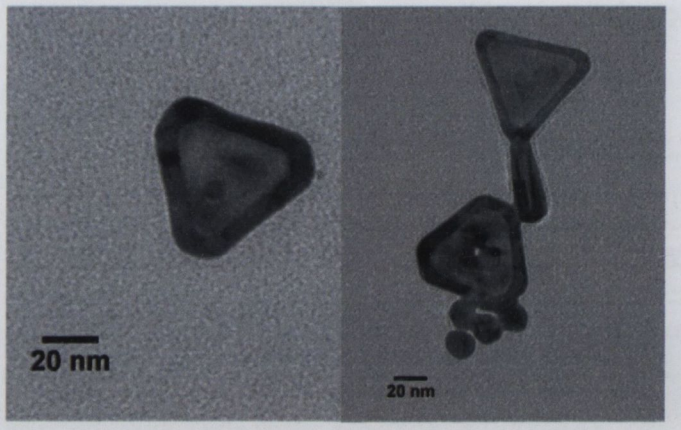

Figure 3.7 TEM images of gold-silver nanoboxes

The formation of nanoboxes can also be successfully identified using absorbance spectroscopy, where nanoboxes demonstrate a blue shift in the UV-Vis absorption spectrum compared to that of silver nanoprisms as shown in Figure 3.8; the shift increases with the thickness of the shell, which is associated with the formation of a gold/silver alloy as it was previously reported.[10]

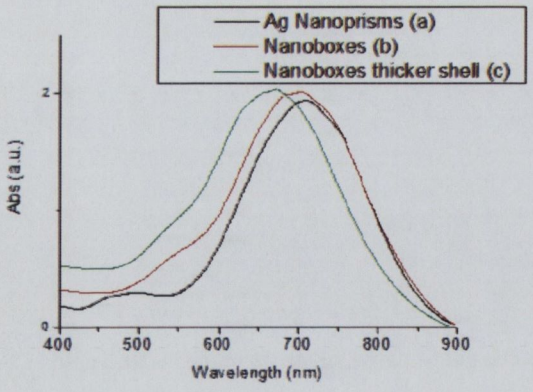

Sample	Diameter (nm)	Shell thickness (nm)
Ag Nanoprisms (a)	57 (± 18)	-
Nanoboxes (b)	58 (± 11)	8 (± 1.6)
Nanoboxes (c)	61 (± 12)	10 (± 2.3)

Figure 3.8 UV-Vis absorption spectra of silver nanoprisms and gold-silver nanoboxes and corresponding particle sizes as measured from TEM images

The postulated growth mechanism for these nanoboxes is through the galvanic replacement of silver by gold despite the presence of excess ascorbic acid. After the initial oxidation, Ag^+ ions are believed to be co-reduced with $HAuCl^-_4$ by ascorbic acid and to form an alloy at the Au/Ag interface that reforms the particle shape while leaving a hollow space in the middle.[10] Such a mechanism would mean that the surface of the nanoparticle is essentially gold, which was confirmed by Energy Dispersive X-ray spectroscopy. As seen on Figure 3.9, the silver content was negligible compared to the gold count.

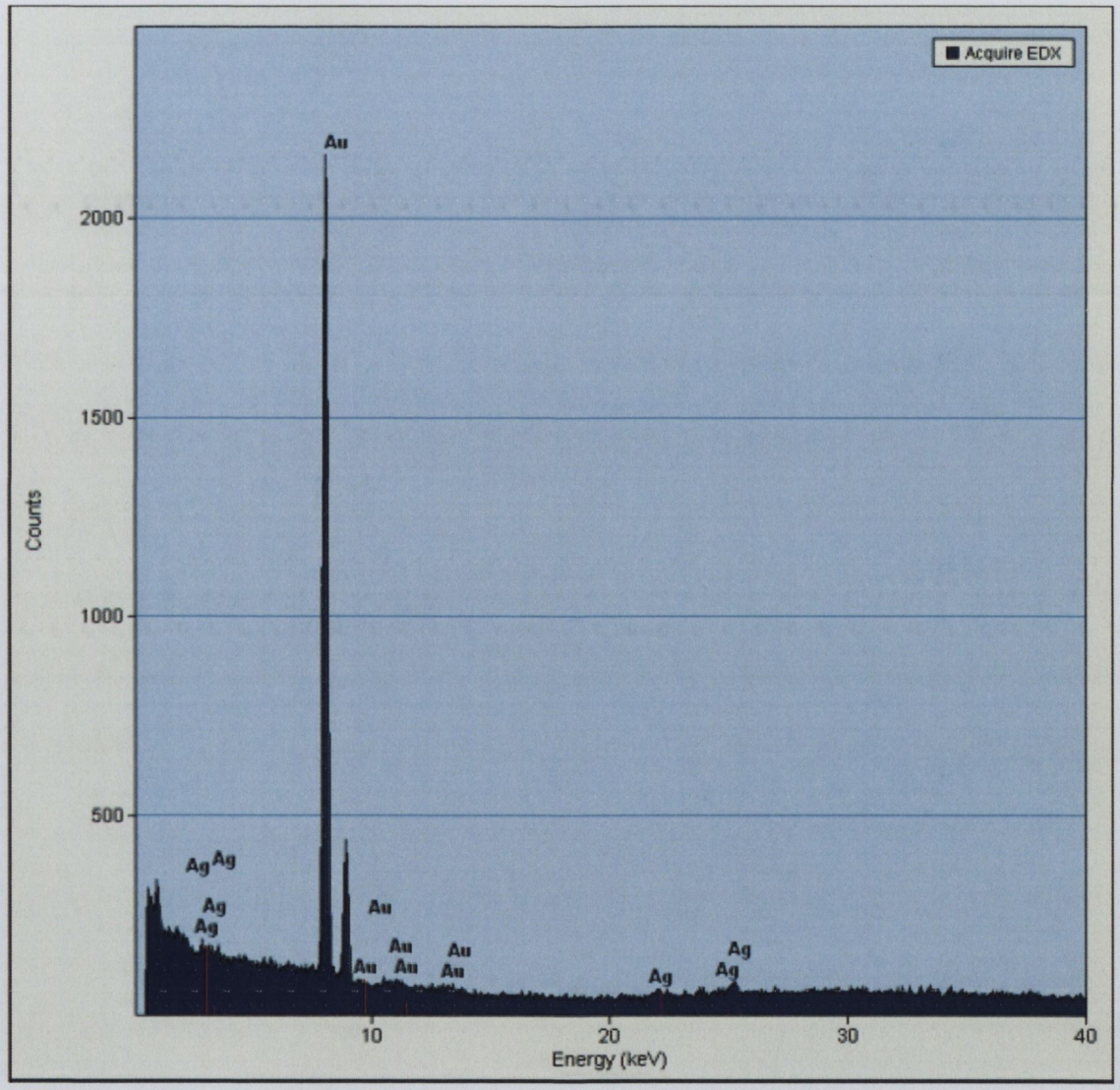

Figure 3.9 EDX scan of AuAg nanoboxes, showing gold as the dominant element

Finally, Scanning Electron Microscopy (SEM) imaging provided further characterisation of the morphology of nanoboxes. It had been assumed so far that they had the same flat triangle outside shape as the template silver nanoprisms.[10] As shown in

Figure 3.10, they actually appeared to have slightly thicker walls on the edges, and a thinner middle part, thus forming ridges. The initial deposition of gold preferentially around the edges would explain this final morphology.

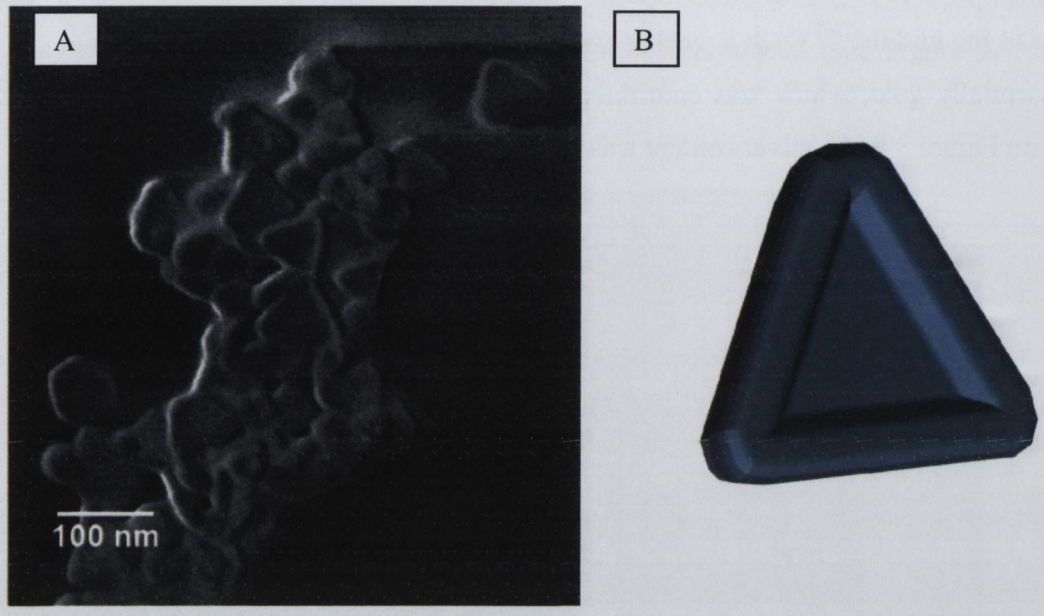

Figure 3.10 (A) SEM image of AuAgNB; (B) Schematic representation of the ridged morphology of AuAgNB

It remained uncertain, although postulated,[10] whether at any stage of their formation these boxes were "open", in which case it might be possible to encapsulate a moiety inside one by having it in the reaction mixture. It was therefore attempted to form the nanoboxes after having introduced a few different materials into the silver nanoprisms suspension.

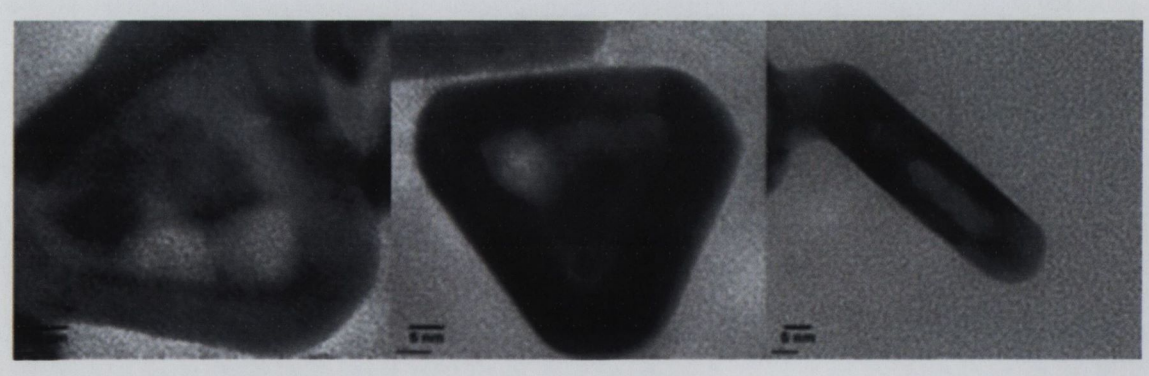

Figure 3.11 TEM images of AuAg nanoboxes formed in presence of CdTe QDs. From sideways, the dark spots appear to be bridges (right). Scale bars 5 nm

First, gelatinated CdTe QDs were used as a species to be encapsulated. They were selected because they are more stable in acidic environments than TGA-capped QDs owing to the gelatine layer. Their presence did not appear to alter the formation of nanoboxes. After removing free QDs from the solution, there was no luminescence remaining. Any QD luminescence is expected to be quenched when in close proximity to a plasmonic nanoparticle and *a fortiori* when inside one. The only way to determine whether they were lodged inside nanoboxes was TEM. As seen in Figure 3.11, some 5 nm spots could be seen in the boxes; however, this could be Au or Ag fragments due to misdirected growth forming bridges.[10] It was therefore impossible to clearly differentiate them from potentially encapsulated QDs. Furthermore, the lower TEM contrast of CdTe compared to gold was likely to make them less visible. Thus it is difficult to make a certain conclusion about the encapsulation of QDs inside nanoboxes.

Beyond the question of encapsulating a moiety inside these nanoboxes appeared the challenge of detecting it. Since the only type of nanoparticle that could be small enough to fit in the boxes (which are approximately 8 nm thick) did not give any conclusive result, a radically different approach was contemplated. The dye 1,1'-diethyl-2,2'-cyanine chloride or pseudoisocyanine chloride (PIC) forms so-called J-aggregates in contact with silver. They are characterised by the creation of an excitonic state from the closely packed dye molecules which results in a sharp absorbance band red-shifted from the normal band of the monomer, at around 570 nm.[11] A smaller peak situated at 475 nm appears when J-aggregates are formed upon contact with Ag nanoparticles. In contact with Au or Au/Ag nanoparticles, however, J-aggregates are characterised by a dip in absorbance, again at 475 nm. Both phenomena are attributed to the coupling of the metal surface plasmon and the dye exciton; a peak absorbance occurs when the plasmon is of a higher energy, whereas a dip appears when it is the other way around.[12] It was expected that J-aggregates would remain detectable inside a gold/silver shell. PIC was thus added to silver nanoprisms and, after verifying the initial formation of J-aggregates, ascorbic acid and chloroauric acid were added as well.

The concentration of PIC greatly influenced the formation of nanoboxes, as seen in Figure 3.12. At low PIC concentration the growth did not seem to be disturbed and the nanoboxes formed normally. As the concentration was increased, they became less regular. For concentrations higher than 15 nmol/L they no longer appeared to be hollow. On the other hand, they clearly generated J-aggregates as shown in the UV-visible absorption

spectra in Figure 3.13. Although the dye molecules might have been lying on the particle surface, the J-aggregate signal was not affected by washings, which suggested that they were either very strongly bound to the surface or trapped inside. Unfortunately, as the PIC concentration was reduced to a level where the nanoboxes could form properly, any J-aggregate signal became too weak and was hindered by the plasmon peak. It should also be noted that bigger nanoprisms were used in the case of lower PIC concentrations, with a plasmon band overlapping the monomer and J-aggregate bands. Therefore, it was again impossible to come to a definitive conclusion regarding the encapsulation of molecules in the nanoboxes.

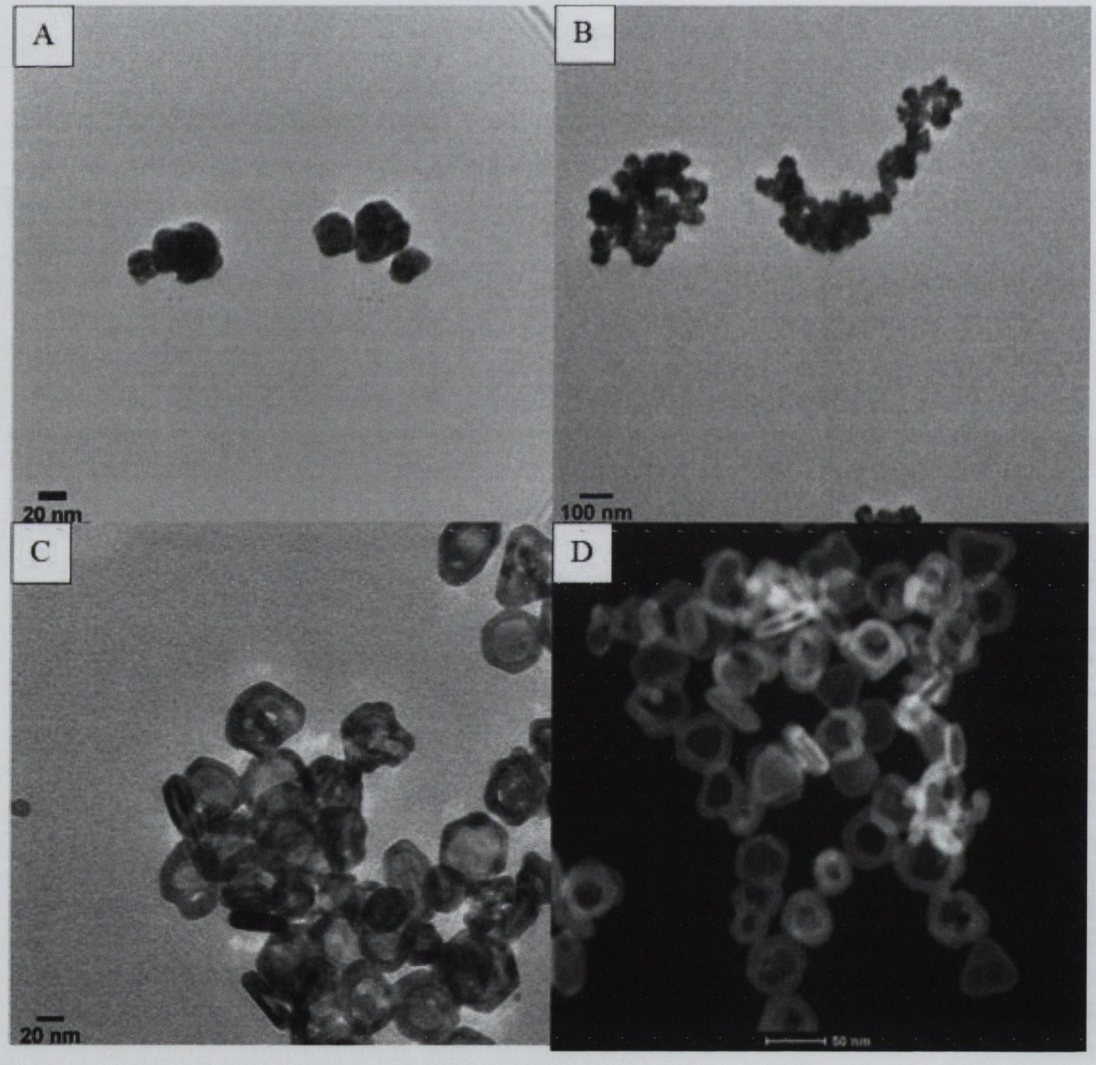

Figure 3.12 TEM images of AuAg nanoboxes formed in 100, 15 and 10 nmol/L PIC respectively (A,B,C); STEM image of AuAg nanoboxes formed in 10 nmol/L PIC.

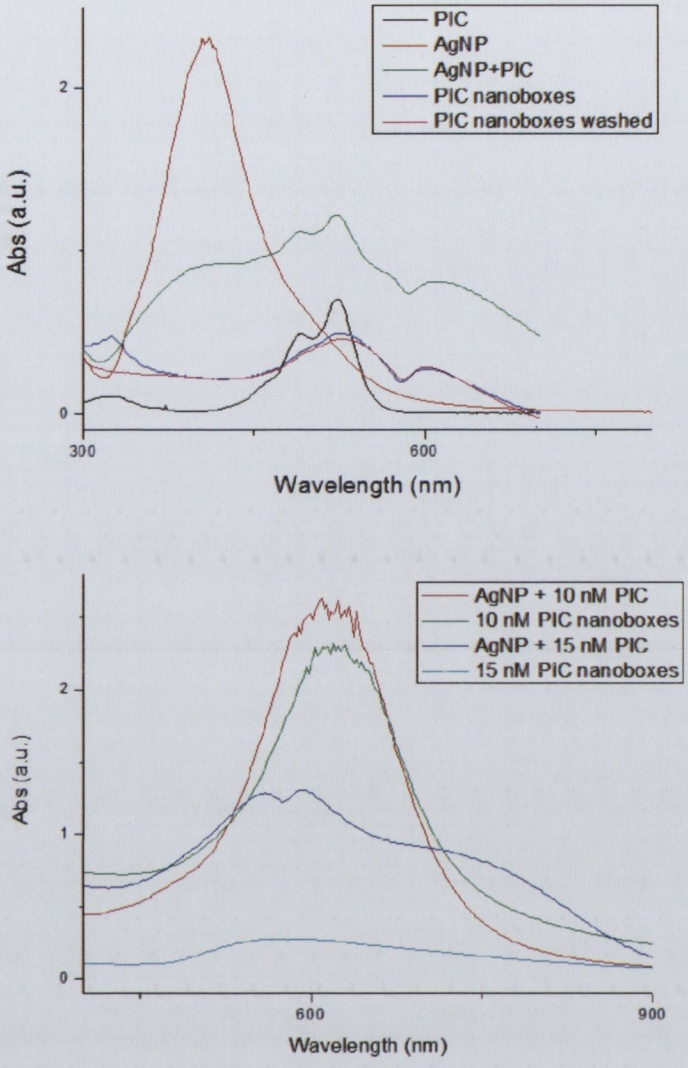

Figure 3.13 UV-Visible absorption spectra of silver nanoprisms and subsequently formed gold/silver nanoboxes, with 100nM (top), 15 and 10nM (bottom) PIC

Fluorescent Lifetime Imaging Microscopy (FLIM) was used to detect any luminescence emerging from J-aggregates and to map out the lifetimes. These measurements were carried out by Prof. Yury Rakovich in the Materials Physics Centre in San Sebastian (Spain). Figure 3.14 presents some sample images obtained with that technique. The patterns observed suggested that J-aggregates may be located around nanoparticle clusters formed on the glass slide. It did not provide any conclusion regarding their encapsulation. Their presence was, however, a positive result, as this system demonstrated interesting FLIM images and might have potential for photonics applications. However, much more detailed studies will be necessary to further investigate this system and explain the observed behaviour.

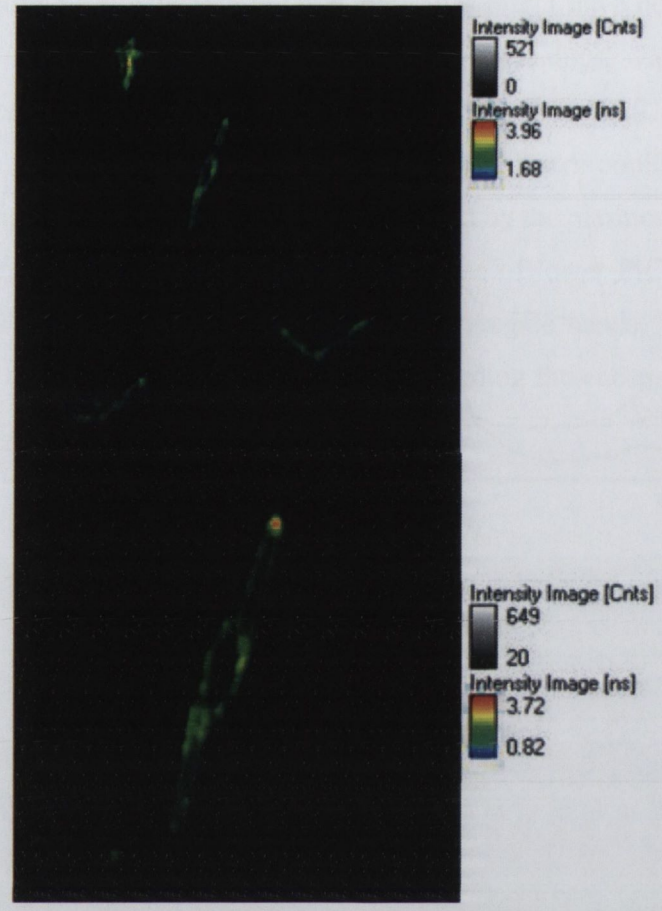

Figure 3.14 Plasmonic imaging of gold-silver nanoboxes

3.3 *In vitro* cellular testing of metal nanoparticles

Gold is a very attractive material for biomedical applications owing to its being essentially inert and biocompatible. Associating these properties with the sensitive and tuneable surface plasmon resonance make gold nanoparticles excellent candidates for bio-sensing, diagnosis or gene expression.[13] When made either anisotropic or optically active, their interactions with biological entities may well be modified. They can be visualised by using their high scatter properties and the dark field setting of an epi-fluorescent microscope. The source is used to excite the plasmonic nanoparticles, and only the scattered light is collected, thus excluding all biological materials. This section describes the different behaviour of various metallic nanostructures in cell cultures, as investigated with the help of Dr. Dania Movia, Institute of Molecular Medicine, Trinity College Dublin.

3.3.1 Chiral gold nanoparticles

Gold nanoparticles (AuNP) were synthesised through the traditional reduction method in the presence of penicillamine in D or L configuration as appropriate. The resulting materials exhibited strong circular dichroism (CD) outside of the ligand optical activity region, as previously reported and reproduced in Figure 3.15.[14] The origin of this new CD is thought to be partly the chiral environment created by the ligand shell and partly a chiral adsorption pattern that distorts the metal crystal. The nanoparticles are thus composed of a mostly achiral core with a chiral "footprint" on the surface atoms. Experimentally, they presented, as expected, mirror image CD, but it should also be noted that there was an inversion of chirality in the plasmon band. It therefore appeared that D-penicillamine (D-Pen) formed L-distorted gold crystals and *vice versa*. Several biological effects can be expected due to behaviour of the two enantiomeric forms. First of all, the two configurations of penicillamine themselves have different interaction patterns with living cells.

Since the structure of penicillamine is close to that of the substrate for a number of enzymes, it can interfere with the metabolic process. Biological systems, however, use L-amino acids to form proteins, so the L enantiomer is a better substitute. This is why L-penicillamine (L-Pen) is toxic by enzyme inhibition.[15] D-Pen, on the other hand, has relatively limited interactions with cells and enzymes and is therefore much less cytotoxic. It readily chelates copper ions, thus preventing them from entering cells and allowing them to be eliminated from the body much faster. This property is the basis for its use in the treatment of Wilson's disease, a rare inherited disorder where there is too much copper in tissues, causing damage to the liver and nervous system.[16] D-penicillamine is also used in the treatment of metal poisoning[17] and rheumatoid arthritis.[18] From these observations we can conclude that if the mechanism of nanoparticle uptake is directed by a specific recognition of the ligands, L-penicillamine stabilised nanoparticles should exhibit a higher level of uptake and potentially cause a higher cytotoxicity. The overall chirality of the nanoparticle, however, should also be considered.

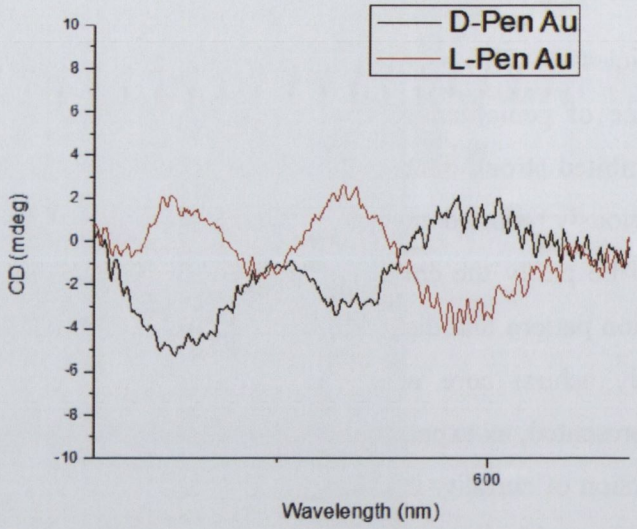

Figure 3.15 CD spectra of D- and L-penicillamine stabilised gold nanoparticles

Adherent mouse BALB/c macrophages (J774 cells) were treated with both enantiomers of nanoparticles and analysed by epi-fluorescence microscopy. Bright and dark field images of cells treated with L-Pen stabilised AuNP (L-Pen AuNP) are shown in Figure 3.16 and that of cells treated with D-Pen stabilised AuNP (D-Pen AuNP) are displayed in Figure 3.17. Due to the very small size of these nanoparticles (around 3 nm as determined by TEM), visualisation *via* scattered light was very challenging. It was possible, however, to detect a few bright spots inside the cells, most likely aggregates of nanoparticles. Quantifying the uptake was made delicate by the low signal that originated mainly from aggregates; therefore the cell behaviours towards the D- or L-enantiomer could not be accurately compared.

The experiment was nonetheless encouraging with regard to the suitability of the imaging technique for metal nanoparticles. Overall the uptake of D- and L-penicillamine stabilised gold nanoparticles appeared to be of similar order, which indicated that it was most likely occurring through non-specific endocytosis of nanoparticle clusters rather than specific ligand-based recognition.

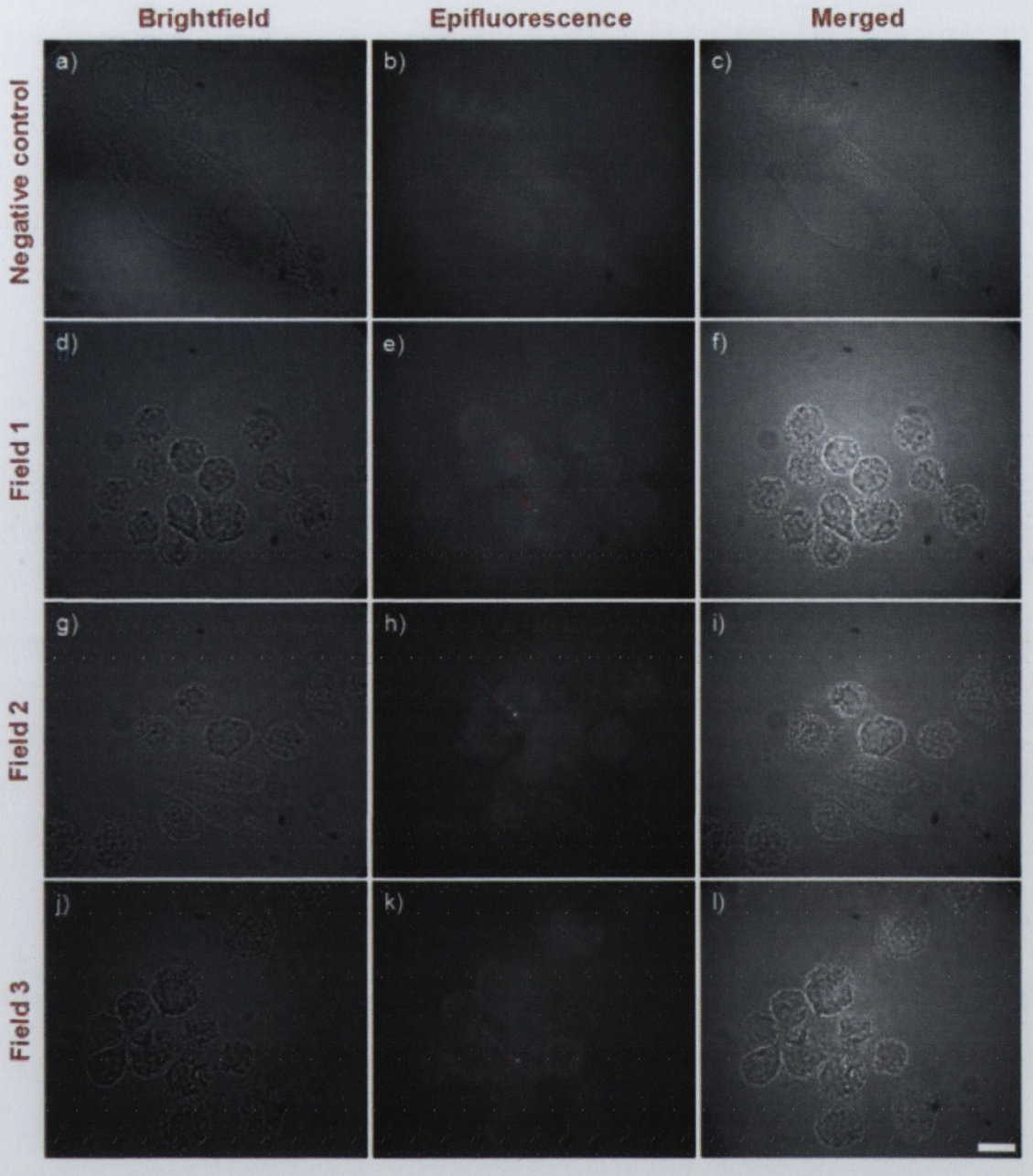

Figure 3.16 (a, d, g, j) Brightfield, (b, e, h, k) epifluorescence and (c, f, i, l) merged images of J774 cells (d-l) with or (a-c) without L-Pen AuNPs. Examples of single resonant metallic NPs, visible as lighter areas inside cells, are highlighted by arrows. Scale bars: 20 μm (100x magnification)

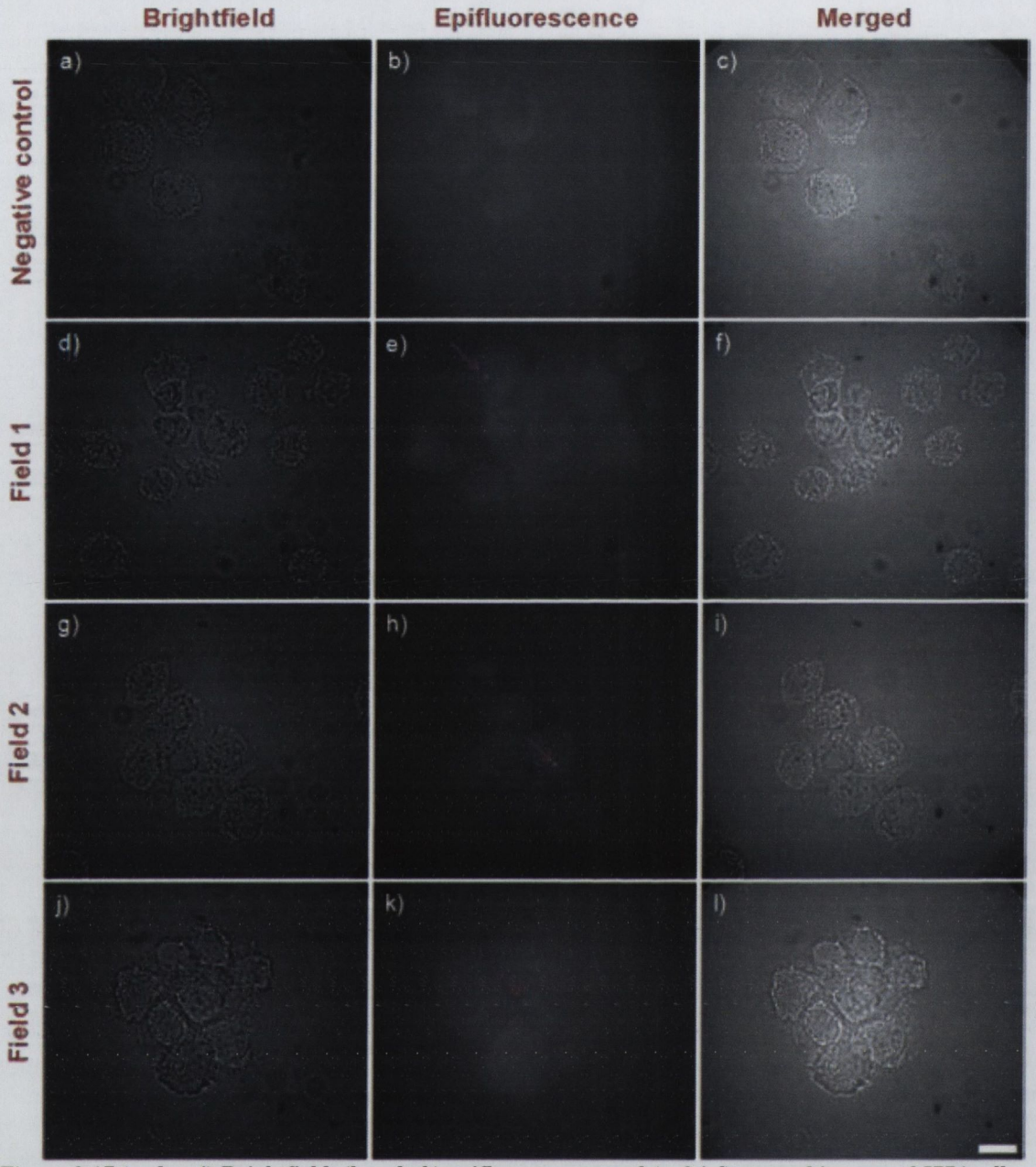

Figure 3.17 (a, d, g, j) Brightfield, (b, e, h, k) epifluorescence and (c, f, i, l) merged images of J774 cells (d-l) with or (a-c) without D-Pen AuNPs. Examples of single resonant metallic NPs, visible as lighter areas inside cells, are highlighted by arrows. Scale bars: 20 μm (100x magnification)

3.3.2 Gold-silver Nanoboxes

3.3.2.a Cellular uptake of gold-silver nanoboxes in 2D cultures

Preliminary *in vitro* testing results with penicillamine-stabilised spherical gold nanoparticles, described in the previous section, enabled us to suggest that gold nanoparticles could be uptaken through endocytosis without ligands playing any recognition role. Our further goal was to investigate the influence of particle size and shape on their *in vitro* behaviour. Two sets of gold-silver triangular nanoboxes were synthesised

as described in section 3.2 Synthesis and characterisation of shape-controlled gold-silver nanostructures, with distinct average triangle heights. They were formed by gold-coating silver nanoprism templates of different edge sizes. Because the growth of initial silver nanoprisms relies on the propagation of defects and the growth speed depends on the position of these defects relative to the particle symmetry, all nanoprisms grow at a slightly different speed. Consequently, as the average height increases, the size distribution broadens. This was reflected in the size (triangle height) measurements based on TEM images, all gathered in Figure 3.18 and Table 3.2.

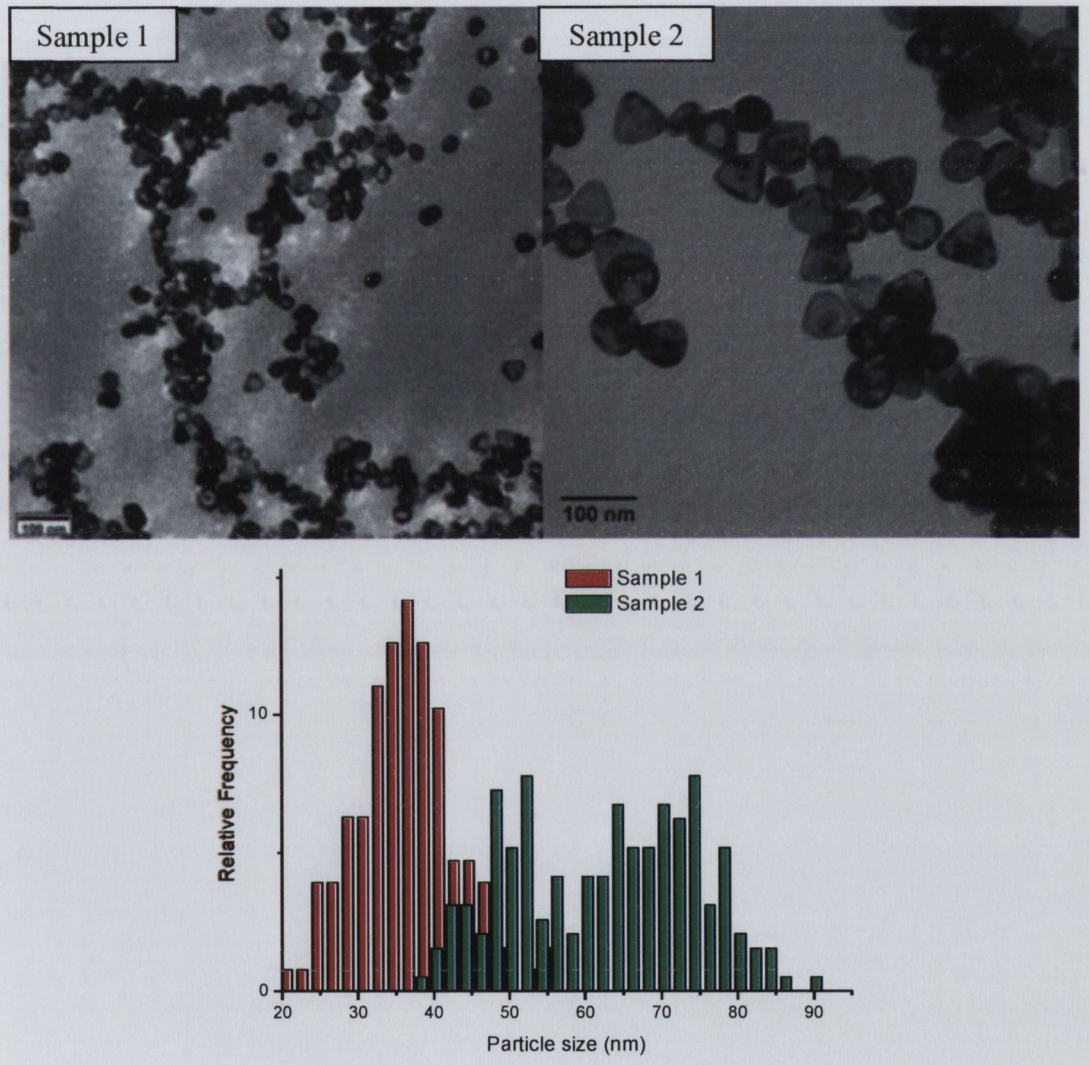

Figure 3.18 Size characterisation of AuAg nanoboxes. Top: TEM images of sample 1 and 2. Bottom: Size distribution of sample 1 and 2 as measured on TEM images.

Table 3.2 Size characteristics of Sample 1 and 2 of AuAg nanoboxes

Sample	Average diameter (nm)	Std deviation	concentration (mol/L)
Sample 1	37	6	1.63462E-10
Sample 2	62	12	4.2E-11

Initially, nanoboxes were tested in mouse macrophages (J774) following the same protocol as for penicillamine-stabilised AuNP. The dark field set-up of the epifluorescent microscope allowed for very clear visualisation of internalised nanoboxes. Their much larger size compared to Pen-AuNP provided a strong localised plasmon resonance which was excited by the epifluorescence light source. Nanoparticles thus appeared as bright dots which were not visible in the negative control, cells with no nanoparticles (Figure 3.19).

The number of internalised nanoboxes for both samples appeared to be very high, nearly filling up the whole cell cytoplasm, while Pen AuNPs only showed as isolated dots. Even when considering the weaker signal of the latter, it seems reasonable to conclude that the uptake of nanoboxes was much higher than the one of AuNPs. This was largely imputable to the size difference, for smaller particles were previously reported not to be endocytosed as easily as bigger ones. In all endocytotic processes, the cargo species must bind to a receptor, an adaptor protein or some other cell membrane constituent in order to trigger the wrapping by the cell membrane, the vesicle formation, and its engulfment.[19] The rate and speed of nanoparticle internalisation are controlled both by the thermodynamics of protein binding and the kinetics of protein diffusion.[20] The bigger the nanoparticle, the more anchor sites and the lower the free energy; on the other hand, the more binding sites needed, the longer the protein recruitment process. There is, therefore, an optimal size for nanoparticles which allows for the most efficient endocytosis;[20] this depends on the cell type, its environment, and also the nanoparticle aspect ratio.[21] Overall, spherical particles of 25 to 50 nm in diameter were found to be the best uptaken while smaller ones had to be internalised in clusters.[20-21] Both samples of nanoboxes were in the appropriate size range for efficient endocytosis.

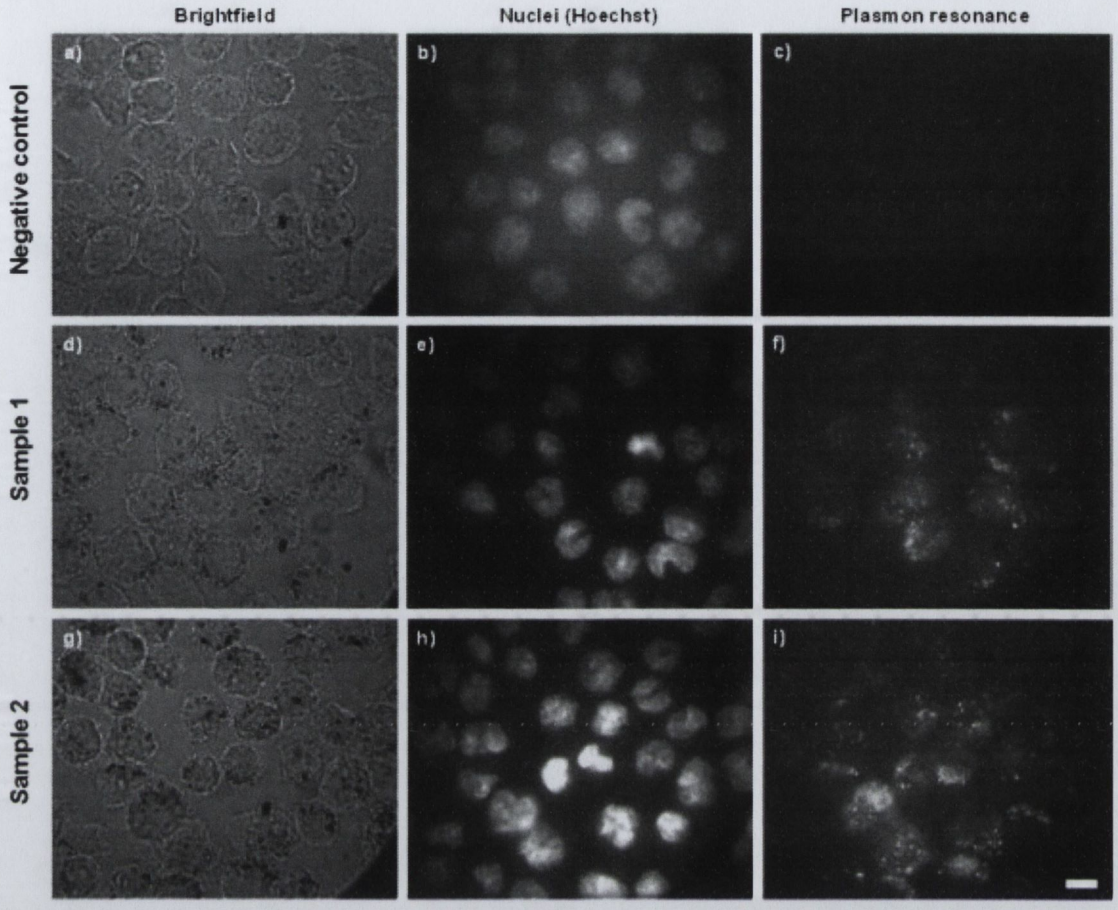

Figure 3.19 (a, d, g) Brightfield, (b, e, h) epifluorescence and (c, f, i) plasmon resonance images of J774 cells incubated (d-i) with or (a-c) without AuAg Nanoboxes. (f, i) Examples of single resonant metallic Nanoboxes, visible as lighter dots, are clearly visible within cells. Scale bars: 20 μm (100× magnification)

Epifluorescent microscopy determined that nanoboxes were interacting with the cells, and the superimposition of bright and dark fields lead to the conclusion that they may also be identified as dark spots in the bright field image, thus making the plasmon resonance image not absolutely necessary. It was therefore possible to use confocal microscopy to verify that the nanoparticles were actually entering the cells as opposed to being only attached to the plasma membrane. In Figure 3.20, the nuclei were stained in blue and the cytoplams in red. Slice by slice imaging of cells allowed for visualisation of the nanoboxes as dark areas within the membrane delimited by the red area. It also suggested that most nanoparticles were located very close to the nuclei, potentially on the membrane, but did not penetrate them.

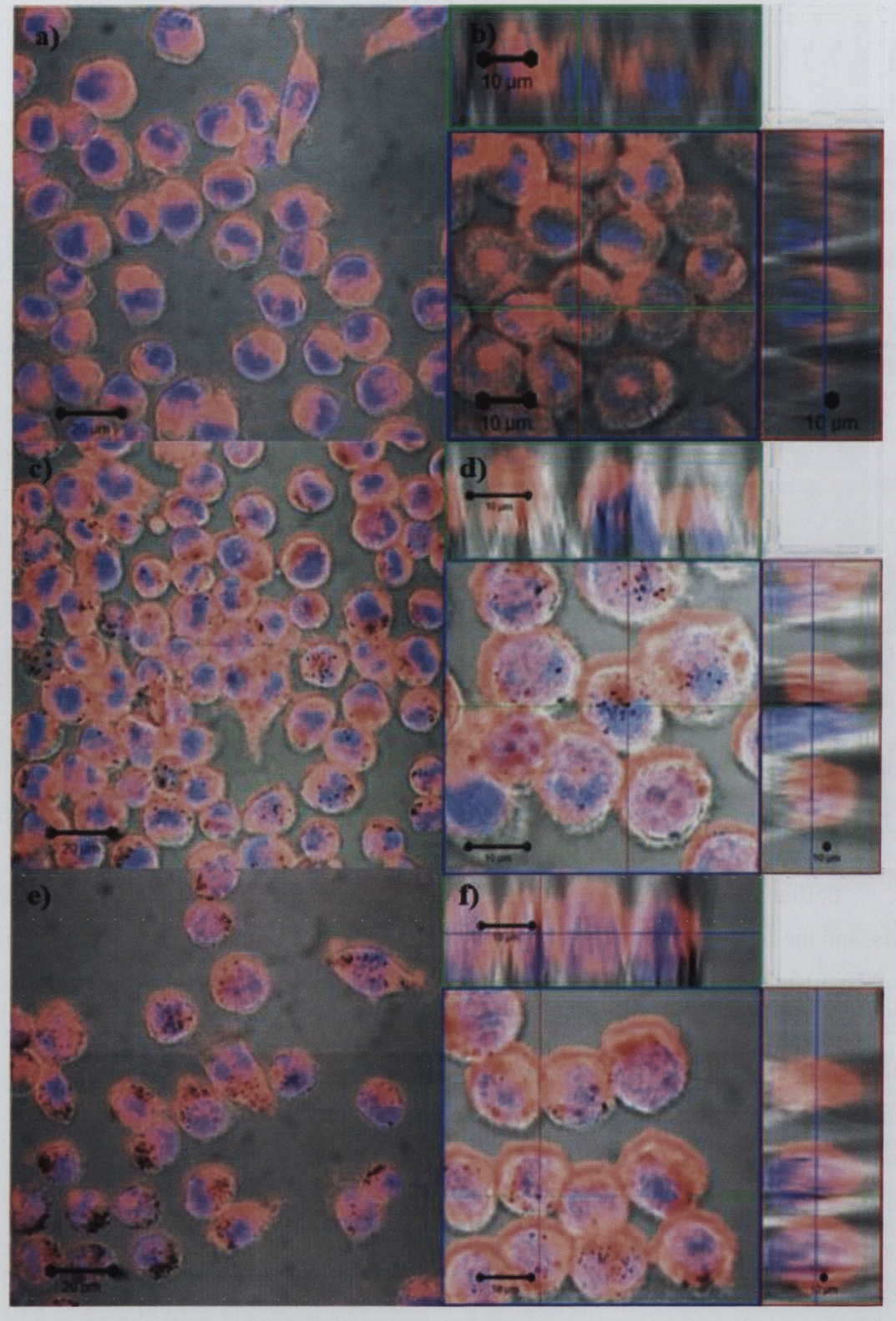

Figure 3.20 Confocal microscopy images of J774 cells incubated with sample 1 (c,d) or sample 2 (e,f) of nanoboxes, and negative control without nanoboxes (a,b). Nuclei are stained in blue and the cell membrane is stained is red. Nanoboxes are visible as dark areas in bright field. 3D projection of Z-stacks (b,d,f) clearly show that nanoboxes are localised within the cells.

Since macrophages are natural phagocytic cells, they tend to take up large materials regardless of their composition. For most biomedical uses, nanoboxes would need to be readily internalised by cells through general endocytotic pathways, as the majority of cells do not have phagocytic capabilities. A549 cells are epithelial carcinoma cells from the lungs of a 58-year old Caucasian male.[22] They do not possess any phagocytic capabilities as opposed to J774 cells. They were exposed to AuAg nanoboxes in the same conditions and demonstrated clearly visible internalisation of nanoparticles, as shown in Figure 3.21. Nanoboxes were again observed in the cytoplasm of most cells. Larger nanoboxes from sample 2 were present in significantly larger amounts than those from sample 1, which was not observed in J774 cells. This confirmed the difference in endocytotic pathways, with phagocytocis being much less dependent on the nature and size of the object.

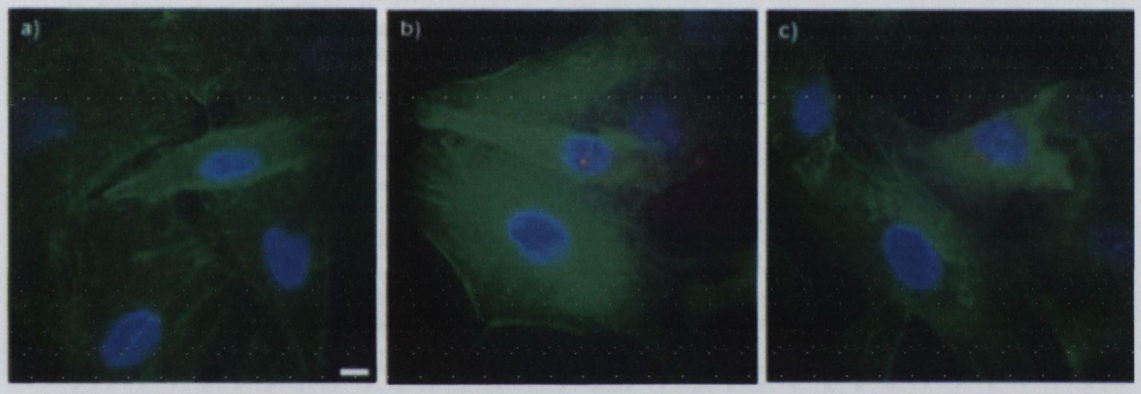

Figure 3.21 Epifluorescence images of 2D cell models of A549 cells incubated (a) without AuAg Nanoboxes or with (b) sample 1, (c) sample 2 AuAg nanoboxes. Nuclei are stained in blue, F-actin filaments in green while single resonant metallic AuAg Nanoboxes localized within the cells are here showed in pseudo-colour (red) for illustrative purposes. Scale bars: 20 μm (100× magnification).

3.3.2.c Cytotoxicity studies

The effects of smaller and larger gold nanoboxes on the viability of A549 cells were investigated in 2D and 3D cultures. Figure 3.22 illustrates the cellular response upon exposure to sample 1 and 2 for 24 hours through the measurements of three major indicators of viability: cell count, lysosomal mass/pH and membrane permeability. The values were compared to that obtained in untreated cell cultures (negative control) and cultures treated with doxorubicin, a well-documented anti-cancer drug.[30] The cell count is the first and most straightforward means to evaluate the degree of cytotoxicity. It not only relates to cell death but also to cell proliferation which may be affected as well. Gold

nanoboxes of either size did not appear to reduce the cell count in the range of concentrations that were used.

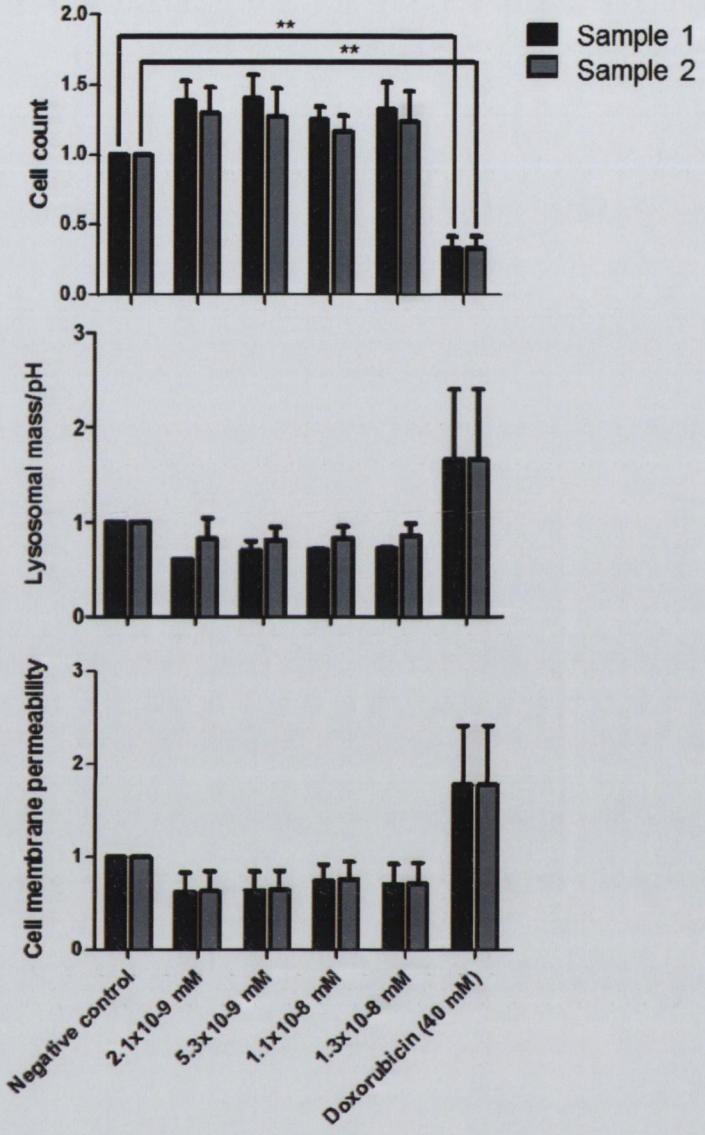

Figure 3.22 Cellular response upon 24 hour-exposure to sample 1 and 2 of nanoboxes in various concentrations: effects on cell count, lysosomal mass and cell membrane permeability. Negative control: untreated cell culture. Positive control: 40 mM doxorubicin. Stars indicate significant variations.

Lysosomes are cell organelles which contain a number of enzymes and an acidic environment destined to break down any cellular waste. Alterations of the normal cell physiology are usually associated with changes with the lysosomal mass and pH. It has been reported that internalised nanoparticles, in particular, tend to cause an increase in that indicator, which may also be associated with the storage and hydrolysis of materials in the

lysosomes.[31] Gold nanoboxes did not induce any significant change in the lysosomal mass/pH parameter, after a 24 hour-exposure, at any concentration tested.

Cell membrane permeability is a non-disputable sign of on-going cell death, and one that can be easily measured through the penetration of selected dyes.[32] Gold nanoboxes did not appear to cause any increase in cell permeability within 24 hours of exposures in concentrations comprised between $2.1x10^{-9}$ and $1.3x10^{-8}$ mM.

Overall, gold-silver nanoboxes demonstrated very low levels of *in vitro* cytotoxicity. Assessment of a series of indicators led to the conclusion that these nanomaterials cause very little disruption to the cells physiology and metabolism within 24 hours of exposures, at concentrations under $2x10^{-8}$ mM. These results are very promising for potential applications of gold-silver nanoboxes for drug delivery and as contrast imaging tools.

Functionalisation and further biological testing of gold-silver nanoboxes are discussed in chapter 4.

3.4 Gold-coating and optical activity of silver nanowires

3.4.1 Preparation of gold-coated silver nanowires

Nanowires are very interesting materials in relation to cellular interactions and sensing, owing to their high aspect ratio. The nano-sized diameter confers upon them similar properties to those of nanoparticles, which differ from the bulk. In addition, being several micron-long provides a huge surface area for interactions. Functionalised nanowires have therefore been shown to be a suitable template for very sensitive detection assays.[35]

Since silver is readily etched in physiological conditions through catalytic oxidation, pure silver nanowires cannot be used as such. Therefore gold-coating, following the same principle as developed for the coating of silver nanoprisms, was expected to provide protection against oxidation while retaining similar plasmonic properties. Furthermore, the use of this technique could enable the synthesis of hollow gold nanotubes which could have interesting optical properties.

Samples of silver nanowires (AgNW) of various lengths 3, 5, 10, 14 and 28 μm, were supplied. All nanowires were 114 nm in diameter. They were prepared through the patented polyol method[36] and kindly provided by Seashell Technology. Figure 3.23 displays a selection of sample pictures of the original silver nanowires from both TEM and STEM. They appeared to be quite uniform and of high purity. The deposition of gold onto silver nanowires was achieved through galvanic replacement using a solution of chloroauric acid which was added to the nanowires. This method has been widely used; it has, however, mostly been aimed at completely replacing the silver to obtain gold nanotubes.[37] In the present work the ratio of gold to silver, concentrations and addition rate were optimised to minimise the oxidation of silver as well as the branching out of gold nanoparticles. Figure 3.24 displays TEM images of the resulting nanostructures for all five lengths of nanowires. The diffusion driven deposition of gold appeared to result in rather inhomogeneous samples where complete replacement of silver had occurred on some nanowires while others were left intact. Having seen little to no variations between the samples, further improvements of the method and characterisation were performed only on the 5 and 14 μm long nanowires. However, it should be noted that longer nanowires tended to break in the process due to the vigorous agitation, sonication, and washing steps that were required.

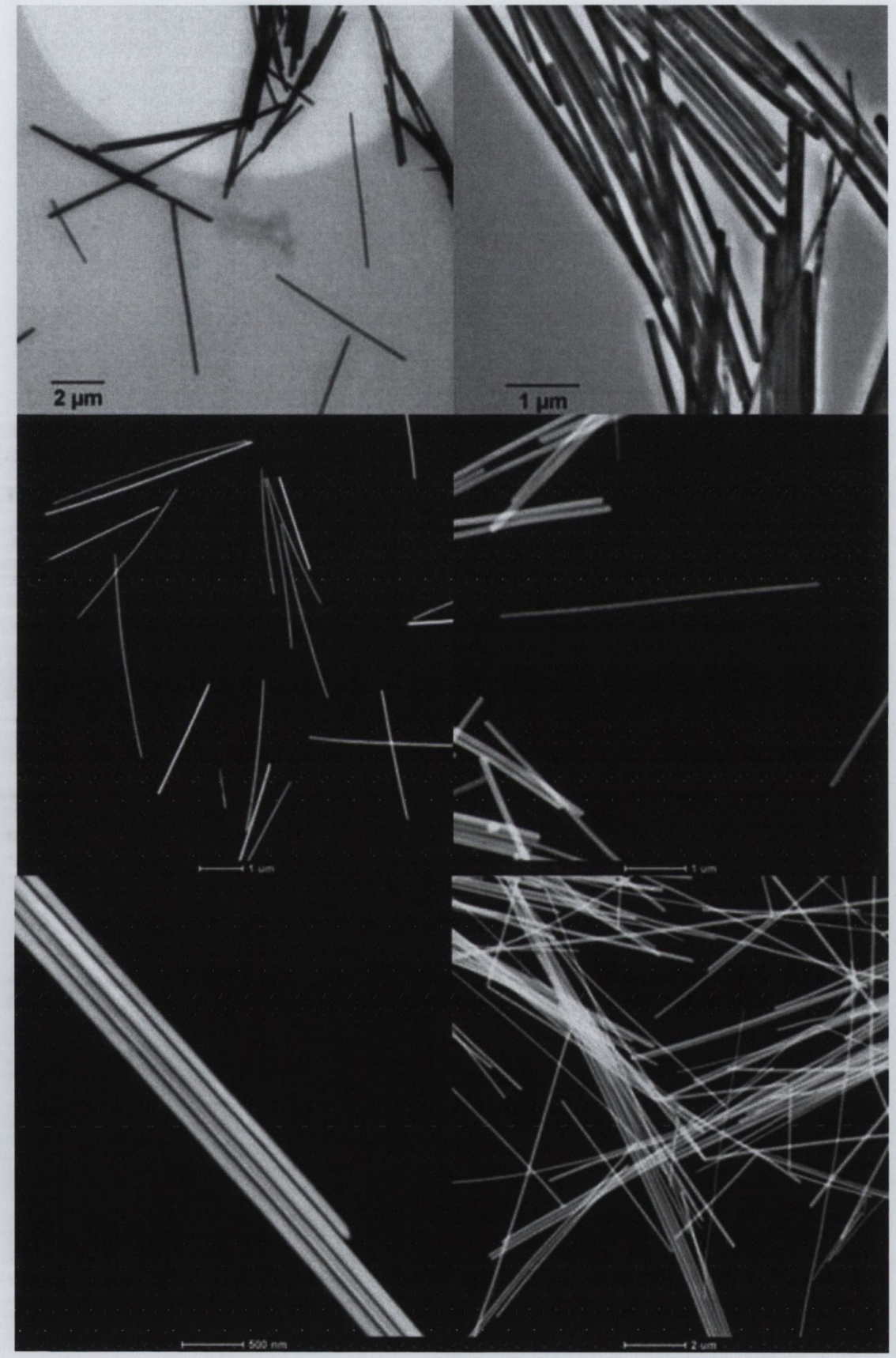

Figure 3.23 TEM (top) and STEM (middle and bottom) images of original silver nanowires

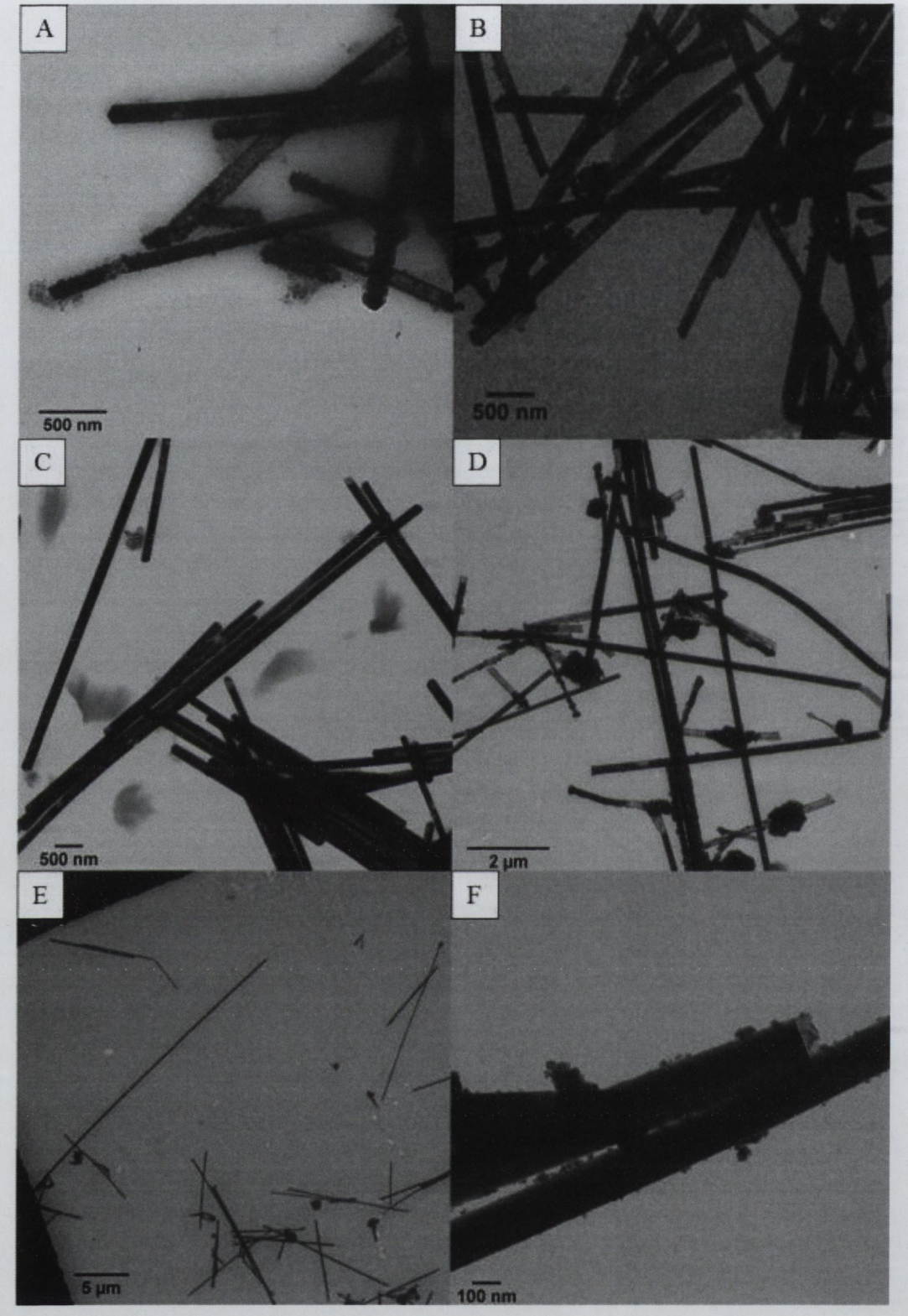

Figure 3.24 TEM images of gold coated AgNW of various lengths. A: 3 µm; B: 5 µm; C: 10 µm; D: 14 µm; E, F: 28 µm

First of all the visible aggregates were assumed to be silver chloride, by-product of the reaction, and were washed out with ammonia.[38] The result of this washing shown in Figure 3.25 confirmed the elimination of the aggregates.

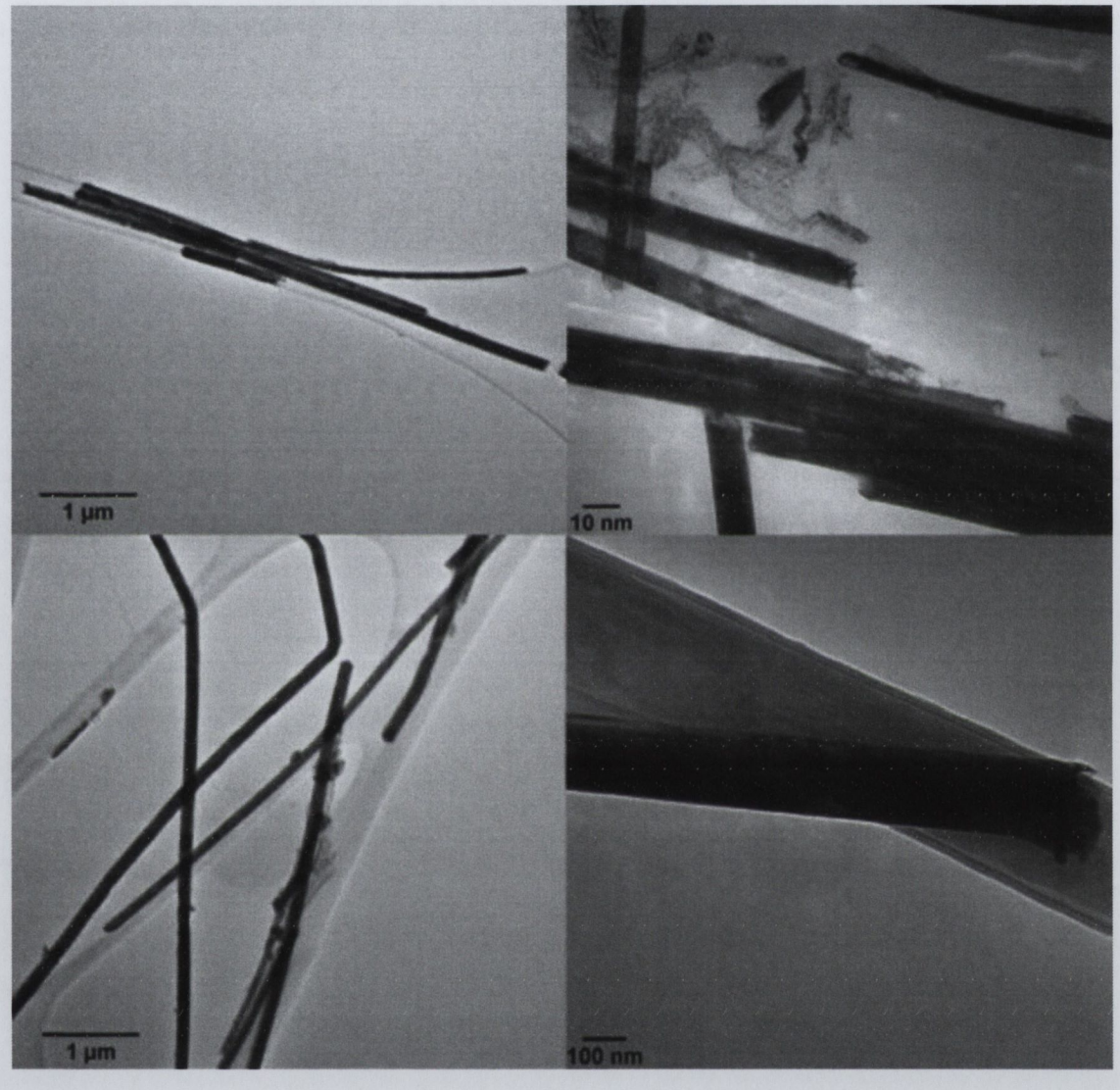

Figure 3.25 TEM images of (top) 5 and (bottom) 14 µm long gold-coated AgNW after washing with ammonia

Further investigation was required to determine whether the nanowires that did not appear hollow were indeed coated with gold. A close examination of HRTEM images highlighted the presence of a visible demarcation on the edges of nanowires which could be attributed to a gold shell (Figure 3.26). However this needed to be confirmed by other means since artefacts are frequent in HRTEM. STEM imaging gave a much clearer

visualisation of the inhomogeneity of the wires, with hollow and full parts (Figure 3.27), owing to the contrast arising from thickness and atomic number. Based on high magnification STEM images, Energy Dispersive X-ray spectroscopy (EDX) spectra were recorded.

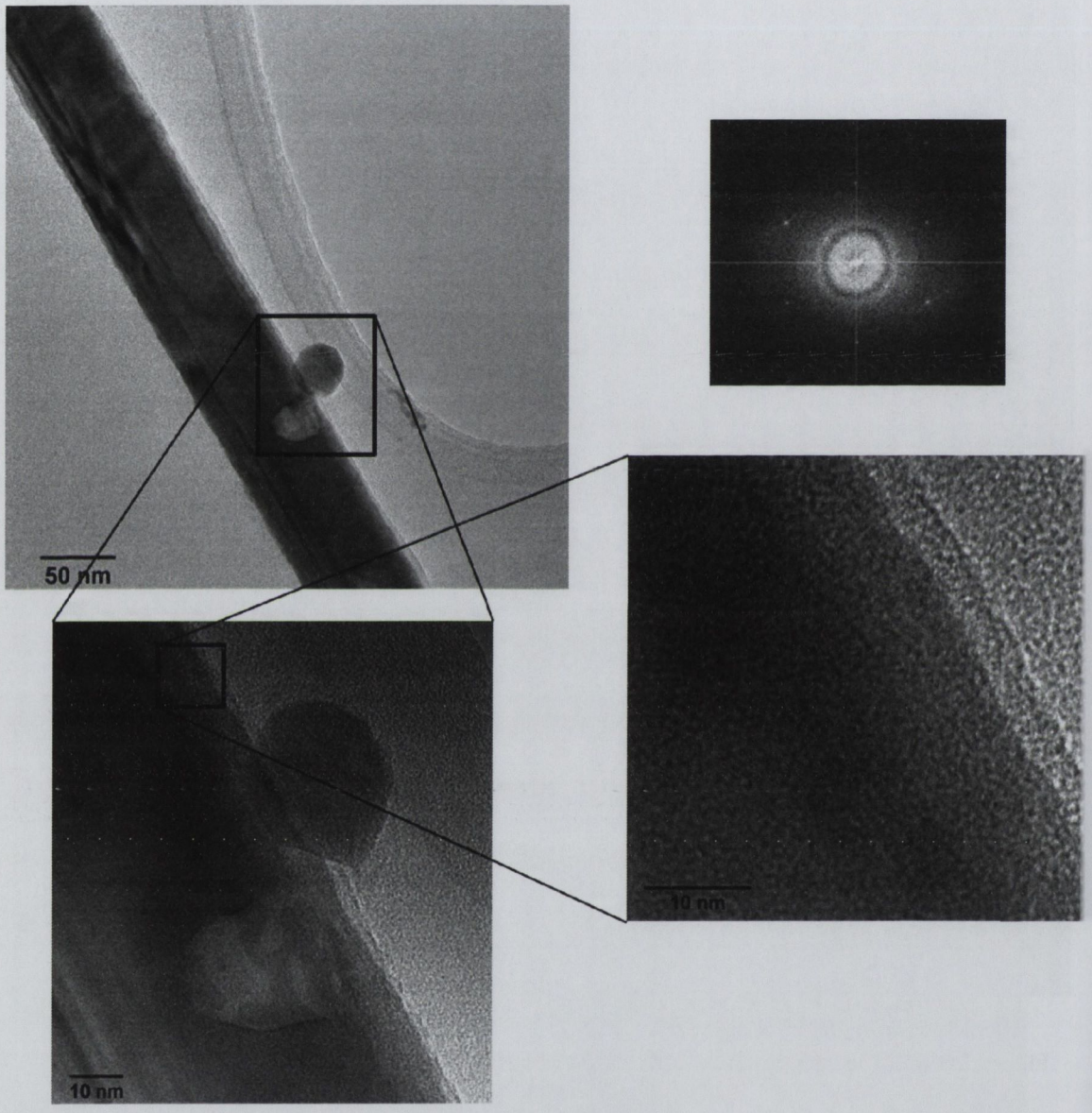

Figure 3.26 TEM images of a single gold-coated AgNW. Close ups on the edge suggesting the presence of a shell. Top Right: Diffraction pattern obtained by Fast Fourier Transform.

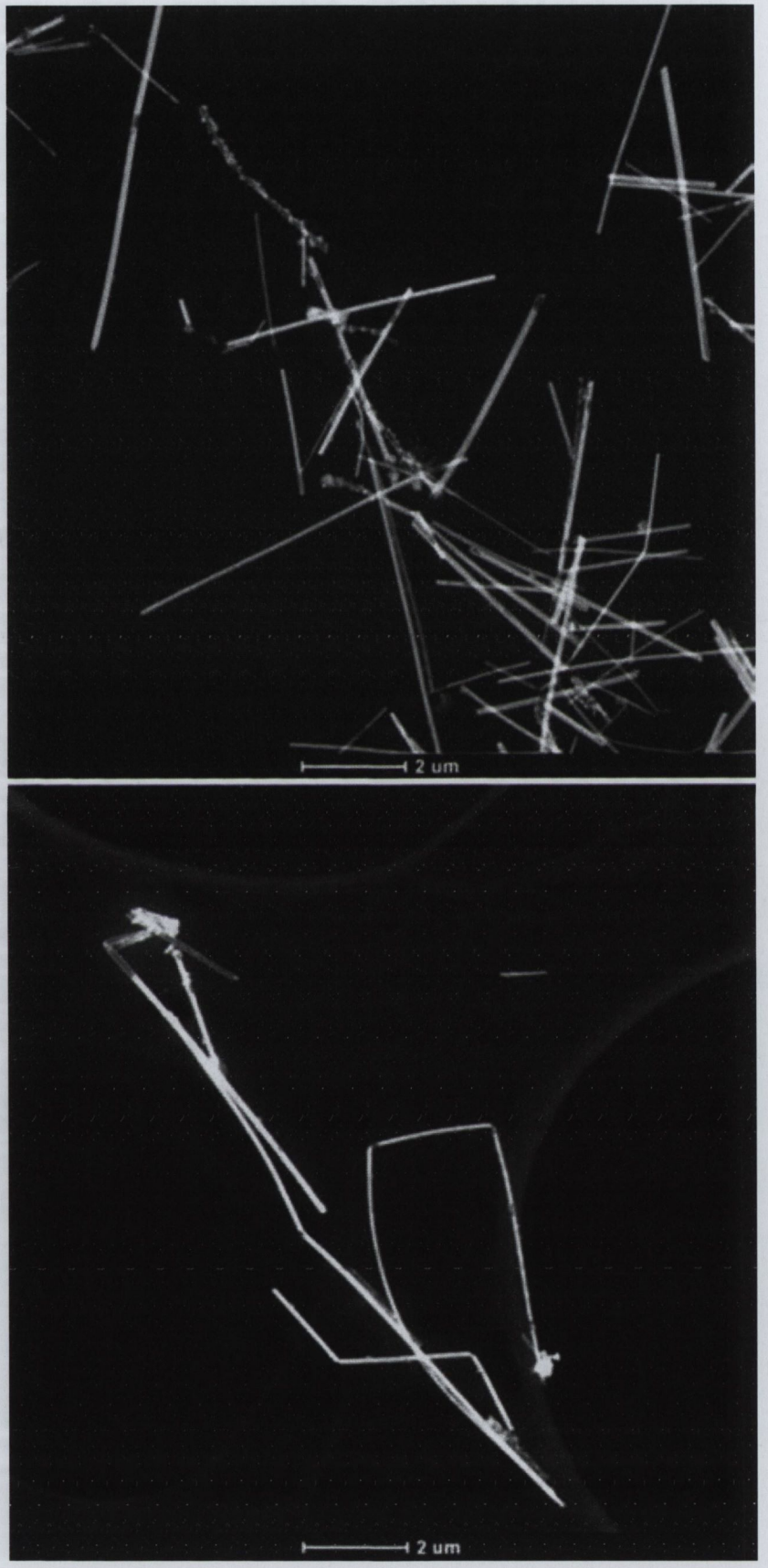

Figure 3.27 STEM images of (top) 5 and (bottom) 14 μm long gold-coated silver nanowires

In places where the nanowires appeared whole and clean of any aggregates on their surface, the EDX spectrum such as the one presented in Figure 3.28 evidenced the presence of gold as well as of silver. In other places, however, particles seemed to be branching out of the nanowires. This was mostly observed where silver was largely replaced and the structure appeared hollow. EDX scans in such places in the specimen indicated a higher ratio of gold to silver and no other elements (Figure 3.29). It was therefore concluded that gold nanoparticles start to grow out of nanowires once all the silver has been oxidised, and, furthermore, these gold particles constitute the few visible aggregates remaining after ammonia treatment.

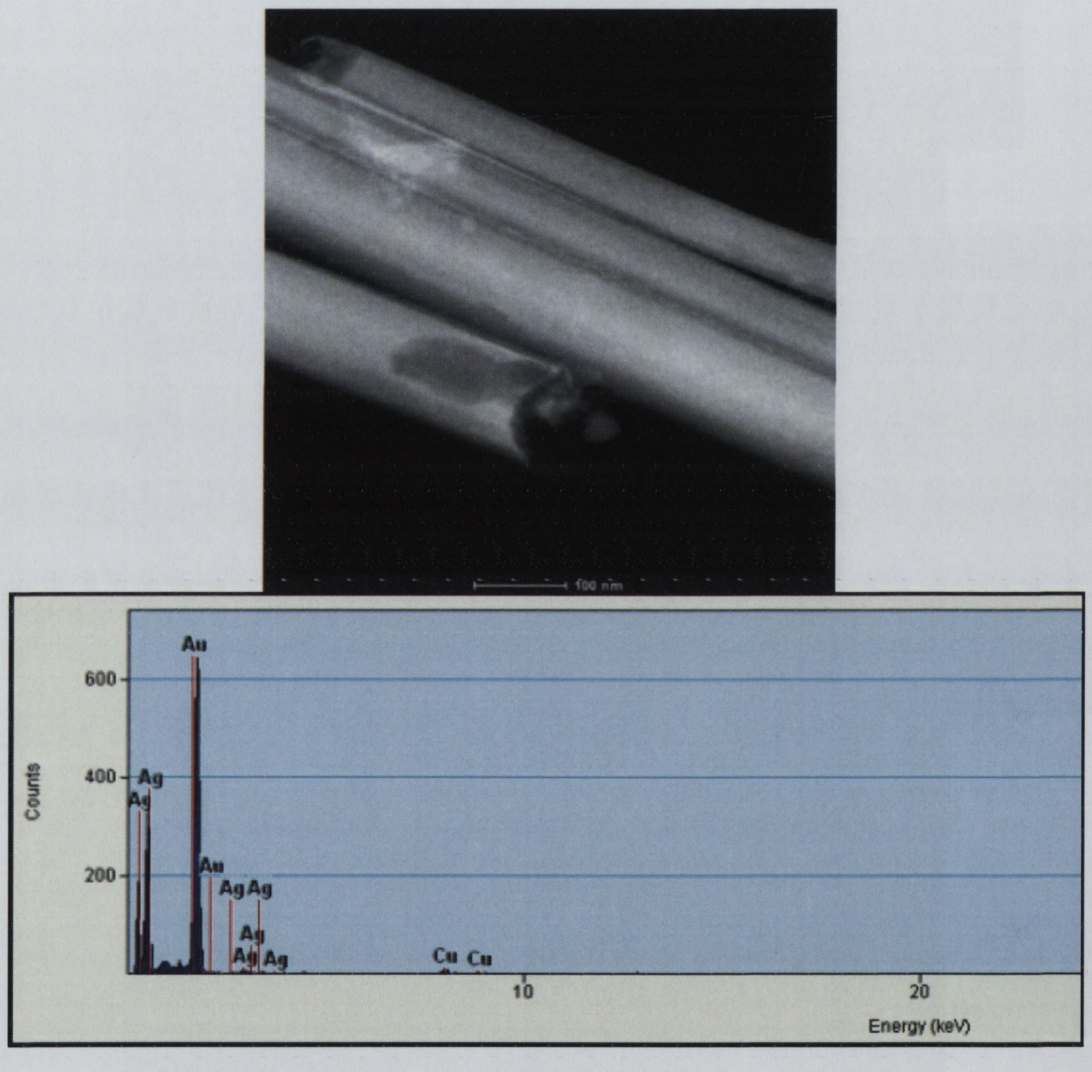

Figure 3.28 STEM image and corresponding EDX spectrum of whole gold-coated silver nanowires

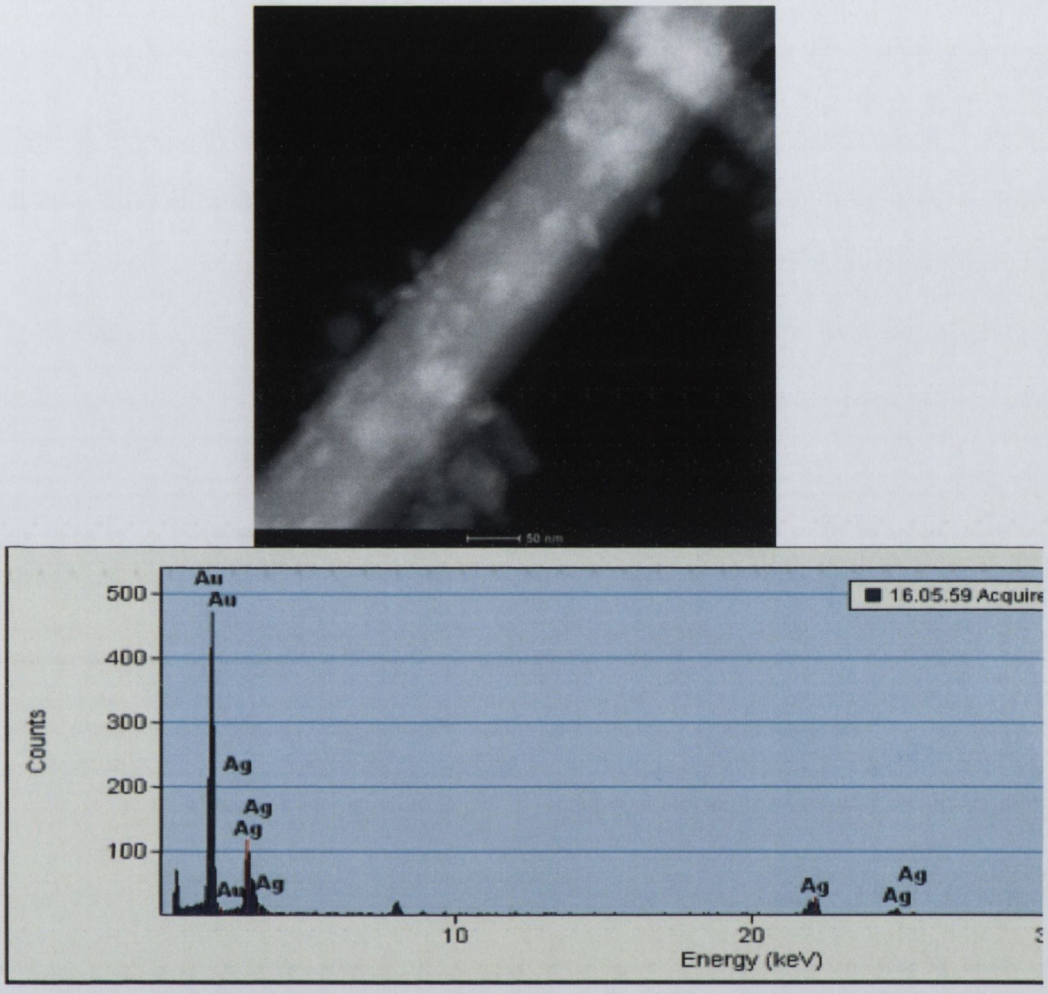

Figure 3.29 STEM image and corresponding EDX spectrum of gold-coated AgNW and gold nanoparticles

Finally, in order to ascertain that the amount of gold deposited on AgNW was sufficient to provide an actual shell, silver was etched away using iron nitrate.[39] The treatment resulted in hollow nanostructures, the majority of which retained the original length of the nanowires. Some aggregates remained, thus confirming that they were composed of gold nanoparticles which could not be dissolved by iron nitrate. TEM images of those gold nanotubes are shown in Figure 3.30.

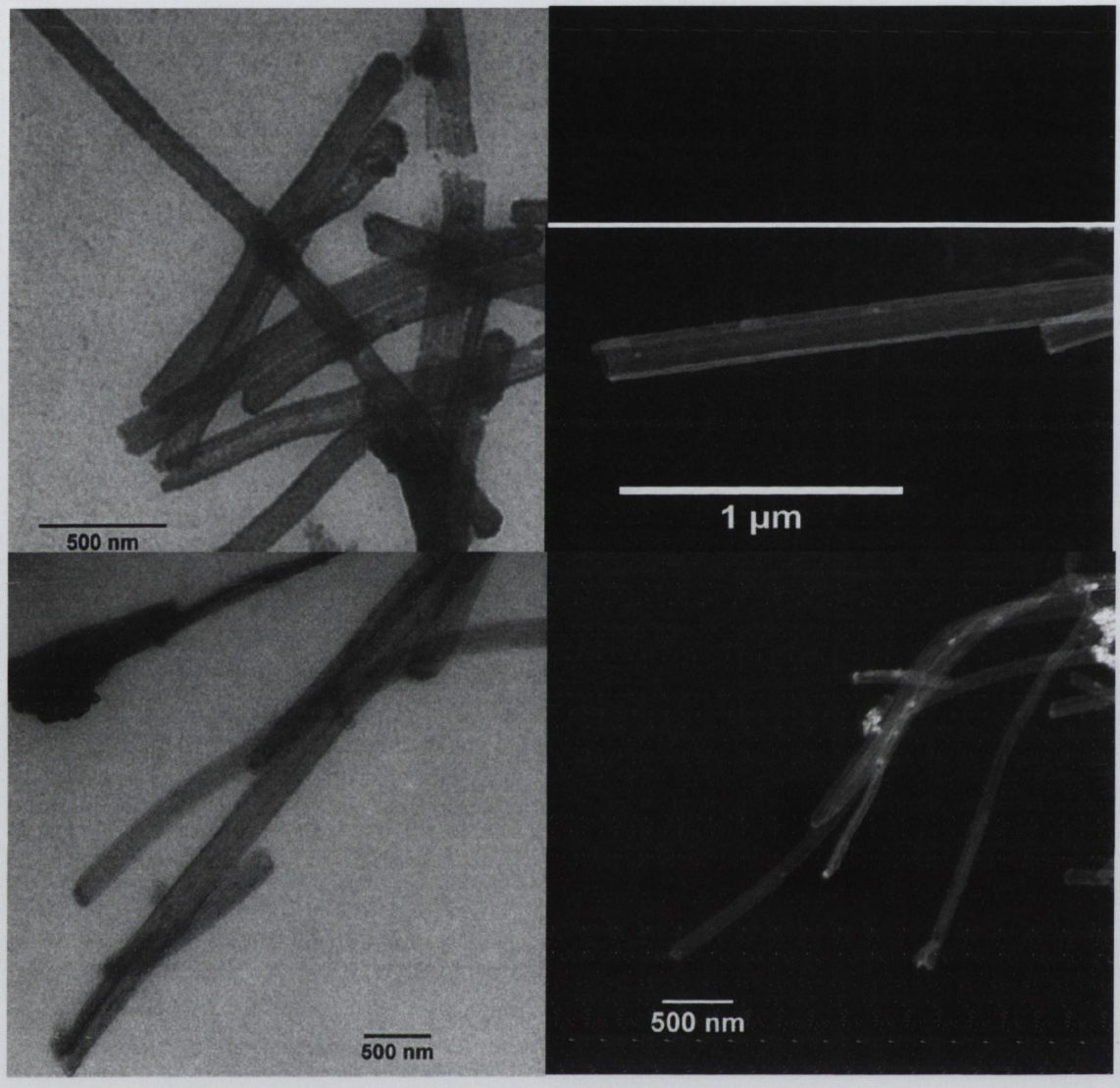

Figure 3.30 TEM images of (top) 5 and (bottom) 14 µm long gold-coated silver nanowires after iron nitrate treatment

The coating of AgNW with a layer of gold was successfully optimised to protect the wires from oxidation without completely replacing the silver. They were intended to be used in animal *in vivo* studies. Previous investigations determined that silver nanowires of over 5 µm in length induced an inflammatory response in pleural space, and could therefore cause effects similar to those of asbestos.[40] In that study, AgNW were used as models of nanofibres with various lengths. However, they were not bio-persistent due to catalytic oxidation of silver in physiological conditions, and therefore only allowed for the study of acute effects. The need for a bio-persistent model of fibres was raised, and the

gold-coating of AgNW was proposed as a solution. Our gold-coated AgNW are now under investigation *in vivo* in murine pleura.

3.4.2 Circular Dichroism of silver nanowires

Silver nanowires were obtained from Seashell Technology, an American company exploiting a patent for the large-scale synthesis of nanowires based on the reduction of silver ions by a polyol in the presence of a stabiliser. These are usually ethylene glycol and polyvinylpyrrolidone (PVP) respectively, neither of which is chiral. Figure 3.35 displays the chemical structure and CD spectrum of PVP. The noise in the UV region is imputable to saturation of the detector due to high absorbance.

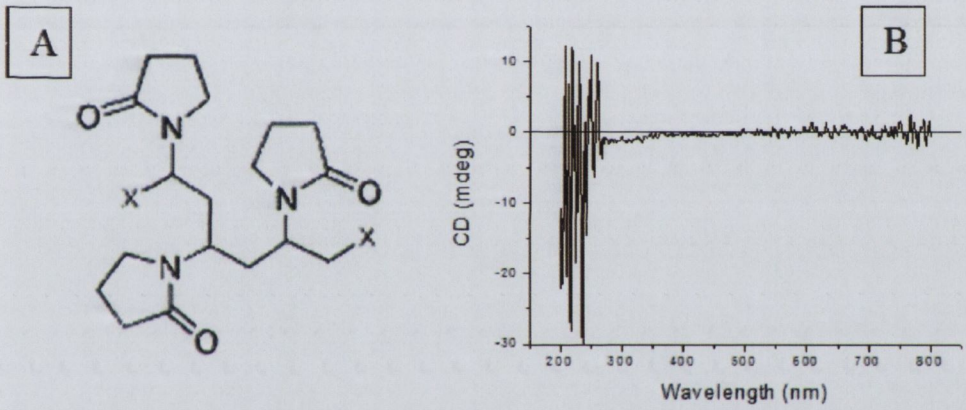

Figure 3.31 (A) Chemical structure of PVP. (B) CD spectrum of PVP.

The CD spectra of 14μm-long AgNW and Au-coated AgNW were recorded and are displayed in Figure 3.32. Two very strong bands, centred at 400 and 700 nm respectively, arose from AgNW which were coated in PVP due to the synthetic process. After coating with gold, however, only the 400 nm band remained, largely reduced in intensity. Since the exact synthesis protocol is unknown, the origin of CD from nanowires remains unclear. For instance, a non-disclosed species might be used in the seeding step. Our experiments however strongly suggest that PVP plays a role in the CD generation, although further investigations are required to elucidate the mechanism. One hypothesis under consideration is the adoption by PVP molecules of a chiral 3D conformation upon binding to silver nanowires.

It was postulated that the origin of CD was a local chiral distortion of the silver crystal structure upon PVP binding in a similar mechanism that was previously reported for silver nanoparticles grown on a DNA template.[41] Subsequent addition of PVP into the AuAgNW suspension led to the complete disappearance of the 400 nm band, and partial restoration of the 700 nm band, as seen in Figure 3.33. This suggested a different type of interaction between PVP adsorbed on gold post-formation of the nanowires compared to that between PVP and silver *in situ.* This supported the deformation of the crystal structure in the latter rather than sole plasmonic enhancement of CD, more likely in the former.

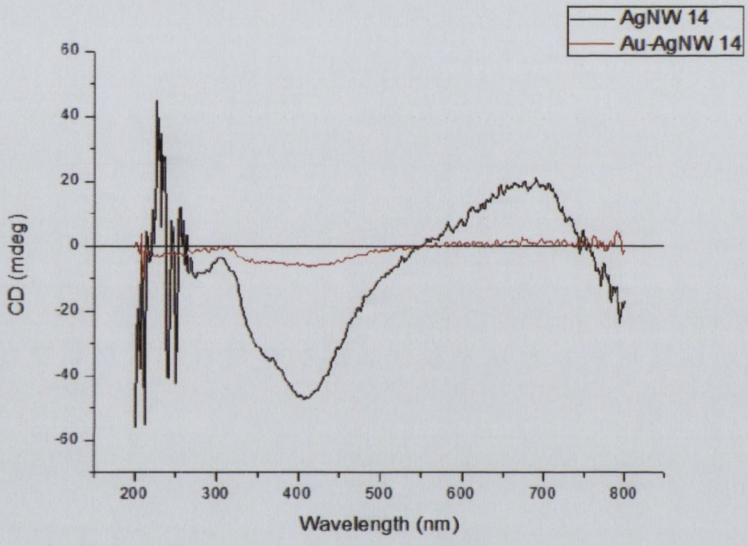

Figure 3.32 CD spectra of 14 μm-long nanowires before and after gold-coating

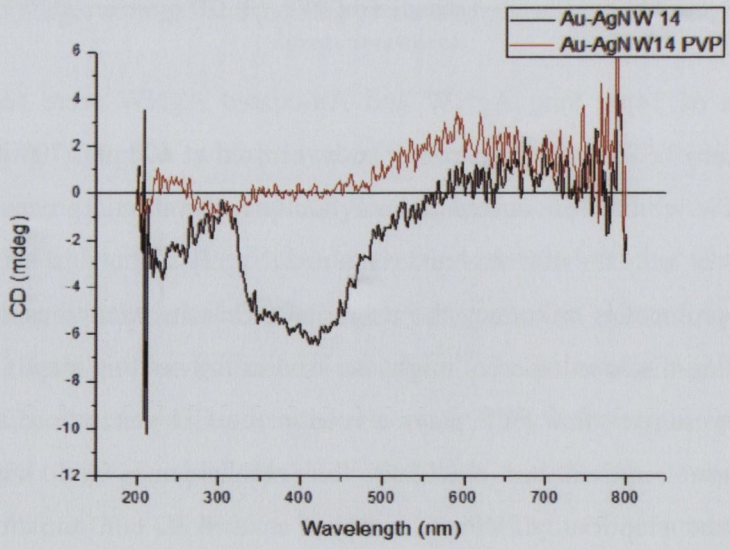

Figure 3.33 CD spectra of 14um-long AuAgNW in absence (black) and presence (red) of added PVP

These observations should be taken into consideration when investigating silver nanowires in biological systems. Chirality should strongly influence the response of live cells towards nanomaterials, due to the chiral nature of all biological species.

3.5 Conclusions

We have prepared a range of anisotropic gold and silver nanostructures and investigated the influence of a number of parameters on their final shape and size. Deposition of gold on silver templates and galvanic replacement reactions led to the formation of hollow nanostructures. Precise control over the ratio of gold to silver allowed us to selectively retain or remove the initial silver nanoparticle.

Preliminary experiments in biological media demonstrated the very low cytotoxicity of gold-silver nanoboxes as well as their high uptake by cells through non-specific endocytosis. Further experiments involve their functionalisation, and loading them with drug molecules for potential biomedical applications, which is discussed in chapter 4. High aspect ratio gold-coated silver nanowires are currently under investigation in animal studies as a model of asbestos-like nanofibre induced chronic inflammation. Their CD signature was charcaterised and opened potentially new reasons and routes of investigations.

Finally, the materials developed and presented in this chapter have been further functionalised and investigated in other parts of this work.

References

[1] S. E. J. Bell, N. M. S. Sirimuthu, *Chemical Society Reviews* **2008**, *37*, 1012-1024.

[2] R. Boyack, E. C. Le Ru, *Physical Chemistry Chemical Physics* **2009**, *11*, 7398-7405.

[3] Z. Wang, S. Zong, W. Li, C. Wang, S. Xu, H. Chen, Y. Cui, *Journal of the American Chemical Society* **2012**, *134*, 2993-3000.

[4] L. A. Austin, B. Kang, C.-W. Yen, M. A. El-Sayed, *Journal of the American Chemical Society* **2011**, *133*, 17594-17597.

[5] J. H. Park, G. von Maltzahn, L. L. Ong, A. Centrone, T. A. Hatton, E. Ruoslahti, S. N. Bhatia, M. J. Sailor, *Advanced Materials* **2010**, *22*, 880-885.

[6] D. Aherne, D. M. Ledwith, M. Gara, J. M. Kelly, *Advanced Functional Materials* **2008**, *18*, 2005-2016.

[7] D. Aherne, D. E. Charles, M. E. Brennan-Fournet, J. M. Kelly, Y. K. Gun'ko, *Langmuir* **2009**, *25*, 10165-10173.

[8] J. A. Edgar, H. M. Zareie, M. Blaber, A. Dowd, M. B. Cortie, in *International Conference on Nanoscience and Nanotechnology (ICONN 2008)* **2008**, pp. 36-39.

[9] G. S. Metraux, Y. C. Cao, R. Jin, C. A. Mirkin, *Nano Letters* **2003**, *3*, 519-522.

[10] D. Aherne, M. Gara, J. M. Kelly, Y. K. Gun'ko, *Advanced Functional Materials* **2010**, *20*, 1329-1338.

[11] I. Struganova, *The Journal of Physical Chemistry A* **2000**, *104*, 9670-9674.

[12] N. Kometani, M. Tsubonishi, T. Fujita, K. Asami, Y. Yonezawa, *Langmuir* **2001**, *17*, 578-580.

[13] M.-C. Daniel, D. Astruc, *Chemical Reviews* **2004**, *104*, 293-346.

[14] C. Gautier, T. Bürgi, *ChemPhysChem* **2009**, *10*, 483-492.

[15] J. Lowther, A. E. Beattie, P. R. R. Langridge-Smith, D. J. Clarke, D. J. Campopiano, *MedChemComm* **2012**.

[16] M. Van Caille-Bertrand, H. J. Degenhart, I. Luijendijk, J. Bouquet, M. Sinaasappel, *Archives of Disease in Childhood* **1985**, *60*, 652-655.

[17] M. Shannon, J. Graef, F. H. Lovejoy Jr, *The Journal of Pediatrics* **1988**, *112*, 799-804.

[18] D. Clerc, D. Salliere, M. Bisson, P. Massias, *Revue du Rhumatisme et des Maladies Osteo- Articulaires* **1983**, *50*, 457-463.

[19] G. J. Doherty, H. T. McMahon, *Annual Review of Biochemistry* **2009**, *78*, 857-902.

[20] B. D. Chithrani, W. C. W. Chan, *Nano Letters* **2007**, *7*, 1542-1550.

[21] X. Li, *Journal of Applied Physics* **2012**, *111*, 024702.

[22] D. J. Giard, S. A. Aaronson, G. J. Todaro, P. Arnstein, J. H. Kersey, H. Dosik, W. P. Parks, *Journal of the National Cancer Institute* **1973**, *51*, 1417-1423.

[23] A. M. Derfus, W. C. W. Chan, S. N. Bhatia, *Advanced Materials* **2004**, *16*, 961-966.

[24] V. Gérard, C. Maguire, D. Bazou, Y. Gun'ko, *Journal of Nanobiotechnology* **2011**, *9*, 50.

[25] B. Prasad, N. Nikolskaya, D. Connolly, T. Smith, S. Byrne, V. Gerard, Y. Gun'ko, Y. Rochev, *Journal of Nanobiotechnology* **2010**, *8*, 7.

[26] B. R. Prasad, G. Mullins, N. Nikolskaya, D. Connolly, T. J. Smith, V. A. Gérard, S. J. Byrne, G.-L. Davies, Y. K. Gun'ko, Y. Rochev, *Journal of Nanobiotechnology* **2012**, *10*, 4.

[27] S. R. MacEwan, D. J. Callahan, A. Chilkoti, *Nanomedicine (Lond)* **2010**, *5*, 793-806.

[28] D. Bazou, A. Castro, M. Hoyos, *Ultrasonics* **2012**, *52*, 842-850.

[29] D. Bazou, M. J. Santos-Martinez, C. Medina, M. W. Radomski, *British Journal of Pharmacology* **2011**, *162*, 1577-1589.

[30] N. I. Foster, *American Journal of Clinical Oncology* **1982**, *5*, 331.

[31] M. J. Reasor, *Toxicology and Applied Pharmacology* **1989**, *97*, 47-56.

[32] G. Majno, I. Joris, *American Journal of Pathology* **1995**, *146*, 3-15.

[33] W. J. van Venrooij, G. J. Pruijn, *Arthritis Research* **2000**, *2*, 249-251.

[34] B. M. Mohamed, N. K. Verma, A. M. Davies, A. McGowan, K. Crosbie-Staunton, A. Prina-Mello, D. Kelleher, C. H. Botting, C. P. Causey, P. R. Thompson, G. J. Pruijn, E. R. Kisin, A. V. Tkach, A. A. Shvedova, Y. Volkov, *Nanomedicine (Lond)* **2012**, *7*, 1181-1195.

[35] A. Prina-Mello, A. M. Whelan, A. Atzberger, J. E. McCarthy, F. Byrne, G.-L. Davies, J. M. D. Coey, Y. Volkov, Y. K. Gun'ko, *Small* **2010**, *6*, 247-255.

[36] Y. Sun, B. Mayers, T. Herricks, Y. Xia, *Nano Letters* **2003**, *3*, 955-960.

[37] Y. Sun, Y. Xia, *Journal of the American Chemical Society* **2004**, *126*, 3892-3901.

[38] K. B. Morris, *Journal of Chemical Education* **1947**, *24*, 236.

[39] C. M. Cobley, M. Rycenga, F. Zhou, Z.-Y. Li, Y. Xia, *The Journal of Physical Chemistry C* **2009**, *113*, 16975-16982.

[40] A. Schinwald, F. Murphy, A. Prina-Mello, C. Poland, F. Byrne, J. Glass, J. Dickerson, D. Schultz, D. Movia, C. Jeffree, W. MacNee, K. Donaldson, *Toxicological Sciences* **2012**.

[41] G. Shemer, O. Krichevski, G. Markovich, T. Molotsky, I. Lubitz, A. B. Kotlyar, *Journal of the American Chemical Society* **2006**, *128*, 11006-11007.

Chapter 4

Nano-composites of Quantum Dots, Metal Nanoparticles and Gelatin

4.1 Introduction

Gelatin is a mixture of peptides extracted from collagen of animal sources. Collagen presents a triple helical structure forming fibres which are arranged in bundles; they make up the connective tissue matrix. Collagen is therefore the main organic component of skin, bone, tendon and other loose connective tissue. Alkali- or acid-based hydrolysis of collagen results in the breaking of covalent bonds between amino acids at random points. Gelatin refers to these random chain molecules. The chemical composition of gelatin is generally similar to that of the parent collagen[1] but their physical properties including melting point and gel strength may vary significantly depending on the preparation process.[2] When dissolved in hot water, the triple helix is denatured by the breaking up of hydrogen and electrostatic bonds to form one, two or three random chain gelatin molecules. Upon cooling, triple helical zones are obtained through cross-linking as well as disordered zones. This phenomenon is responsible for the gelling property of gelatin. Since it is naturally present in the body, it is highly biocompatible and the commercial form, gelatine, is commonly used in food products and drug tablets. Gelatin can be formed into nanoparticles and loaded with a drug[3-5] to serve as a delivery vehicle, or a "nano-tablet".

QDs are luminescent nanoparticles which have been widely investigated for their narrow and tunable emission in the visible range. Applications in the fields of biological imaging have flourished[6] but their potential for diagnostics or photodynamic therapy[7] is limited by their intrinsic toxicity.[8-9] This may be counteracted by isolating the cadmium-based core of QDs from the environment with a shell of biocompatible material. The synthesis of gelatine-coated CdTe QDs, or "Jelly Dots",[10] was developed in our group and the resulting nanoparticles exhibited significantly lower cytotoxicity than CdTe QDs stabilised with short ligands such as thioglycolic acid (TGA), even with prolonged exposure.[11-12] The use of nanoparticles for cancer therapy lies in their potential ability to

specifically target tumours whilst demonstrating as little toxicity as possible to the surrounding tissues. This could be achieved by binding a bio-marker to the gelatin coating.

Folic acid (FA) is commonly known as vitamin B9. It is involved in a range of metabolic mechanisms and has a beneficial effect on a number of conditions from birth defects to dementia.[13] It is usually prescribed during pregnancy as a food supplement to support healthy foetus development. In particular, it plays a crucial role in DNA synthesis and chromosome maintenance. For this reason, tumour cells from a variety of cancer types over-express folate receptors to sustain their fast proliferation. Folic acid has been proven to be an efficient drug carrier to enhance the delivery to targeted cancer cells.[14]

The aim of the work presented in this chapter was the preparation and studies of a range of nano-composites based on gelatin-coated QDs. We intended to further investigate the potential applications of "Jelly Dots" for biomedical applications by functionalising them with folic acid and testing them in selected cell lines. Preliminary studies include the study of TGA-capped and gelatin-coated CdTe QDs in those cell lines to compare the fate of the different types of nanoparticles and the behaviour of each cell line when exposed to them. Another objective of the work was to investigate other approaches for synthesising gelatin-QD composites. Finally, the preparation of gelatin-metal nanoparticle composites was carried out, as well as their functionalisation for targeted drug delivery.

4.2 Synthesis, characterisation and *in vitro* study of CdTe QDs

4.2.1 Influence of reflux time

In our work we used the standard water-based synthesis of CdTe QDs initially developed by Gaponik *et al.*[15] In this approach a basic solution (pH adjusted with NaOH) of $Cd(ClO_4)_2$ and an appropriate amount of the thiol stabilizer is treated by H_2Te gas which is generated by the chemical decomposition of Al_2Te_3 powder by concentrated sulphuric acid. This process initially results in non-luminescent CdTe-based clusters, which are then heated under reflux at 130° C for several hours to result in a crude solution of CdTe QDs. The growth is essentially driven by the diffusion and coalescence of monomers which can either be Cd-ligand complexes or smaller clusters since Ostwald ripening is predominant.[16] The size of the QDs can be tuned by altering the reflux time, with elongated reflux times resulting in larger QDs, coupled with a red shift of both the

absorption and emission maxima. Although the effect of reflux time on CdTe QD growth is well documented,[17] a direct observation of the influence of all parameters was necessary to be able to accurately predict the diameter or the position of the exciton or photoluminescent (PL) emission of QDs prepared with our set-up.

Figure 4.1 therefore shows the evolution of the absorption spectrum as the reflux time increases. During the first hour the spectrum did not show any distinct exciton peak, meaning that the QDs were not yet fully formed. At this stage, the solution only contained an inhomogeneous mixture of non-luminescent nano-clusters. After a few hours though, a clear exciton peak appeared and progressively shifted to higher wavelengths (red shifting) with time. It eventually saturated as can be deduced by the similarity of the 48h and 72h spectra. It should be noted that from 24h on, the peak became less sharp as the size distribution broadened.

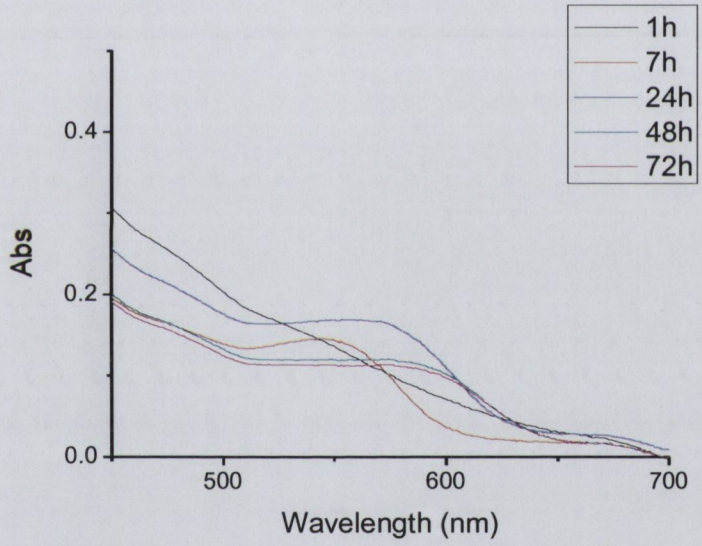

Figure 4.1 Influence of reflux time on the absorption spectrum of TGA-capped CdTe

Photoluminescence emission spectra were also recorded at various time points during reflux, as shown in Figure 4.2. The spectrum taken at 1h was flat as expected given the absorption spectrum corresponding to the precursor nano-clusters which are not luminescent. With increasing reaction time, an emission peak appeared and its intensity tended to increase while red-shifting. It can be viewed as rather broad with a full width at half maximum (FWHM) of nearly 60 nm, indicating a broad size distribution;[18]

subsequent size-selective precipitation of this crude solution using isopropanol resulted in several fractions, each exhibiting a much narrower peak (typically around 40 nm).

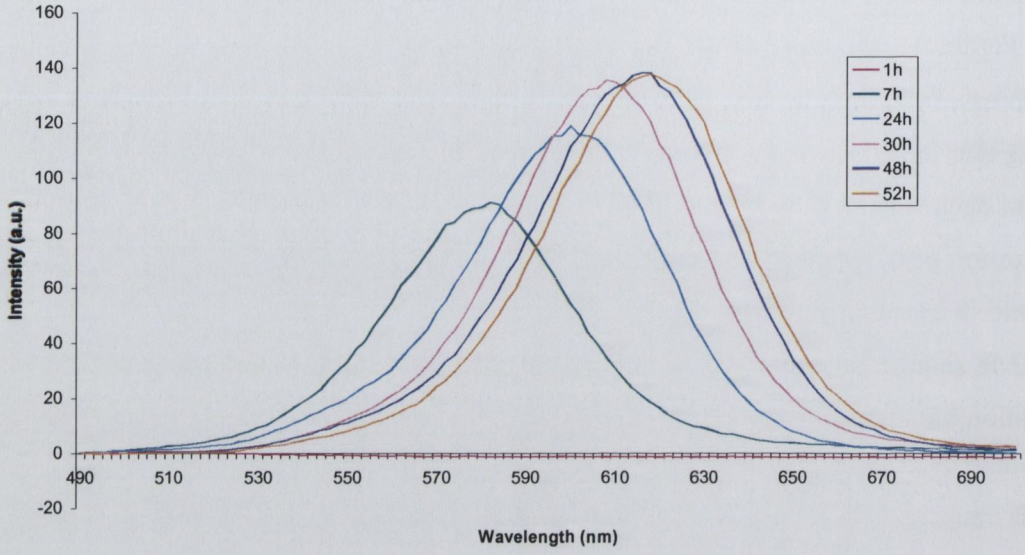

Figure 4.2 Influence of reflux time on the emission spectrum of TGA-capped CdTe

4.2.2 Importance of ligand choice

Ligands have a strong influence on stabilisation of QDs as well as on their Quantum Yield (QY).[17] They may also be chosen for their functional groups which will provide selected surface properties depending on the intended application. In this work we varied the surface charge of QDs by changing the surface stabiliser. Two different thiol-terminated ligands were used to stabilise CdTe QDs: thio-glycolic acid (TGA) and cysteamine. TGA being a carboxylic acid, it provides a negative surface charge to the particle at basic pH. Cysteamine on the other hand is water-soluble and positively charged at slightly acidic pH owing to its terminal amine group. However, the luminescence of QDs is quenched in strong acidic conditions, hence cysteamine-stabilised QDs are much less stable and more difficult to work with than TGA-capped ones. Figure 4.3 shows zeta potential measurements that confirmed that the ligands each provide different surface charges to the QDs: TGA-capped QDs had an average zeta potential of -40 mV (+/- 5), whereas cysteamine-stabilised QDs had an average of +23 mV (+/- 1). The lower surface charge of cysteamine-stabilised QDs also indicated a lower stability of the nanoparticle

suspension which could be observed as they tended to degrade much faster than the TGA-capped ones.

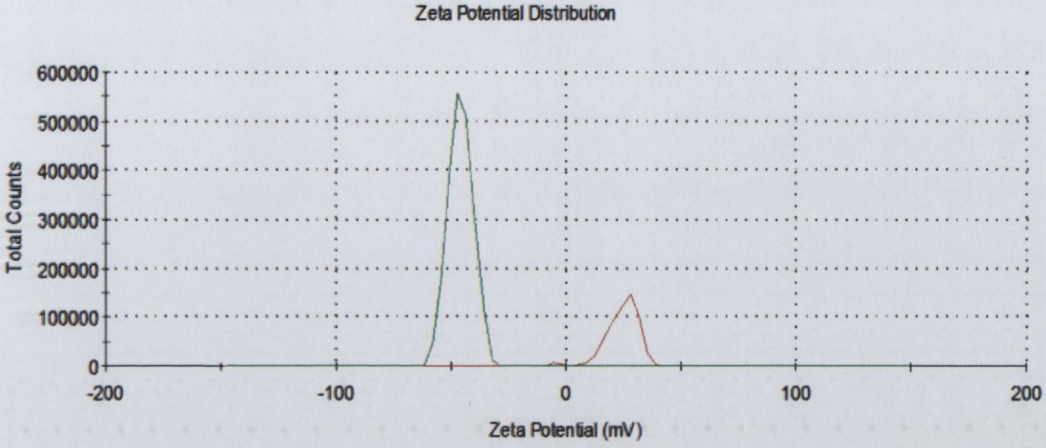

Figure 4.3 Zeta potential graphs of TGA- (green) and Cysteamine- (red) stabilised CdTe QDs

4.2.3 Synthesis and characterisation of gelatin-coated CdTe QDs

The synthesis of TGA-capped CdTe QDs can be performed in the presence of various polymers.[6] In particular, incorporation of gelatin during the preparative procedure[19] was previously reported by our research group to improve the quantum yield as well as reduce the cytotoxicity of QDs. It was thus demonstrated that gelatin provided a protective coating on the particles, so-**called "Jelly Dots"**.[10-11]

In order to demonstrate that the use of polymeric coatings can globally improve the cytotoxicity and quantum yields of QDs, in our work, three polymers were tested using the same conditions as the preparation of gelatin-coated TGA-capped CdTe QDs. These included polyethylene glycol (PEG) 400, polyvinyl alcohol (PVA) and polyethylene imine (PEI). All three are water-soluble and biocompatible, and therefore reasonable candidates for passivating the surface of CdTe QDs as well as reducing their cytotoxicity.[20-22] None of the polymers tested showed improvements which were as good as gelatin in terms of quantum yield. PEG and PVA did not seem to dramatically alter the quality of the particles one way or the other. QDs synthesised in presence of PEI were insoluble in water at neutral pH where secondary amines were not protonated, however they remained luminescent. They also appeared to reach a maximal diameter faster than observed with

other ligands as suggested by the shorter emission wavelength. Figure 4.4 gathers those observations.

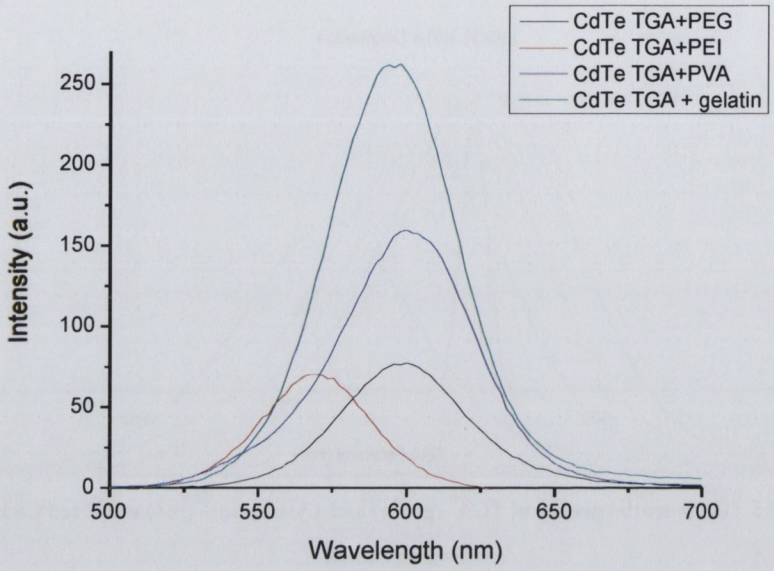

Figure 4.4 Emission spectra of TGA-capped CdTe synthetised in presence of PEG, PEI, PVA and gelatin respectively

The discrepancies in PL intensity obtained with all four polymer coatings may be explained by their respective structures represented in Figure 4.5. In the case of PVA, the hydroxyl groups can easily bind to the surface of QDs through either cadmium atoms or TGA molecules, with little steric hindrance. This may result in good capping of surface defects and therefore the relatively high QY compared to that obtained with PEI and PEG. The arrested growth of QDs prepared with PEI may be attributed to the absence of negative charge on the polymer chain. After capping with PEI, the electrical double layer of QDs is composed of counter anions which prevent the diffusion of negatively charged $Cd(TGA)_2^{2-}$ monomers and further growth of the nanocrystals. The poor solubility of PEI in cold water explains their precipitation once the reaction mixture cooled down. Overall, the major improvement induced by gelatin compared to all others was attributed to the multiple binding possibilities through various functional groups as well as its gelling property at room temperature, providing excellent surface defects capping and protection from oxidation by water.

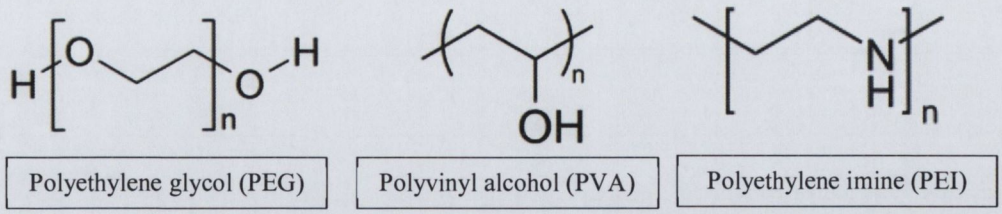

Figure 4.5 Chemical structures of PEG, PVA and PEI

Gelatin was thus selected as the preferred material for coating and functionalisation of TGA-capped CdTe QDs due to its versatility, stability and ease of use. The cellular uptake of gelatinated QDs was investigated with comparison to the original TGA-capped QDs prior to further modification as developed in the next sections.

2.1.4 Cellular uptake of TGA-capped CdTe QDs

Throughout the project QD-based materials were tested in the cell lines Caco-2 and HT-1080. The former was extracted from a 72-year old Caucasian male colon adenocarcinoma. The latter was derived from the fibrosarcoma of a 35-year-old Caucasian man. Both cell lines are epithelial in morphology and adherent. Live cells were stained with Calcein acetoxymethyl which is cleaved by esterases in cells and therfefore illuminates the whole cytoplasm. Fixed cells were stained using 4',6'-diamidino-2-phenylindole (DAPI) which binds to double-stranded DNA.

Red-emitting (580 nm) TGA-capped CdTe QDs were incubated for four hours with both cancer cell cultures which demonstrated significantly different behaviours. In the case of the Caco-2 line, only 17% of the cells exhibited internalized QDs, whereas 56% of the HT-1080 cells had taken up QDs, as illustrated by Figure 4.6. Caco-2 cells were previously reported to not efficiently take up a variety of nanoparticles;[23] HT-1080 is a more aggressive cell line than Caco-2, with its doubling time being 26 hours[24] compared to 62 hours for Caco-2 (according to the American Type Culture Collection database). This implies that HT-1080 cells need a larger amount of nutrient and are likely to develop their unspecific endocytosis capability to increase the probability of uptake of random nutrient, especially when the nutrient supply is low as it was in our case.[25]

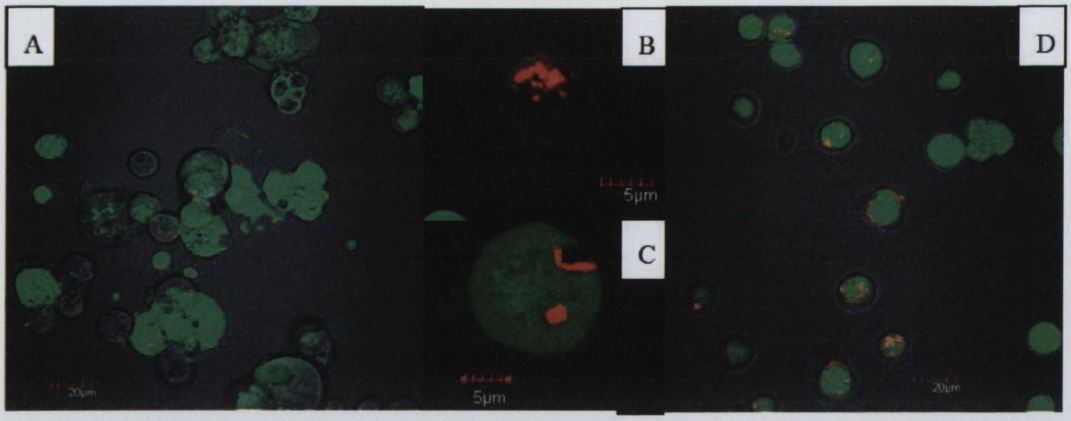

Figure 4.6 Confocal microscope images of (A, B) Caco-2 cells and (C, D) HT-1080 cells incubated for four hours with TGA-capped CdTe QDs (red) and counter-stained with Calcein-AM (green). Overlay of red (excitation 543 nm) and green (excitation 488 nm) (A, D) and bright field (B,C) channels.

The use of confocal microscopy allowed to visualise the cells slice by slice and thereby to ensure that QDs were indeed internalised as opposed to only bound to the plasma membrane. Figure 4.7 displays a three-plane projection of sample images of Caco-2 and HT-1080 cells treated with TGA-capped QDs. They clearly demonstrate that the red QDs are surrounded by green calcein in all directions, thus proving that they are located inside the cytoplasm. All confocal microscopy images presented in the thesis were taken in middle sections of cells. Three-plane projections are available in Appendix 2.

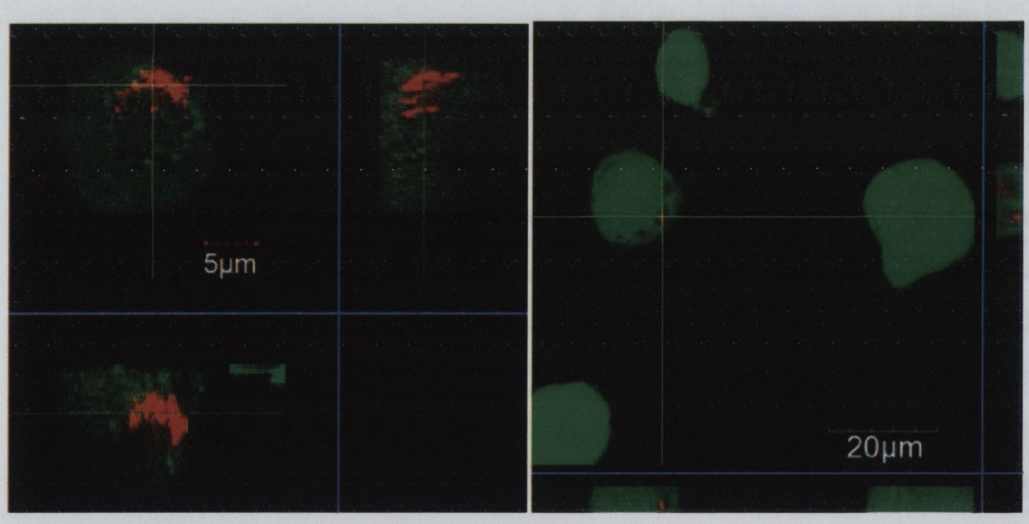

Figure 4.7 Three-plane projection of confocal microscopy slice by slice images of (left) Caco-2 and (right) HT-1080 cells treated with TGA-capped QDs (red) and counter-stained with calcein-AM. Overlay of red (excitation 543 nm) and green (excitation 488 nm) channels.

The presence of QDs as distinguishable red spots in the cytoplasm of both cell lines suggested their localisation in vesicles and thus a non-specific endocytotic pathway (Figure 4.6). Although these spots were not identified as specific organelles, previous studies indicated that they could be endosomes[26] or lysosomes.[27] Initial suggestion that they may be part of the Golgi apparatus was disproved by a co-localisation experiment using a Golgi-specific dye (Appendix 3).

Exposure to TGA-capped CdTe QDs also appeared to have a clear effect on cell proliferation and viability, especially in the case of HT-1080 cells which exhibited major morphological evidence of apoptotic cell death. Untreated HT-1080 cells retained their typical extended, branched cytoplasm and pseudopodial attachments. After treatment with TGA-capped CdTe QDs however, most cells were shrunk and rounded which are common features of cells undergoing apoptosis. As seen in Figure 4.8, morphological changes were not as clear for Caco-2 cells as they normally retain a globular shape and small adhesion surface on glass dishes even when healthy. Cells which had entered apoptosis could in some cases be morphologically identified by blebbing of the membrane. However, the use of calcein-AM to stain live cells (up to late stage of apoptosis) allowed quantification of cell proliferation in both culture types. After incubation with QDs, the number of live cells remaining in the culture was reduced by 74% for HT-1080 and 20% for Caco-2 cells compared to control cultures that were not exposed to the nanoparticles as illustrated by Figure 4.8. It thus appears that the more QDs the cells are able to internalise the more they are affected, which suggests a direct link between uptake and cytotoxicity.

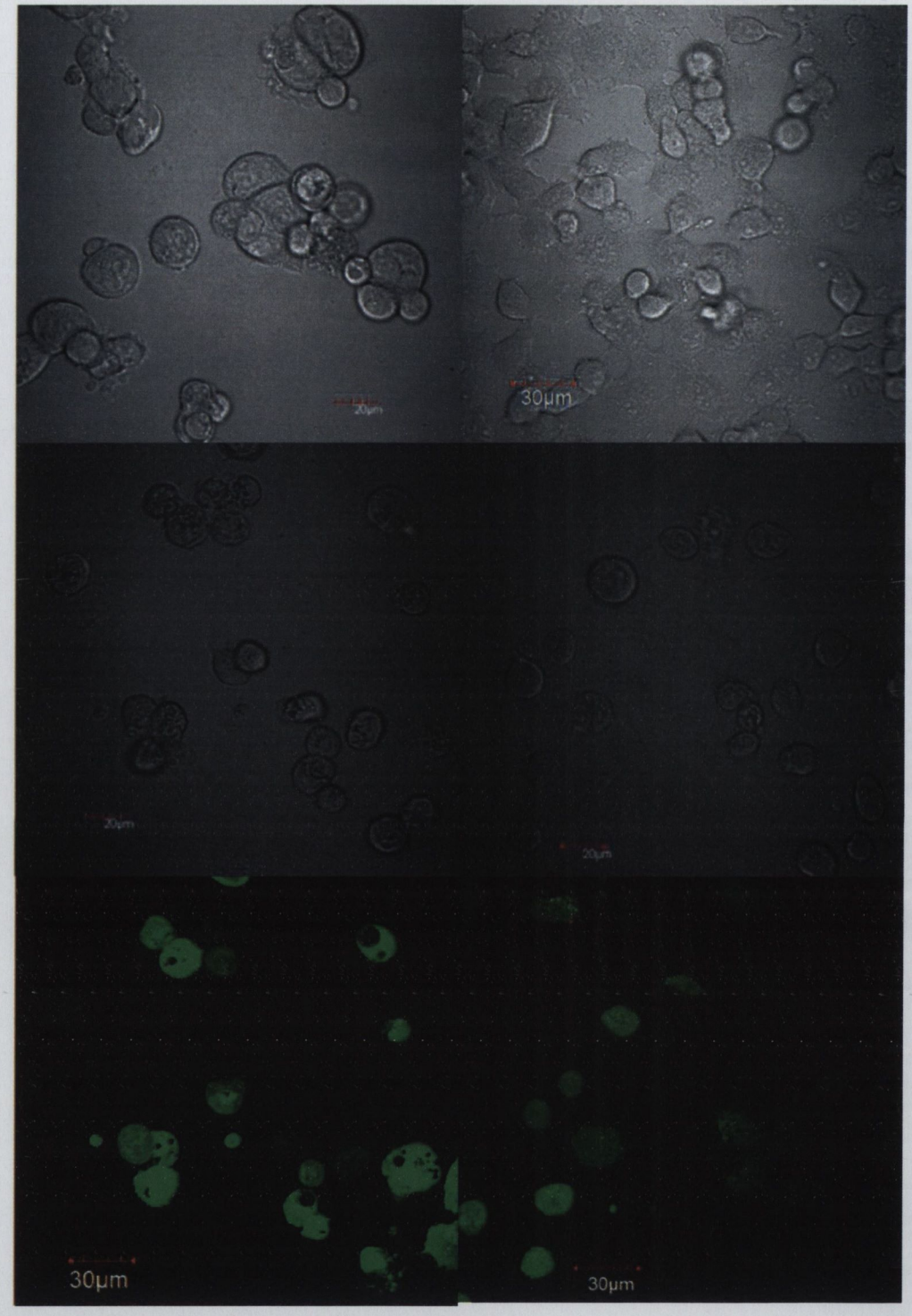

Figure 4.8 Bright field confocal microscope images of (A) Caco-2 cells control culture, (B,C) Caco-2 cells incubated with TGA-capped CdTe QDs, (D) HT1080 cells control culture and (E,F) HT-1080 cells incubated with TGA-capped CdTe QDs. (A, B, D, E) bright field images; (C, F) Overlay of red QD (excitation 543 nm) and green Calcein AM (excitation 488 nm) channels.

2.1.5 Cellular uptake of gelatin-coated TGA-capped (TGA-Gel) CdTe QDs

Red-emitting (594 nm) TGA-Gel QDs were incubated with both cell lines in the same conditions as TGA QDs. The overall uptake was much lower than that for TGA QDs, but the differences between cell lines followed a similar trend: only 6% of Caco-2 and 14% of HT-1080 cells exhibited QD internalisation as illustrated by Figure 4.9.

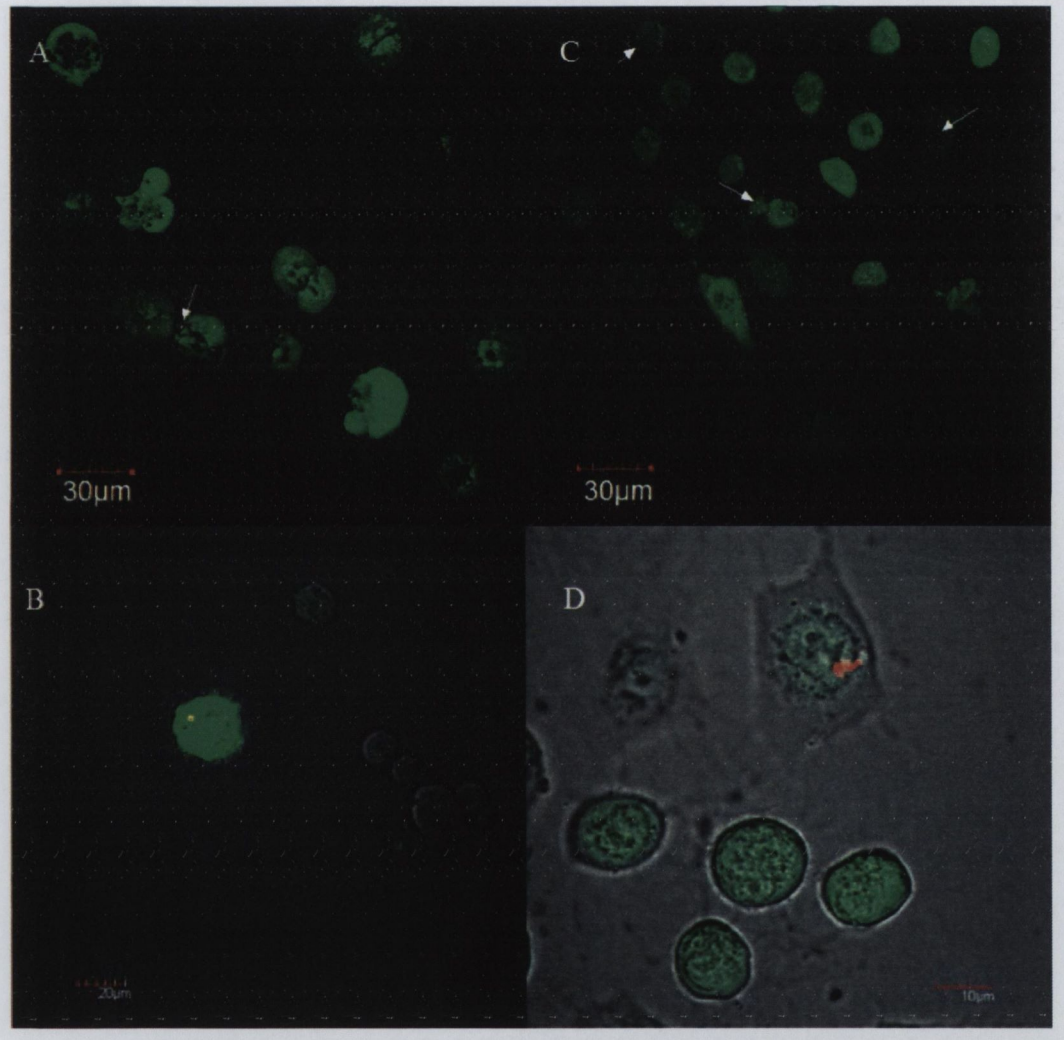

Figure 4.9 Confocal microscope images of (A,B) Caco-2 cells and (C,D) HT-1080 cells incubated with Gelatinated TGA-capped CdTe QDs (red) and counter-stained with Calcein-AM (green). Arrows indicate internalised QDs in wide field. Overlay of red (excitation 543 nm) and green (excitation 488 nm) (A, C) and bright field (B,D) channels

On the other hand, TGA-gel QDs appeared to be much less cytotoxic than the original TGA QDs, as indicated by the differences in morphology that could be observed on HT-1080 cells. As outlined in the previous paragraph, cultures treated with TGA QDs displayed major cell rounding and shrinkage, as well as lower proliferation. Although still observable, these features were far less generalised with TGA-gel QDs as can be seen in Figure 4.10. Previous studies have determined that gelatinated QDs exhibited lower cytotoxicity than TGA QDs towards THP-1 (macrophages)[10] and PC12 (neuron-like) cells.[11-12] More detailed biological investigations would be required to obtain quantitative values regarding cytotoxicity in Caco-2 and HT-1080 cells; qualitative results however indicated a similar trend to that measured in other cell lines. The very low uptake of TGA-gel QDs raised the question of a relationship between uptake and cytotoxicity. The reduction in deleterious effects could be due to the absence of QDs inside the cells. This hypothesis was disregarded on the basis that not only cells presenting internalised TGA QDs showed signs of apoptosis. It is believed that gelatin reduces the cytotoxicity of QDs by preventing the leaking of Cd^{2+} ions.[28] Whether metal ions are released inside or outside the cell membrane, they will still interfere with the cell metabolism and cause apoptosis.[29]

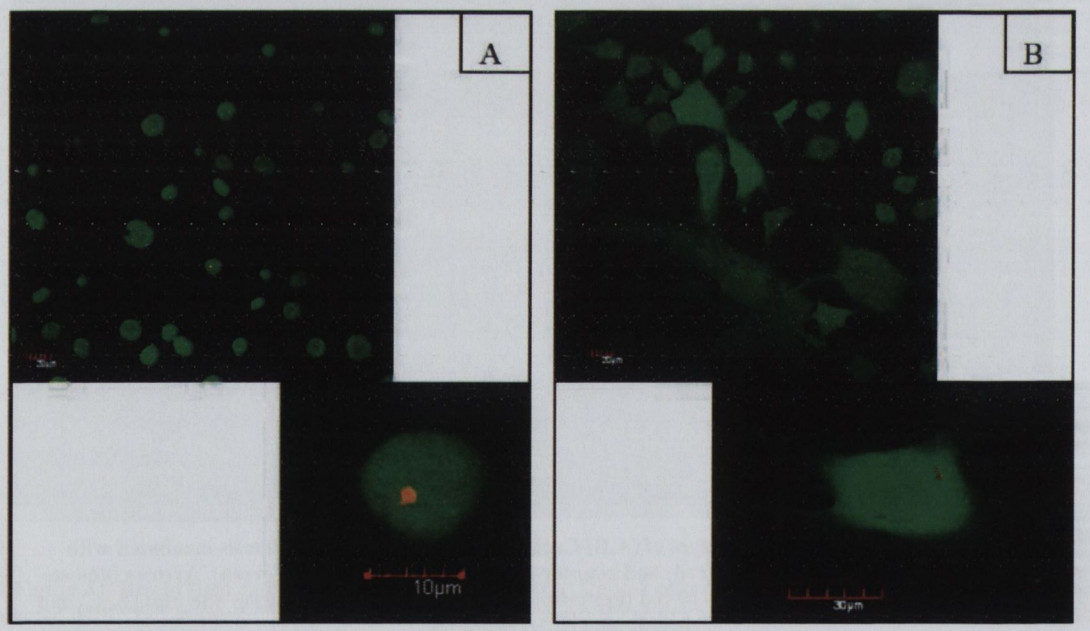

Figure 4.10 Confocal microscope images of HT-1080 cells incubated with (A) TGA-capped and (B) Gelatinated TGA-capped CdTe QDs (red) and counter-stained with Calcein-AM (green). Overlay of red (excitation 543 nm) and green (excitation 488 nm) channels.

In summary, the comparison of the behaviour of these two human cell lines after four hours of incubation with gelatinated and non-gelatinated TGA-capped CdTe QDs showed that live cells were able to spontaneously uptake nanoparticles which eventually resulted in cell death with cell-dependent susceptibilities. As this behaviour was consistent with previous studies,[11-12, 18, 30] this provided a solid basis for testing of more complex nano-composites in those two particular cell lines.

4.3 Folic acid-functionalised QDs

Owing to their small sizes, aqueous solubility, biocompatible coating and ease of functionalisation, QDs have been widely applied as fluorescent bio-labels. A further attractive property for such tasks includes site-specificity. In the present work, we combined improved biocompatibility provided by a gelatine coating with an increased uptake from cancerous cells over-expressing folic acid receptors. While the conjugation of folic acid (FA) to various nanoparticle types *via* a polymer spacer has been widely reported,[31-36] herein we describe a new, rapid, one-pot synthesis of folic acid–conjugated gelatine-coated TGA-capped CdTe QDs.[37] The uptake of the resulting particles by cancer cells was assessed in Caco-2 cells which naturally over-express folate receptors (FR)[38] and HT1080 cells which do not.[24]

The synthesis of bio-functionalised nanoparticles often involves the two-step process of forming the nanoparticles prior to coupling the biomolecule of interest to an appropriate functional group from the ligands. One very common approach is carbodiimide coupling whereby the ligand's carboxylic acid is activated by a molecule such as 1-ethyl-3-(3-dimethylaminopropyl) carbodiimide (EDC) to form an unstable intermediate which will react with an amine group on the biomolecule and thus covalently bind it to the nanoparticle.

Figure 4.11 depicts the reaction mechanism for the example of CdTe QDs to be conjugated with amine-modified oligonucleotides. This strategy however presents the major drawbacks of exposing the nanoparticles to a very low pH which affects their stability.[39] In the case of QDs such treatment leads to partial quenching of luminescence even when controlling the pH with a buffer solution due to the destabilisation of the ligand shell and reaction of the carboxy groups.[40-41] Another interesting approach is the use of "click chemistry" consisting of the spontaneous reaction between functional groups in mild

conditions, such as alkyne and azide moieties in presence of a catalyst.[39] This is however limited to a few combinations of functional groups and may therefore require prior modification of ligands or biomolecule.

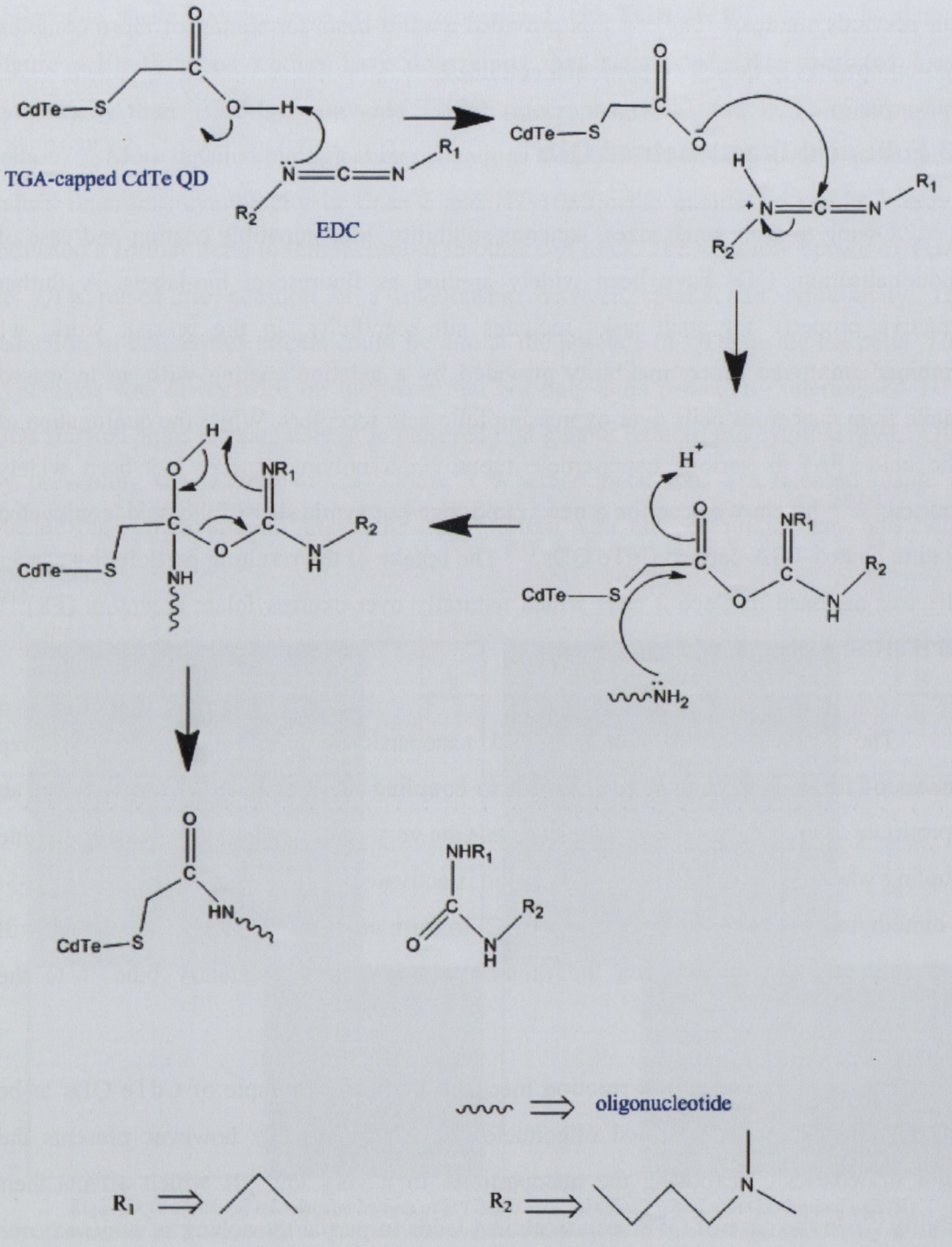

Figure 4.11 Schematic of the EDC coupling reaction in the case of an oligonucleotide bearing a terminal amine group to be bound to carboxylic acid functionalised CdTe QD

In the present work, a one-step *in situ* strategy was developed in order to maximize the yield and minimise luminescence quenching. Gelatin-coated QDs were used, which allowed the use of the swelling property of gelatine and exploration of the possibility of adsorption or incorporation of biomolecules into it.[42] Gelatin also provides a range of functional groups available for covalent binding. Following these observations, two synthetic routes were explored for the formation of QD-FA nano-composites: in the first one FA was added to the gelatin-coated CdTe reaction mixture before cooling to promote physical non-covalent incorporation into the gelatin layer; in the second one EDC was added in order to covalently bind FA to gelatin. Resulting materials were characterised and compared with plain gelatin-coated CdTe QDs.

For clarity purposes, gelatine-coated TGA-capped CdTe will be referred to as QD(A), gelatine-coated TGA-capped CdTe QDs with incorporated FA as QD(B) and gelatine-coated TGA-capped CdTe to which FA was conjugated *via* 1-ethyl-3-(3-dimethylaminopropyl) carbodiimide (EDC) coupling as QD(C). Their schematic structures are presented in Figure 4.12.

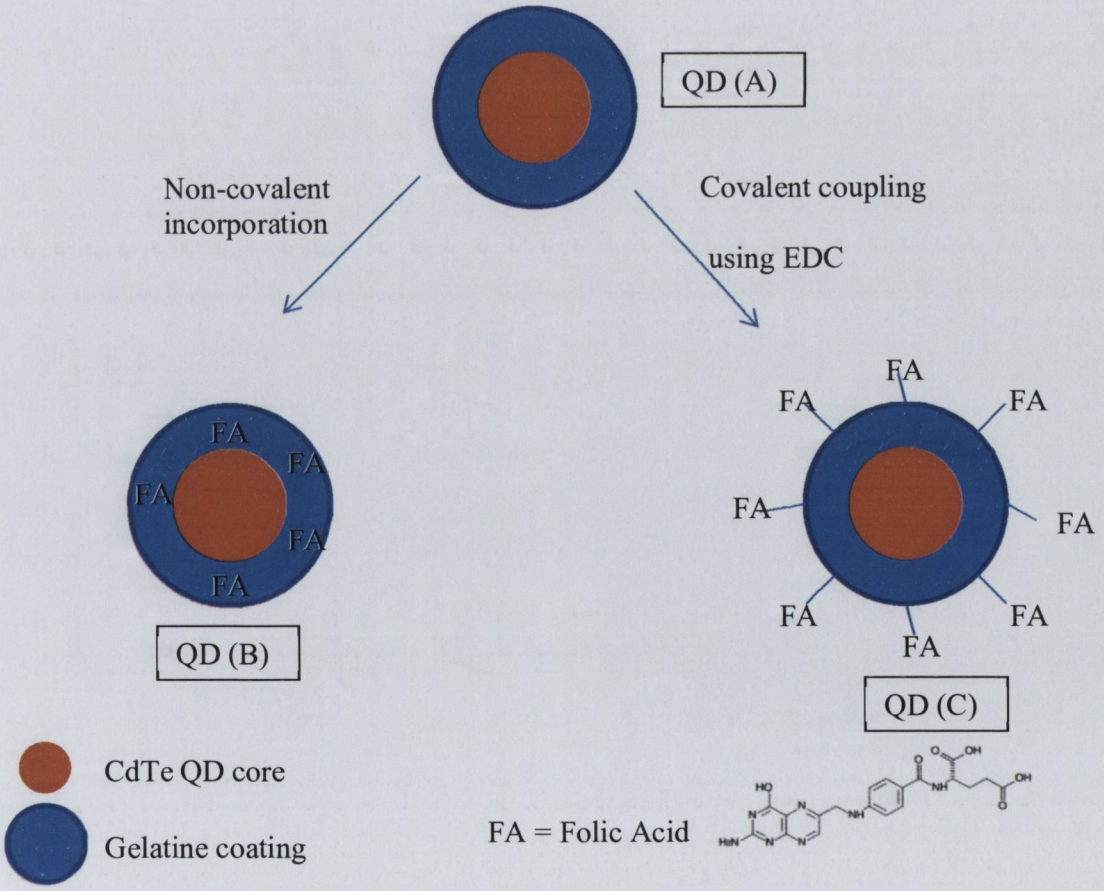

Figure 4.12 Schematic representations of QD (A) - gelatine coated, (B) - with FA incorporated into the gelatine layer and (C) - with FA covalently bound to the surface

4.3.1 Characterisation of FA-modified QDs

Samples of QD(A), (B) and (C) with similar spectroscopic properties were prepared: their maximum absorption (emission) wavelengths were respectively 556 (594), 554 (594) and 552 (586) nm, as shown in Figure 4.13. A quantum yield of 19%, 19% and 21% was recorded for QD (A), (B) and (C) respectively. The quantum efficiency was considered satisfactory for biological imaging.

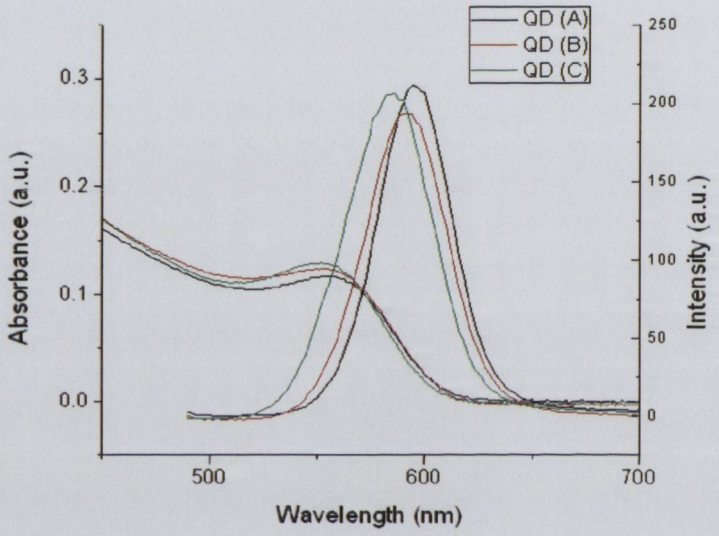

Figure 4.13 UV-visible absorption and PL emission spectra of selected samples of QD (A), (B) and (C). Excitation: 480 nm.

The luminescence lifetime decay was measured for each composite using Time Correlated Single Photon Counting (TCSPC) at the maximum emission wavelength and provided further evidence of the surface modification. Figure 4.14 displays the luminescence lifetime curves. The shorter (τ_1) and longer (τ_2) lifetimes from the biexponential fit are presented in Table 4.1 along with their respective contributions (B_1 and B_2). As previously reported, gelatine-coated QDs tend to exhibit a similar τ_1 and a longer τ_2 compared to original TGA-capped QDs, which indicates the involvement of surface states in charge carrier recombination and a reduction of non-radiative decay pathways.[10] QD(C) exhibited sligtly longer luminescence decay which could be attributed to greater surface passivation by cross-linked gelatin. Despite having the same quantum yield, QD (B) exhibited much shorter lifetimes than QD(A). The origin of this extremely short luminescence decay is unclear. A decrease in τ_2

would usually be associated with a reduction of the surface defect emission. Given the very large hydrodynamic diameter of these particles, it is possible that a thicker organic shell provides better protection from oxidation and thereby leads to fewer surface defects being introduced. Such a phenomenon would however usually result in an increase in the QY which is not the case here. Another explanation for the shorter τ_1 and τ_2 would be the possibility of electron transfer to FA molecules located close to the surface. This would provide additional pathways for the recombination of charge carriers, but these pathways are traditionally non-radiative and result in a decrease in QY, which is not observed in the case of QD (B). It is therefore postulated that a much more complicated system exists here, involving complex exciton recombination dynamics. Both a reduction in surface defect traps coupled with electron transfer to FA molecules might be involved in reducing the lifetime while maintaining the QY by **balancing each other's effect. In depth spectroscopic analysis** (e.g. transient absorption spectroscopy) would be required to fully elucidate the mechanisms involved. The result acertained nonetheless that the surface of QD (B) had been modified compared to QD (A) and (C). It could be overall concluded that our synthesis had successfully produced three types of QDs with different surface modifications.

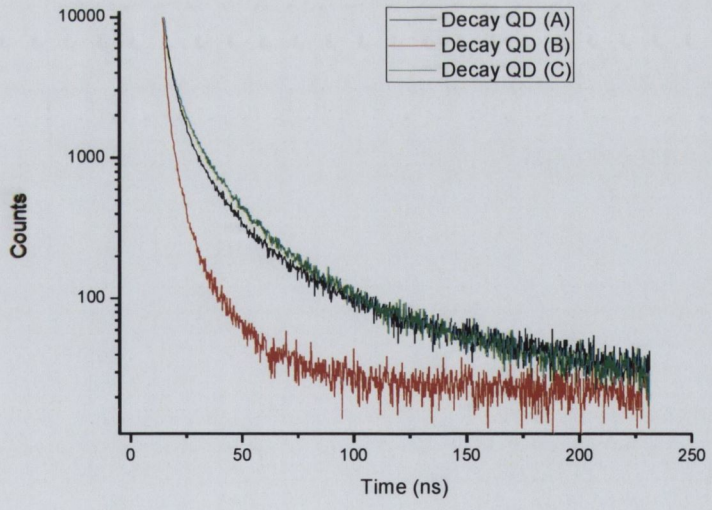

Figure 4.14 Luminescence decay curves obtained by TCSPC for QD(A), (B) and (C)

Table 4.1 Luminescence decay measurements. τ_1: shorter lifetime; τ_2: longer lifetime; B_1: relative contribution of T_1; B_2: relative contribution of T_2; χ^2: correlation factor

Sample	τ_1 (ns)	τ_2 (ns)	B_1(%)	B_2(%)	χ^2
QD (A)	4.05	17.24	39	61	0.98
QD (B)	3.11	12.39	60	40	1.04
QD (C)	4.38	18.24	32	68	0.98

The three types of QDs were further characterised by Transmission Electron Micrioscopy (TEM), Dynamic Light Scattering (DLS) and Zeta Potential measurements. Results are presented in Table 4.2. The presence of organic material on the surface strongly influences DLS measurement as it affects the water shell that surrounds each particle as they move in suspension, where hydrogen bonding and van der Waals interactions are important. It does not however impact the core size of the particles as measured from TEM images shown in Figure 4.15. This is why there were significant apparent discrepancies between the core and hydrodynamic diameters as pictured in Figure 4.16.

Table 4.2 Size of QDs as measured by TEM and DLS, and their zeta potential

Sample	Core diameter (nm)	Hydro-dynamic diameter (DLS by number) (nm)	Poly-dispersity index (PDI)	Zeta potential (mV)
QD (A)	4.2 (+/- 0.7)	8.2	0.570	-19 (+/- 1.7)
QD (B)	4.8 (+/- 0.8)	27.7	0.312	-52 (+/- 2.7)
QD (C)	4.9 (+/- 0.9)	4.7	0.195	-20 (+/- 4.1)

In the case of QD (A), the gelatine shell was responsible for the hydrodynamic diameter being more than double the core diameter. QD (B) had very large hydrodynamic radius and zeta potential compared to the two other types, demonstrating effective incorporation of FA in the gelatin layer. Due to the nature of the preparative process, it was expected that random parts of FA molecules should be protruding from the gelatin shell, thus being potentially available for cellular recognition, while others would be intertwined within the gelatin chains causing it to be unable to contract back to

its parent small and compact size and therefore increasing the hydrodynamic radius of the particles. There are also possibilities of interparticle cross-linking forming small aggregates. The overall increased organic material coating on the surface also led to an increase in the negative surface charge. The better stabilisation implied by the high zeta potential was also reflected in the lower polydispersity index (PDI).

QD (C) was prepared by treating QD (A) with EDC in order to covalently bind FA (through its amine functional groups) to gelatin. One side effect of the treatment is the cross-linking of gelatin through intra- and inter-molecular reactions of carboxylic groups with amino groups of the protein.[5, 43] This led to shrinkage and reduced swellability of the gelatin shell, providing a smaller hydrodynamic radius[5] as confirmed by the present results, as well as the presence of fewer carboxylic groups available on the surface, providing a less negative surface charge after functionalisation with FA.

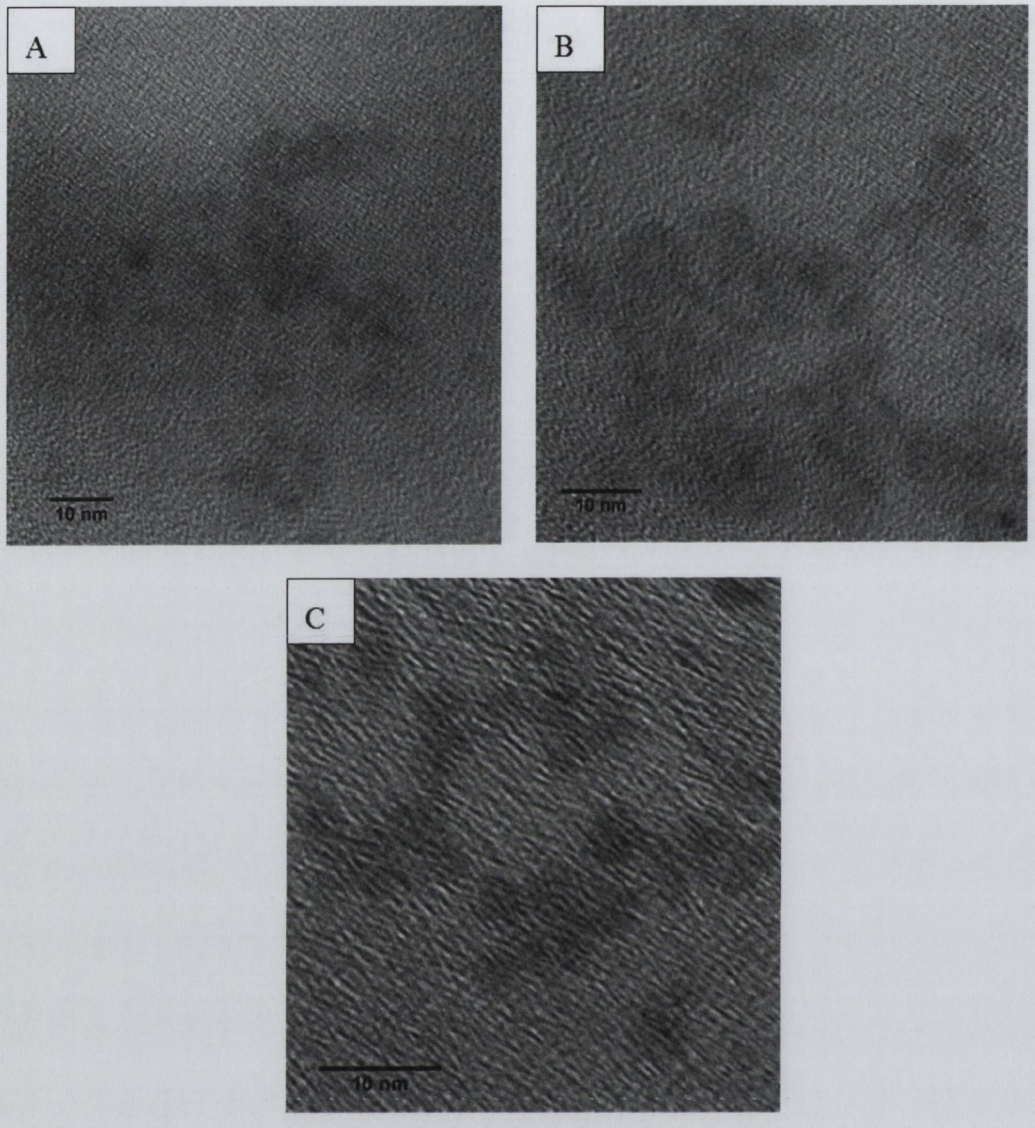

Figure 4.15 TEM images of QD (A), (B) and (C) as labelled

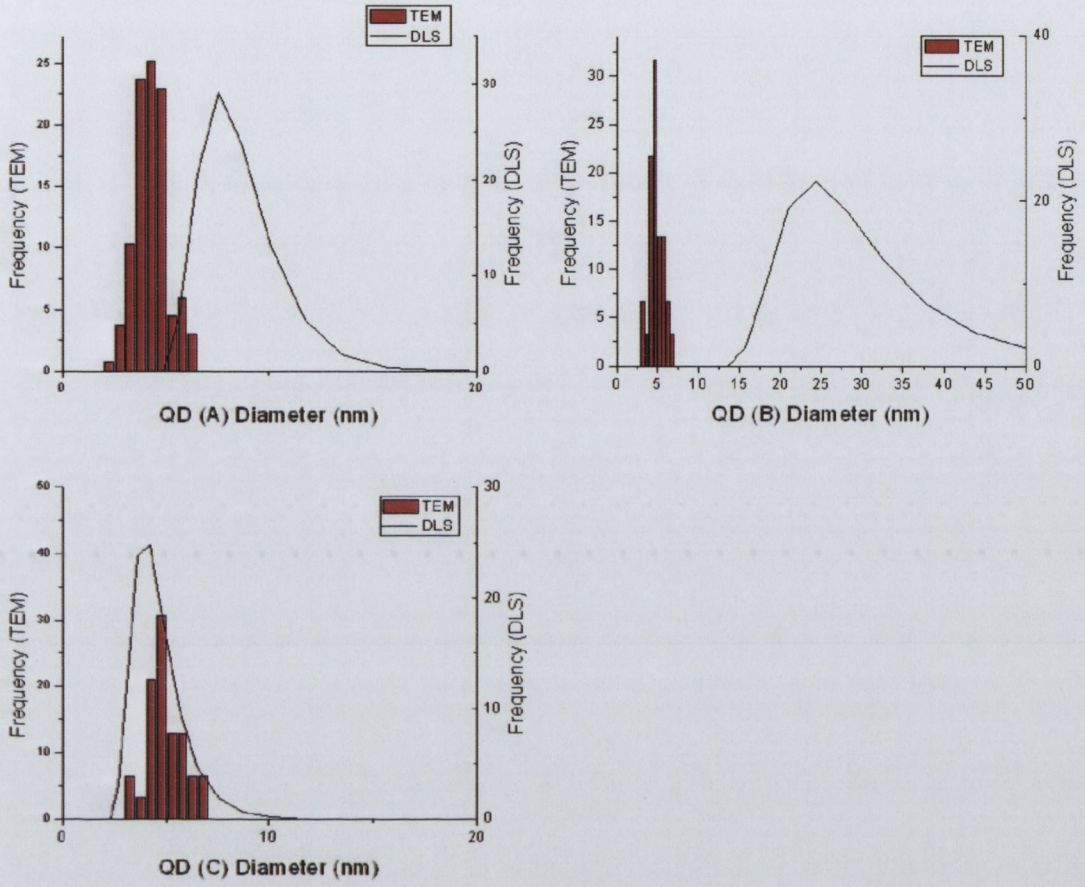

Figure 4.16 Comparison of core diameter as measured by TEM and hydrodynamic diameter from DLS for all three types of QDs

4.3.2 Biological testing of FA-modified QDs

The spontaneous cellular uptake of QD(A), (B) and (C) was investigated and compared in Caco-2 (human colon adenocarcinoma) and HT-1080 (human fibrosarcoma) cells. Confocal microscopy images of treated cells are shown in Figure 4.17.

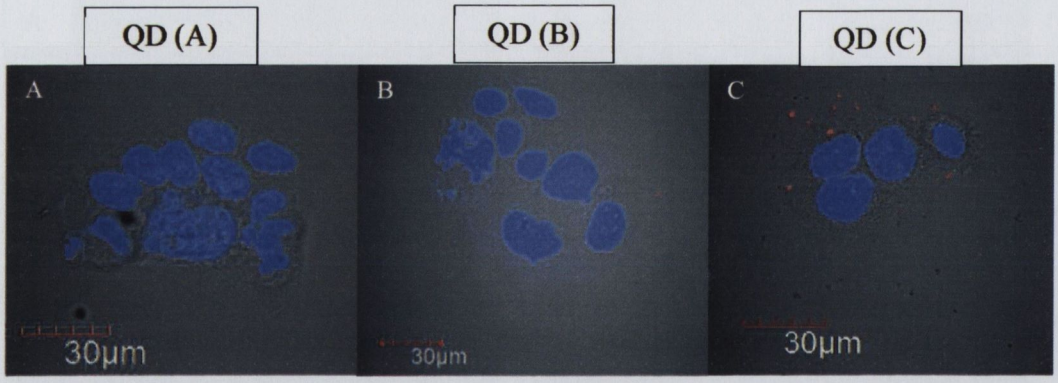

Figure 4.17 Confocal microscope images of Caco-2 cells treated with QD(A) (panel A), (B) (panel B) and (C) panel (C). Nuclei were stained with DAPI (blue), QDs emit in the red. Blue (excitation 405 nm) and red (excitation 543 nm) luminescence were merged with the bright field where cell membranes are visible.

Caco-2 cells were previously reported to not efficiently take up a variety of nanoparticles;[23] however, since they are known to over-express folate receptors,[38] the folic acid molecules present on the surface of nanoparticles were expected to significantly increase the uptake by these cells.

As shown in Figure 4.18, QD (A) and (B) were very similarly uptaken by the cells, with an average of 22 and 24% of cells exhibiting internalised QDs respectively. FA incorporated into the nanoparticle shell using the swelling technique appeared to have no significant effect on particle uptake, which was a reasonable outcome as the FA molecules would have random orientations and be partially trapped in gelatin due to the preparative technique, therefore binding of the recognition site to receptors on the cells may be hindered. On the other hand, QD (C) where FA molecules were covalently bound to the gelatine shell through their terminal amine, displayed a higher uptake of 66 %. It should also be noted than significantly more discrepancies were observed between experiments with QD (A) and (B) with standard deviations of 0.22 and 0.12 respectively, while the uptake of QD (C) was very consistent over all experiments with a standard deviation of 0.01. This was an indication of the mechanisms of endocytosis involved in all three cases. The internalisation of QD (C) was expected to be *via* receptor-mediated endocytosis. QD (A) on the other hand should be uptaken through non-specific endocytosis due to their lack of recognition molecule. This endocytotic pathway is more dependent on the metabolic state of the cells and its activation is strongly influenced by the cells' needs for nutrients. Although all experiments were carried out under the same conditions, parameters such as the

passage number of the cell culture may vary and explain the discrepancies in results. Consistent with this observation, it appeared that QD (B) were mostly uptaken through non-specific endocytosis and therefore that FA molecules were not generally available for bio-recognition.

To confirm that the increased uptake observed for QD (C) was related to the presence of covalently bound FA, a competition assay was performed with free FA. Results are displayed in Figure 4.18. In the case of QD (C) internalisation was reduced to 38% due to the presence of free FA. As expected the free FA molecules blocked the cellular receptors and QD (C) could therefore only be internalised by non-specific endocytosis. On the other hand, the percentage uptake of QD (A) was increased by the presence of free FA (57 %) almost to almost the level of QD (C) alone (66 %). In this case, free FA could be adsorbed onto gelatin thus helping receptor-mediated internalisation of QDs into the cells. The uptake of QD (B) was moderately increased by free FA (40 %) because the presence of randomly orientated FA molecules on the nanoparticle surface would limit the ability of more molecules to be adsorbed. Overall it was reasonably concluded that the observed increase in cellular uptake was directly linked to the presence of FA on the surface of the particles, in particular, covalently bound FA was significantly more successful at enhancing cell uptake behaviour than both incorporated FA-QDs and native parent QDs. QD (B) also proved to be of very little interest for biomedical applications since it did not stimulate receptor-mediated endocytosis.

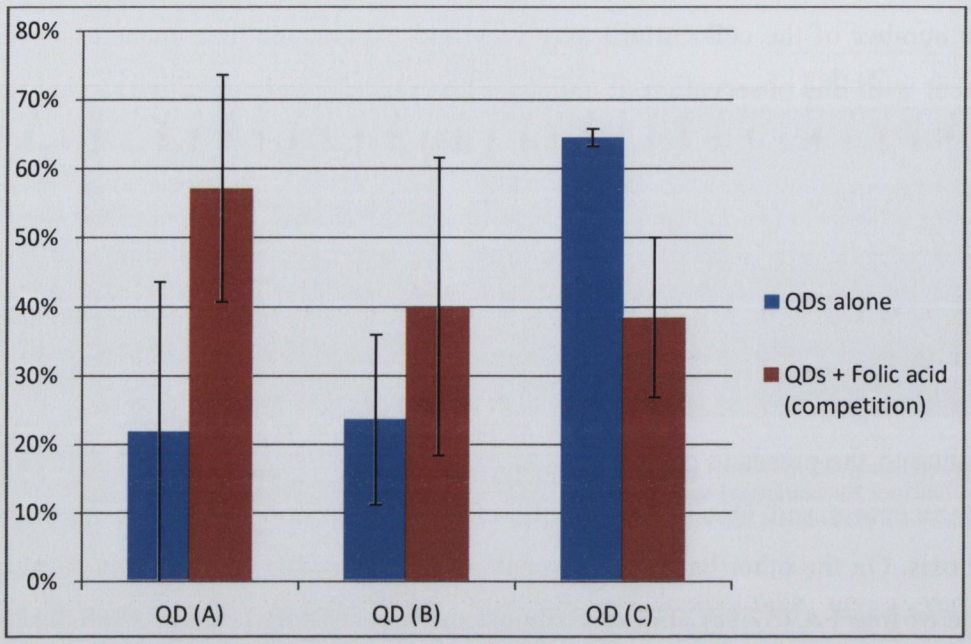

Figure 4.18 Percentage of Caco-2 cells exhibiting internalised QDs (A, B or C respectively) in absence (blue) and presence (red) of free FA in the cell culture medium after four hours incubation

Preliminary cytotoxicity studies were conducted on QDs (A) and (C) in presence and absence of free FA using a Calcein AM viability assay. The results are shown in Table 4.3. Calcein AM is a fluorescent dye which is able to penetrate the cell membrane. Its fluorescence is only released upon action of esterases in the cytoplasm. Since only viable cells produce active esterases, it can be used to assess cytotoxicity.[44]

Table 4.3 Cytotoxicity of FA modified QDs towards Caco-2 cells

Type	QD(A)	QD(A) +FA	QD (C)	QD(C) +FA
Cell death	23%	32%	59%	48%
Uptake	22%	57%	66%	38%

Thiol-stabilised aqueous CdTe QDs have been reported to be generally more toxic than ones produced through the organic route due to their lack of protective shell.[45] Adding a layer of gelatin however was found to reduce their cytotoxicity [11] which is believed to arise mainly from the release of cadmium ions.[45] Another critical aspect of QD toxicity is the size of the nanoparticles. In our study we used large (4.8 nm), red-emitting QDs which have been reported to be less toxic than smaller ones (< 3.5 nm), mostly because they are not able to penetrate as deep in the cell; they remain in the cytoplasm and are not able to enter the nucleus.[46] The cytotoxicity of the QDs under investigation here appeared to be

related to their uptake to a certain extent. QD (C) induced more cell death than QD (A) (59 % against 23 %) and were also internalised in larger amounts (66 % against 22 %). The relationship between cell death and uptake however is not linear and is likely not the only parameter involved. FA-modified QDs tend to be more cytotoxic than bare gelatinated QDs, which may be explained by their blocking of the FA receptors thus depriving the cells of this essential nutrient. Adding free FA to the incubation medium reduced the cytotoxicity of QD (C) by counter-acting this effect, and increased the cytoxicity of QD (A) by adsorbing onto the gelatin, favouring QD uptake and not being metabolised by the cells. This makes FA-modified QDs potential candidates for targeted cancer therapy, but more in-depth biological studies would be required in order to guarantee good enough specificity.

As a preliminary assessement of the specificity of FA-QDs towards cells over-expressing FA receptors, the nanocomposites were also tested in HT1080 (human fibrosarcoma) cells which only expressed a normal amount of FA receptors.[24] Preliminary studies in section 4.2 showed that HT1080 cells tend to uptake much more QDs than Caco-2. HT-1080 is a more aggressive cell line than Caco-2, with its doubling time being 26 hours[24] compared to 62 hours for Caco-2 (according to the American Type Culture Collection database). This implies that HT-1080 cells need a larger amount of nutrient and are likely to develop their unspecific endocytosis capability to increase the probability of uptake of random nutrient, especially when the nutrient supply is low as it was in our case.[25] The folic acid molecules present on the surface of particles were expected to increase the uptake by HT-1080 cells to a certain extent since they are not completely deprived of receptors, but the relative increase should be less than for Caco-2 cells where the amount of receptors is much higher.[47] Results confirmed these previous assumptions as shown in Figure 4.19 as well as Figure 4.20 where the percentages of cells exhibiting internalised QDs were expressed relative to the initial uptake of gelatinated QDs without FA.

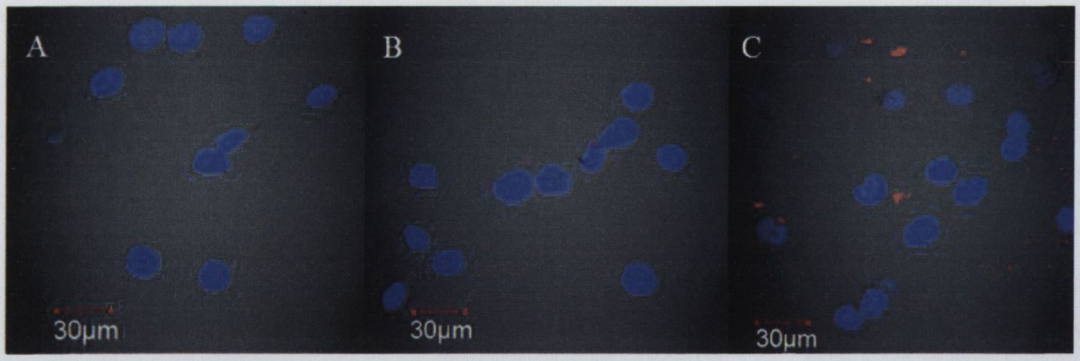

Figure 4.19 Confocal microscope images of HT-1080 cells treated with QD(A) (panel A), (B) (panel B) and (C) panel (C). Nuclei were stained with DAPI (blue), QDs emit in the red. Blue and red luminescence was merged with the bright field where cell membranes are visible.

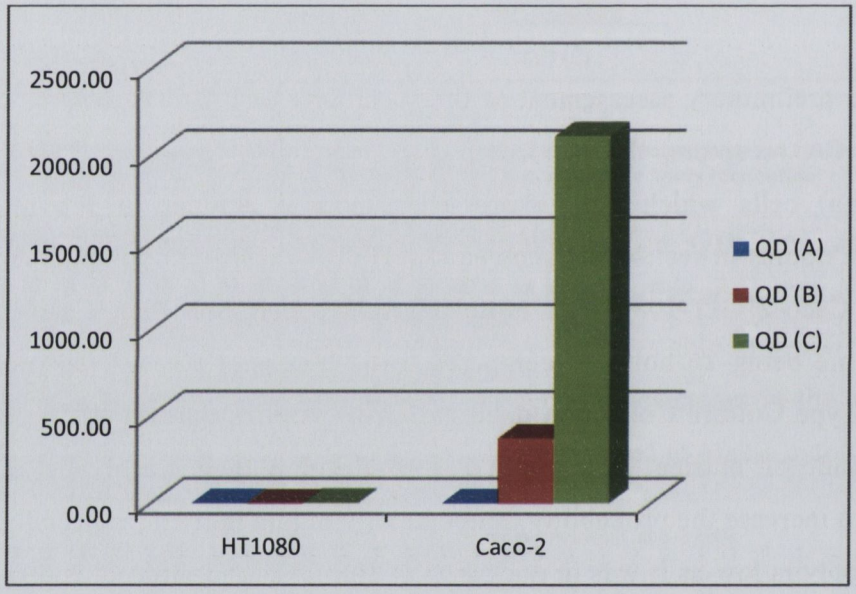

Figure 4.20 Differential uptake of QD (A), (B) and (C) by HT1080 and Caco-2 cells. The respective uptakes of QD (A) are taken as a reference to show the relative increase for both cell lines

It was thus demonstrated that gelatinated CdTe QDs can be functionalised through *in situ* binding of a biologically relevant molecule, such as FA. Although it could be readily incorporated into the gelatin shell, said molecule was only available for selective bio-recognition and uptake when covalently bound through a terminal group to a gelatin segment. The incorporation strategy may potentially be adapted for drug delivery applications coupled with targeting.

4.4 Caspase Inhibitor- and Antibody-modified QDs

Brain ischemia is an insufficient blood flow to the brain. Ischemic events induce, in the first instance, neuronal cell death in the ischemic core. This is followed by increased activation of microglia and neuroinflammation in the region surrounding the core, known as the penumbra. Activation of microglia is thought to lead to an inflammatory cascade which may perpetuate cell loss post-ischemia in the penumbra. Therefore the need for an effective post-ischemic therapeutic is of great importance.[48]

Caspases, or **c**ysteine-dependent **asp**artate-directed prote**ases**, are a family of enzymes which play a very important role in inflammation, apoptosis and necrosis. The NLRP3 inflammasome is a collection of proteins which includes the apoptosis-associated speck-like protein (ASC), the protease caspase 1 and the NOD receptor. The recruitment of NLRP3 leads to the proteolytic cleavage of caspase 1 to its active form and thereby the processing of pro-IL-1β to active inflammatory cytokine Interleukin 1β (IL-1β).[48] Recent studies have suggested that activation of this inflammasome by ATP, released from dying neurons, plays a role in ischemic-induced injury. Here we propose the use of NLRP3 inflammasome targeting nanoparticles as a possible post-ischemic therapeutic.

Caspase1 inhibitors I and II[49] and anti-ASC antibody[50] have the ability to stop the inflammatory cascade by inactivating caspase1 and ASC respectively. Their conjugation to nanoparticles was expected to improve their uptake by microglial cells and thereby to reduce the inflammation more efficiently. As a proof of concept for this strategy, gelatinated CdTe QDs were selected as drug carriers. As can be seen in Figure 4.21, Caspase1 inhibitor I and caspase1 inhibitor II have very similar structures apart from the aldehyde group in Inhibitor I which is replaced by a chloromethylketone group in Inhibitor II.

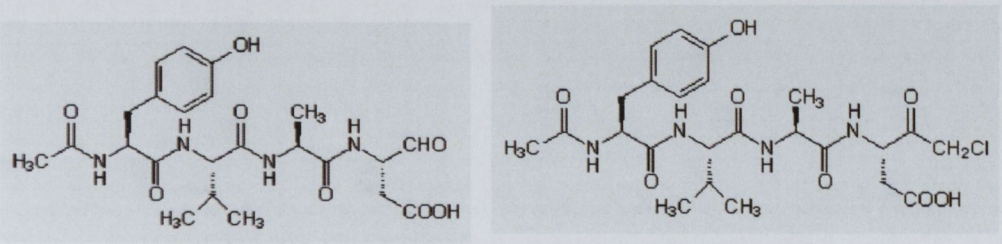

Figure 4.21 Structure of caspase1 inhibitor I (left) and II (right)

The conjugation reaction involved the spontaneous reaction of a carbonyl group from the inhibitor molecule with an amine from gelatin. The reaction results in the formation of an imine.

Inhibitors were added to QD suspensions and incubated overnight on a shaker at room temperature. Excess inhibitor was then removed by purification in a Sephadex G25 column. PL spectra of the QD-Caspase Inhibitor I (QD-Inh I) and QD-Caspase Inhibitor II (QD-Inh II) conjugates were recorded and compared to the original QDs at the same concentration, as displayed in Figure 4.22. A 22 % decrease in intensity was observed for QD-Inh I compared to the original QDs, and a 15 % decrease was recorded for QD-Inh II. A small amount of quenching is usually to be expected upon conjugation of biomolecules due to the possibility of energy or electron transfer. The larger degree of quenching observed for QD-Inh I suggested a higher loading of Inhibitor I than Inhibitor II had been achieved. This was also expected considering the presence of the aldehyde group on Inhibitor I which is more accessible for reaction than ketones.

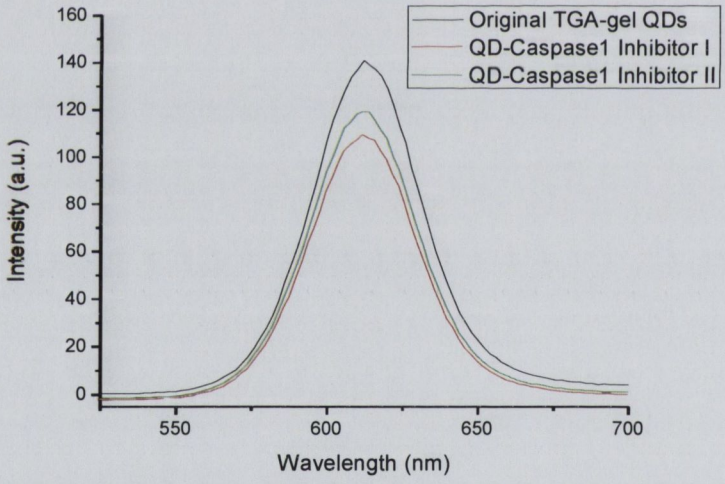

Figure 4.22 PL spectra of TGA-gel QDs before and after conjugation to Caspase1 Inhibitor I and II respectively

Another type of inflammasome-targeting QD-conjugate was produced using the ASC (F-9) anti-ASC antibody. In this case conjugation was achieved by carbodiimide coupling as described in the previous section. After purification on Sephadex column to remove unbound antibody molecules, the PL measurement presented in Figure 4.23 highlighted a 37 % quenching of luminescence after conjugation. For the same reason as

with the inhibitors, this was taken as an evidence of successful attachment of antibodies. The QD-antibody conjugates will be referred to as QD-Ab.

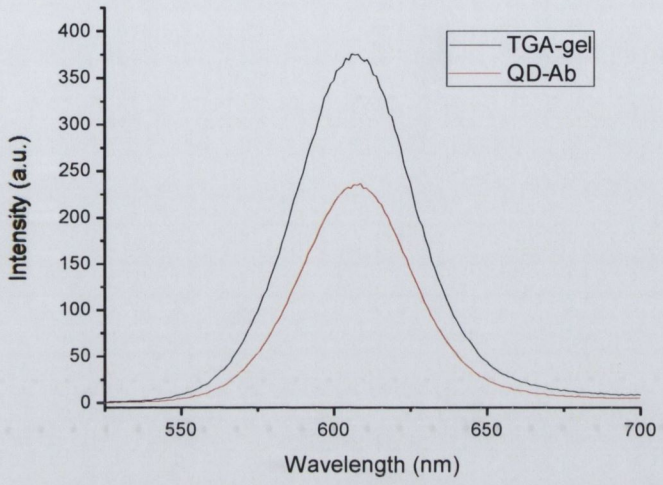

Figure 4.23 PL spectra of original TGA-gel QDs and QD-Ab conjugates

TGA-gel QDs, QD-Inh I, QD-Inh II and QD-Ab were subsequently tested in mixed glia, microglia and astrocytes from neonatal Wistar rats. Cultures were treated with ATP and inflammasome-targeting nanoparticles, control nanoparticles or inhibitors and antibodies alone, and IL-1β and caspase 1 activity and cellular fluorescence were assessed.

Caspase 1 inhibitor- and anti-ASC antibody- conjugated nanoparticles were preferentially taken up by microglial cells when compared with astrocytes or neurons. The conjugated QDs inhibited ATP-induced release of IL-1β to a greater extent than the unconjugated inhibitors or antibody as shown in Figure 4.24. NLRP3-targeting nanoparticles were also shown to be significantly more effective at inhibiting IL-1β release for up to 6 hours after ATP treatment compared with the unconjugated inhibitors and antibodies.

NLRP3-targeting inflammasome particles are a potentially novel, cell specific, therapeutic for the treatment of ischemia induced chronic inflammation. Nanoparticles that were conjugated with compounds that target the NLRP3 inflammasome were more effective at reducing the ATP induced release of IL-1β from glial cells than the compounds alone. Their ability to also reduce IL-1β, subsequent to ATP treatment, demonstrated the potential for these nanoparticles to be an effective post-ischemic therapeutic strategy.

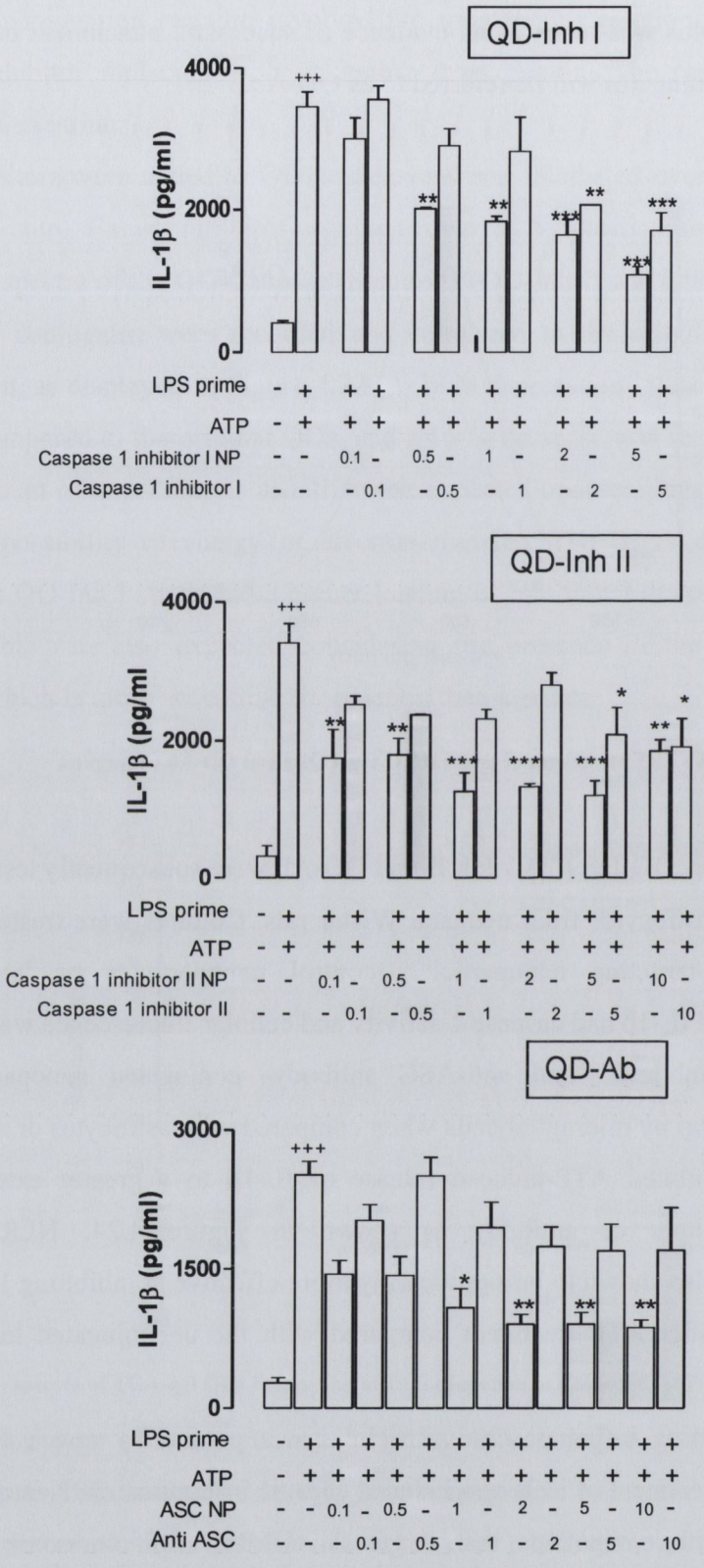

Figure 4.24 Concentration of released IL-1β upon activation with ATP and treatment with various concentrations of either Inhibitor I or II, anti-ASC antibody or their QD conjugates

4.5 Gelatin-mediated QD aggregates

Most of the research to date was focused of individual small (below 6 nm) QDs. However, some photonic and biomedical applications require larger particles. For instance, 25 to 50 nm nanoparticles are better internalised by cells due to the balance between the thermodynamics of membrane binding and the kinetics of protein diffusion.[51] We believe that gelatin is a very convenient material to create luminescent clusters of QDs. The same approach, using gelatin, can also be used to form hybrid systems where energy transfer can occur. In this case type of small, green-emitting QDs may act as an energy donor, while another type, larger and red-emitting may constitute an energy acceptor. The main conditions for Förster (or Fluorescent) Resonant Energy Transfer (FRET) to occur are the spectral overlap between the donor emission and the acceptor absorption and a small enough distance between the two species. Assemblies of QDs allowing fulfilment of the latter condition may be obtained using different types of interactions between ligands. The gelling property of gelatin was used here to agglomerate the particles.

Red-emitting, TGA-gel QDs were heated to 70°C for 3 min. A reduction in PL intensity and a small red-shift of the emission profile were observed, as seen in Figure 4.25. These effects were attributed to the aggregation of QDs which may introduce more defect and non-radiative pathways for the recombination of charge carriers.

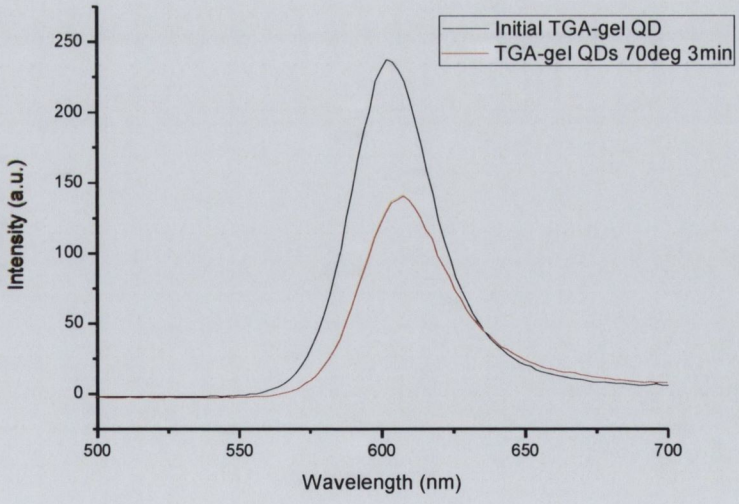

Figure 4.25 PL emission spectra of TGA-gel QDs before (black) and after (red) heating at 70 °C for 3 min (excitation 480 nm)

The same treatment was applied to a mixture of TGA-capped QDs (emission 564 nm) and TGA-gel QDs (emission 600 nm) in equal concentrations. PL spectra displayed in Figure 4.26 were recorded immediately after mixing, and every minute during heating. The spectra showed a gradual quenching of the donor emission and simultaneous enhancement of the acceptor emission. Energy transfer was thus observed, suggesting that aggregates of QD with two different sizes were formed. It should however be noted that the acceptor enhancement was not to the same extent as the donor quenching, suggesting that some of the energy was lost through non-radiative decay pathways.

These aggregates were characterised by DLS, as illustrated in Figure 4.27. The TGA and TGA-gel QDs had hydrodynamic diameters of 6 and 10 nm respectively. The difference was due both to the variation in core size and to the presence of gelatine which increasing the hydrophilicity of TGA-gel QDs. After being heated for 3 min, TGA-gel QDs formed aggregates with an average hydrodynamic diameter of 24 nm, while the mixture of the two species resulted in 16 nm aggregates. Here again the difference was attributed to the presence of smaller particles in the mixtures as well as a lower amount of gelatin since only half of the QDs were gelatinated.

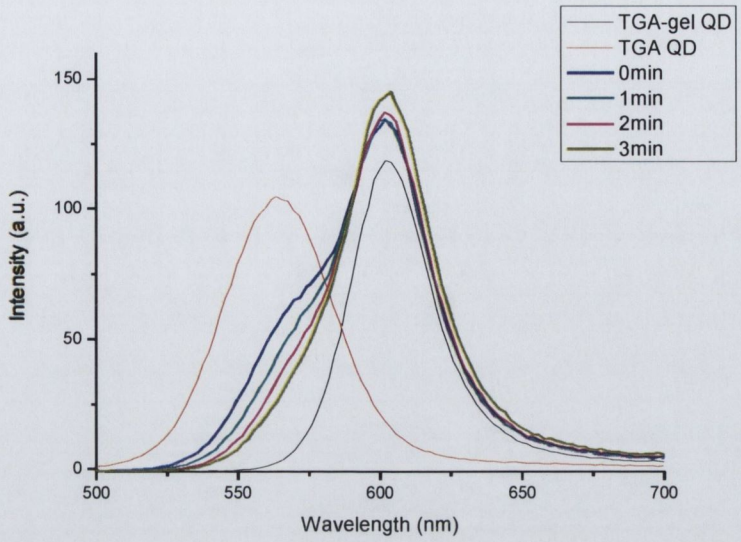

Figure 4.26 PL spectra of TGA and TGA-gel QDs, and their mixture heated at 70 °C after 0, 1, 2 and 3 min.

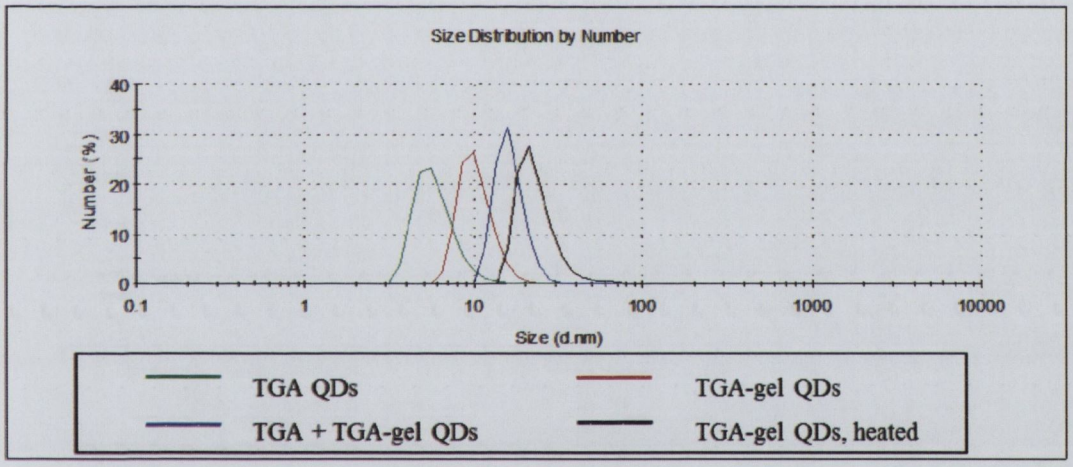

Figure 4.27 DLS measurements of TGA QDs, TGA-gel QDs, TGA-gel QDs after heating at 70 °C for 3 min and a mixture of the two species heated at 70 °C for 3 min.

Further characterisation of the aggregates was performed by electron microscopy. It should be noted that these types of QDs tend to aggregate on TEM grids after drying independently of any pre-treatment. The images displayed in Figure 4.28 and Figure 4.29 should therefore be analysed with caution. They do confirm the presence of two sizes of QDs in the case of the mixture, with fairly defined necklace structures. For TGA-gel only on the other hand, only random aggregates were observed. This could be due to the absence of gelatin on the smaller QDs in the first case which reduced the possibilities of agglomeration and provided a degree of directional assembly.

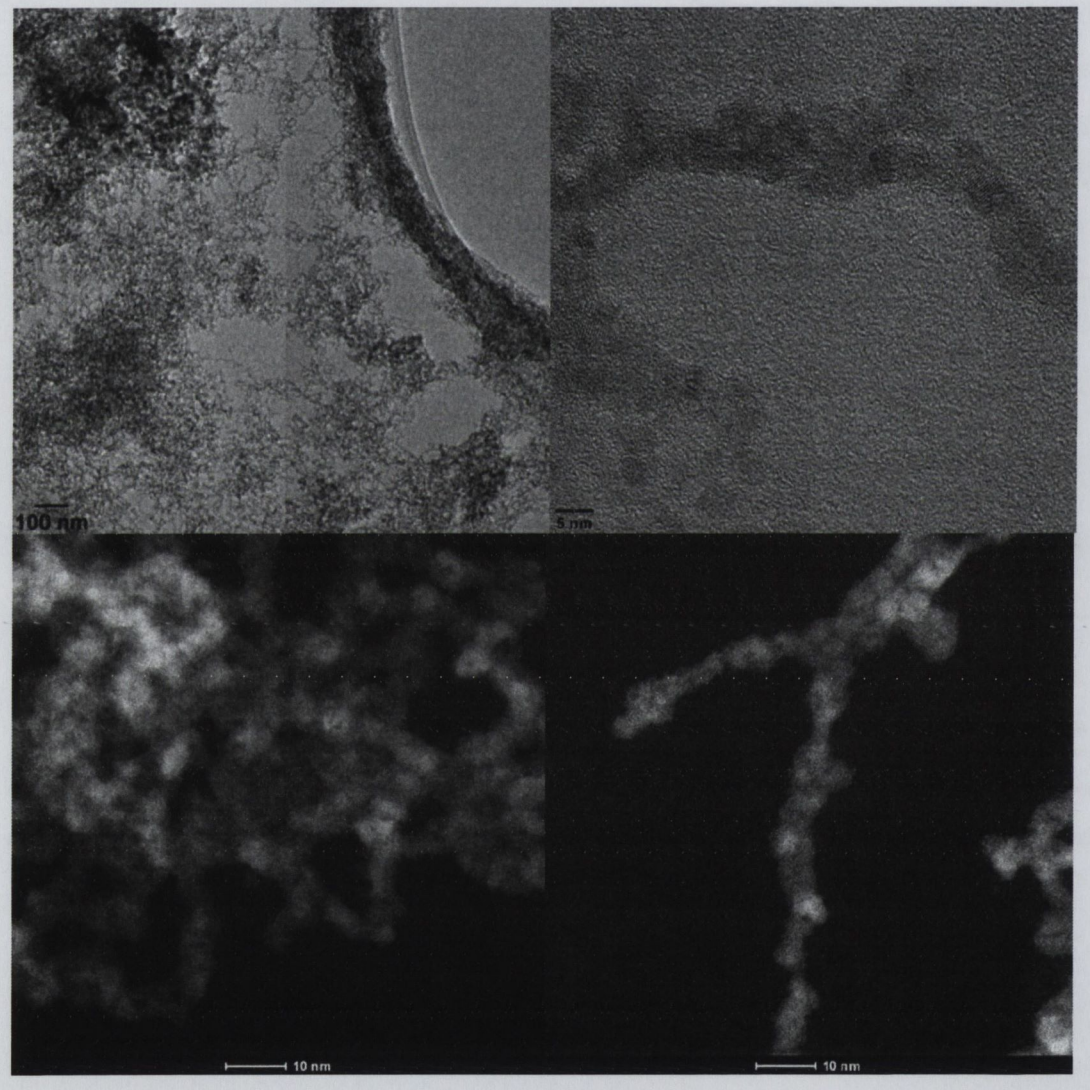

Figure 4.28 TEM (top) and STEM (bottom) images of a 1:1 mixture of small (3.5 nm) TGA-capped and large (4.5 nm) TGA-gel CdTe QDs, heated at 70 °C for 3 min

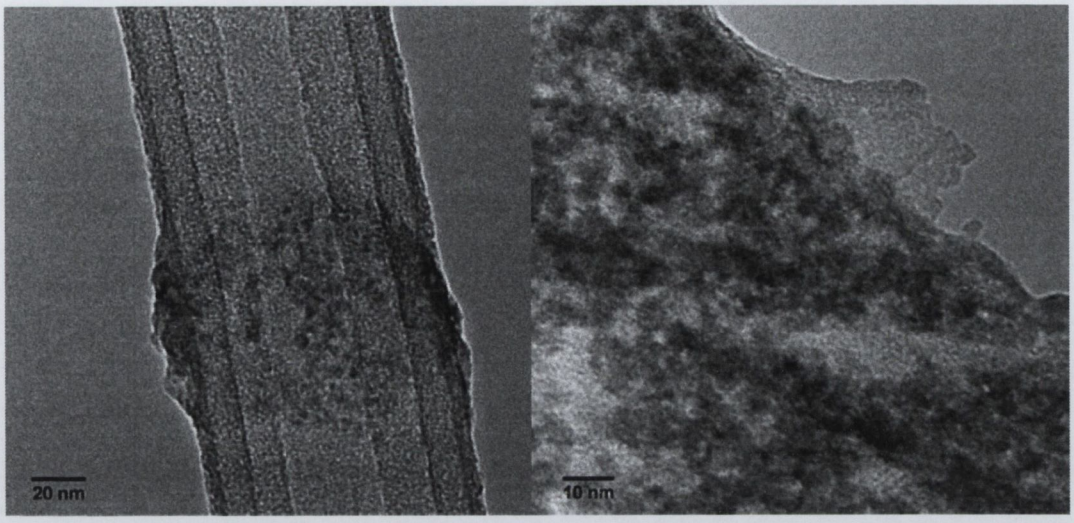

Figure 4.29 TEM images of TGA-gel QDs after heating at 70 °C for 3 min

In conclusion, gelatin-mediated QD aggregates were successfully formed, and FRET was observed in these systems. The size of the resulting composites as determined by DLS should improve their uptake by live cells.[51] Their quantum yield however was overall reduced due non-radiative energy dissipation.

4.4 QD-loaded gelatin nanoparticles

The term "Jelly dots" was coined to describe gelatin-coated-QD composites produced according to a bottom-up approach. A top-down method was also explored, where gelatin nanoparticles were formed and subsequently loaded with pre-formed QDs. The synthesis of gelatin nanoparticles has been widely used and optimised.[3] They have been proven to be suitable for drug encapsulation and targeted delivery.[4, 52] This approach has been used to form gelatin-coated and linked clusters of QDs in an attempt to increase both QY through FRET and cellular uptake by size effect.

4.5.1 Optimisation of gelatin nanoparticles

The gelatin nanoparticle synthesis employed herein was that originally developed by Coester *et al.*[3]. It is based on a two-step desolvation process, where gelatin powder is dissolved in water and acetone is used to precipitate it out. The first step is aimed at narrowing the size distribution of gelatin molecules in order to form homogeneous nanoparticles in the second step. The nanoparticles are eventually cross-linked with

glutaraldehyde to stabilise them. The diameter of particles produced by this method could be tuned by varying conditions such as the reaction temperature, the amount of sediment after the first desolvation step, the pH and the addition rate of acetone.[53] The as-produced particles however were all over 100 nm in diameter. For the purpose of making small QD clusters encapsulated in gelatin, 10 to 30 nm nanoparticles were desirable.

The synthesis of smaller gelatin nanoparticles was attempted by modifying the agitation method in the second desolvation step. In the published procedure this step is carried out under stirring. Ultrasonic agitation however provides greater localised energy and was therefore expected to produce smaller particles.[54] This approach however yielded particles with a very broad size distribution as observed using scanning transmission electron microscopy (STEM) as shown in Figure 4.30, where the presence of two different populations of nanoparticles was observed. This was thought to be caused by localised 'hot spots' generated by the ultrasonic waves causing the extended growth of some nanoparticles in the sample, leading to the wide size distribution observed.

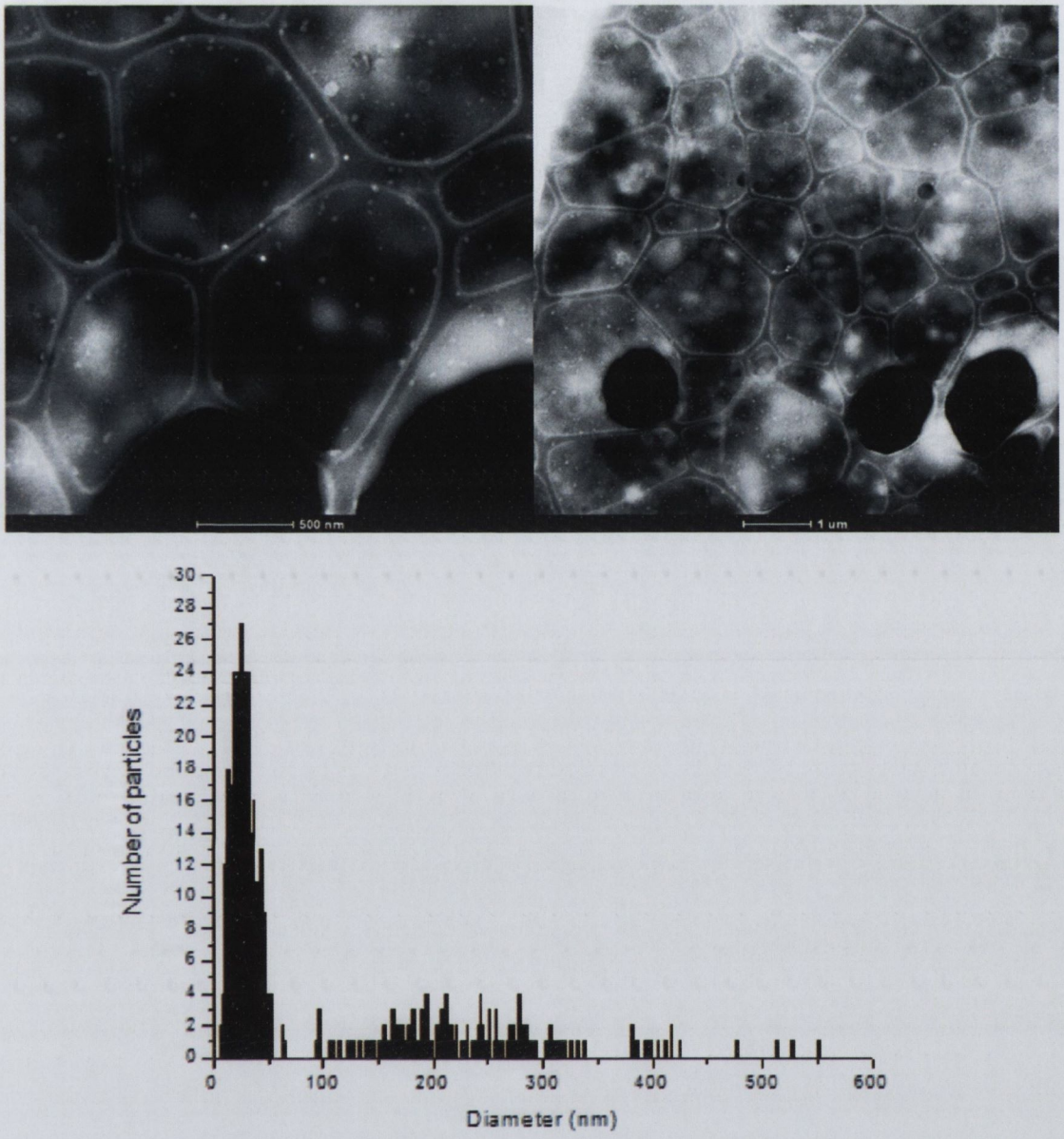

Figure 4.30 STEM images of gelatin nanoparticles synthesised using ultrasonic agitation (top). Size distribution of gelatin nanoparticles as measured on STEM images (bottom).

Different fractions could be separated from the mixture by size selective precipitations through successive mild centrifugations. DLS confirmed successful separation through the progressive decrease in average diameter after each centrifugation step as shown in Figure 4.31.

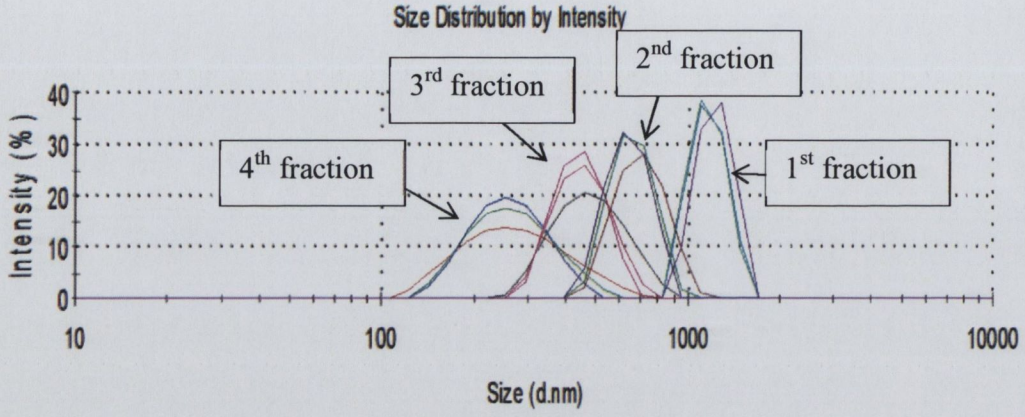

Figure 4.31 DLS measurements of four fractions successively obtained by size selective precipitation of gelatin nanoparticles synthesised using ultrasonic agitation. (Three measurements are displayed for each fraction)

Unfortunately, due to the propensity of gelatin to cross-link and aggregate in suspension, the preparation of nanoparticles with a hydrodynamic radius less than 200 nm was elusive. As smaller QD clusters were desirable for our outcome (<50 nm), this approach was thus abandoned.

4.5.2 Incorporation of QDs in gelatin nanoparticles

TGA-capped CdTe QDs were incorporated in large gelatin nanoparticles by performing the second desolvation step in presence of QDs. Some luminescence remained visible from the QD-loaded nanoparticles, although the relatively low loading and non-negligible absorption of gelatin particles resulted in a lowered quantum yield in comparison to the parent QDs as shown in Figure 4.32. The excitation spectrum shown in Figure 4.33 also revealed that highest emission was obtained when exciting at the maximum absorption wavelength of gelatin, 330 nm, as opposed to the traditional band edge of QDs. This suggested the incorporation of QDs in thick gelatin entities.

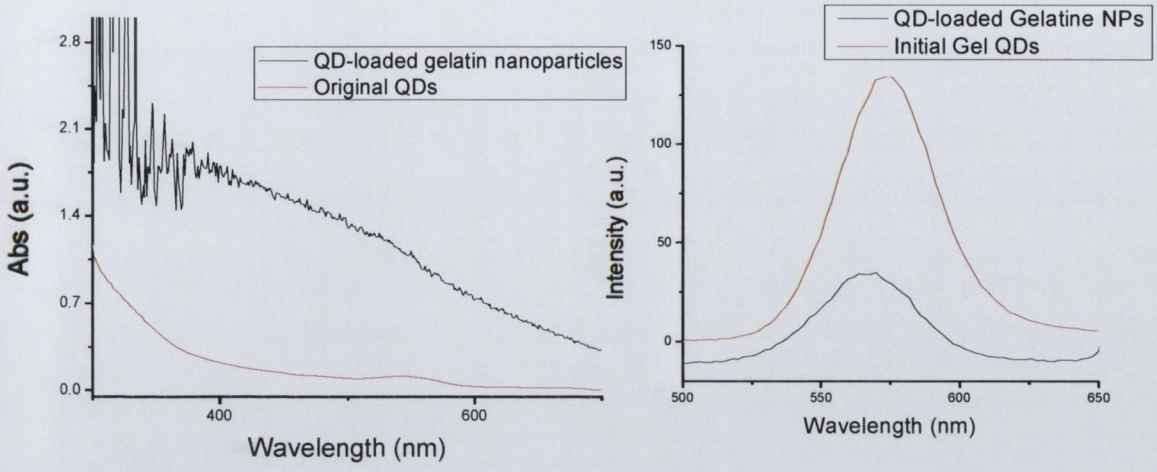

Figure 4.32 UV-visible absoption (left) and PL emission spectra of initial QDs and QD-loaded gelatin nanoparticles. (Excitation: 330 nm)

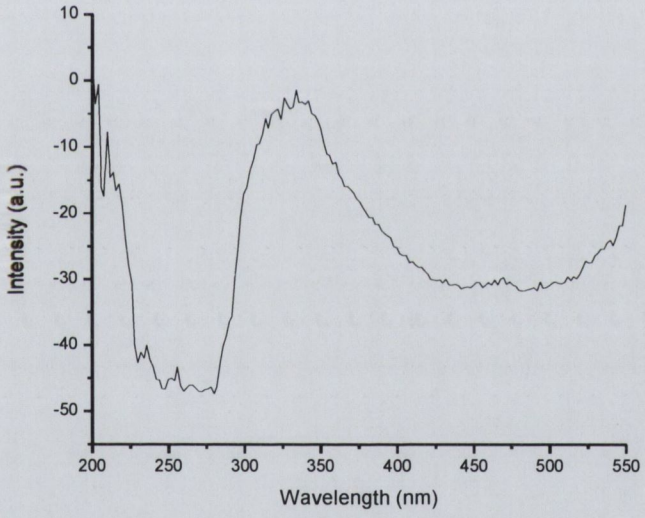

Figure 4.33 Excitation spectrum of QD-loaded gelatin naoparticles at the maximum emission: 568 nm

The usual formation of gelatin particles as well as their loading with QDs was confirmed by STEM imaging (Figure 4.34). This technique was most suitable for these composites as contrast arises mainly from the difference in atomic number (Z) and thickness. The heavy CdTe QDs would therefore appear very bright compared to gelatin. Regular TEM only allowed the visualisation of the QDs due to the very low contrast arising from gelatin (Figure 4.35). The difference in focus distance among the visible QDs

nonetheless indicated that they were embedded in gelatin of significant thickness. Some shadows were also visible, which may correspond to areas of denser gelatin.

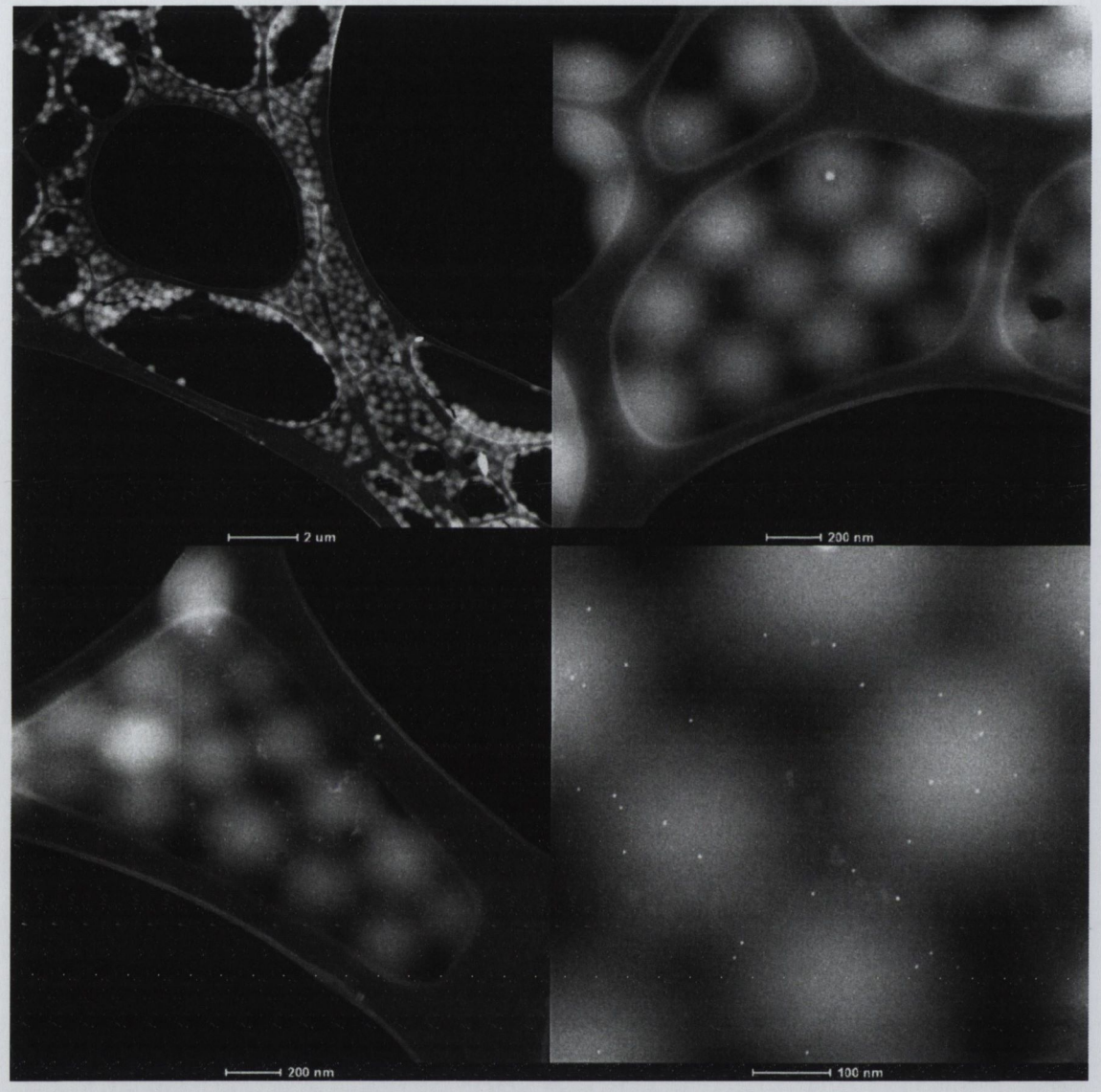

Figure 4.34 STEM images of QD-loaded gelatin nanoparticles, where the gelatine shell can be observed as a sphere of ~300 nm diameter and the QDs are visible as very bright ~5 nm spots distributed within the gelatine sphere.

Figure 4.35 TEM images of QD-loaded gelatin nanoparticles, where only QDs are visible.

The average particle diameter measured from these images was 302 nm (+/- 52 nm). It should be noted however that samples for analysis by STEM have to be dried down, thus causing the gelatin to shrink. In addition, the low melting point of gelatin meant that the nanoparticles were visibly melting under the electron beam. The images were taken from only one scan to limit this effect, but it may not have been totally avoided. Size measurements were therefore confronted to DLS measurements of the hydrodynamic radius which was on average 1111 nm (+/- 117 nm). The corresponding graph is displayed in Figure 4.36. On the contrary to STEM, DLS gives a larger diameter than the actual one due to hydrogen bonding and van der Waals interactions, as well as particle aggregation.

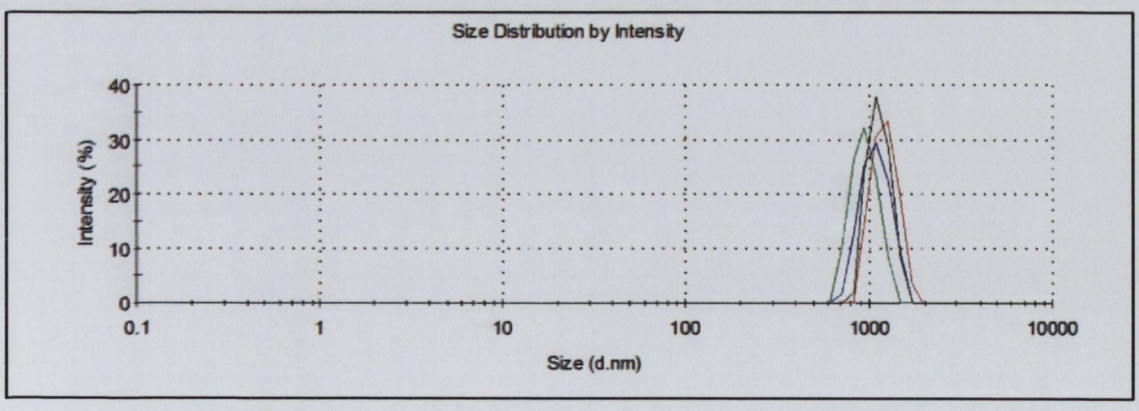

Figure 4.36 DLS measurements of QD-loaded gelatin nanoparticles

Building on the insight into the interactions of QDs with gelatin, and the behaviour of gelatin under various conditions acquired here, more composites involving metal nanoparticles were created as discussed in the next section.

4.6 Gelatin-coated metal nanoparticles

4.6.1 Gelatin-coated silver nanoprisms

Since the silver nanoprisms described in chapter 3 have typical dimensions in the 20-70 nm range, they present good potential for being internalised into cells. Their coating with gelatin is expected to improve their biocompatibility and provide a platform for functionalisation. Following a similar strategy to that which led to synthesis of gelatin-coated QDs, metal nanoparticles were in turn embedded in a gelatin shell. Silver nanoprisms were pre-formed and subsequently mixed with an aqueous solution of gelatin at moderately elevated temperature and under vigorous stirring. Varying the amount of gelatin allowed control over the thickness of the coating as assessed by measuring the hydrodynamic radii of the final nano-composites (Figure 4.37).

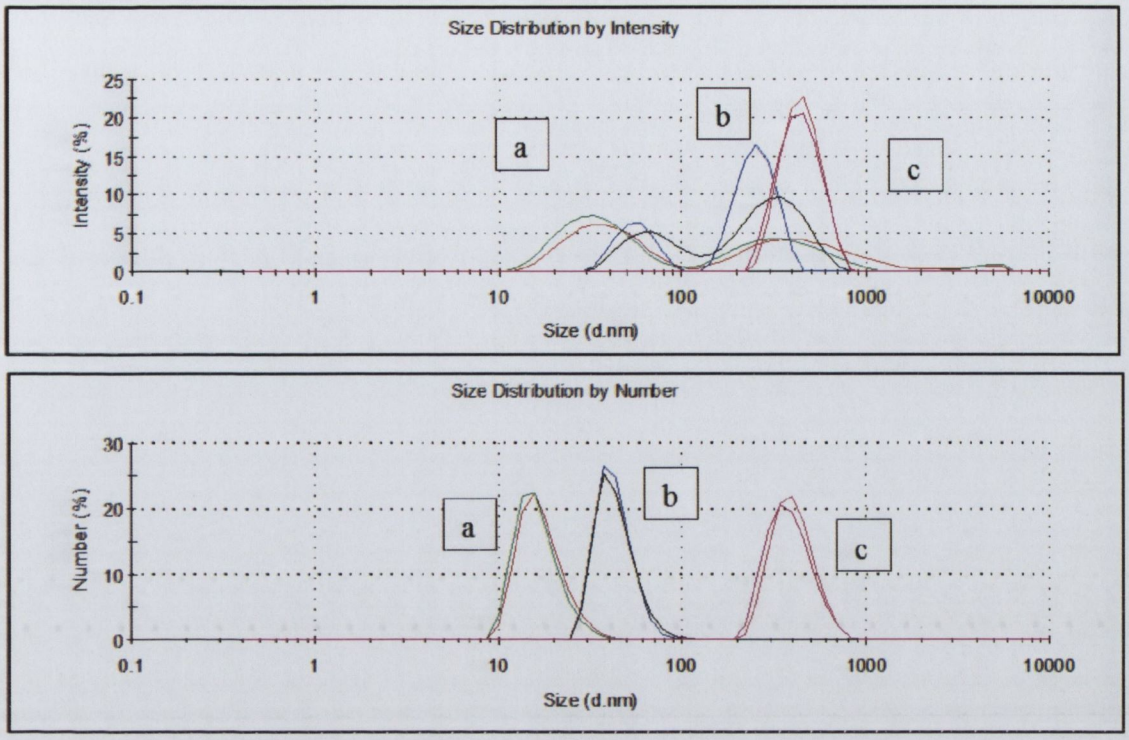

Figure 4.37 DLS measurements of silver nanoprisms (a) and gelatin-coated silver nanoprisms produced with (b) 0.01 g and (c) 0.05 g of gelatin. The top graph shows the size distribution by intensity and the bottom one shows the extrapolated distribution by number.

DLS measurements primarily give a size distribution by intensity which can be converted into a size distribution by number considering that larger particles scatter a high light intensity. Figure 4.37 displays the hydrodynamic diameters for original silver nanoparticles and for those coated with increasing amounts of gelatin. The former exhibited the dual peak typical of anisotropic structures. The bigger size corresponds to the flat triangular face of the nanoprisms while the smaller one reflects on the edge. After coating with a small amount of gelatin, the spectrum still displayed two peaks. Their relative intensity however was inverted, and the smaller one shifted to larger sizes. This suggested that the nanoparticles mostly retained their shape but that a layer of gelatin was indeed present. When increasing the amount of gelatin only one peak remained, shifting to bigger sizes. As the coating became thicker, it gradually turned into an overall symmetrical shape. The presence of gelatin around the nanoprisms was also supported by UV-visible absorption spectra as shown in Figure 4.38. The composites formed with a low amount of gelatin partially retained the plasmon band of silver nanoprisms, whereas it was no longer distinguishable for the ones produced with a larger amounts of gelatin. The plasmon band was likely to be masked by the strong broad absorbance of a thick gelatin shell. The size

distribution by intensity accounts for variations in particle morphology, whereas size distribution by number offers a clearer visualisation of the gradual size increase alone.

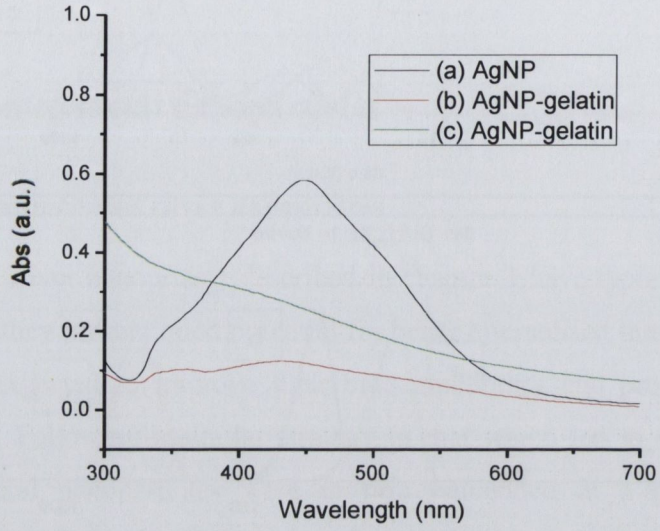

Figure 4.38 UV-visible absorption spectra measurements of silver nanoprisms (a) and gelatin-coated silver nanoprisms produced with (b) 0.01 g and (c) 0.05 g of gelatin.

Such gelatin-silver nano-composites could potentially be very useful for drug delivery applications. The gelatin coating would protect both the silver from catalytic oxidation in physiological media and tissues from the cytotoxic effects of silver, thus improving biocompatibility. Additionally, it provides a platform for functionalisation as well as incorporation of markers or drug molecules which would be released upon heating and melting of the gelatin. As a proof of concept and to allow visualisation in TEM, QDs were incorporated into the gelatin shell of the coated nanoprisms. DLS measurements (Figure 4.39) indicated that no significant change in the hydrodynamic radii occurred due to the presence of QDs. This was expected due to the small size of QDs (< 5 nm).

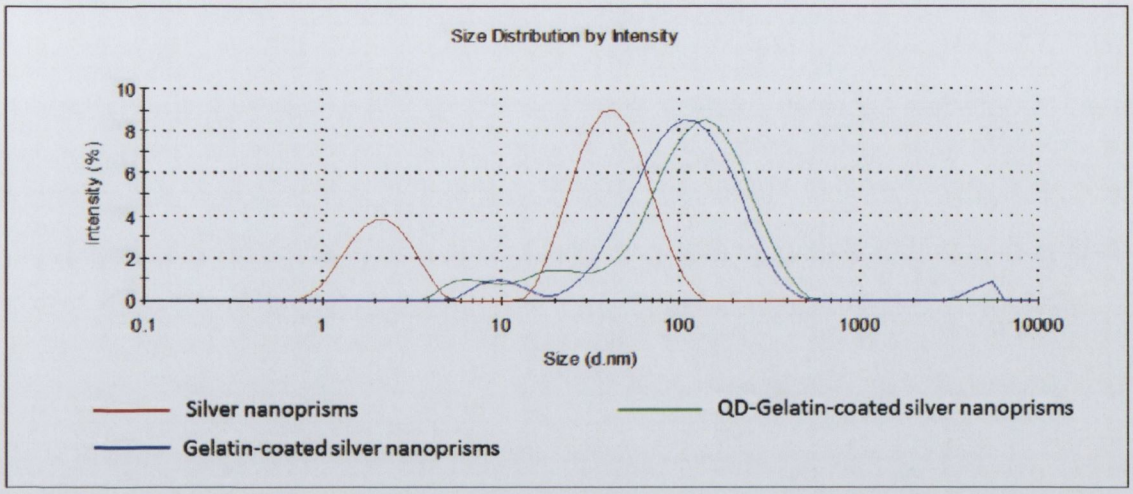

Figure 4.39 DLS measurements of silver nanoprisms (red), gelatin-coated silver nanoprisms (blue) and QD-gelatin-coated silver nanoprisms (green)

TEM images, displayed in Figure 4.40, confirmed that the average size of nanoprisms remained the same in all three samples, as well as the presence of QDs all around them in sample (c) (panels c and d). They were clearly aligned around the edges, as well as on the flat face of the triangles, but not in direct contact with the nanoprisms. The small gap can be accounted for by the presence of the gelatin layer. The composites tended to aggregate on the TEM grid, but linear arrangements of QDs around nanoprisms were visible even in these clusters. Unfortunately, the short separation distance between the two types of materials, only 1 to 2 nm, resulted in complete quenching of QDs.

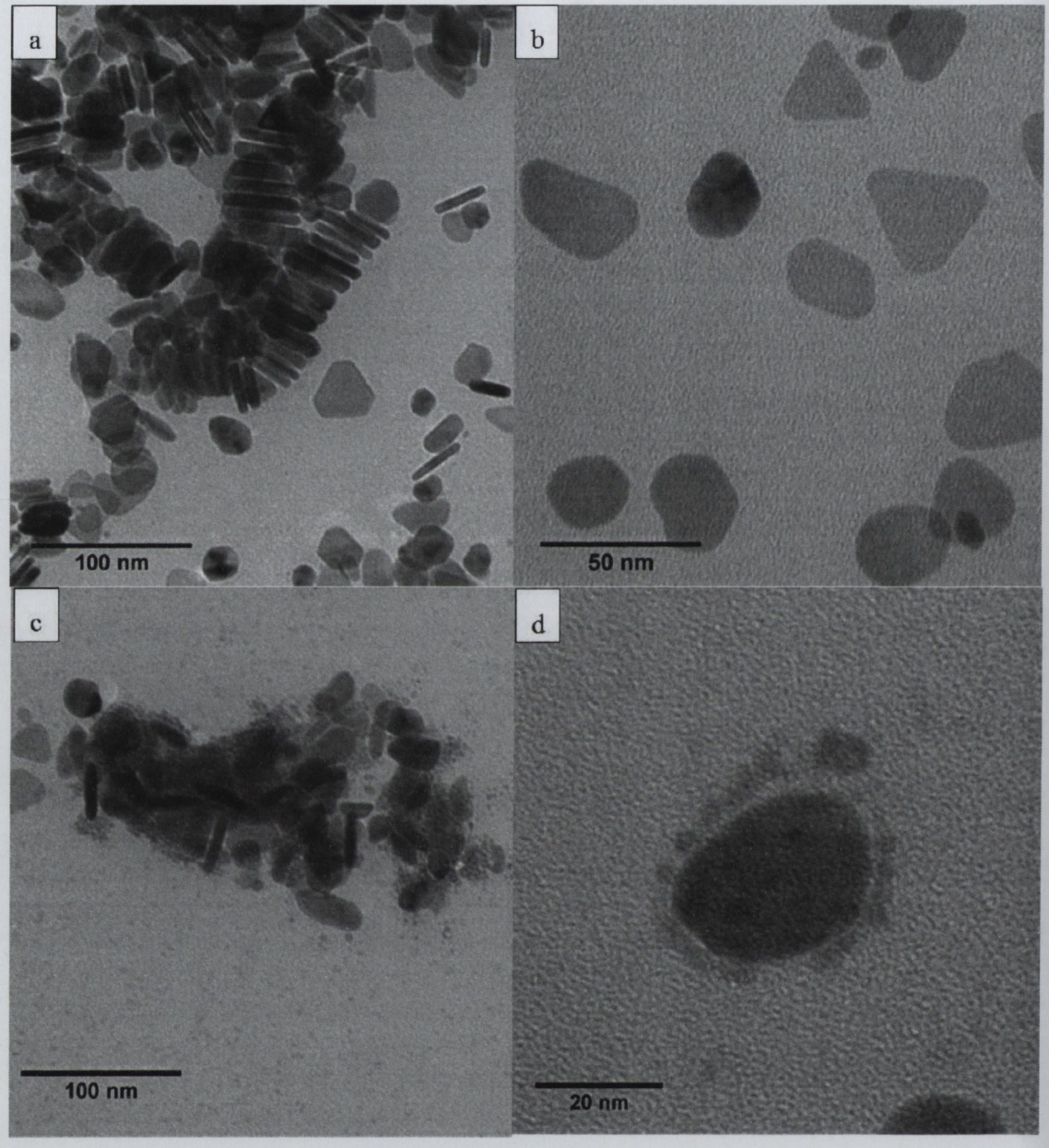

Figure 4.40 TEM images of initial silver nanoprisms (a), gelatin-coated silver nanoprisms (b) and QD-gelatin silver nanoprisms (c,d)

4.6.2 Drug-loaded, functionalised, gelatin-coated gold-silver nanoboxes

Based on the model we developed by trapping QDs in a gelatin shell around silver nanoprisms, the same approach was used to create targeted drug delivery vehicles. In chapter 3, we demonstrated that gold-silver nanoboxes were well internalised by epithelial cancer cells and that they exhibited very low cytotoxicity. They were therefore selected as the core material for the new nanocomposites. In order to induce toxicity towards cancer cells, the drug selected for incorporation was Paclitaxel (PCTX), a mitotic inhibitor used in current chemotherapy. Folic acid (FA) was chosen as a targeting element aimed at increasing the nanocomposite uptake by cancer cells over-expressing folate receptors. The chemical structures of paclitaxel and folic acid are displayed in Figure 4.41.

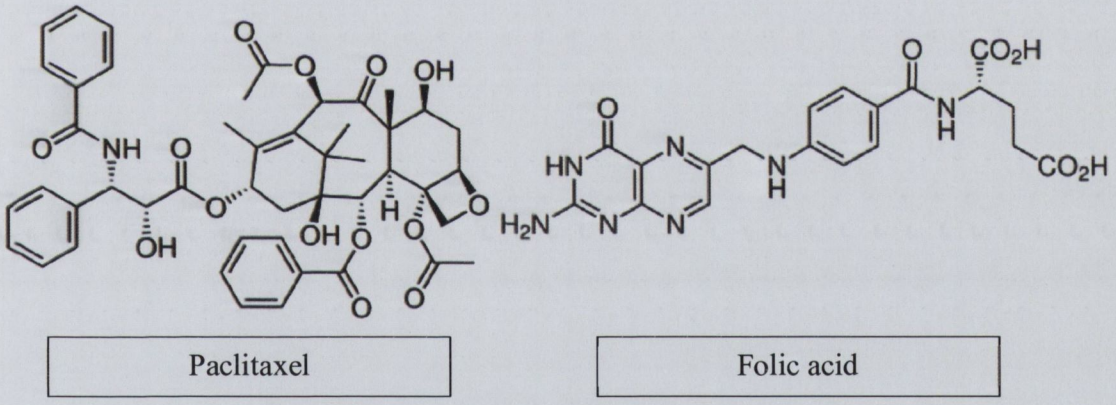

Figure 4.41 Chemical structures of paclitaxel and folic acid

The same procedure as described in the previous section was used to produce gelatin-coated gold-silver nanoboxes (AuAgNB-gel) and paclitaxel-loaded gelatin-coated gold-silver nanoboxes (AuAgNB-gel-PCTX). A third type of materials, AuAgNB-gel-PCTX-FA, was produced by binding FA to the gelatin layer following the method developed in section 4.3. Figure 4.42 provides a schematic representation of the three types of composites thusly prepared.

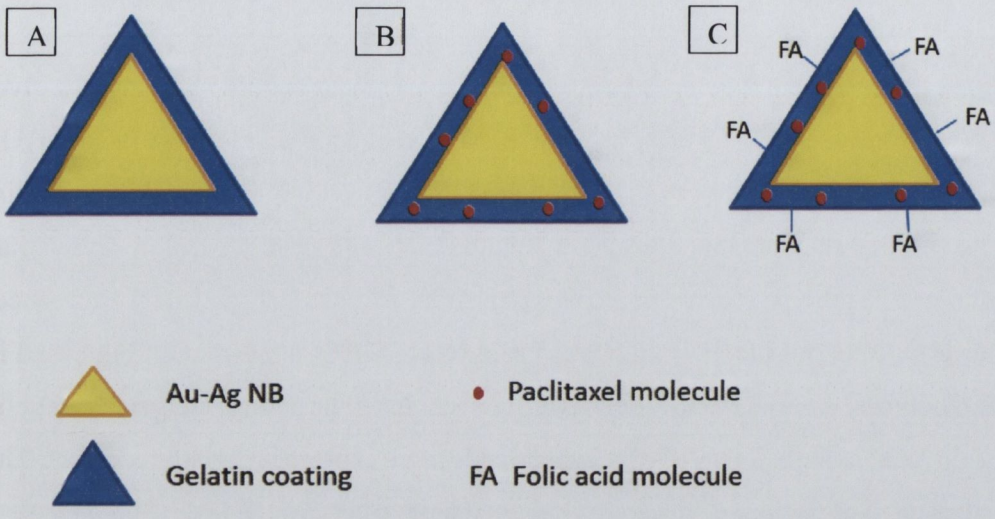

Figure 4.42 Schematic representation of (A) AuAgNB-gel, (B) AuAgNB-gel-PCTX and (C) AuAgNB-gel-PCTX-FA

The resulting materials were characterised by DLS measurements and compared to that of the original AuAgNB; the graphs are presented in Figure 4.43 and the values in Table 4.4.

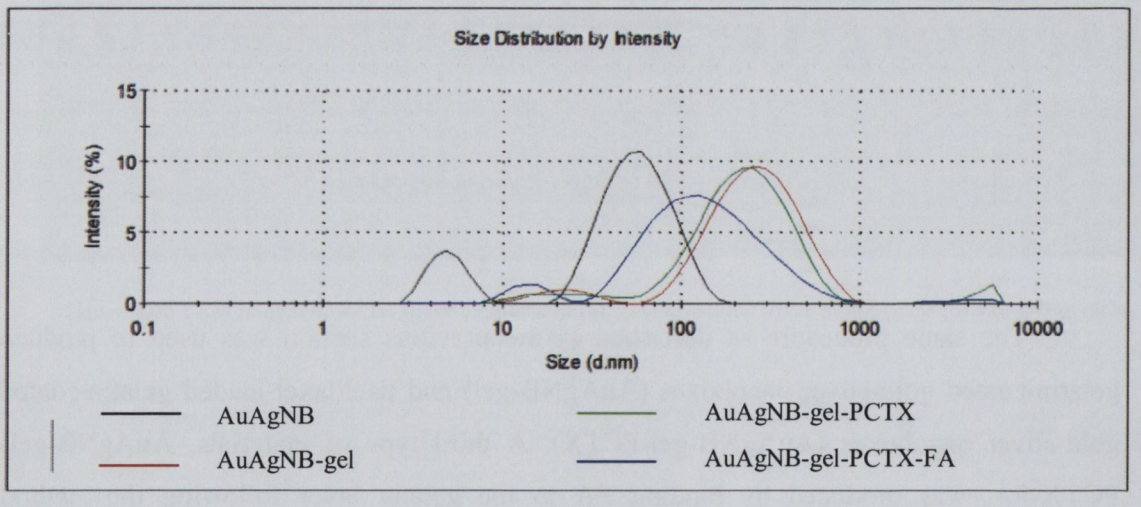

Figure 4.43 DLS measurements of AuAgNB, AuAgNB-gel, AuAgNB-gel-PCTX and AuAgNB-gel-PCTX-FA

Table 4.4 DLS and Zeta potential measurements of AuAgNB, AuAgNB-gel, AuAgNB-gel-PCTX and AuAgNB-gel-PCTX-FA

Sample	Height (nm)	Thickness (nm)	PdI
AuAgNB	61 (+/- 2)	5 (+/- 0.1)	0.606
AuAgNB-gel	290 (+/- 13)	28 (+/- 6)	0.476
AuAgNB-gel-PCTX	277 (+/- 22)	30 (+/- 7)	0.486
AuAgNB-gel-PCTX-FA	166 (+/- 12)	17 (+/- 2)	0.477

DLS measurements exhibited the two peaks characteristic of flat structures. The peak in larger sizes corresponds to the height of the flat triangular face, while the smaller one arises from the thickness of the nanobox. For unmodified gold-silver nanoboxes, the hydrodynamic dimensions matched the core dimensions measured on TEM. It was indeed expected that the nanoboxes would bear very few stabilisers and citrate molecules are very small compared to the particles. After coating with gelatin, the hydrodynamic dimensions increased by 4.8 times on average. The addition of Paclitaxel in the gelatin shell resulted in a very small decrease in the average hydrodynamic dimensions. This can be attributed to the mostly hydrophobic nature of the paclitaxel molecules which may be partially exposed thus reducing the Van der Waals interactions with water molecules. This is also reflected in the slightly lower zeta potential. Covalent bonding of folic acid to the gelatin shell *via* EDC activation resulted in a much stronger reduction in the hydrodynamic dimensions to 2.7 the initial ones (on average). This is consistent with what was previously observed on EDC coupling of FA to QDs. EDC has a side effect of crosslinking the gelatin molecules thus making it more compact.

On close examination in HRTEM, it was possible to distinguish patches of gelatin on and around the nanoboxes, as illustrated in Figure 4.44. The images suggested that the synthesis did not produce a full gelatin shell; it should however be noted that a thin layer of gelatin would not be dense enough to be visible in TEM. STEM imaging revealed the presence of organic materials burning under the beam and creating a blur as seen in Figure 4.45. This observation, together with DLS measurements, supported the presence of a substantial gelatin layer on the nanoboxes.

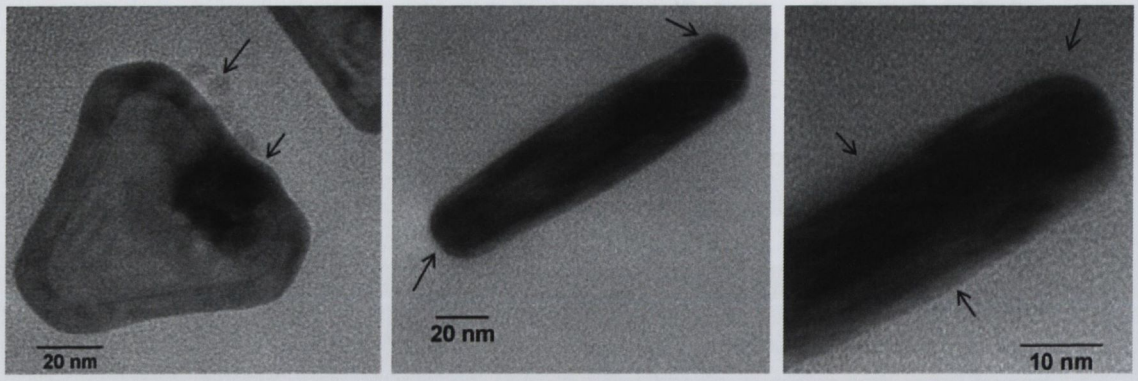

Figure 4.44 HRTEM images of AuAgNB-gel. Arrows point to patches of gelatin.

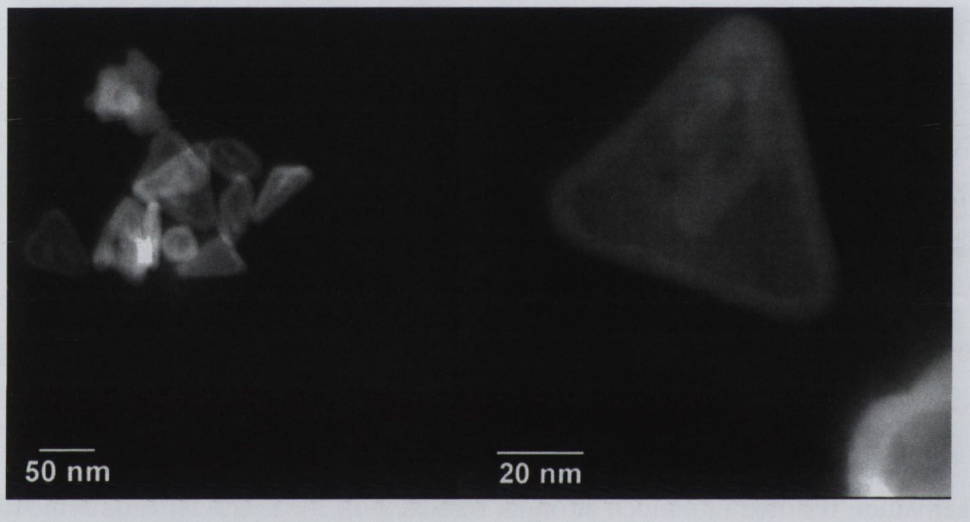

Figure 4.45 STEM images of AuAgNB-gel

As expected, AuAgNB-gel-PCTX and AuAgNB-gel-PCTX-FA did not present any morphological difference visible in TEM or STEM, with presence of organic materials similar to that of AuAgNB-gel. Figure 4.46 displays sample images illustrating these observations.

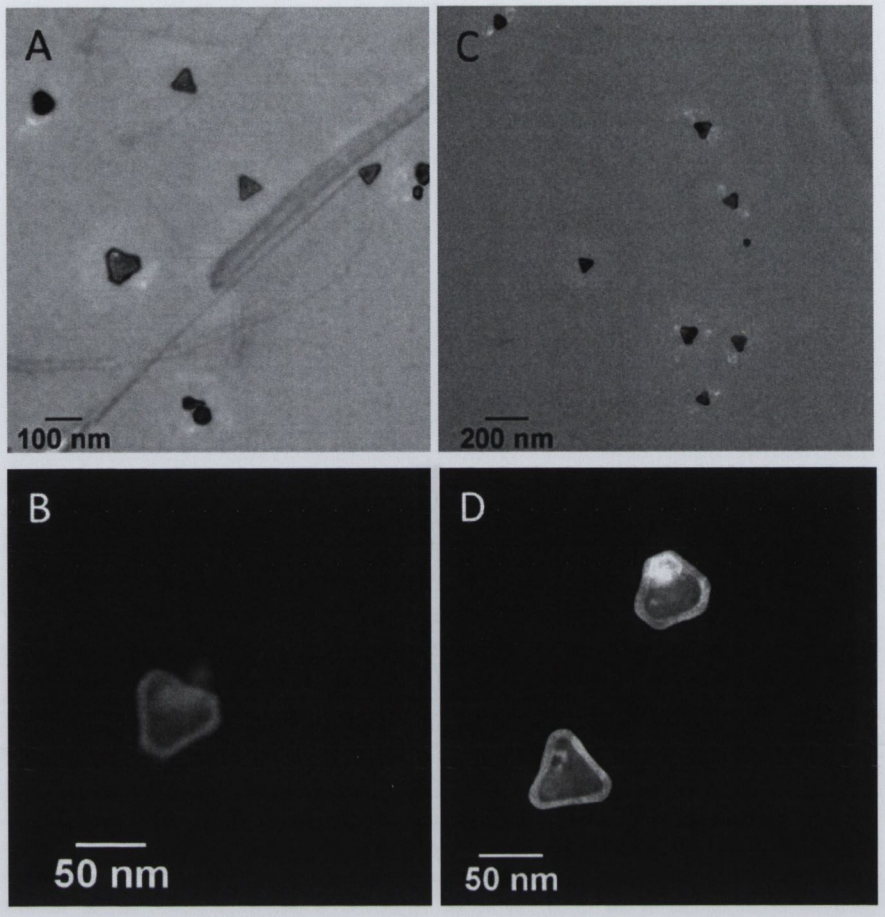

Figure 4.46 (A, C) TEM and (B, D) STEM images of (A, B) AuAgNB-gel-PCTX and (C, D) AuAgNB-gel-PCTX-FA

It could be concluded, from the characterisation described above, that we successfully produced three different types of nanocomposites based on gold-silver nanoboxes. The samples have been prepared for future *in vitro* biological testing of these materials in order to assess the presence and bioavailability of folic acid and paclitaxel.

4.7 Conclusions

Gelatin was used to synthesise a series of nano-composites with CdTe QDs and silver nanoprisms which have been characterised in terms of their cellular behaviour and structural features. Previously developed "Jelly Dots" were used as the basis for folic-acid functionalised QDs. Two cell lines were studied when treated with TGA-capped CdTe QDs, Jelly Dots and Folic acid-modified QDs. The gelatin coating reduced the overall cellular uptake of QDs but also improved their biocompatibility. Folic acid-modified QDs

exhibited increased levels of uptake by cells over-expressing folate receptors, a useful property for the development of potential diagnostics tools and targeted therapeutics.
Another approach towards the formation of QD loaded gelatin nanoparticles was developed and investigated. Despite its success in terms of production of new composites, it was however not found to provide any further clear advantages over the previously optimised method.

Further adopting this approach to demonstrate its utility in the preparation of a variety of nanocomposite materials, silver nanoprisms were successfully embedded in gelatin and subsequently decorated with QDs. This approach can be potentially used to create drug carriers. Gelatin has thus been demonstrated to be a versatile and useful material in the coating of nanoparticles, providing a biocompatible shell, which has the further advantages of ease of further surface functionalisation as well as a low melting point, providing enormous potential in the area of triggered drug delivery agents. Further to this, the use of QDs which can be specifically targeted to cancer cells and are well-known to be cytotoxic, as core agents in such composites will further allow the fabrication of triggered therapeutic agents.

References

[1] J. E. Eastoe, *Biochem J.* **1955**, *61*, 589-600.

[2] F. Badii, N. K. Howell, *Food Hydrocolloids* **2006**, *20*, 630-640.

[3] K. L. C. J. Coester, H. Von Briesen, J. Kreuter, *Journal of Microencapsulation* **2000**, *17*, 187-193.

[4] K. Zwiorek, *Gelatin Nanoparticles as Delivery System for Nucleotide-Based Drugs*, Hut, **2006**.

[5] N. Adhirajan, N. Shanmugasundaram, M. Babu, *Journal of Microencapsulation* **2007**, *24*, 659-671.

[6] J. Drbohlavova, V. Adam, R. Kizek, J. Hubalek, *International Journal of Molecular Sciences* **2009**, *10*, 656-673.

[7] A. Rakovich, D. Savateeva, T. Rakovich, J. F. Donegan, Y. P. Rakovich, V. Kelly, V. Lesnyak, A. Eychmller, *Nanoscale Research Letters* **2010**, *5*, 753-760.

[8] S. J. Cho, D. Maysinger, M. Jain, B. Roder, S. Hackbarth, F. M. Winnik, *Langmuir* **2007**, *23*, 1974-1980.

[9] T. S. Hauck, R. E. Anderson, H. C. Fischer, S. Newbigging, W. C. W. Chan, *Small* **2010**, *6*, 138-144.

[10] S. J. Byrne, Y. Williams, A. Davies, S. A. Corr, A. Rakovich, Y. K. Gun'ko, Y. P. Rakovich, J. F. Donegan, Y. Volkov, *Small* **2007**, *3*, 1152-1156.

[11] B. Prasad, N. Nikolskaya, D. Connolly, T. Smith, S. Byrne, V. Gerard, Y. Gun'ko, Y. Rochev, *Journal of Nanobiotechnology* **2010**, *8*, 7.

[12] B. R. Prasad, G. Mullins, N. Nikolskaya, D. Connolly, T. J. Smith, V. A. Gérard, S. J. Byrne, G.-L. Davies, Y. K. Gun'ko, Y. Rochev, *Journal of Nanobiotechnology* **2012**, *10*, 4.

[13] M. Lucock, *Molecular Genetics and Metabolism* **2000**, *71*, 121-138.

[14] C. P. Leamon, J. A. Reddy, *Advanced Drug Delivery Reviews* **2004**, *56*, 1127-1141.

[15] N. Gaponik, D. V. Talapin, A. L. Rogach, K. Hoppe, E. V. Shevchenko, A. Kornowski, A. Eychmuller, H. Weller, *The Journal of Physical Chemistry B* **2002**, *106*, 7177-7185.

[16] H. Zhang, Y. Liu, C. Wang, J. Zhang, H. Sun, M. Li, B. Yang, *ChemPhysChem* **2008**, *9*, 1309-1316.

[17] N. Gaponik, D. V. Talapin, A. L. Rogach, K. Hoppe, E. V. Shevchenko, A. Kornowski, A. Eychmuller, H. Weller, *The Journal of Physical Chemistry B* **2002**, *106*, 7177-7185.

[18] S. Byrne, S. Corr, T. Rakovich, Y. Gun'ko, Y. Rakovich, J. Donegan, S. Mitchell, Y. Volkov, *Journal of Materials Chemistry* **2006**, *16*, 2896 - 2902.

[19] V. A. Gérard, Y. K. Gun'ko, B. R. Prasad, Y. Rochev, *Vol. 906* (Ed.: M. Soloviev), Humana Press, **2012**, pp. 275-281.

[20] G. Paradossi, F. Cavalieri, E. Chiessi, C. Spagnoli, M. K. Cowman, *Journal of Materials Science: Materials in Medicine* **2003**, *14*, 687-691.

[21] K. Susumu, B. C. Mei, H. Mattoussi, *Nature Protocols* **2009**, *4*, 424-436.

[22] A. R. Vancha, S. Govindaraju, K. V. L. Parsa, M. Jasti, M. Gonzales-Garcia, R. P. Ballestero, *BMC Biotechnology* **2004**, *4*.

[23] M. S. Cartiera, K. M. Johnson, V. Rajendran, M. J. Caplan, W. M. Saltzman, *Biomaterials* **2009**, *30*, 2790-2798.

[24] R. Suraiya, A. N.-R. Walter, M. T. Eva, A. Paul, B. G. Murray, *Cancer* **1974**, *33*, 1027-1033.

[25] A. Jordan, R. Scholz, P. Wust, H. Schirra, S. Thomas, H. Schmidt, R. Felix, *Journal of Magnetism and Magnetic Materials* **1999**, *194*, 185-196.

[26] J. K. Jaiswal, H. Mattoussi, J. M. Mauro, S. M. Simon, *Nature Biotechnology* **2003**, *21*, 47-51.

[27] Z. Yu, M. Lan, W. Pei-Nan, L. Si-Jia, C. Ji-Yao, G. Jia, Y. Wu-Li, W. Chang-Chun, *Small* **2008**, *4*, 777-780.

[28] B. R. Prasad, E. O'Connell, T. J. Smith, V. A. Gérard, Y. K. Gun'ko, Y. Rochev, *Vol. 906* (Ed.: M. Soloviev), Humana Press, **2012**, pp. 171-183.

[29] L. B. Zimmerhackl, F. Momm, G. Wiegele, M. Brandis, *American Journal of Physiology - Renal Physiology* **1998**, *275*, F143-F153.

[30] S. Byrne, Y. Williams, A. Davies, S. Corr, A. Rakovich, Y. Gun'ko, Y. Rakovich, J. Donegan, Y. Volkov, *Small* **2007**, *3*, 1152 - 1156.

[31] J.-H. Kim, H. H. Jang, S.-M. Ryou, S. Kim, J. Bae, K. Lee, M. S. Han, *Chemical Communications* **2010**, *46*, 4151-4153.

[32] K. G. Li, J. T. Chen, S. S. Bai, X. Wen, S. Y. Song, Q. Yu, J. Li, Y. Q. Wang, *Toxicology in Vitro* **2009**, *23*, 1007-1013.

[33] R. S. Zeng, T. T. Zhang, J. C. Liu, S. Hu, Q. Wan, X. M. Liu, Z. W. Peng, B. S. Zou, *Nanotechnology* **2009**, *20*, 8.

[34] J. E. Schroeder, I. Shweky, H. Shmeeda, U. Banin, A. Gabizon, *Journal of Controlled Release* **2007**, *124*, 28-34.

[35] D. J. Bharali, D. W. Lucey, H. Jayakumar, H. E. Pudavar, P. N. Prasad, *Journal of the American Chemical Society* **2005**, *127*, 11364-11371.

[36] Y. Zhang, N. Huang, *Journal of Biomedical Materials Research Part B-Applied Biomaterials* **2006**, *76B*, 161-168.

[37] V. Gérard, C. Maguire, D. Bazou, Y. Gun'ko, *Journal of Nanobiotechnology* **2011**, *9*, 50.

[38] M. M. Doucette, V. L. Stevens, *J. Nutr.* **2001**, *131*, 2819-2825.

[39] R. A. Sperling, W. J. Parak, *Philosophical Transactions of the Royal Society A: Mathematical, Physical and Engineering Sciences* **2010**, *368*, 1333-1383.

[40] I. L. Medintz, H. T. Uyeda, E. R. Goldman, H. Mattoussi, *Nat Mater* **2005**, *4*, 435-446.

[41] A. R. Clapp, E. R. Goldman, H. Mattoussi, *Nature Protocols* **2006**, *1*, 1258-1266.

[42] M. Jahanshahi, Z. Babaei, *African Journal of Biotechnology* **2008**, *7*, 4926-4934.

[43] H.-C. Liang, W.-H. Chang, H.-F. Liang, M.-H. Lee, H.-W. Sung, *Journal of Applied Polymer Science* **2004**, *91*, 4017-4026.

[44] S. Neri, E. Mariani, A. Meneghetti, L. Cattini, A. Facchini, *Clinical and Diagnostic Laboratory Immunology* **2001**, *8*, 1131-1135.

[45] M. Bottrill, M. Green, *Chemical Communications* **2011**, *47*, 7039-7050.

[46] J. Lovrić, H. S. Bazzi, Y. Cuie, G. R. A. Fortin, F. M. Winnik, D. Maysinger, *Journal of Molecular Medicine* **2005**, *83*, 377-385.

[47] W. K. Moon, Y. Lin, T. O'Loughlin, Y. Tang, D.-E. Kim, R. Weissleder, C.-H. Tung, *Bioconjugate Chemistry* **2003**, *14*, 539-545.

[48] D. Brough, P. J. Tyrrell, S. M. Allan, *Trends in Pharmacological Sciences* **2011**, *32*, 617-622.

[49] N. A. Thornberry, H. G. Bull, J. R. Calaycay, K. T. Chapman, A. D. Howard, M. J. Kostura, D. K. Miller, S. M. Molineaux, J. R. Weidner, J. Aunins, et al., *Nature* **1992**, *356*, 768-774.

[50] Santa Cruz Biotechnology Inc., *ASC (F-9): sc-271054 Datasheet*, **2007**.

[51] B. D. Chithrani, W. C. W. Chan, *Nano Letters* **2007**, *7*, 1542-1550.

[52] S. Azarmi, Y. Huang, H. Chen, S. McQuarrie, D. Abrams, W. Roa, W. H. Finlay, G. G. Miller, R. Löbenberg, *Journal of pharmacy & pharmaceutical sciences* **2006**, *9*, 124-132.

[53] K. Zwiorek, *Doctoral dissertation*, Ludwig-Maximilians-Universität München (Munich, Germany), **2006**.

[54] G. L. Davies, A. Barry, Y. K. Gun'ko, *Chemical Physics Letters* **2009**, *468*, 239-244.

Chapter 5

Oligonucleotide-Nanoparticle Composites

5.1 Introduction

Nucleotides are the building blocks of nucleic acids and consist of a nitrogeneous base (nucleobase), a sugar (either ribose or 2-deoxyribose) and a phosphate group. Short sequences of these are called oligonucleotides and can be synthesised from DNA or RNA with virtually any desired sequence and terminal functional group.[1] They have been widely used in probing applications and especially diagnostics, since they can be made complementary to a target sequence.[3] Most applications require for the oligonucleotide, acting as the recognition element, to be coupled to a detection element which translates the binding event into a measurable signal. For instance, colorimetric biosensors have been developed based on the aggregation of gold nanoparticles upon nucleic acid recognition.[4]

Oligonucleotides have also been proven to be very useful for forming assemblies of nanoparticles in a highly controlled way, with a great degree of complexity. For instance, chiral assemblies were obtained using gold nanoparticles of four different sizes.[5] Very few studies, however, consider the oligonucleotide-nanoparticle conjugates as materials of their own, with new intrinsic properties.

Metal nanoparticles (NPs) have raised much interest in recent years due to their unique optical and electronic properties. Functionalising their surface with biomolecules has lead the way for applications in fields as various as biosensing,[6] drug delivery[7] and Surface Enhanced Raman Spectroscopy (SERS).[8]

Chirality is not a property usually associated with metal NPs; however it is very common when looking at biomolecules. Therefore, induction or enhancement of a Circular Dichroism (CD) signal using metal NPs could be a new tool for highly responsive sensing. While naturally occurring biomolecules demonstrate a very high degree of homogeneity in a macroscopic ensemble and therefore produce strong and consistent CD signals (mostly in the UV range), creating macroscopically chiral nanocrystals is very challenging. Although

the atoms forming nanocrystals are most likely to assemble in a non-symmetrical manner, it is nearly impossible to control all of their positions and therefore to ensure that all nanocrystals exhibit the same chirality. There is consequently no overall CD signal emerging from a nanocrystal suspension.

So far, new CD signals in the visible range in metal nanostructures were achieved, mainly for metal nano-clusters with a relatively small number of atoms and with the help of chiral molecules.[9-13] An example is Au clusters (~ few hundreds atoms) synthesized on DNA templates and giving new plasmonic CD lines.[10] In the present work we aimed to create an artificial chirality from an interaction between well-defined nanoscale building blocks. It was recently shown that Coulomb interactions between nanoscale objects are theoretically[14] able to produce new plasmonic CD lines in the visible range. Rather than trying to create a chiral arrangement of single atoms, one can create an assembly of interacting chiral and non-chiral nanoscale blocks, involving metal nanocrystals and chiral oligonucleotide molecules.

Gold and silver nanoparticles, on the other hand, exhibit surface plasmon resonance which results in local electromagnetic field enhancement. This property has been successfully used to enhance the luminescence of variety of fluorophores.[15-17] It is believed that the localised surface plasmon excitation results in the confinement of light and consequently in large local optical near-field enhancements. This, however, only happens if the fluorescent species is close enough to be affected by the plasmonic field, but not so close that it is quenched through non-radiative energy transfer. The main conditions for observing plasmon-enhanced luminescence are therefore a controlled distance between the fluorophore and the plasmonic species and a spectral overlap of emission and plasmon.

The conjugation of oligonucleotides to Quantum Dots (QDs) has been much less reported than to gold nanoparticles despite the multiple ways this can be achieved. Thiol-modified oligonucleotides may be bound directly to the surface of QDs through ligand exchange[18]. Alternatively, they may be covalently coupled through another functional group to the ligands, to an additional shell, or to a polymer coating.[19] Recently, another method has been developed to co-stabilise QDs with thiolated oligonucleotides added *in situ*.[20] Most applications of these conjugates involve the detection of a target DNA sequence through quenching or optical coding[21].

Fluorescent Resonant Energy Transfer (FRET) has been observed in multiple QD-oligo systems[20] although not in cell cultures. Nanosensors based on the FRET mechanism have been demonstrated,[22-23] and it has been shown that FRET can be used for colour tuning or the generation of white-light-emitting structures.[24-25] Furthermore, light-harvesting structures have been designed based on FRET,[26-27] which could be implemented as part of detectors or photovoltaic structures.

The aim of the work presented in this chapter is to prepare new nano-assemblies using combinations of QDs, metal nanoparticles and oligonucleotides and to investigate their physical and optical properties. Different compositions were studied in order to "mix and match" the fundamental properties of each of the components:

- Oligonucleotides are chiral and are able to bind to their complementary sequence. That hybridisation is reversible and can be easily undone by moderate heat;
- Metal nanoparticles exhibit surface plasmon resonance (SPR) which translates into strong enhancement of electromagnetic fields, especially in aggregates;
- QDs are intrinsically luminescent, and their quantum efficiency is strongly influenced by the environment. PL emission may either be quenched or enhanced by energy transfer processes.

The oligonucleotide (oligo) sequences used in this work were as follows:

- oligo 1: 5' NH2- A10 TAG GAA TAG TTA TCA (Tps6) 3'
- oligo 2: 5' NH2 - A10 TGA TAA CTA TTC CTA (Tps6) 3'
- oligo 3.1: 3'-Tps6-ACT.ATT.GAT.AAG.GATps6-5'
- oligo 3.2: Tps6-ACT.ATT.GAT.AAG.GAT-5'
- oligo 3.comp: 5'-TGA.TAA.CTA.TCC.CTA-3'

Tps6 refers to a T6 phosphorothioate tail or six thymine-based nucleotides where one oxygen atom was replaced with a sulphur atom in the phosphate group.

5.2 Circular dichroism in oligonucleotide-metal nanoparticle conjugates

It was reported in the literature that plasmonic species may induce an enhancement of circular dichroism (CD) from chiral molecules located on their surface, as well as a new signal in the plasmon resonance wavelength range.[28] Oligonucleotide-metal nanoparticle conjugates were considered an appropriate new system to investigate their CD signature.

To start with a most simple system, spherical gold NPs were conjugated to oligonucleotides *via* their 3' end T6 phosphorothioate groups. The conjugation of thiol-modified oligonucleotides to gold particles has been widely reported; however it usually involved a single terminal thiol group.[6, 29-32] Here, the affinity of the T6-phosphorothioate-modified oligonucleotide for gold NPs was assessed as a proof of concept before performing the conjugation with more highly shaped metal nanostructures. The UV-visible absorption spectra of bare and oligonucleotide-conjugated particles, displayed on Figure 5.1, showed a 7 nm red shift of the plasmon band, from 519 to 526 nm. This may be held as a first evidence of conjugation[6] as the red shift is induced by a modification of the dielectric constant of the environment and electronic interactions of the oligonucleotide molecules with the metal core.[33]

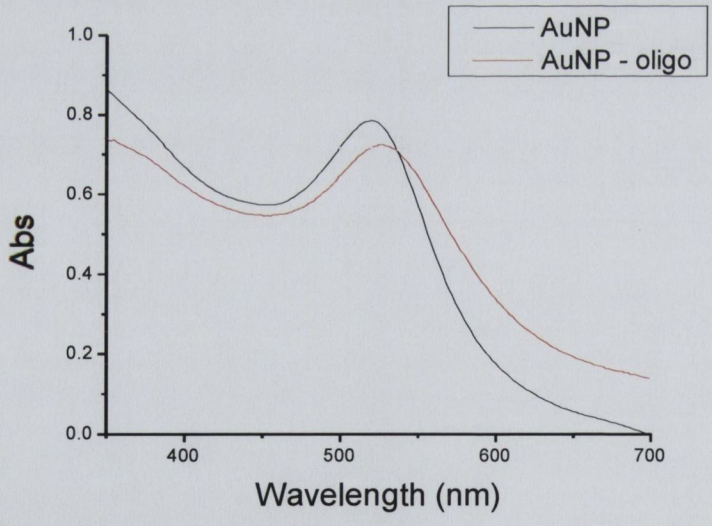

Figure 5.1 UV-visible absoprtion spectra of gold nanoparticles before and after oligonucleotide conjugation showing a 7 nm shift of the plasmon band

The presence of oligonucleotides on the particle surface resulted in an increase in the hydrodynamic radius which was assessed by Dynamic Light Scattering (DLS) measurements. Bare gold NPs had an average hydrodynamic diameter of 20 nm (+/- 0.5 nm), whereas for conjugated particles it was 70 nm (+/- 2 nm) as shown in Figure 5.2. The oligonucleotide-conjugated spherical gold NPs did not show any major morphological or size differences compared to the original particles as observed on Transmission Electron Microscope (TEM), displayed in Figure 5.3.

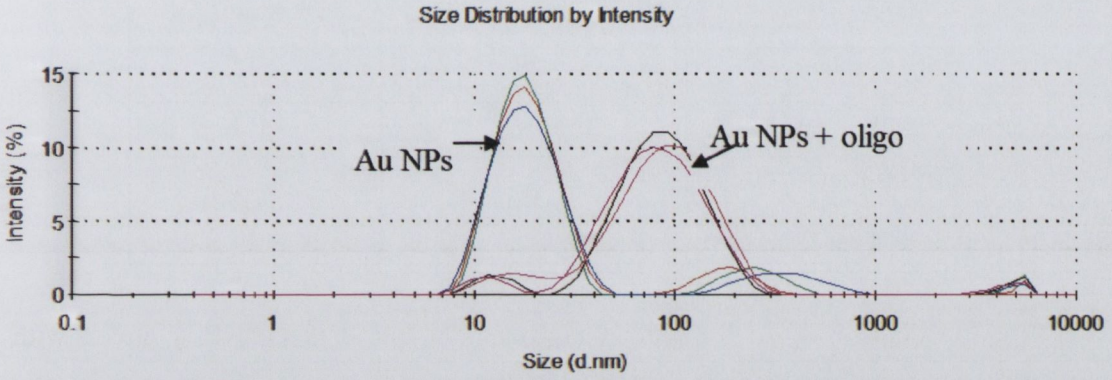

Figure 5.2 DLS measurements of bare and oligonucleotide-conjugated spherical gold nanoparticles

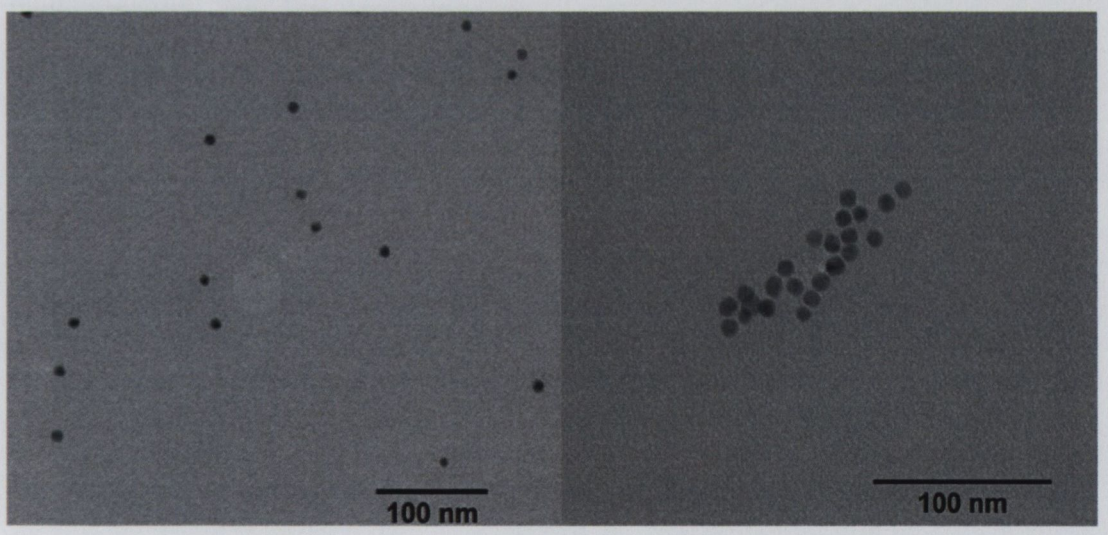

Figure 5.3 TEM images of bare (left) and oligonucleotide-conjugated (right) AuNPs

Table 5.1 presents the zeta potential measurements of gold nanoparticles before and after conjugation, as well as the free oligonucleotide. AuNP-oligo conjugates exhibited a smaller negative charge than either component on their own. This could be attributed to the replacement of several citrate molecules with one oligonucleotide, as well as the presence of the terminal amine which may reduce the overall negative charge. A zeta potential value between +30 and -30 mV means that the particles may be poorly stabilised and tend to aggregate.

Table 5.1 Zeta potential of gold nanoparticles, oligonucleotides and their conjugates

Sample	Zeta potential (mV)	Std deviation
AuNP	-29	2.15
oligonucleotide	-30	2.88
AuNP-oligonucleotide conjugate	-18	3.05

Recently Govorov *et al.* demonstrated that non-chiral metal NPs coupled with surrounding chiral molecules (such as oligonucleotides and proteins) could enhance the CD signals of the chiral molecules as well as induce new CD signals in the plasmon region.[14] The basis for the mechanism of this CD generation is that the chiral molecules (oligonucleotides) typically do not absorb at the plasmonic wavelength (around 520nm), but they are optically-active and rotate light at this wavelength. CD could thus be thought of as a potential technique to monitor the conjugation of oligonucleotides to gold NPs over time.

However, the results shown in Figure 5.4 indicated that gold NPs did not induce any significant change in the oligonucleotide CD signal when they were incubated together for up to four days with gradually increasing sodium chloride concentration. These conditions were found optimal for a high loading of oligonucleotides on the nanoparticles.[29] On the other hand, a strong signal appeared after centrifugation and washing of the conjugates. The process caused partial aggregation of the particles as revealed by a 5 nm further red-shift in the plasmon band and confirmed by TEM. This also explained the change in CD response as it was reported that larger particles and aggregates induced a stronger CD signal at the plasmon wavelength.[34]

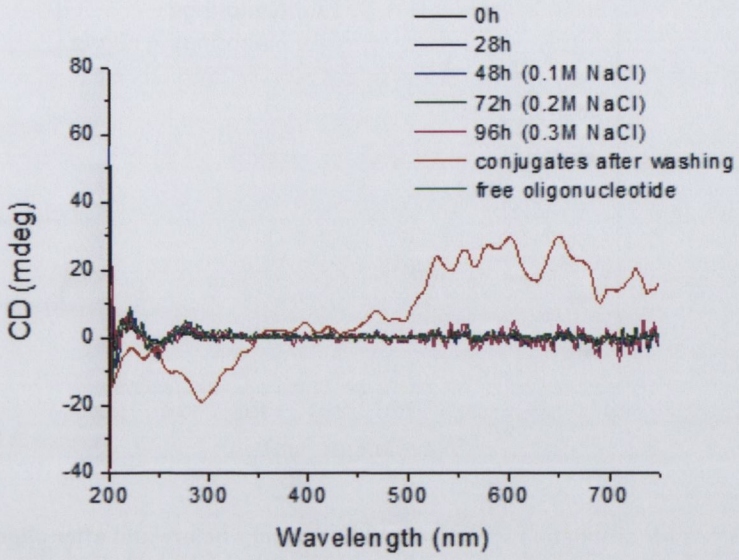

Figure 5.4 CD spectra of AuNPs incubated with oligonucleotides over time with increasing NaCl concentration, and after washing by centrifugation

It is believed that hot spots are created in plasmonic nanoparticles aggregates, giving rise to a huge enhancement of electric fields in inter-nanoparticle junctions. As chiral molecules get trapped in these hot spots and disperse circularly polarised light, this in turn is enhanced by the plasmonic field to produce an amplified CD in the plasmon region, or "plasmon-induced" CD signal.[14, 28, 35]

Using the same method as previously described to conjugate oligonucleotides to spherical gold NPs, 3'- phosphorothioate-modified oligonucleotides were bound to gold nanorings (NRs). The UV-Visible absorption spectrum (displayed on Figure 5.5) of oligonucleotide-conjugated AuNRs showed a 12 nm red shift associated with a broadening of the plasmon band compared to that of bare particles. The peak broadening was attributed to partial aggregation of the rings due to cross-linking of the oligonucleotides. The shift suggested effective conjugation exhibited by a modification of the dielectric constant of the surrounding medium as well as electronic interactions with the metal core.

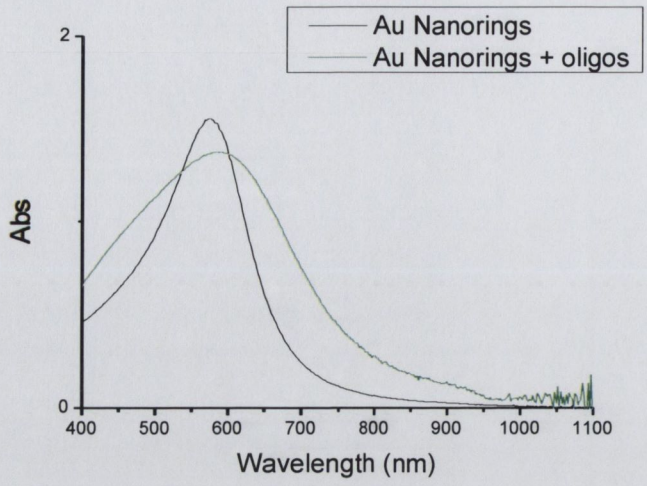

Figure 5.5 UV-visible absoprtion spectra of gold nanorings before and after oligonucleotide conjugation showing a 12 nm shift of the plasmon band

Similarly to spherical NPs, the TEM images (Figure 5.6) did not show any significant difference in size and morphology between the bare and the oligonucleotide-conjugated gold nanorings. They did however indicate a high degree of aggregation which was confirmed by DLS measurements, showing a large increase in the hydrodynamic radius (see Figure 5.7).

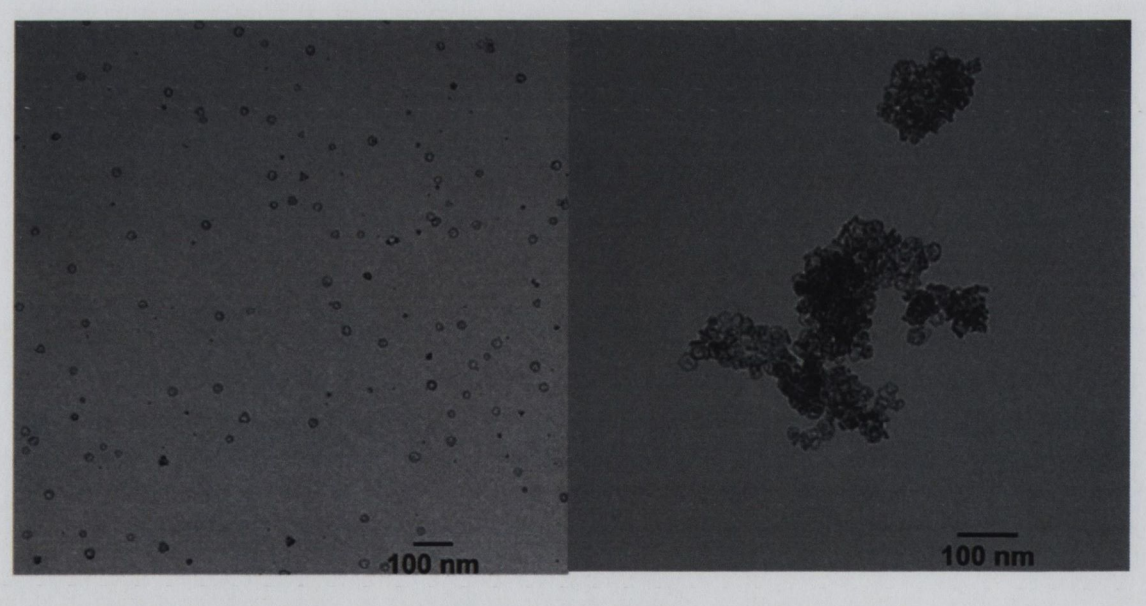

Figure 5.6 TEM images of bare (left) and oligonucleotide-conjugated (right) gold nanorings

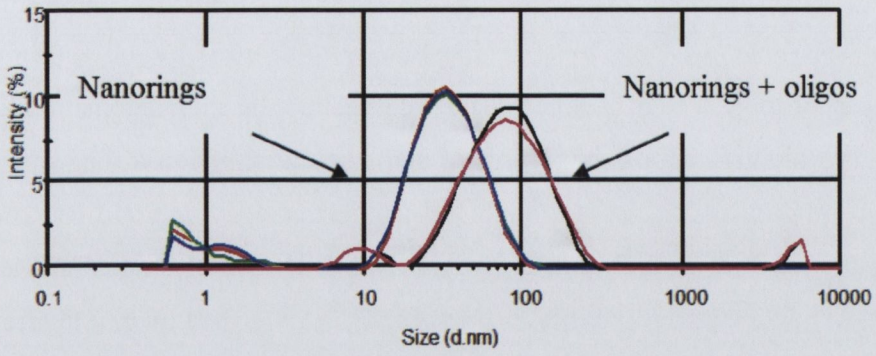

Figure 5.7 DLS measurements of bare and oligonucleotide-conjugated spherical gold nanorings

Finally, the CD response of the oligonucleotide-conjugated gold nanorings was monitored over time in the same way as for spherical particles and gave comparable results, as shown in Figure 5.8; no significant change in the response was observed until after washing when a CD signal appeared in the plasmon resonance region which was attributed to plasmon-induced response from the oligonucleotide molecules in aggregates.

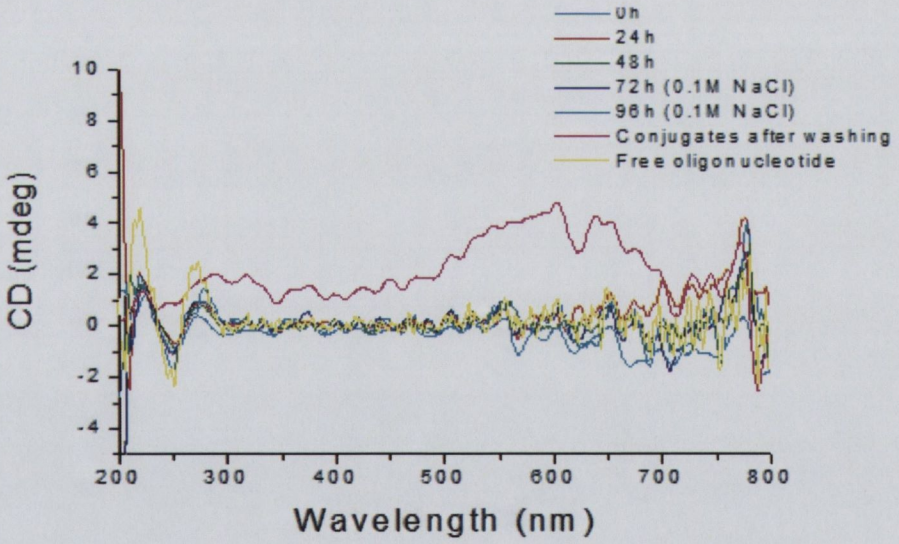

Figure 5.8 CD spectra of gold nanorings incubated with oligonucleotide over time with increasing concentrations of NaCl and after washing

The same method was employed again to immobilise oligonucleotides on gold nanoboxes (NB), and the resulting composites were characterised using the same techniques as for spherical NPs and NRs. The UV-visible absorption spectrum of

conjugated NBs exhibited a 5 nm red shift (from 527 to 532 nm) of the plasmon band characteristic of the presence of oligonucleotides on the surface of the particles. There was a further 9 nm shift after washing by centrifugation, accompanied by the appearance of lower energy absorption which accounted for aggregation of the nanoparticles. TEM (Figure 5.10) also highlighted a large degree of aggregation, although drying effects and aggregation on the grid tend to be very high for nanoboxes, even unmodified. The three aforementioned spectra are presented in Figure 5.9. A similar CD phenomenon was again observed, although with a lower intensity as with AuNP and NR, as shown in Figure 5.11.

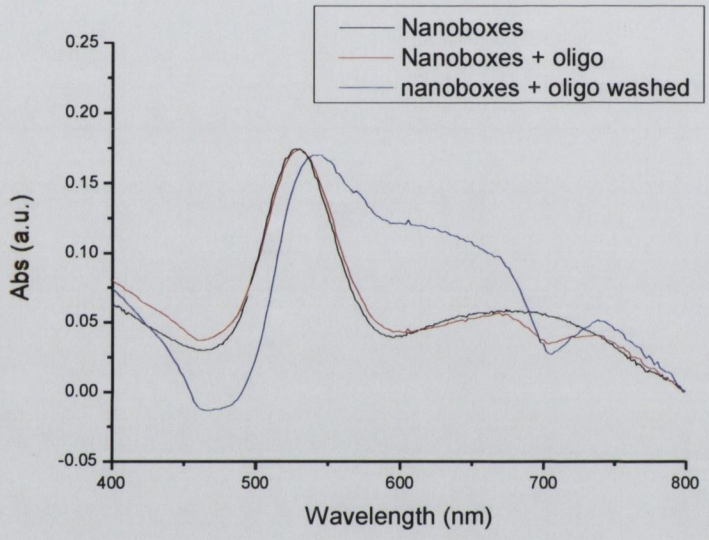

Figure 5.9 UV-visible absoprtion spectra of gold nanoboxes before and after oligonucleotide conjugation showing an initial 5 nm shift of the plasmon band

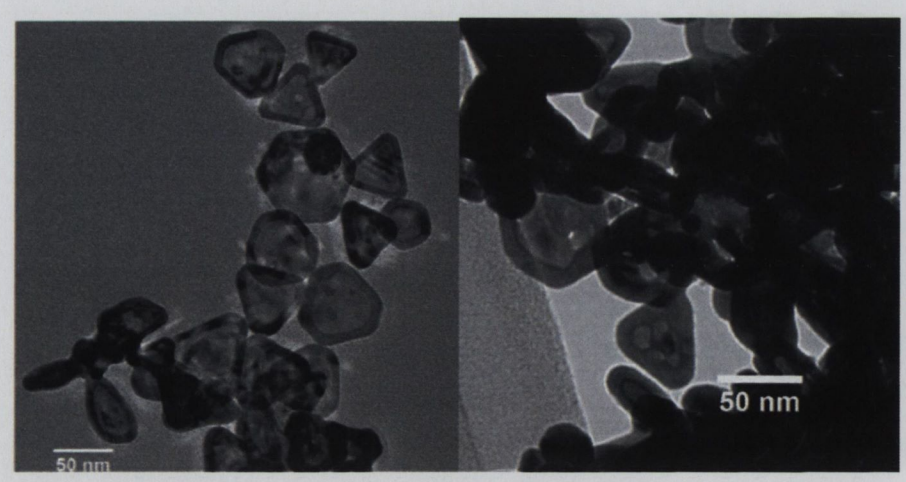

Figure 5.10 TEM images of bare (left) and oligonucleotide-conjugated (right) Au-Ag nanoboxes

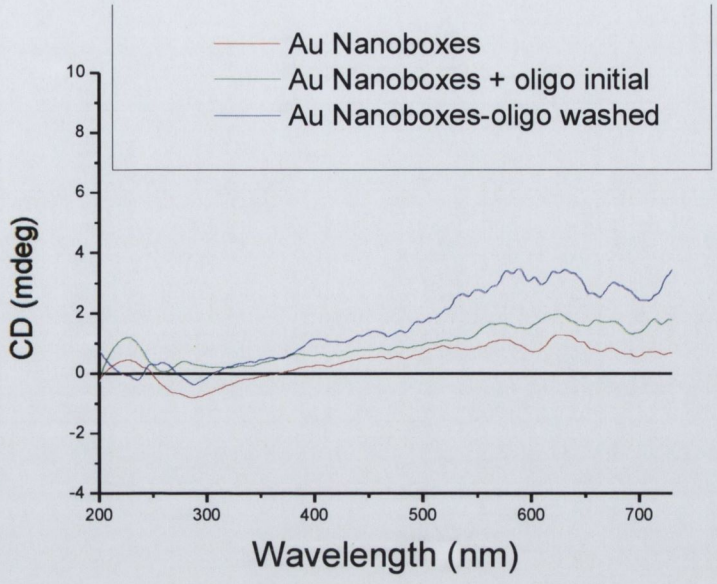

Figure 5.11 CD spectra of bare and oligonucleotide-conjugated Au nanoboxes, as well as after washing by centrifugation

An important observation in this study is that the plasmon-induced CD band (500-700 nm) appears for aggregated nanocrystals of very different geometry (NPs and nanorings). This observation is consistent with the Coulomb hot-spot mechanism since plasmonic hot spots will appear in both NP and nanoring systems. Looking more closely, CD bands of NPs and NRs look similar. They form a broad spectral structure starting at ~500 nm and ending at ~700 nm. As described above, we can interpret these CD structures as CD signals appearing due to Coulomb molecule-metal interaction in the plasmon hot-spot junctions between nanocrystals (NPs or NRs). These junctions (hot spots) contain greatly-enhanced electric fields that result in an enhancement of dynamic Coulomb interaction between chiral molecules and plasmons. Another remarkable observation, that is consistent with the Coulomb-interaction picture, is that the observed plasmon CD structures resemble very much calculated spectra of the electric-field enhancement in the hot spot between two or several Au spheres.[2, 36] The calculated spectra for enhancement factors have a broad structure spanning from 500 to 700nm as illustrated by Figure 5.12 from the literature.

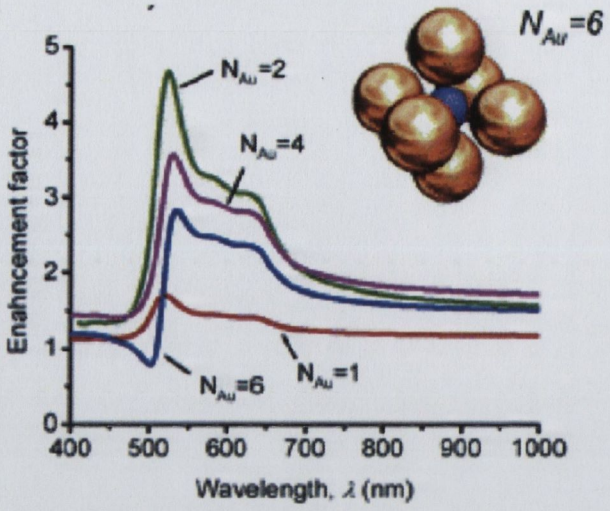

Figure 5.12 Calculated averaged plasmonic enhancement factors for the plasmonic hot spot in the centre of an assembly of N_{Au} nanoparticles. Inset: Geometry of one particular complex with $N_{NP} = 6$; the plasmonic hot spot is located in the centre of the system indicated as a blue sphere.[2]

Since it was demonstrated that the nanoparticle shape did not significantly influence the apparition of plasmon-induced CD, the rest of the study was only conducted on spherical gold nanoparticles. In order to verify that particle aggregation was not the only cause for the CD signal appearing after washing of the conjugates, aggregation in absence of chiral molecules was induced by increasing concentrations of sodium chloride. The size of thereby formed aggregates was monitored both by UV-Visible absorption spectroscopy and DLS (see Figure 5.13).

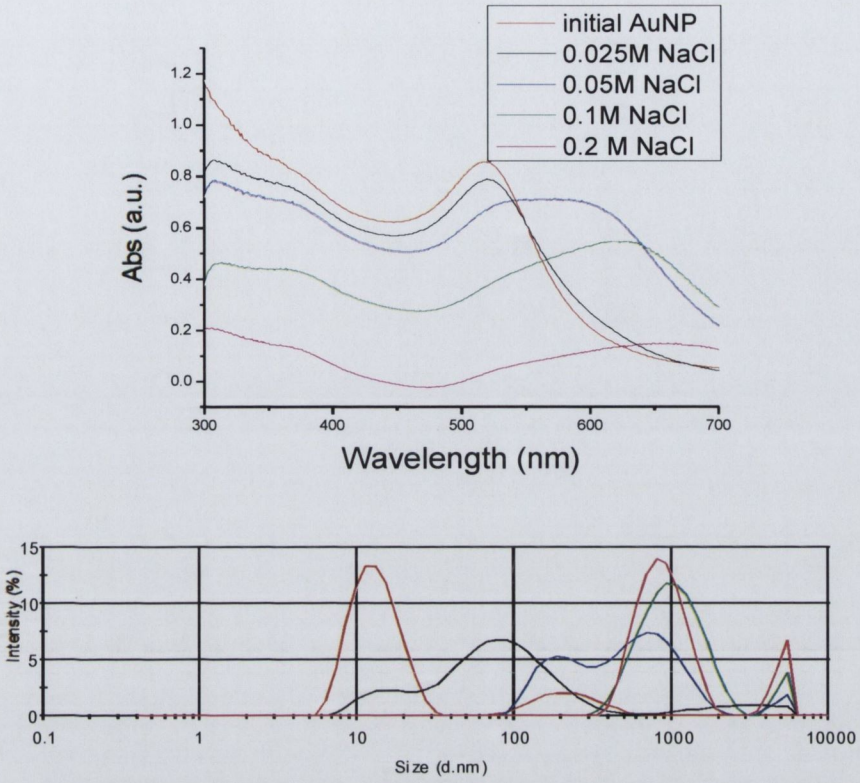

Figure 5.13 Monitoring of the size of aggregates induced by increasing concentrations of NaCl, by UV-Vis absorption spectroscopy (top) and DLS (bottom)

As shown in Figure 5.14, no plasmon induced signal was found for any of the pure aggregates, suggesting that they were not themselves chiral.[37] It could thus be assumed that the CD signal observed in the case of conjugates was related to the interaction between the chiral oligonucleotide molecules and the plasmonic particles.

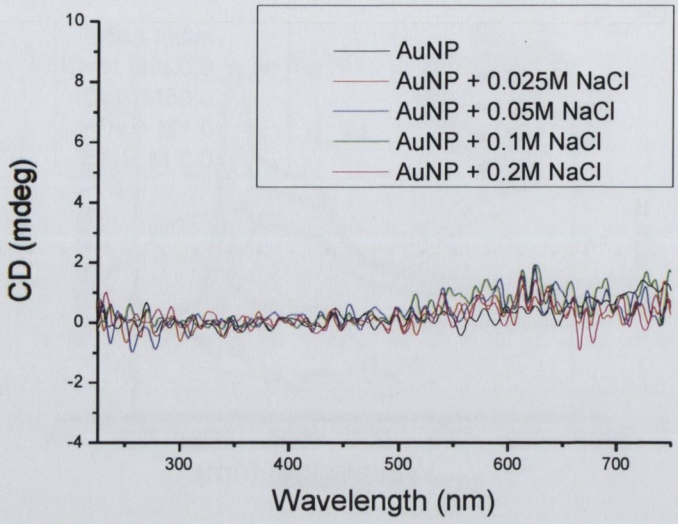

Figure 5.14 CD response of aggregated spherical gold NPs

Final proof of the crucial role of centrifugation was obtained by submitting the Au-NP conjugates to ultrasonic agitation in order to break the aggregates, which resulted in a reduced CD. It could be restored to its original level by centrifuging again as shown in Figure 5.15.

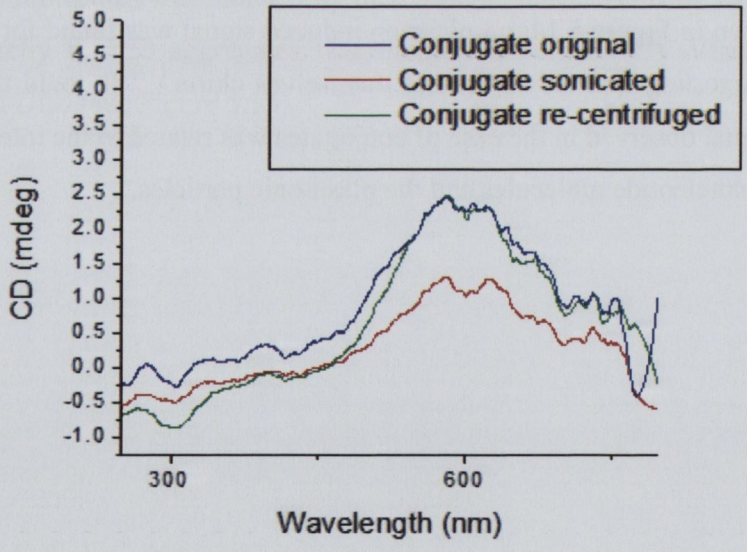

Figure 5.15 Effect of sonication and centrifugation on CD signal of oligonucleotide-AuNP conjugates

Finally, the oligo-AuNP conjugates were hybridised with the complementary sequence. This should have a double effect of changing the chiral species from single-stranded (ss)- to double-stranded (ds)-DNA as well as to double the overall DNA loading.

A further red-shift in the plasmon band, from 526 to 532 nm was observed of hybridisation of the complementary strand. After centrifugation it shifted again to 536 nm (530 nm for ss-conjugates). The CD signal however remained constant, depending only on the degree of aggregation as illustrated by Figure 5.16. CD of ds-conjugate was measured immediately after hybridisation, prior to any washing. The UV-visible absorption spectrum revealed the presence of oligonucleotide in high concentration, giving rise to a very strong CD in the UV. In the plasmon range, however, the signal was similar to that of de-aggregated ss-conjugates. Centrifugation and replacement of the supernatant with water eliminated excess oligonucleotides as confirmed by the CD spectra, and restored the signal to that of aggregated ss-conjugates.

Hybridisation of the complementary strand thus appeared to have no effect on the CD of conjugates which suggested that it was not sensitive to the amount loaded. It should be noted however that the DNA sequence used here was relatively short (25 bp) which may be the reason why it did not make any significant difference.

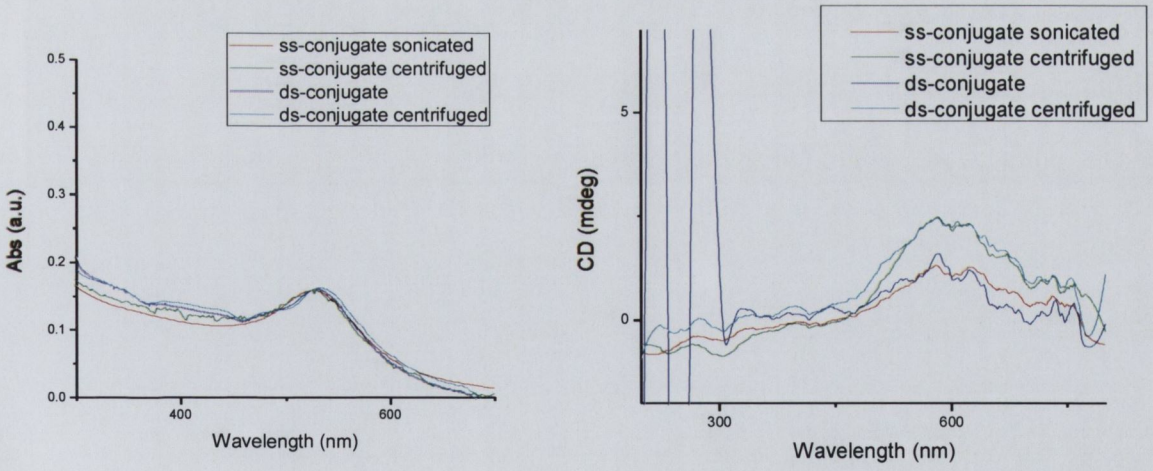

Figure 5.16 UV-Visible absorption (left) and CD (right) spectra of gold nanoparticles conjugated with ss- and ds-oligonucleotides, before after centrifugation-induced aggregation

In principle, CD signals at the plasmonic wavelength can appear due to chiral surface states created by a chiral adsorbate. This interpretation for a CD signal at the plasmon wavelength was suggested by Katz *et al.*[38] However, plasmonic CD signals in our system appeared only after aggregation which is thought to enhance the molecule-plasmon interactions. This suggests that the mechanism based on the Coulomb and electromagnetic interactions between chiral molecules and plasmons is a reasonable explanation for the observed plasmonic CD signals. Thus the new nanoconjugates demonstrated plasmon-induced CD signal from the oligonucleotide molecules in the plasmonic region of the NPs which is consistent with theoretical predictions.[14] We believe that these new chiral nanomaterials could find a range of potential applications in new plasmonic devices and chiral sensing.

To further assess the role of the plasmon-active species in the generation of CD signal, non-plasmonic particles, namely TGA-capped CdTe quantum dots (QDs), were conjugated with the oligonucleotides. The 5' end amine function was used to covalently bind the oligonucleotide to a TGA molecule on the surface of the QDs *via* carbodiimide (EDC) coupling, as described in chapter 4. The carboxylic acid group of TGA was first activated by using EDC, to prepare for subsequent coupling reaction with the oligonucleotide terminal amine.

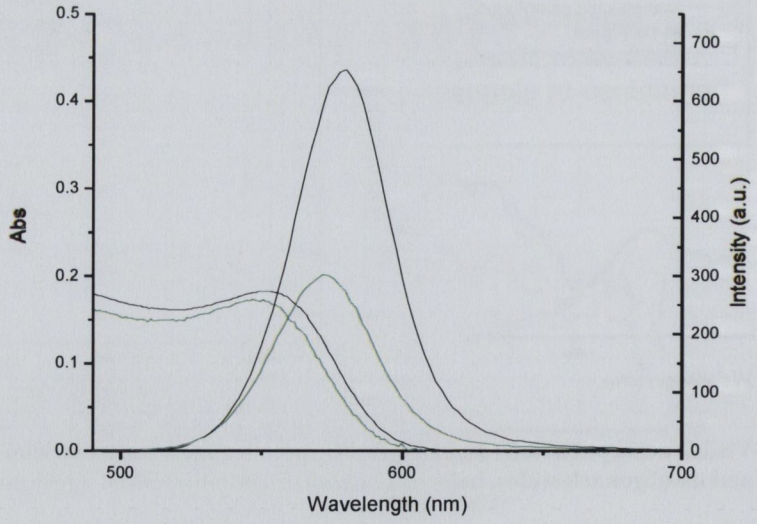

Figure 5.17 UV-visible absorption and PL emission spectra of TGA-capped CdTe QDs before (black) and after (green) oligonucleotide conjugation

The absorption and PL spectra of oligonucleotide-conjugated QDs (Figure 5.17) showed a blue shift and decrease in the luminescence intensity. This was attributed to partial degradation induced by EDC rather than an effect of the oligonucleotides. DLS measurements as shown in Figure 5.18 confirmed the presence of smaller, partially etched particles, as well as bigger ones compared to the initial QDs. The increase in the hydrodynamic radius suggested effective conjugation of the oligonucleotides.

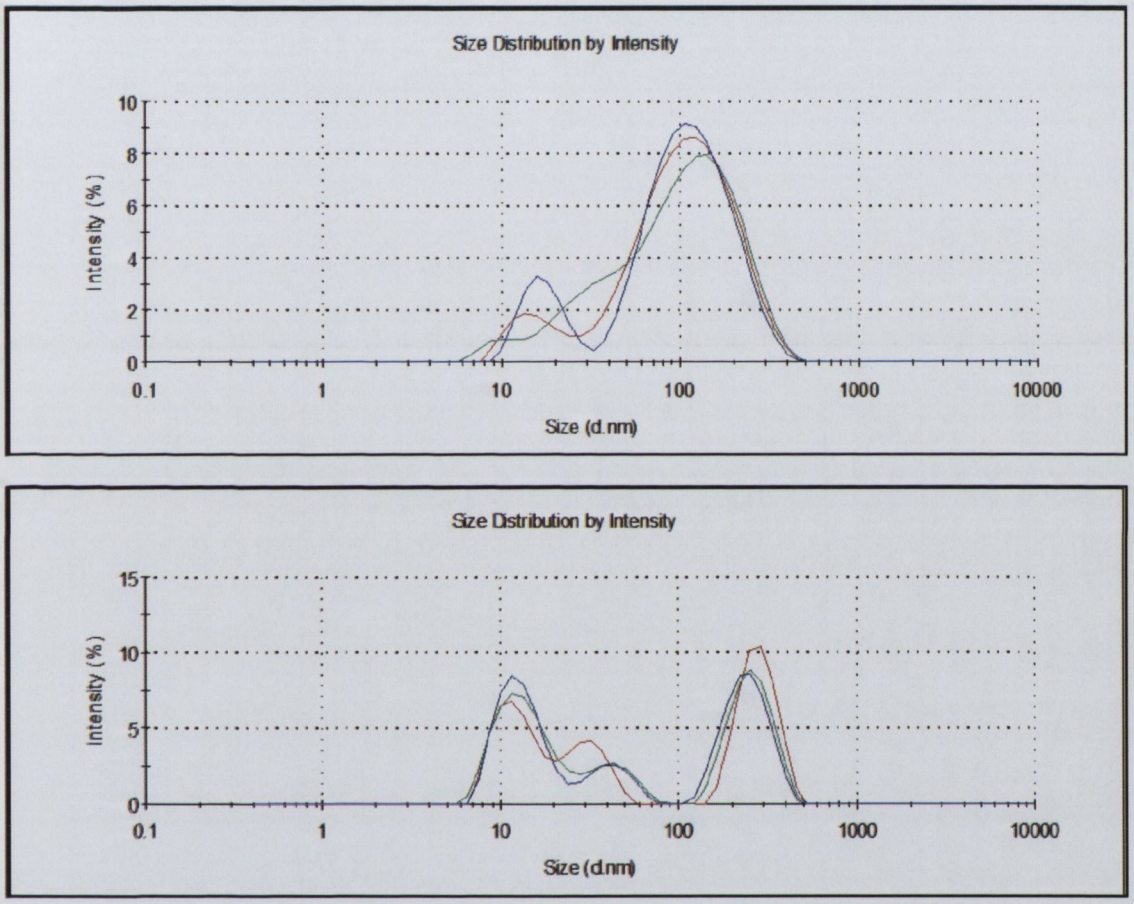

Figure 5.18 DLS measurements of bare (top) and oligonucleotide-conjugated (bottom) TGA-capped CdTe QDs

Further characterisation of the conjugated QDs involved zeta potential measurements. The results are presented in Table 5.2 Zeta potential measurements of TGA-capped CdTe QDs with and without conjugated oligonucleotidesTable 5.2. Both the initial TGA-capped CdTe QDs and the free oligonucleotides bore a strong negative charge, as expected. The conjugates, however, had a lower absolute value of zeta potential.

Table 5.2 Zeta potential measurements of TGA-capped CdTe QDs with and without conjugated oligonucleotides

Sample	Zeta potential (mV)	Std deviation
TGA-capped CdTe QD	-35	0.7
oligonucleotide	-30	2.8
QD-oligonucleotide conjugate	-22	1.5

Although the conjugation was mainly achieved through EDC coupling of the 5' end oligonucleotide amine group to the carboxylic acid group of TGA, the 3' end thiol groups may also bind to the surface of QDs *via* ligand exchange. As TGA is a very small molecule compared to an oligonucleotide, one of the latter could replace several TGA molecules. This mechanism would explain the decrease in surface charge.

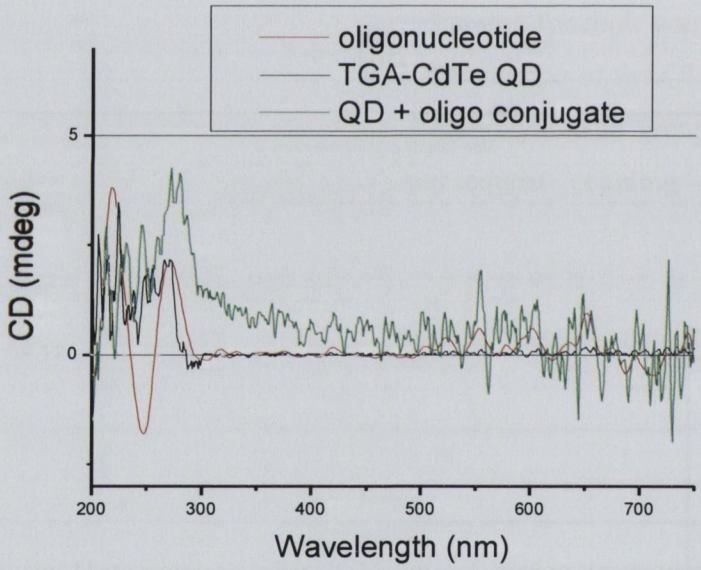

Figure 5.19 CD signal of TGA-capped CdTe QDs conjugated with oligonucleotides

In contrast to metal nanoparticles, these QD conjugates did not demonstrate any CD signal in the region between 450 and 750 nm (this region includes the exciton peaks) after washing by centrifugation (Figure 5.19), suggesting that plasmon resonance plays an essential role in the process. Indeed, we would qualitatively expect the chiral molecule-plasmon Coulomb interaction to be much stronger than the molecule-exciton coupling.

Another factor arising from the covalent binding of oligonucleotides to TGA molecules is the distance between the chiral molecule and the QD surface which is non-negligible, whereas it was previously assumed to be at least partially in contact with the gold nanoparticle surface.

It should also be noted that chiral CdS and CdSe nanoparticles have been previously reported, but in these nanostructures the chirality and emitting properties were induced by chiral surface defects.[39-42] In this section we only consider oligonucleotide-nanoparticle systems where conjugation is achieved on pre-formed nanoparticles, either through ligand exchange or covalent coupling, so no chiral deformations of the crystal structure should be involved. Other modes of conjugations will be investigated in the rest of the chapter.

5.3 Oligonucleotide-mediated assemblies of nanoparticles

5.3.1 Oligonucleotide-mediated assembly of gold nanoparticles

The use of oligonucleotides to create controlled assemblies of metal nanoparticles into increasingly complex structures has been largely explored in recent years.[5, 43-44] They usually rely on the immobilisation of two distinct sequences on two types of particle and a linker sequence with domains complementary to each other, or the direct use of two complementary sequences.

The conjugation of thiol-modified oligonucleotides to gold particles has been widely reported in the literature; however it usually involved a single terminal thiol group.[6, 29-32] Here, a T6-phosphorothioate-modified oligonucleotide was used, which was expected to provide much stronger binding. Two approaches were compared for the conjugation to gold nanoparticles and subsequent assembly: the traditional ligand exchange reaction and the *in situ* formation of oligonucleotide-stabilised gold nanoparticles.

5.3.*1.a Gold nanoparticles modified through ligand exchange*

The ligand exchange reaction was presented in the previous section and demonstrated effective binding of oligonucleotides to the gold nanoparticles, giving rise to new CD. Here complementary sequences (oligo 1 and oligo 2) were attached to two sets of particles which were subsequently mixed together. Such reaction was reported in the

literature[4] to form polymeric networks of nanoparticles evidenced by a large red-shift of the plasmon band. Typically the initial 520 nm band would shift to 526 nm for conjugated particles and to 576 nm for the aggregates.[4] In the present case however, only the first shift was observed, as displayed in Figure 5.20. The failure to produce the second shift could be attributed to two combined effects: first, the T6-phosphorothioate tail meant that each oligonucleotide was bound to the surface through six thiol groups, thus reducing the number of oligonucleotides to be immobilised on each particle; second, the A_{10} spacer was relatively short compared to what has usually been used. Therefore, the binding sequence was close to the surface and hybridisation may have been hindered due to steric effects. As a result, a tightly packed network of particle was unlikely to be generated.

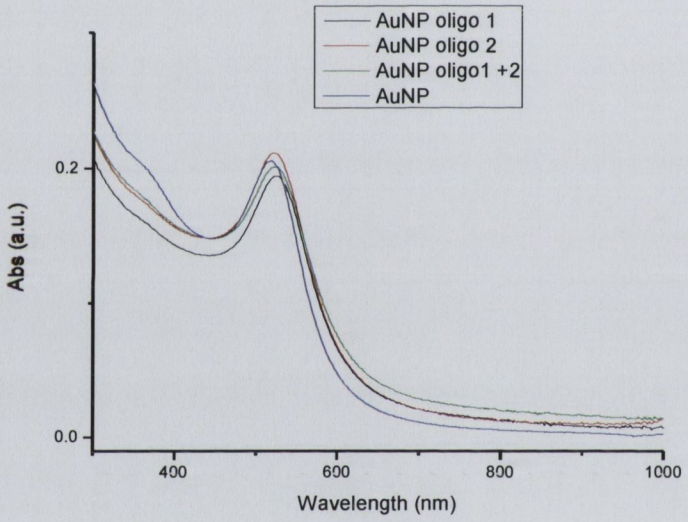

Figure 5.20 UV-Visible absorption spectra of oligonucleotide-conjugated gold nanoparticles, assemblies and initial nanoparticles

5.3.*1.b In situ synthesis of oligonucleotide-modified gold nanoparticles*

In situ synthesis of oligonucleotide-AuNP was performed in order to try to increase the loading. A similar red-shift from 520 to 526 nm was observed in the absorption spectra of these new conjugates. They exhibited larger hydrodynamic radii than the ones formed by ligand exchange, as well as more negative zeta potentials, as summarised in Figure 5.21 and Table 5.3. These were evidence of a higher loading of oligonucleotide on the gold nanoparticles. Despite this improvement, complete aggregation through hybridisation of complementary sequences still was not observed.

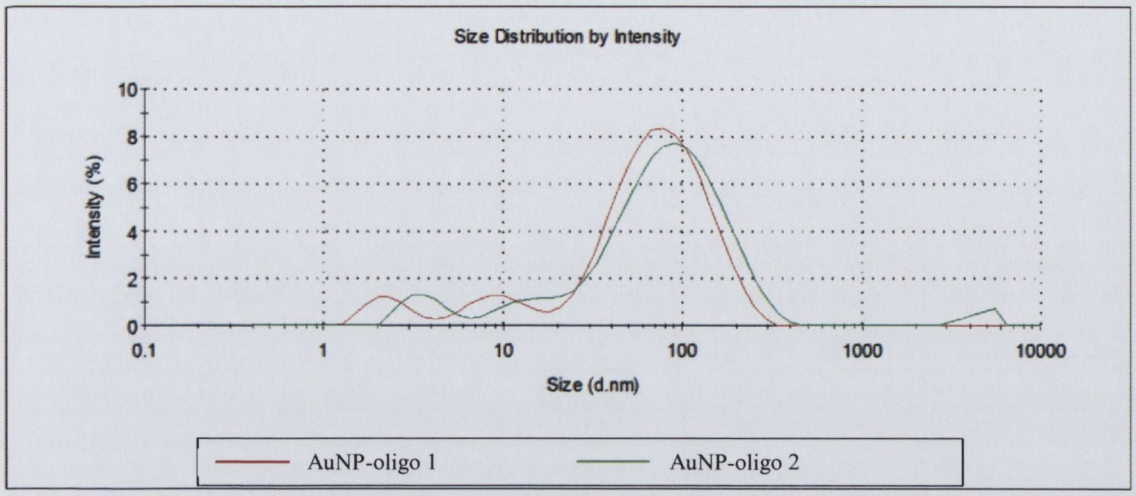

Figure 5.21 DLS measurments of AuNP-oligo conjugates formed *in situ*

Table 5.3 Zeta potential measurements of AuNP-oligo conjugates

Sample	Zeta potential (mV)	Std deviation
AuNP	-29	2.15
oligonucleotide	-30	2.88
AuNP-oligo 1 ligand exchange	-18	3.05
AuNP-oligo 2 ligand exchange	-24	1.31
AuNP-oligo 1 *in situ*	-44	1.44
AuNP-oligo 2 *in situ*	-47	0.25

Hybridisation and nanoparticles assembly was still limited by the oligonucleotide length, but we developed here a method for rapid immobilisation of oligonucleotide on gold nanoparticles with high loading which could be used for further applications.

To induce a higher degree of aggregation of the conjugates, another type of **oligonucleotide was designed, with the following sequence**: 3'-Tps6-ACT.ATT.GAT.AAG.GATps6-5' **(oligo** 3.1). The presence of thiol groups on both ends would allow for conjugation to two distinct nanoparticles. In order to avoid for the

sequence to loop on itself, it was pre-incubated with the complementary sequence minus the phosphorothioate tails (oligo 3.comp). The double stranded structure was hoped to provide sufficient rigidity. For comparison, the same ss-sequence with only one thiolated end was also bound to a set of nanoparticles. Wavelengths of maximum absorptions for AuNPs with oligo3.1, oligo3.2, and oligo3.1 + oligo3.comp were found at 520nm, 521nm, and 532nm respectively (Figure 5.22). The longer wavelength of 532nm was an evidence of a higher degree of aggregation obtained with the ds-oligonucleotide thiolated on both ends, although not as strong as anticipated.

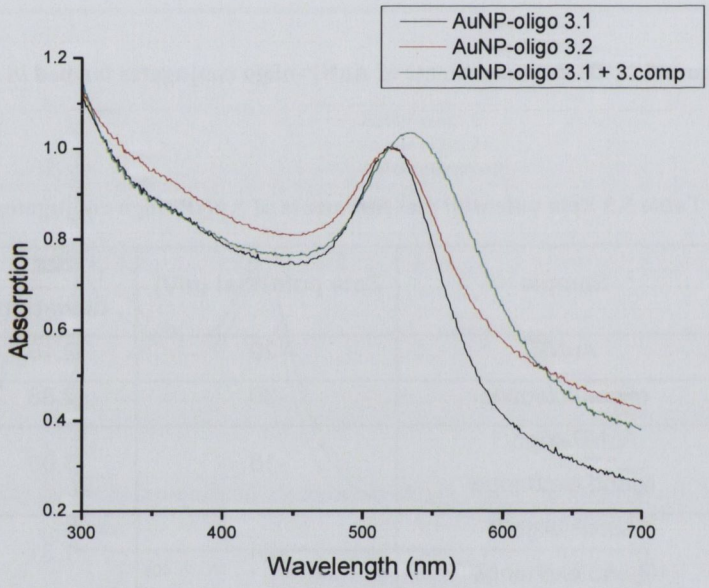

Figure 5.22 UV-Visible absorption spectra of gold nanoparticles conjugated with oligo 3.1, oligo 3.2 and oligo 3.1 pre-incubated with oligo 3.comp

Using DLS, the hydrodynamic diameters of the particles conjugated with oligo3.1, oligo3.2, and oligo3.1 + oligo3.comp were found to be 14.11 nm, 20.72 nm, and 19.44 nm respectively as shown in Figure 5.23. The polydispersity index (PdI) was quite high for AuNPs, with oligo3.1 and oligo3.1 + oligo3.comp, at 0.577 and 0.592 respectively, indicating the particles were not very uniform in size due to the presence of clusters.

Overall a higher degree of aggregation was obtained with the duplexed oligonucleotide. These results were consistent with the absorption spectra. The zeta potential for each was found to be -50 mV, -41.8 mV, and -30.8 mV in the same order. In the case of oligo3.1, the possibility of oligonucleotides looping on themselves explained

the more compact hydrodynamic diameter and the higher zeta potential due to the negatively charged DNA backbone being exposed.

Overall the oligonucleotides used here only gave moderate results in terms of controlling the assembly of nanoparticles. The strategy nevertheless seemed promising and could be optimised by varying the oligonucleotide sequence and length.

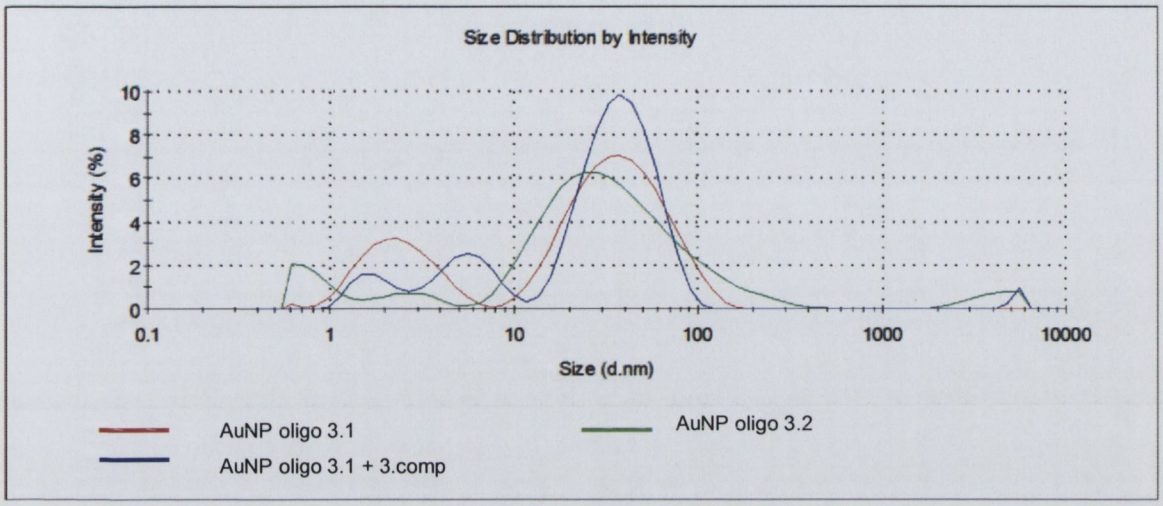

Figure 5.23 DLS measurements of gold nanoparticles conjugated with oligo 3.1, oligo 3.2 and oligo 3.1 pre-incubated with oligo 3.comp

5.3.2 Oligonucleotide-mediated assemblies of QDs and AuNPs

5.3.2.a. Assembly of spherical gold nanoparticles and QDs

Using the same approach as for assembling gold nanoparticles in the previous paragraph, the hybridisation of complementary oligonucleotides was employed to form AuNP-QD nanocomposites. Such composites could exhibit interesting optical properties due to possibilities of energy transfer. Figure 5.24 provides a schematic representation of the synthetic strategy as well as a TEM image of a resulting nanostructure. It represents the ideal case where several QDs were coupled to a single gold nanoparticle.

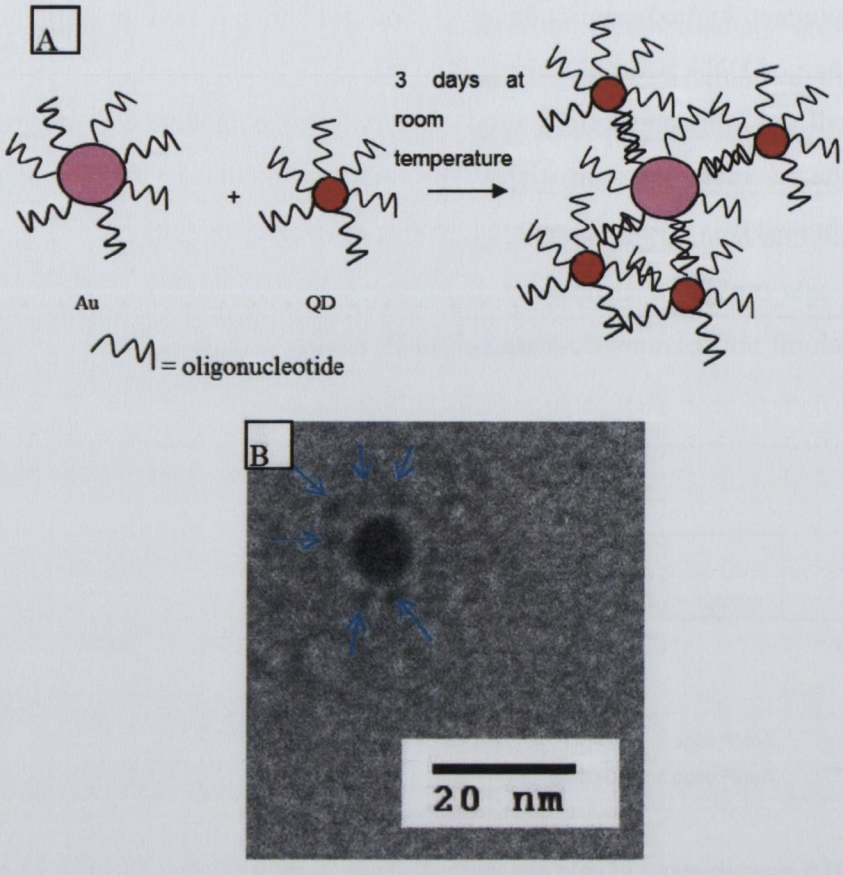

Figure 5.24 (A) Schematic of the duplex-induced assembly of a spherical gold nanoparticle and QDs. (B) TEM image of QDs (designated by arrows) bound to a gold nanoparticle through oligonucleotide duplex formation.

To get more insight into the coupling reaction, titration experiments were performed. An excess of QD-oligo2 was added to AuNP-oligo1 in different ratios. The mixture was incubated on a shaker at room temperature for 72h. No visible change was observed during the first two days. On the third day however, aggregation was visible by a clear change of colour. UV-Visible absorption spectra are presented in Figure 5.25, along with the spectra for the same concentration of QD-oligo and AuNP-oligo when alone.

Aggregation was very significant for AuNP:QD ratios of 1:12.5 and 1:25, with very broad absorptions and a peak shifted to 598 and 617 nm respectively. With larger amounts of QD however the absorption spectra resembled more that of AuNP-oligo, with maxima at 530 and 528 nm respectively. These observations suggested the coupling of complementary oligonucleotides did indeed occur. With the lower ratios of QD to gold, there were more binding sites available on AuNP than there were QD, therefore a single QD could bind to two AuNP thus bringing them very close together. This phenomenon would be responsible

for the large absorbance shift characteristic of aggregation which was also observed in TEM (Figure 5.26). When the ratio was increased however, there were enough QDs to surround each AuNP, producing the ideal structures seen in Figure 5.24. The QD shell around AuNP would prevent aggregation. In very large excess of QDs, even unbound QDs could participate in keeping AuNPs apart, as seen in Figure 5.27. Some PL emission remained immediately after addition, but a dramatic quenching of luminescence was observed in all cases after 72h as illustrated by Figure 5.28. Overall these results suggested that assemblies occurred and resulted in QD quenching. HRTEM images (Figure 5.27) indicated that the distance between AuNP and bound QD was in the 2 to 3 nm range. This falls in the distance range where non-radiative energy transfer to the metal nanoparticles is expected to occur.[45]

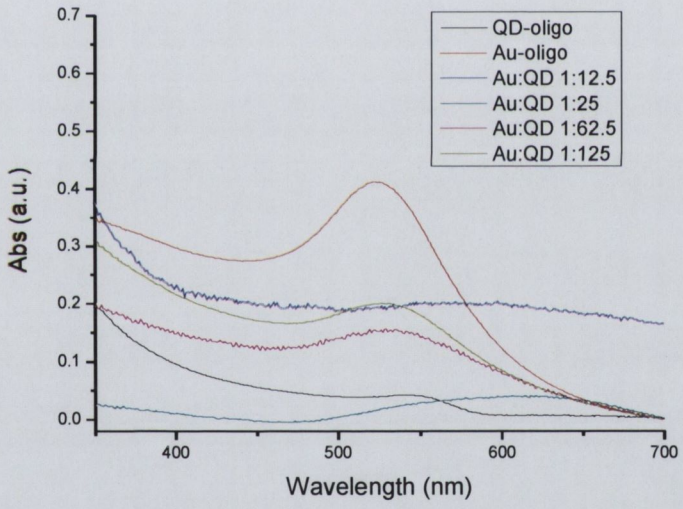

Figure 5.25 UV-visible absorption spectra of Au-oligo, QD-oligo, and mixtures of them in various ratios

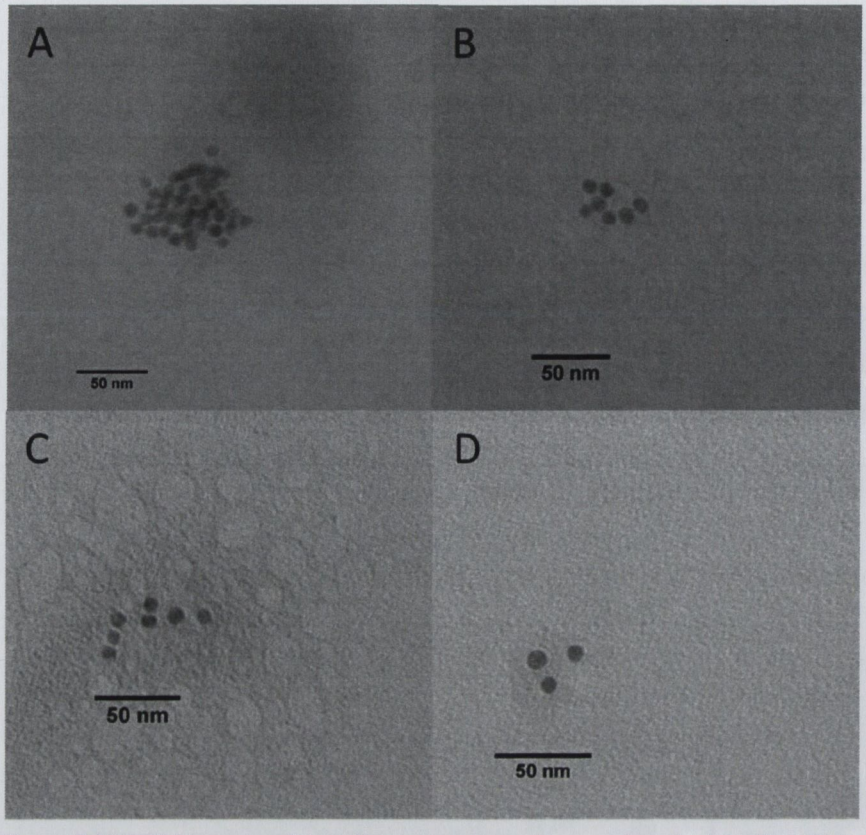

Figure 5.26 TEM images of Au-oligo nanocomposites produced with (A) 1:12.5, (B) 1:25, (C) 1:62.5, and (D) 1:125 ratios of AuNP to QD. Aggregation decreased as the ratio increased.

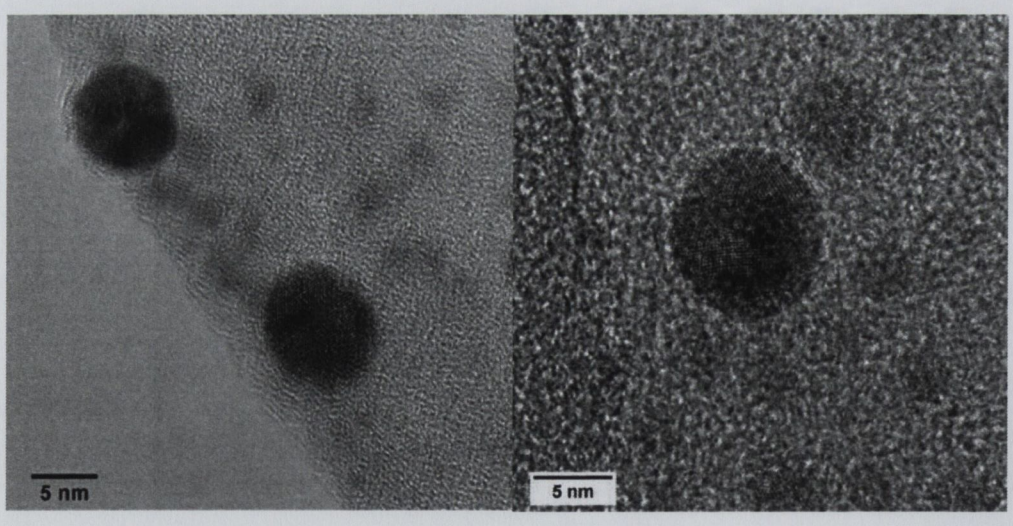

Figure 5.27 HRTEM images of Au-oligo nanocomposites produced with a 1:125 ratio of AuNP to QD

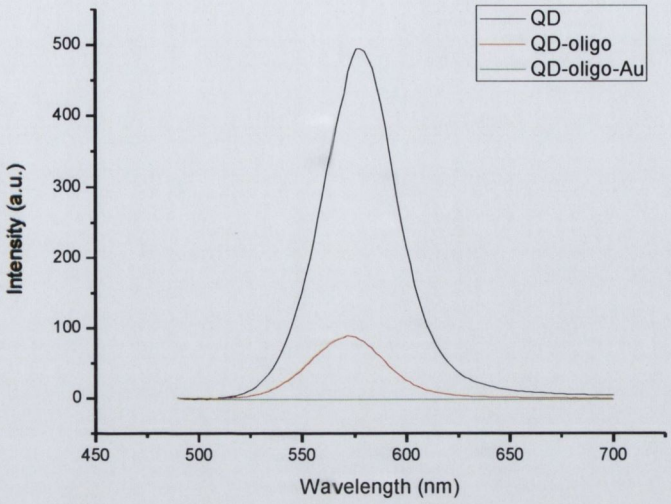

Figure 5.28 PL emission spectra of original QDs, QD-oligo conjugates and Au-oligo nanocomposites (excitation 480 nm)

Finally, CD spectra of the nanocomposites were recorded and compared to that of QD-oligo which previously demonstrated no CD in the plasmon region. Figure 5.29 shows that the presence of AuNP did not induce any more CD. Since AuNP were separated by QDs this supported again the importance of plasmonic hot-spots in the generation of CD.

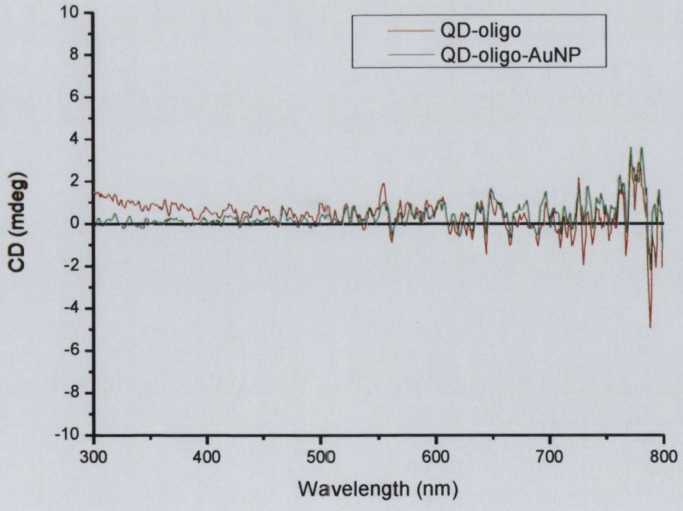

Figure 5.29 CD spectra of oligonucleotide-modified QD and subsequent ds-oligo mediated assembly of QD and AuNP

The second approach used to assemble spherical gold nanoparticles and QDs was to bind a pre-conjugated gold particle to a TGA-capped CdTe QD *via* EDC coupling. AuNP and QD were therefore bound through single-stranded (ss) oligonucleotide rather than double-stranded (ds) as in the previous method. Using a low concentration of QDs allowed formation of one-to-one assemblies which could be observed on TEM, as shown in Figure 5.30.

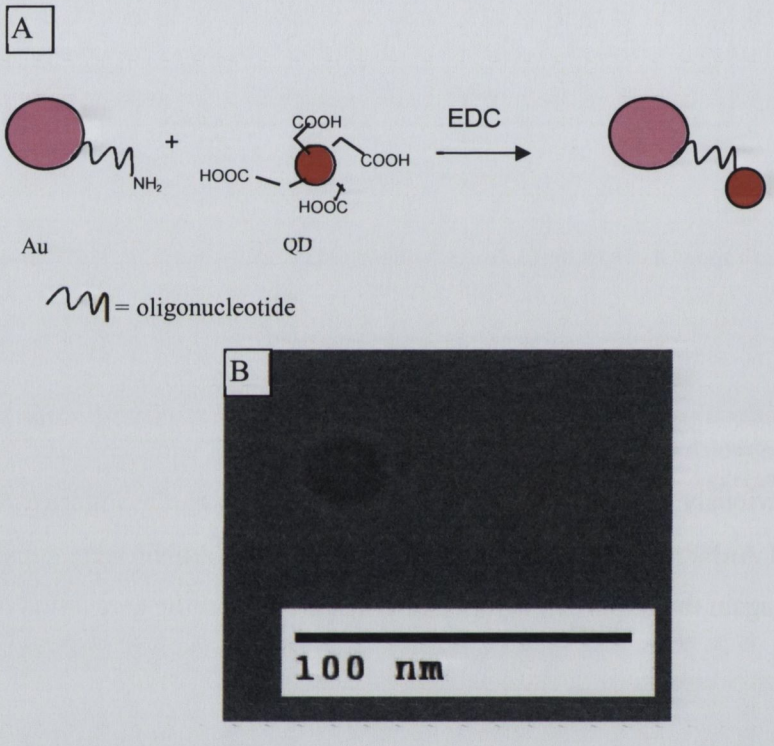

Figure 5.30 (A) Schematic of the direct assembly of a spherical gold nanoparticle and a QD through the ss-oligo method. (B) TEM image of a QD bound to a spherical nanoparticle through oligonucleotide conjugation.

In this case, aggregation due to the coupling of particles occurred much faster than with the hybridisation strategy. A strong shift in absorbance was already observed after 30 min of reaction. As seen in Figure 5.31, the initial 520 nm plasmon band of gold nanoparticles shifted to 526 nm after conjugation to oligonucleotides, then to 544 nm after 30 min of incubation with EDC-activated QDs, to 548 nm after 60 min and to 550 nm after 90 min. The broadening of the peak was also a sign of aggregation.

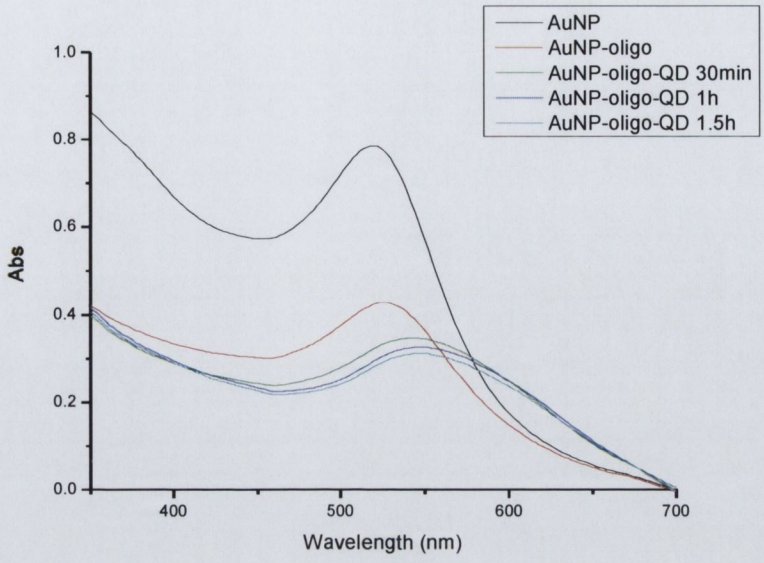

Figure 5.31 UV-visible absorption spectra of AuNP-QD composites formed over time through single-stranded oligonucleotide binding

To ensure that the shift observed was indeed imputable to the conjugation of oligo, the same experiment was repeated in absence of oligo, all other parameters remaining the same. As depicted in Figure 5.32, an initial shift to 540 nm occurred after 30 min, as a result of the presence of two species with different absorption bands, but the spectrum remained unchanged thereafter.

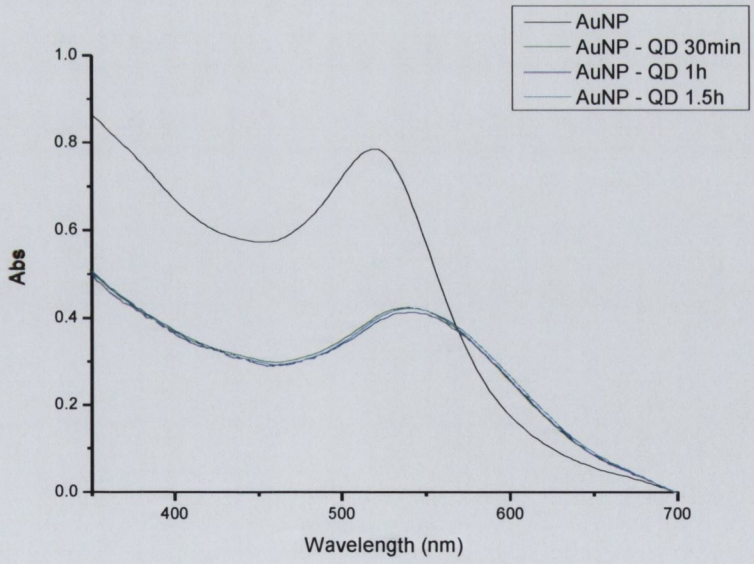

Figure 5.32 UV-visible absorption spectra of AuNP mixed with QD in absence of oligo

TEM imaging clearly revealed the accumulation of QDs on gold nanoparticles which remained mostly isolated from each other as illustrated by Figure 5.33. This was all consistent with the moderate shift in absorbance compared to the reference 576 nm for aggregated AuNP.[4]

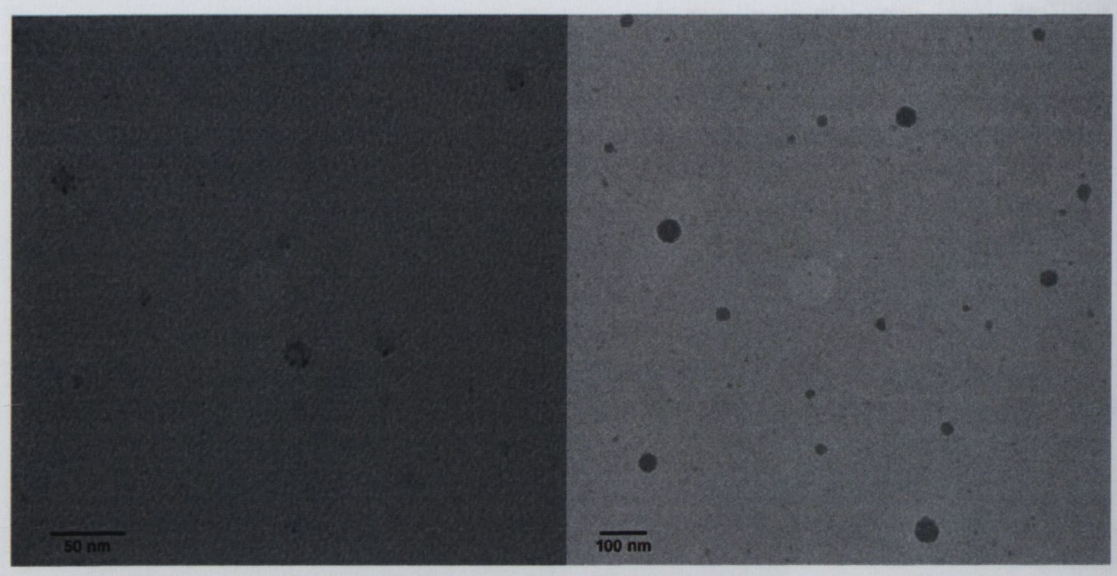

Figure 5.33 TEM images of AuNP-oligo-QD composites formed by the ss-oligo route

Most luminescence was lost upon mixing of QDs with AuNPs, with only negligible emission measured in absence of oligo as seen in Figure 5.34.

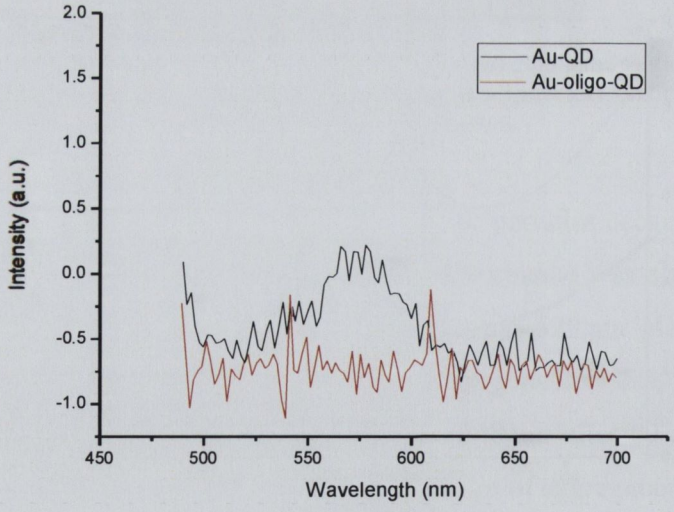

Figure 5.34 PL emission spectra of Au-QD nanocomposites formed through the ss-oligo method and mixture of AuNP and QD without oligo. (excitation 480 nm)

The ss-oligo approach thus appeared to be successful and to induce particle binding much faster than the ds-oligo approach. This was consistent with the mode of binding. Amine to carboxylic coupling with carbodiimide activation is known to be quick, as opposed to the duplexation of DNA strands, especially when steric effects of nanoparticles can hinder the bounding of complementary sequences. Here again all luminescence was quenched as the QD to gold distance was much reduced.

5.3.2.b Assembly of gold nanorings and QDs

The duplex approach described above was also applied to binding QDs to gold nanorings (AuNR), as illustrated by Figure 5.35 and Figure 5.36. QD-oligo2 and AuNR-oligo 1 conjugates were incubated together for three days to allow complementary sequences to bind to each other.

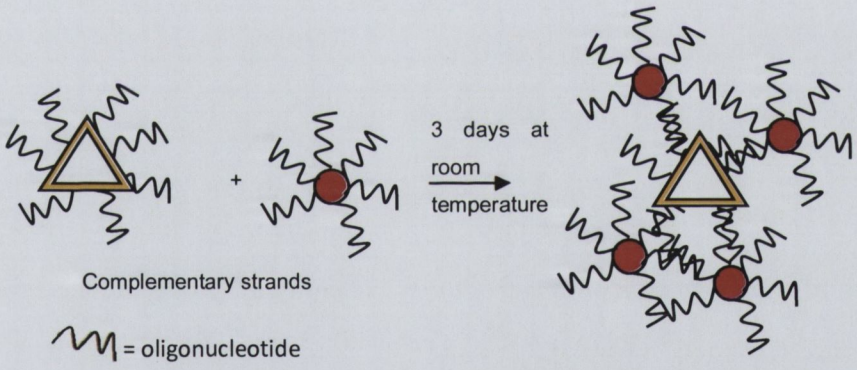

Figure 5.35 Schematic of the duplex-induced assembly of gold nanorings and QDs.

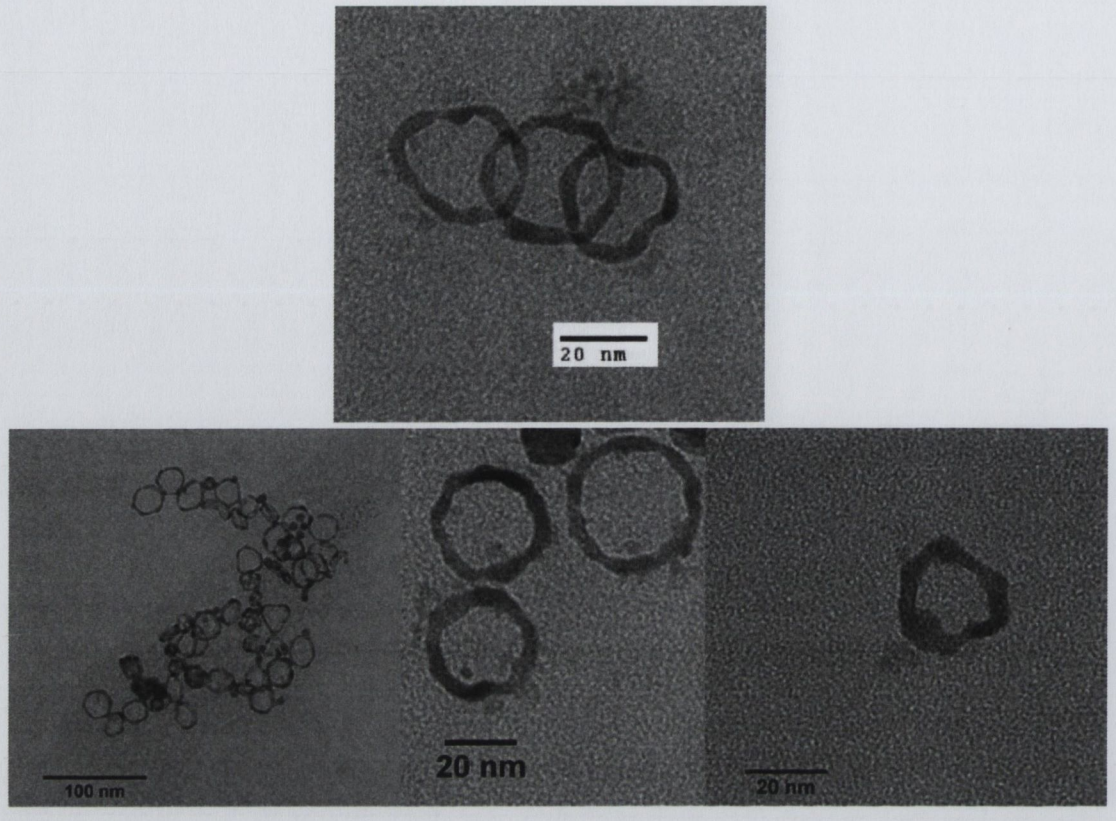

Figure 5.36 TEM images of QDs bound to gold nanorings through oligonucleotide duplex formation.

AuNR-oligo conjugates were reported in the previous section to demonstrate a weak CD in the 500-800 nm region due to plasmonic enhancement of the circular dispersion from the oligonucleotides. Figure 5.37 shows that QD did not significantly affect CD which remained extremely weak. This is consistent with the observation that the presence of QDs did not modify the creation of hot spots in the nanoring system, due to the large surface area of the latter compared to the size of QDs.

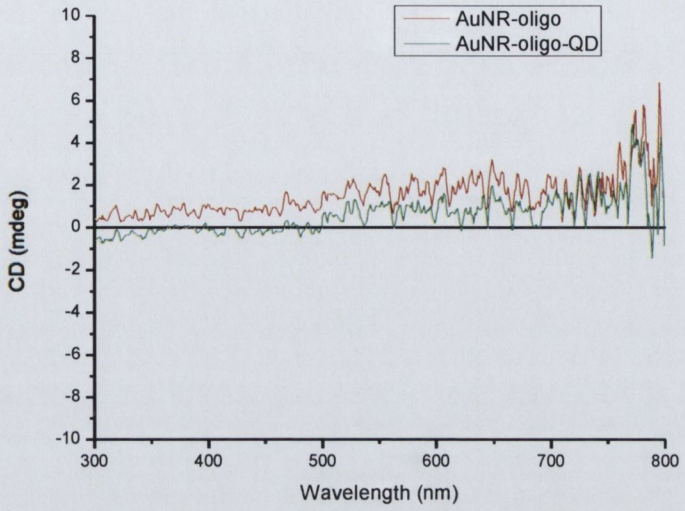

Figure 5.37 CD spectra of oligonucleotide-modified AuNR and subsequent assembly with QDs

In all cases, the luminescence of QDs as part of assemblies of nanoparticles was completely quenched. This was easily explained by energy transfer to the metallic nanoparticles which are maintained at a short distance by the oligonucleotide link, which can be held as further evidence of effective conjugation. Unfortunately, quenching of the QDs means that this could be an issue if such systems were to be used for fluorescent labelling, sensing and tracking applications.

The origin of quenching was further investigated. Although quenching was easily explainable by the non-radiative energy transfer to gold nanoparticles phenomenon, the role of EDC treatment could not be neglected. The role of oligonucleotide binding should also be further discussed.

Successive additions of a dilute solution of EDC to a QD suspension allowed the measurement of the effect of the treatment on QD luminescence. EDC would always be added greatly in excess in order to ensure activation of all binding sites. The number of TGA ligands on a given 4 nm QD is estimated to be 300 to 400 based on the modelling of the zinc blende structure.[46] EDC should be in excess compared to the ligand available rather than to the QDs themselves. To displace the reaction towards activation of all carboxylic acid groups, it was decided to start with an excess of 2400 EDC moles per mole of QD. Figure 5.38 displays the absorption and emission spectra recorded after each addition of EDC. The shape of the absorption spectrum was not significantly altered. PL

emission however gradually decreased upon addition of EDC and shifted to slightly longer wavelength with very high ratios. It is believed that the binding of EDC to TGA destabilises the ligand shell, thus introducing more surface defects which are responsible for the lowering of quantum yield. Ultimately, smaller particles are not sufficiently stabilised and precipitate out of solution which translates into a red shift of the emission. The 1:48000 ratio was selected as a suitable intermediate level for all experiments.

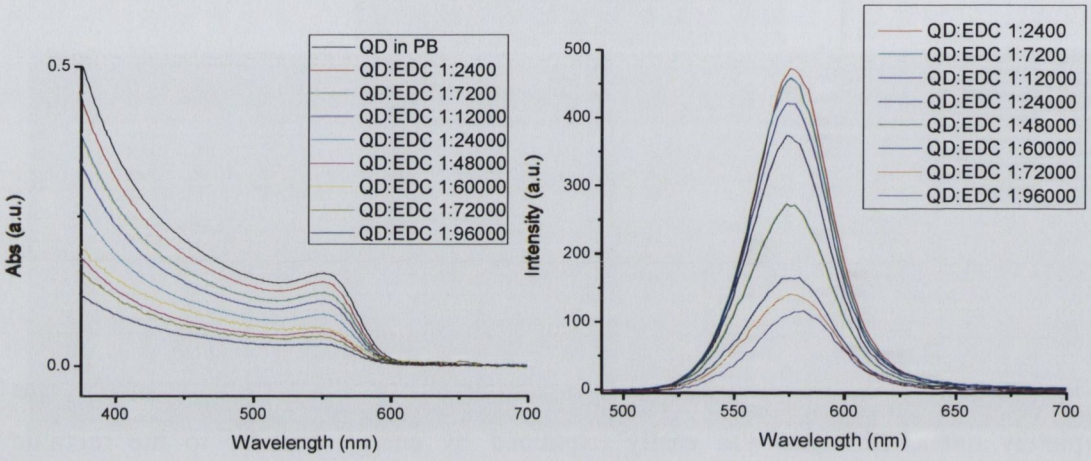

Figure 5.38 UV-visible absorption (left) and PL emission (right) spectra of QDs treated with increasing amounts of EDC. PL emission spectra were normalised against concentration

Comparisons were then made in the luminescence quenching by EDC, by unbound gold nanorings and by oligonucleotide-conjugated gold nanorings. As seen in Figure 5.39, unbound gold nanorings only induce a small amount of quenching, indicating that most QDs remain at sufficient distance from the gold particles. In the presence of EDC, the quenching is increased three-fold, and the combined effect of EDC metal nanoparticles made the luminescence drop down to about a tenth of its initial value. The formation of conjugates, however, had a slightly less dramatic effect on the emission. The red-shift observed in the case of the QD-oligo-AuNR conjugates, as well as when EDC is absent, would be the only indication of the presence of gold nanorings. The quantum yield of QDs is very sensitive to the chemical environment and especially to the nature of ligands. The attachment of oligos and metal nanoparticles instead of EDC molecules constitutes a modification of the QD chemical environment which may induce such a change in the emission. These results confirmed that QD quenching was caused by a combined effect of

EDC treatment and energy transfer to metal nanoparticles; they also reasserted the success of the conjugation reaction.

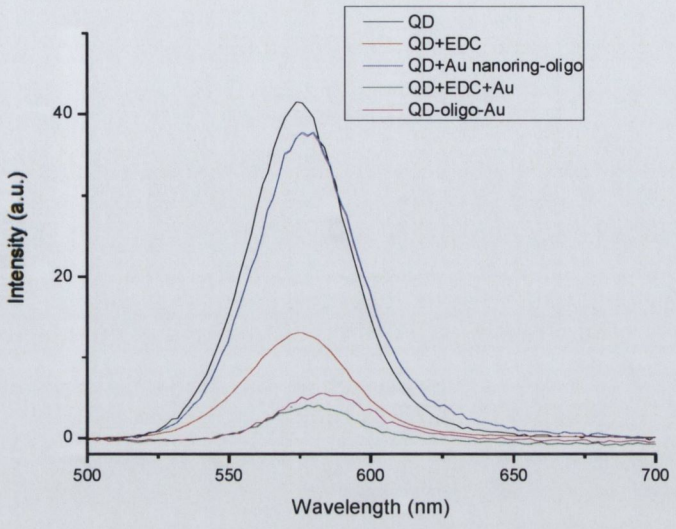

Figure 5.39 PL emission spectra of QD on their own, QD treated with EDC, QD mixed with gold nanorings, QD and gold nanorings in presence of EDC (no oligo) and the final QD-gold nanoring conjugates.

It was thus demonstrated that both double-stranded and single-stranded oligonucleotide binding strategies were valid to form composites. The latter appeared to be faster, but also to damage the QDs by depleting part of the ligands and thereby reducing their luminescence. Using longer sequences may allow to retain or to even enhance QD luminescence in the double-stranded strategy, but not in the single-stranded approach since the effects of EDC would still be predominant.

5.4 Oligonucleotide-mediated QD interactions

Recently, Tikhomirov *et al.* published a method for producing oligonucleotide-modified CdTe QDs using phosphorothioate-functionalised oligonucleotide sequences.[20] They also demonstrated how the number of strands to be immobilised on a single QD is highly dependent on the QD-binding domain of oligonucleotides as well as the particle diameter.

On the other hand, QDs are excellent candidates for the observation of fluorescence resonant energy transfer (FRET)[20, 47] owing to their narrow and symmetrical emission spectra. In this work, a range of oligonucleotide-modified QDs were produced and fully characterised. The role of hybridisation and melting of ds-DNA in QD interactions was

investigated, and the occurrence of energy transfer was studied with various degrees of spectral overlap between donor and acceptor. Finally, the potential of thusly produced nano-composites for *in vitro* biological imaging was assessed.

5.4.1 Synthesis of oligonucleotide-QD conjugates and evaluation of their hybridising ability

Complementary sequences of oligonucleotides bearing a T6 phosphorothioate tail at their 3' end and an amino function at their 5'-end (oligo 1 and oligo 2) were used to synthesise three series of oligo-stabilised QDs. The procedure was adapted from the work of Tikhomirov *et al.*[20] A range of QD sizes were thus produced and enabled to interact through DNA hybridising. The optical properties of the new composites were investigated, as well as their behaviour in *in vitro* cell cultures.

The presence of oligonucleotides on the surface of QDs and their ability to hybridise with the complementary sequence immobilised on other QDs was assessed by several techniques. First circular dichroism (CD) spectra were recorded for QDs modified with complementary oligonucleotides separately as well as when mixed together at a 1:1 molar ratio. They exhibited a weak signal in the 500-800 nm range which corresponds to the position of the exciton peak. The corresponding spectra are displayed in Figure 5.40.

We reported in section 5.2 that plasmonic nanoparticles may induce CD in that region when an oligonucleotide, is immobilised on their surface and aggregation occurs.[48] It was also demonstrated that QDs did not produce such an effect when oligonucleotides were coupled to the TGA ligand. In the present case however, oligonucleotides were bound directly to the surface of QDs which allowed for closer interactions. The T6 phosphorothioate tail was assumed to lay on the surface which meant that a chiral moiety was in direct contact with the particle surface. When bound to the ligand however, electrostatic repulsion between the carboxylic acid groups and the DNA backbone prevented such contact. Direct sulphur to cadmium bonding would also reproduce the type of interactions that previously lead to chiral QDs, where it was shown that CdS or CdSe stabilisation with D-/L-penicillamine imprinted a degree of chirality on the crystal structure.[39, 41]

Overall CD in the exciton region was very weak compared to that observed with plasmonic nanoparticles, which confirmed again the predominant role of Coulomb

interactions between the plasmon and the chiral molecule in the process of CD generation. The hydrisation of complementary sequences of oligonucleotides bound to QDs did not induce any variation in the signal; further aggregation may occur in this case but no CD enhancement could be observed in the absence of plasmonic hot spots.

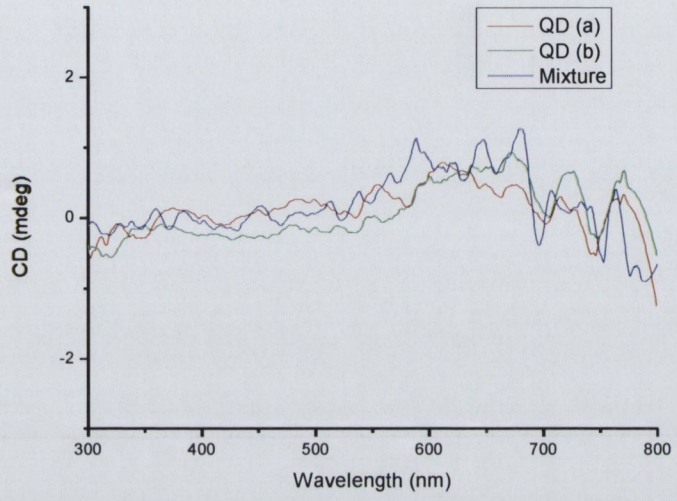

Figure 5.40 CD spectra of QDs modified with complementary oligonucleotide sequences and their mixture in 1:1 ratio

For further assessment of the binding effect of oligonucleotides, a 1:1 mixture of QD-oligo 1 and QD-oligo 2 was scanned by dynamic light scattering (DLS) in order to measure the evolution of the hydrodynamic diameter over time. Figure 5.41 displays the graph of hydrodynamic diameter distribution of QD assemblies from 0 to 55 min of incubation.

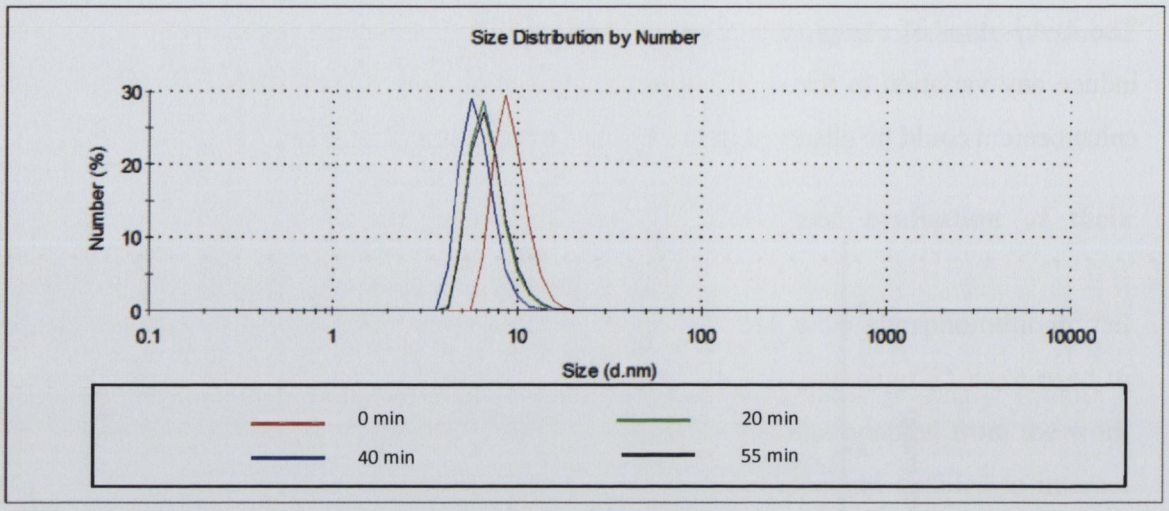

Figure 5.41 DLS measurements of a 1:1 mixture of QDs modified with complementary oligonucleotide sequences and incubated for 0 to 55 min

The initial mixing of both types of QDs resulted in an average diameter of around 10 nm with a polydispersity (PDI) of 0.431. As incubation time was increased, the PDI did not significantly vary, the average diameter however slightly decreased to around 7 nm after 20 min and remained in that range afterwards. This indicated that clusters were formed in the first 20 min and packed more tightly with time. The cluster size suggested that they were dimers.

The role of oligonucleotide hybridisation in the process was ascertained by measuring the hydrodynamic diameter of the same one-to-one mixture with increasing temperature. Results are displayed on Figure 5.42. For temperatures up to 65°C the cluster size fluctuated between 10 and 35 nm while the PDI rose to 0.510 on average. These two effects were mainly imputable to thermic agitation. Further heating however led to a dramatic increase in average diameter. The measured values were 41 (+/-5) nm at 75 °C, 174 (+/-15) nm at 85 °C and 326 (+/- 50) at 90 °C. It was therefore concluded that the distance between nanoparticles in the nanoclusters increased when the temperature was higher than the oligonucleotides melting temperature. Thus the QDs moved further apart but remained grouped together as there was no mechanical agitation. Diffusion would lead over time to a reduction in measured size as QDs can eventually be seen as individual particles.

HRTEM imaging of the 1:1 mixture of QD-oligo 1 and QD-oligo 2 supported the presence of dimers as illustrated in Figure 5.43, although general aggregation made it difficult to ascertain this conclusion.

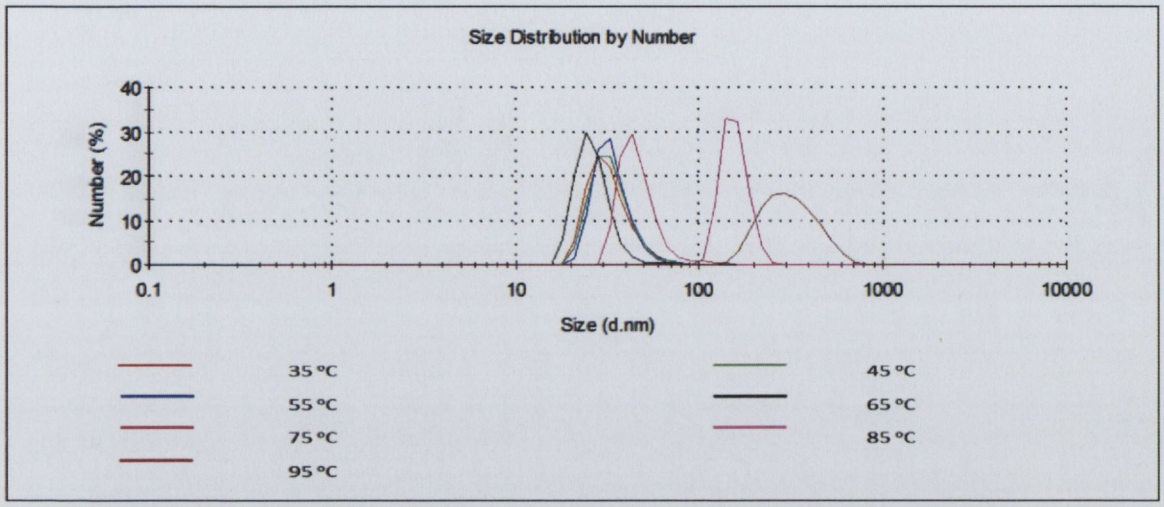

Figure 5.42 DLS measurements of a 1:1 mixture of QDs modified with complementary sequences of oligonucleotides at increasing temperatures

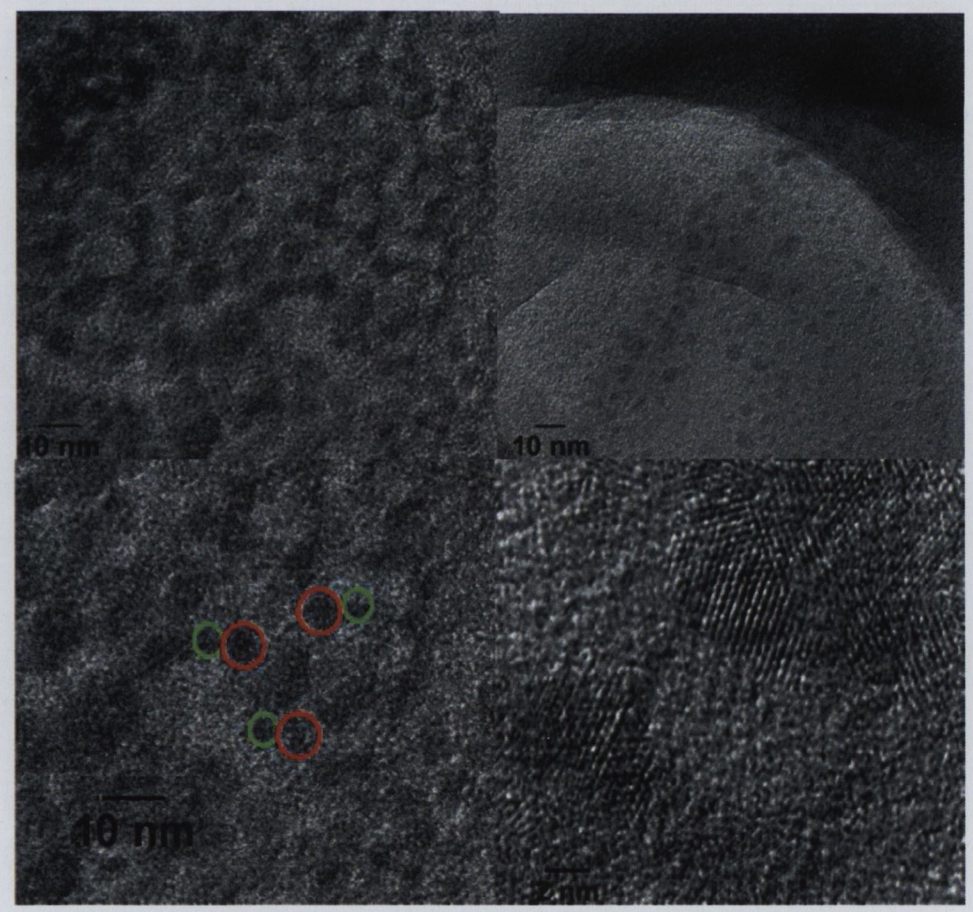

Figure 5.43 HRTEM images of oligonucleotide-mediated assemblies of QDs. Some green-red QD dimers are highlighted as circled in green and red.

Finally the influence of the ratio in which complementary oligonucleotide-QD conjugates were mixed was investigated by electrophoresis. This technique allowed visualisation of the degree of homogeneity in the sample by sorting the particles according to their size and charge. The results are presented in Figure 5.44.

Single QDs usually exhibit the spread pattern that was observed on lanes 1 and 2. They have a continuous distribution of sizes which does not lead to distinct bands as when separating proteins or DNA fragments by this method. Electrophoresis has also been used to separate nanoparticles bearing different numbers of oligonucleotides.[49] In the present case however the oligonucleotides were only 25 bp-long, and thus too short to induce any clear variation in electrophoretic mobility.

Both samples of QD-oligo therefore exhibited a very spread out band. The electrophoretic mobility of nanoparticles is known to decrease with increasing diameters.[49] QD-oligo 1 was made of slightly smaller QDs which on average should have a higher mobility. They indeed displayed an overall faster migration than QD-oligo 2 which were larger. Upon mixing to increasing ratios, a clearer band started to appear in the lower mobility region. This effect suggested that hybridisation not only occurred but also gave rise to relatively homogeneous assemblies. In the 1:1 mix there was still some spreading to higher mobilities indicating that it was not homogeneously composed of dimers but probably of larger aggregates, as well as dimers and remaining single particles. When increasing the ratio, the band consistently grew darker and confirmed the formation of larger aggregates.

In Tikhomirov's work[20] the valency of oligonucleotide-modified QDs was measured for QDs prepared with the same method that was followed here. It was shown to depend on the length of the QD-binding domain of the oligonucleotide and the QD diameter. In our case the QD-binding domain was a T6 tail, therefore all QDs are estimated to have a valency of two to three for the donors and three to four for the acceptors. Homogeneity seemed to be achieved with a 3:1 ratio which would be consistent with the valency of three to four predicted by Tikhomirov's work.[20]

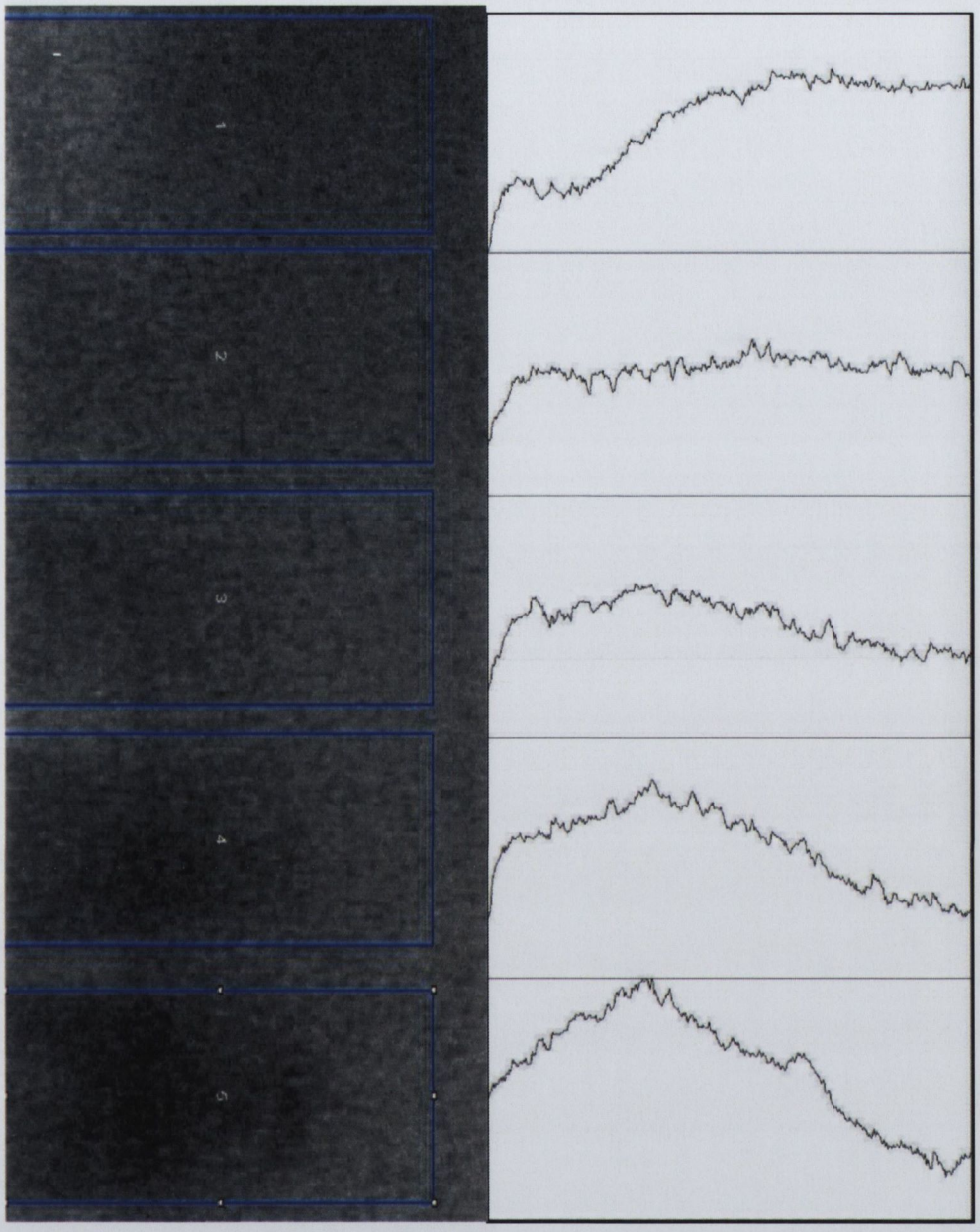

Figure 5.44 Gel electrophoresis of oligonucleotide-QD conjugates. Photograph of the gel (left) and intensity plot of the lanes (right). Lanes loaded as follows: 1) QD-oligo 1; 2) QD-oligo 2; 3) 1:1 mix of QD-oligo 1 and 2; 4) 2:1 mix of QD-oligo 1 and 2; 5) 3:1 mix of QD-oligo 1 and 2.

5.4.2 FRET studies

Having ensured the presence and hybridisation ability of complementary oligonucleotides on QD surfaces (in the previous section), we investigated the energy transfer capability of the nano-composites. Three sets of donor-acceptor pairs were synthesised. Their optical characteristics are displayed in Table 5.4.

Table 5.4 Characterisation of oligonucleotide-modified QDs

Sample	Oligonucleotide	Absorption (nm)	Emission (nm)	Quantum yield	Diameter (nm)	Zeta potential (mV)
Donor (a)	Oligo-2	525	558	27%	2.7	-44
Acceptor (a)	Oligo-1	556	592	25%	3.7	-29
Donor (b)	Oligo-1	535	560	50%	2.9	-35
Acceptor (b)	Oligo-2	601	644	51%	5.2	-40
Donor (c)	Oligo-2	531	567	6%	2.9	-47
Acceptor (c)	Oligo-1	556	592	25%	3.7	-29

In pair (a), the donor emission and acceptor absorption perfectly overlapped which was expected to produce very efficient energy transfer. In the second case, pair (b) the PL emissions were well separated which enabled good discrimination between them. In the third pair, there was near complete overlap both of absorption and emission spectra, allowing for mutual energy transfer. In each pair, the donor and acceptor were functionalised with oligonucleotide sequences complementary to each other.

Energy transfer in each donor-acceptor pair was investigated by measuring the PL emission of various donor-acceptor solutions of different composition. The donor quenching and acceptor enhancement were plotted against the donor-to-acceptor ratio. The donor quenching is defined as the ratio of the donor intensity in the mixed solution to that of the pure donor at the same concentration. Similarly the acceptor enhancement is defined as the ratio of the acceptor intensity in the mixed solution to that of the pure acceptor at the same concentration. It should be noted that donor and acceptor QDs can bind to each other in multiple configurations through oligonucleotide hybridisation and that the complementary domain is approximately 5 nm in length (15 base-pairs).[50] The predicted valency of our QD-oligo conjugate was three to four.[20]

In the first pair (donor (a) – acceptor (a)), as shown in Figure 5.45, the donor was rapidly quenched for ratios up to 0.5:1 where it reached 30% of the original value, and remained stable for ratios up to 1:1. When the acceptor was in excess, all donor QDs could be assumed to bind to acceptor QDs and to be quenched by them. For these lower ratios,

clusters of one donor and two or more acceptors could also form. It led to a slight degree of acceptor quenching through acceptor-to-acceptor intra-ensemble energy transfer due to spectral overlap of the acceptor absorption and emission. Enhancement of the acceptor PL thus was not observed as long as it was in excess.

When the donor-to-acceptor ratio was further increased, the donor emission slightly recovered and plateaued at around 40% of the original value. This was attributed to the possibility of donor-to-donor energy transfer due to partial overlap of donor absorption and donor emission spectra.[47] Meanwhile the acceptor emission was gradually enhanced up to 160% of its original value, thus confirming the occurrence of energy transfer.

When looking at a donor-acceptor pair (b) with well separated absorptions and emissions the interaction pattern appeared slightly different, as presented in Figure 5.46. At low donor-to-acceptor ratios, a similar trend of rapid donor quenching was observed, down to around 20%. The acceptor emission, however, was immediately enhanced to 120% and remained around that level independently of the amount of donor. The high FRET efficiency at low donor-to-acceptor ratio was due to the high quantum yield of both sets of QDs, while the rapid saturation of the acceptor enhancement was attributed to the spectral separation. As more donor was added its emission slightly recovered due to donor-to-donor intra-ensemble energy transfer but remained below 50%.

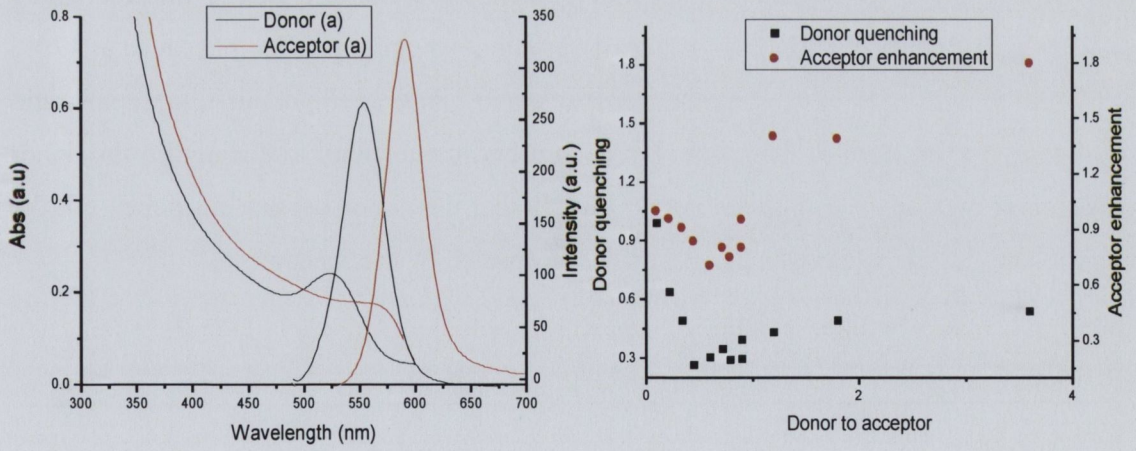

Figure 5.45 Left: Donor (a) and acceptor (a) UV-visible absorption and PL emission spectra. Right: Donor (a) quenching and acceptor (a) enhancement versus donor-to-acceptor ratio

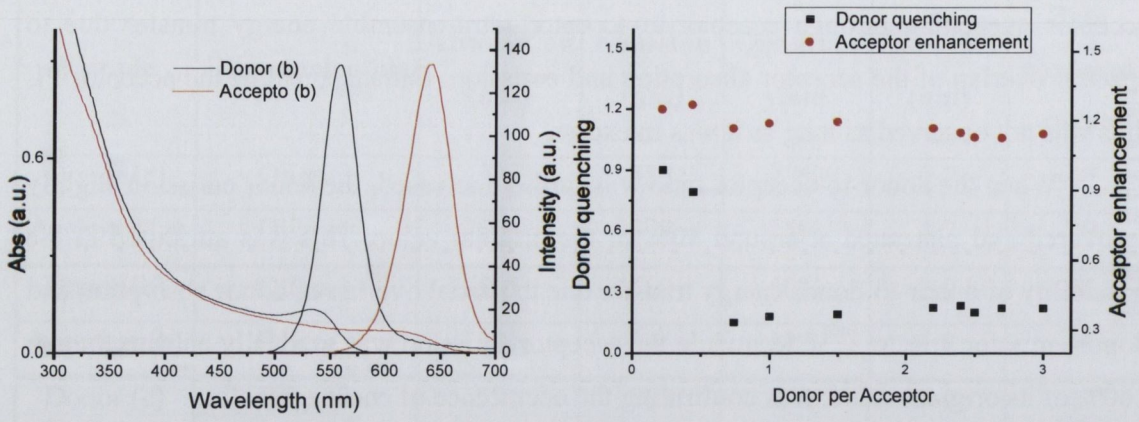

Figure 5.46 Left: Donor (b) and acceptor (b) UV-visible absorption and PL emission spectra. Right: Donor (b) quenching and acceptor (b) enhancement versus donor-to-acceptor ratio

Figure 5.47 shows how donor (c) and acceptor (c) had almost completely overlapping spectra. This meant that FRET could occur from acceptor to donor as well as from donor to acceptor. At low donor-to-acceptor ratio the so-called "acceptor" was quenched and the "donor" emission was enhanced. The species in excess was most likely to surround the other one through oligonucleotide hybridisation, thus transferring more energy than it received. When the ratio reached one-to-one the "acceptor" emission had fully recovered, while the donor was still 140% of its original value. It should be noted that the "donor" had a very rather low quantum yield of 6% and any energy transfer would therefore translate into a high percentage of variation. Its emission then plateaued at 120% while the acceptor emission continuously rose up to 180% as the donor-to-acceptor ratio was increased. Because of the spectral overlap it became difficult to distinguish the donor emission at high ratio. It is therefore very likely that the donor became quenched but the emission at that particular wavelength was compensated by the acceptor.

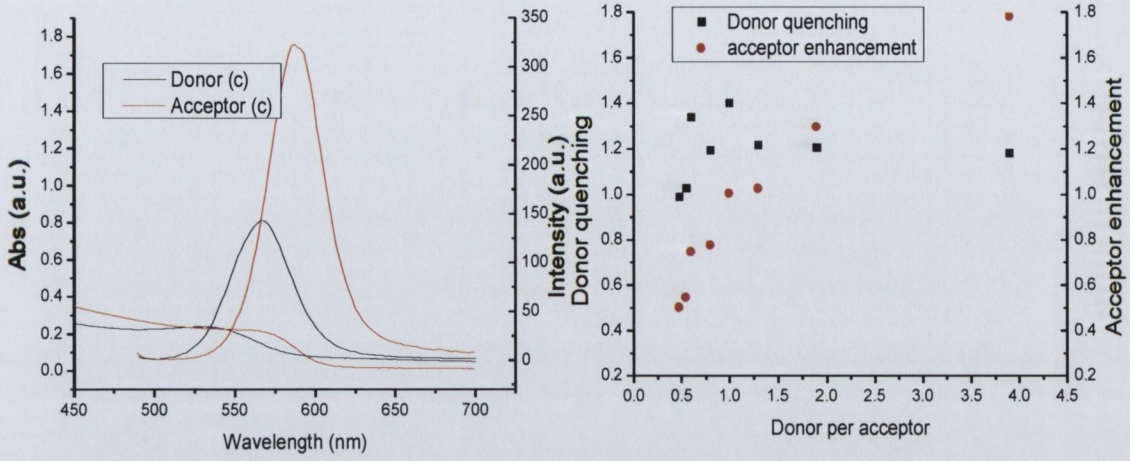

Figure 5.47 Left: Donor (c) and acceptor (c) UV-visible absorption and PL emission spectra. Right: Donor (c) quenching and acceptor (c) enhancement versus donor-to-acceptor ratio

In all cases, energy transfer was observed between QDs modified with complementary oligonucleotide sequences, and there was always a range of ratio for which one was quenched and the other was enhanced.

5.4.3 In vitro biological testing of Oligonucleotide-QD conjugates

Finally the oligonucleotide-modified QDs were investigated in live cell culture in order to test their potential use for *in vitro* studies based on the observation of hybridisation or separation of complementary DNA sequences and the observation of FRET.

In such experiments, minimising the spectral overlap of the fluorophores is extremely important in order to avoid bleed-though artefacts in confocal microscopy. This term refers to the phenomenon whereby the emission of one species is collected in both channels, and can only be reduced by decreasing the barrier filter range either for the excitation or the emission. In the case of QDs, separate excitation of each species is made impossible by the common broad absorption at energy higher than the band edge. This means that the emission spectra of the donor and the acceptor must be well separated to allow the quantitative FRET studies. Figure 5.48 illustrates the issue when imaging donor QD (a) and acceptor (a) in HT-1080 cell cultures. QD emissions were centred at 558 and 592 nm respectively therefore the best combination of filters were found to be 490-550 nm (green) and above 560 nm (red). Although the donor QD was only visible in the green

channel, the acceptor emitted in both channels. Therefore, only the donor-acceptor pair (b) was found suitable for quantitative *in vitro* FRET experiments.

Figure 5.48 Example of spectral bleed-through. Confocal microscope images of HT-1080 cells exhibiting internalised QDs. Top: donor (a). Bottom: acceptor (a). Left column: excitation 488 nm, emission 490-550 nm. Middle column: excitation 543 nm, emission above 560 nm. Right column: overlay of both channels with bright field.

Donor-acceptor (a) however provided some insight into the behaviour of QD-oligo conjugates in cells. When donor and acceptor were pre-incubated together for an hour in order to allow hybridisation to occur, the QDs were uptaken in very large aggregates, which was not observed when they were added simultaneously to the cell culture with no prior mixing. It was therefore concluded that the oligonucleotides effectively bound QDs together and that the binding persisted in live cells, but that the process was hindered either by diffusion issues or chemical interactions in the cell medium. The presence of distinct green, orange and red colours as seen in Figure 5.49 indicated that little or no energy transfer occurred. This was consistent with the observation that, at one-to-one ratio, none of the two species was quenched.

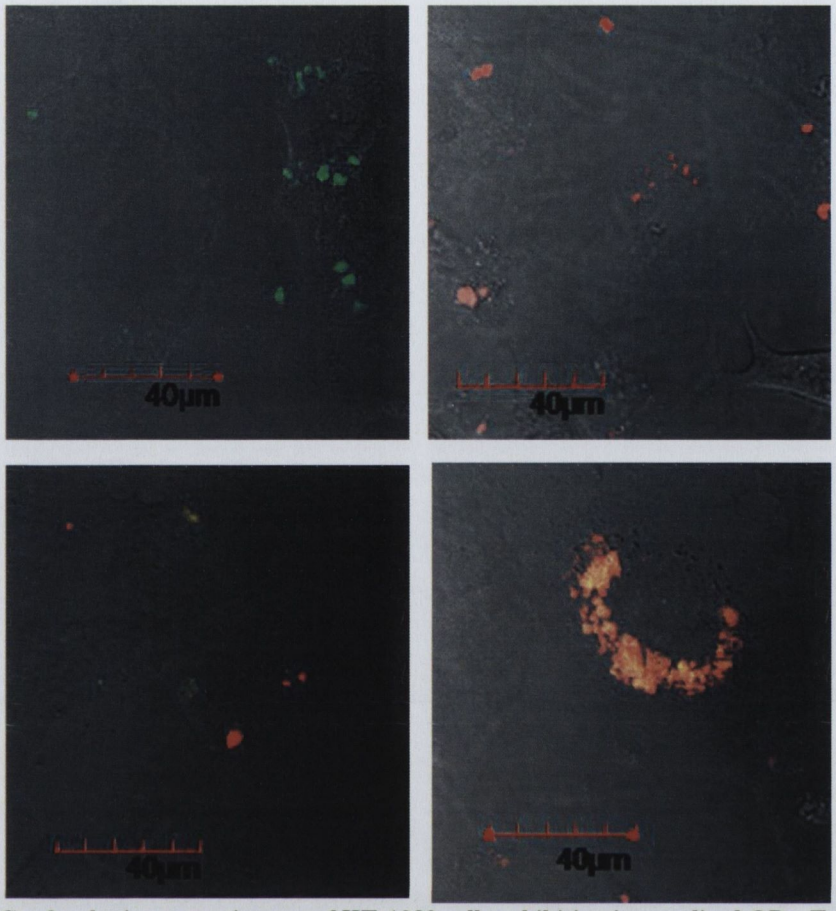

Figure 5.49 Confocal microscope images of HT-1080 cells exhibiting internalised QDs. Top left: donor (a). Top right: acceptor (a). Bottom left: donor (a) and acceptor (a) added simultaneously. Bottom right: donor (a) and acceptor (a) with pre-incubation.

Two cultures of HT-1080 cells from human fibrosarcoma were incubated with donor (b) and acceptor (b) respectively. Both types of QDs were readily uptaken and could be observed as isolated spots in the cytoplasm, green for the donor and red for the acceptor (pseudo-coloured for clarity purposes). A third culture was then incubated with donor and acceptor together, with no prior mixing. This resulted in the appearance of a few orange and yellow spots in the cells cytoplasm when overlaying the green and red channels, which indicated co-localisation of donor and acceptor, but green and red spots could mostly be seen.

Pre-incubation of donor and acceptor in equal concentrations for an hour and subsequent addition to the cell culture however resulted in the donor luminescence completely disappearing and the acceptor emission appearing enhanced. Thus this system

clearly demonstrated energy transfer (FRET) inside live HT-1080 cells. Example confocal images of all four types of cultures are displayed in

Figure 5.50. It was therefore concluded that preformed assemblies of QDs persisted in cell cultures but that binding did not spontaneously occur in that biological medium. The disappearance of all green emission confirmed the occurrence of FRET in the system with near complete quenching of the donor QDs.

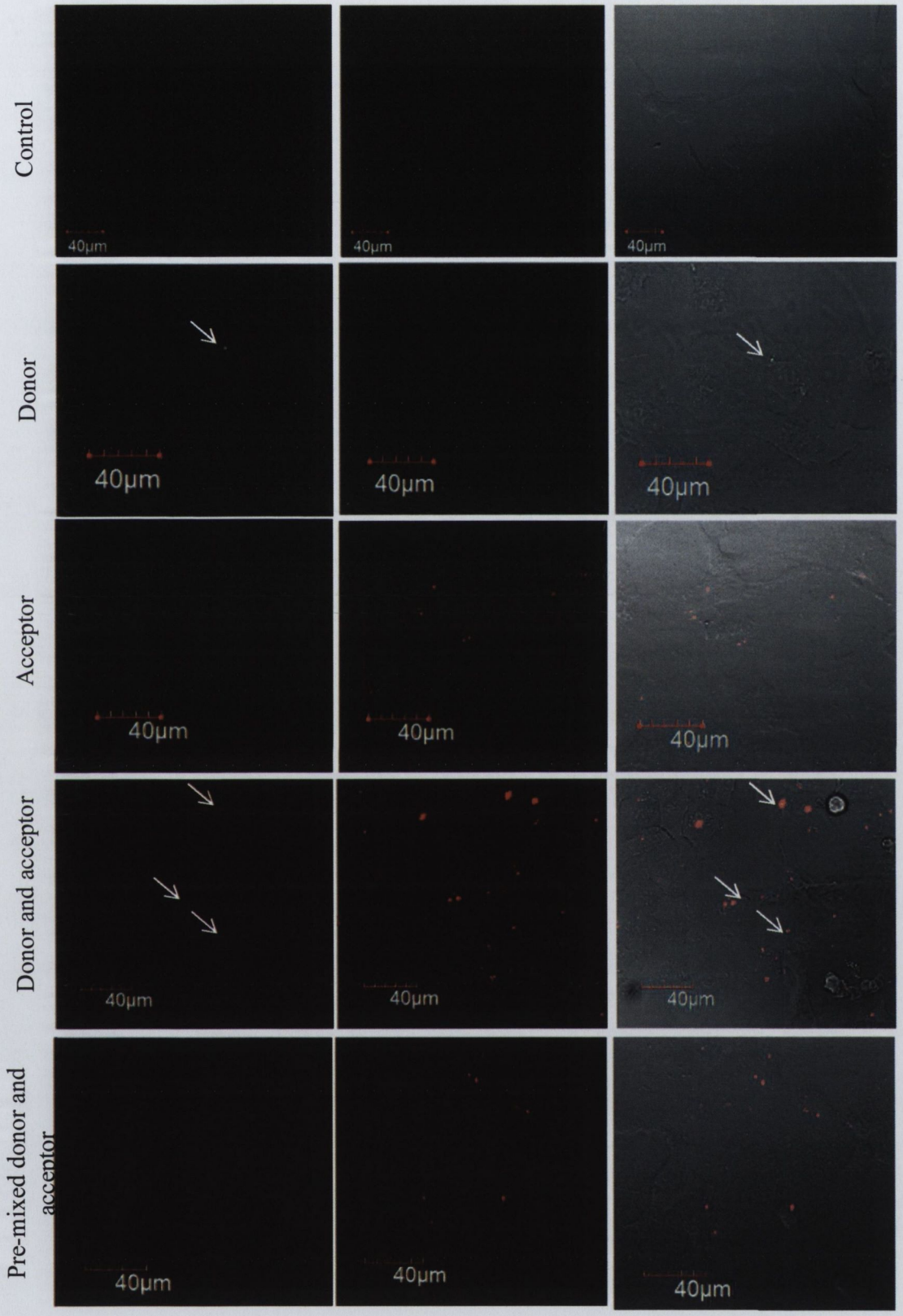

Figure 5.50 Confocal microscope images of HT-1080 cells exhibiting internalised QDs. First row: negative control; second row: donor (b); third row: acceptor (b); fourth row: donor (b) and acceptor (b) added simultaneously; fifth row: donor (b) and acceptor (b) with pre-incubation. First column: excitation 543 nm, emission 603 nm; second column: excitation 633 nm, emission 668 nm. Arrows indicate green QDs

Overall, these experiments proved that our composites were suitable for energy transfer studies in cell cultures *in vitro*. Further development of the system would open opportunities of *in vitro* sensing and elucidation of cellular mechanisms.

5.5 Conclusions

A range of new nano-composites comprising nanoparticles and oligonucleotides have been prepared and their optical properties have been investigated.

Plasmon-induced CD was measured for a variety of gold nanoparticles conjugated with oligonucleotides. It was shown to be highly dependent on nanoparticle aggregation but not as dependent on the particle shape. Further investigations are required for the development of chiral sensors based on this system.

The hybridisation property of complementary sequences of oligonucleotides was used to assemble nanoparticles. A range of characterisation techniques were employed to confirm the involvement of oligonucleotide hybridisation in the phenomena observed. When assembling QDs and AuNPs, complete quenching of the luminescence was recorded, which could be used for sensing. Longer oligonucleotide sequences should also be employed in this approach in order to achieve plasmonic enhancement of luminescence.

FRET was observed in oligonucleotide-mediated assemblies of QDs and its dependence on spectral overlap was investigated. As-produced aggregates were tested in cell cultures and were readily uptaken. Moreover, with an appropriate spectral overlap, FRET was demonstrated in live cells. This system has potential applications in biological imaging and *in vitro* biosensing.

Overall, we demonstrated the versatility of our conjugation methods, whether *in situ*, by ligand exchange, or by covalent coupling, and their adaptability to a range of materials. The investigation of the new nano-composites provided potential tools for the development of chemo- or bio-sensors.

References

[1] E. Defrancq, Y. Singh, N. Spinelli, *Current Organic Chemistry* **2008**, *12*, 263-290.

[2] A. O. Govorov, G. W. Bryant, W. Zhang, T. Skeini, J. Lee, N. A. Kotov, J. M. Slocik, R. R. Naik, *Nano Letters* **2006**, *6*, 984-994.

[3] Z. Wang, Y. Lu, *Journal of Materials Chemistry* **2009**, *19*, 1788-1798.

[4] R. Elghanian, J. J. Storhoff, R. C. Mucic, R. L. Letsinger, C. A. Mirkin, *Science* **1997**, *277*, 1078-1081.

[5] A. J. Mastroianni, S. A. Claridge, A. P. Alivisatos, *Journal of the American Chemical Society* **2009**, *131*, 8455-8459.

[6] J. J. Storhoff, R. Elghanian, C. A. Mirkin, R. C. Mucic, R. L. Letsinger, *Journal of the American Chemical Society* **1998**, *120*, 1959-1964.

[7] K. Hamad-Schifferli, J. J. Schwartz, A. T. Santos, S. Zhang, J. M. Jacobson, *Nature* **2002**, *415*, 152-155.

[8] F. McKenzie, D. Graham, *Chemical Communications* **2009**, 5757-5759.

[9] C. Gautier, T. Bürgi, *ChemPhysChem* **2009**, *10*, 483-492.

[10] T. Molotsky, T. Tamarin, A. B. Moshe, G. Markovich, A. B. Kotlyar, *The Journal of Physical Chemistry C* **2010**, *114*, 15951-15954.

[11] J. George, K. G. Thomas, *Journal of the American Chemical Society* **2010**, *132*, 2502-2503.

[12] I. E. Santizo, F. Hidalgo, L. A. Perez, C. Noguez, I. L. Garzon, *The Journal of Physical Chemistry C* **2008**, *112*, 17533-17539.

[13] V. Kitaev, *Journal of Materials Chemistry* **2008**, *18*, 4745-4749.

[14] A. O. Govorov, Z. Fan, P. Hernandez, J. M. Slocik, R. R. Naik, *Nano Letters* **2010**, *10*, 1374-1382.

[15] P. Anger, P. Bharadwaj, L. Novotny, *Physical Review Letters* **2006**, *96*, 113002.

[16] V. K. Komarala, Y. P. Rakovich, A. L. Bradley, S. J. Byrne, Y. K. Gun'ko, N. Gaponik, A. Eychmuller, *Applied Physics Letters* **2006**, *89*, 253118-253113.

[17] P. P. Pompa, L. Martiradonna, A. Della Torre, F. Della Sala, L. Manna, M. De Vittorio, F. Calabi, R. Cingolani, R. Rinaldi, *Nature Nanotechnology* **2006**, *1*, 126-130.

[18] H. Han, J. Zylstra, M. M. Maye, *Chemistry of Materials* **2011**, *23*, 4975-4981.

[19] W. J. Parak, D. Gerion, D. Zanchet, A. S. Woerz, T. Pellegrino, C. Micheel, S. C. Williams, M. Seitz, R. E. Bruehl, Z. Bryant, C. Bustamante, C. R. Bertozzi, A. P. Alivisatos, *Chemistry of Materials* **2002**, *14*, 2113-2119.

[20] G. Tikhomirov, S. Hoogland, P. E. Lee, A. Fischer, E. H. Sargent, S. O. Kelley, *Nature Nanotechnology* **2011**, *6*, 485-490.

[21] N. L. Rosi, C. A. Mirkin, *Chemical Reviews* **2005**, *105*, 1547-1562.

[22] A. Miyawaki, J. Llopis, R. Heim, J. M. McCaffery, J. A. Adams, M. Ikura, R. Y. Tsien, *Nature* **1997**, *388*, 882-887.

[23] I. L. Medintz, S. A. Trammell, H. Mattoussi, J. M. Mauro, *Journal of the American Chemical Society* **2003**, *126*, 30-31.

[24] N. Cicek, S. Nizamoglu, T. Ozel, E. Mutlugun, D. U. Karatay, V. Lesnyak, T. Otto, N. Gaponik, A. Eychmüller, H. V. Demir, *Applied Physics Letters* **2009**, *94*, 061105.

[25] S. Chanyawadee, P. Lagoudakis, R. Harley, M. Charlton, D. Talapin, H. Huang, C. Lin, *Advanced Materials* **2010**, *22*, 602-+.

[26] T. Franzl, T. A. Klar, S. Schietinger, A. L. Rogach, J. Feldmann, *Nano Letters* **2004**, *4*, 1599-1603.

[27] J. Lee, A. O. Govorov, N. A. Kotov, *Nano Letters* **2005**, *5*, 2063-2069.

[28] A. O. Govorov, *The Journal of Physical Chemistry C* **2011**, *115*, 7914-7923.

[29] S. J. Hurst, A. K. R. Lytton-Jean, C. A. Mirkin, *Analytical Chemistry* **2006**, *78*, 8313-8318.

[30] R. C. Mucic, J. J. Storhoff, C. A. Mirkin, R. L. Letsinger, *Journal of the American Chemical Society* **1998**, *120*, 12674-12675.

[31] C. M. Niemeyer, B. Ceyhan, M. Noyong, U. Simon, *Biochemical and Biophysical Research Communications* **2003**, *311*, 995-999.

[32] J. J. Storhoff, C. A. Mirkin, *Chemical Reviews* **1999**, *99*, 1849-1862.

[33] A. Moores, F. Goettmann, *New Journal of Chemistry* **2006**, *30*, 1121-1132.

[34] I. Lieberman, G. Shemer, T. Fried, Edward M. Kosower, G. Markovich, *Angewandte Chemie International Edition* **2008**, *47*, 4855-4857.

[35] I. Lieberman, G. Shemer, T. Fried, Edward M. Kosower, G. Markovich, *Angewandte Chemie International Edition* **2008**, *47*, 4855-4857.

[36] F. J. Garcia de Abajo, *The Journal of Physical Chemistry C* **2008**, *112*, 17983-17987.

[37] Z. Fan, A. O. Govorov, *Nano Letters* **2010**, *10*, 2580-2587.

[38] J.-M. Ha, A. Solovyov, A. Katz, *Langmuir* **2009**, *25*, 10548-10553.

[39] M. P. Moloney, Y. K. Gun'ko, J. M. Kelly, *Chemical Communications* **2007**, 3900-3902.

[40] S. D. Elliott, M. P. Moloney, Y. K. Gun'ko, *Nano Letters* **2008**, *8*, 2452-2457.

[41] S. A. Gallagher, M. P. Moloney, M. Wojdyla, S. J. Quinn, J. M. Kelly, Y. K. Gun'ko, *Journal of Materials Chemistry* **2010**, *20*, 8350-8355.

[42] J. E. Govan, E. Jan, A. Querejeta, N. A. Kotov, Y. K. Gun'ko, *Chemical Communications* **2010**, *46*, 6072-6074.

[43] S. A. Claridge, S. L. Goh, J. M. J. Frechet, S. C. Williams, C. M. Micheel, A. P. Alivisatos, *Chemistry of Materials* **2005**, *17*, 1628-1635.

[44] S.-J. Park, A. A. Lazarides, J. J. Storhoff, L. Pesce, C. A. Mirkin, *The Journal of Physical Chemistry B* **2004**, *108*, 12375-12380.

[45] M. Lunz, V. A. Gerard, Y. Gun'Ko, V. Lesnyak, N. Gaponik, A. Susha, A. L. Rogach, A. L. Bradley, *Nano Letters* **2011**, *11*, 3341-3345.

[46] H. Zhang, Z. Zhou, B. Yang, M. Gao, *The Journal of Physical Chemistry B* **2002**, *107*, 8-13.

[47] C. Higgins, M. Lunz, A. L. Bradley, V. A. Gerard, S. Byrne, Y. K. Gun'ko, V. Lesnyak, N. Gaponik, *Optics Express* **2010**, *18*, 24486-24494.

[48] V. A. Gerard, Y. K. Gun'ko, E. Defrancq, A. O. Govorov, *Chemical Communications* **2011**, *47*, 7383-7385.

[49] R. A. S. T. Pellegrino, A. P. Alivisatos, and W. J. Parak, *Journal of Biomedicine and Biotechnology* **2007**, *2007*, 9.

[50] C. Rivetti, S. Codeluppi, *Ultramicroscopy* **2001**, *87*, 55-66.

Chapter 6

Conclusions and Future Work

6.1 Conclusions

In this work, a series of new nanocomposite materials based on CdTe Quantum Dots and metal nanoparticles have been prepared and investigated. These materials have a broad range of potential applications in biological imaging, biomedicine and sensing. The main conclusions of our work are summarised below.

First of all, the preparation of anisotropic gold and silver nanoparticles was optimised. The mechanism of formation of hollow "nanoboxes" was investigated by exploring the possibility of encapsulating materials. Metal nanoparticles also demonstrated good internalisation in live cells and low cytotoxicity. They are therefore good candidates for drug delivery applications.

Secondly, we used gelatin to develop a variety of composite nanomaterials. It was demonstrated that gelatin improves the stability and biocompatibility of nanomaterials, and constitutes a substrate for further functionalisation. Folic acid was covalently bound to gelatinated QDs and was successfully recognised by cancer cells thus increasing the nanoparticle uptake. Metal nanoparticles were also coated in gelatin with various thicknesses and QDs were trapped in the shell. This resulted in a model for a multi-functional system combining a nanoparticle as a vehicle, a drug molecule encapsulated in a gelatin layer and a recognition element at the surface.

Thirdly, oligonucleotides were specially designed to be conjugated to QDs or metal nanoparticles. Using the terminal amine, the phosphorothioate tail and the hybridising capability of complementary sequences, we prepared a series of composites of various compositions and configurations. This was proven to be a very useful tool for investigating the optical properties of QDs, metal nanoparticles, and combinations of them both. Gold nanoparticles exhibited new CD in the Plasmonic range when modified with oligonucleotides which opened a new direction in CD studies and can be potentially used for chiral sensing. FRET was observed in QD systems; we highlighted the dependence on

spectral overlap as well as its persistence in *in vitro* cell cultures. This could potentially be used for bioimaging and elucidation of metabolic mechanisms. Nanocomposites of QDs and metal nanoparticles were also produced and studies of these systems have shown that the interaction between QDs and metal nanostructures leads to luminescence quenching. Such a system can also potentially be used for sensing. We believe that the use of longer oligonucleotides should prevent quenching. Overall we have demonstrated the versatility of our conjugation methods and the possibilities of our functionalised oligonucleotides.

Overall, it is expected that this research work will contribute to the development of new nanomaterials and further progress in the areas of bionanotechnology and biosensing.

6.2 Preliminary studies and future work

Future work will involve further development of functional nano-composites for biomedical applications. It will include the development of our functionalised gelatinated QDs with different biomolecules to serve more targeted purposes.

In depth biological studies of functionalised gold-silver nanoboxes will be carried out. Conditions for optimal drug loading and release will be investigated as well as the functionalisation with target elements with better selectivity and specificity than folic acid.

The oligonucleotide-mediated approach to assemblies of QDs and metal nanoparticles should provide a platform for energy transfer-based bio- and chemo-sensing. Varying the length of the oligonucleotide sequences will give control over luminescence quenching or enhancement.

We also aim to investigate the emergence of circular dichroism (CD) in nanoparticle systems and its consequences for biological interactions.
Our preliminary studies and future work are detailed below.

6.2.1 Heparin-modified QDs

This part of the work was carried out in close collaboration with Dr. Tatsiana Rakovich and Ciaran Maguire, Institute of Molecular Medicine, Trinity College Dublin.

Heparin is a sulphated polysaccharide which is mainly known for its anti-coagulant properties. Its structure is presented in Figure 6.1. Heparin chains can range from 3,000 to

30,000 Da and carry 75 to 100 negative charges each, making heparin one of the most charged biomolecules.

Heparin is synthesised and stored in mast cells which are located either in connective or mucosal tissues and are part of the immune system. Heparin, or more accurately its sulphate derivative, is involved in a number of biological processes such as anticoagulation, regulation of cell differentiation and cell growth through growth factors and control of chemokine signalling.[3]

Heparin can selectively bind to a receptor called Mac-1 which is found on macrophages, and be internalised that way.[4] It has also been shown that heparin-modified polymer microspheres were able to enter eukaryotic cells *via* a process similar to that of the bacteria *Chlamydia trachomatis*.[5] Furthermore, internalised heparin has exhibited cytotoxicity towards cancer cells by interfering with transcription factor activity and inducing apoptosis.[2]

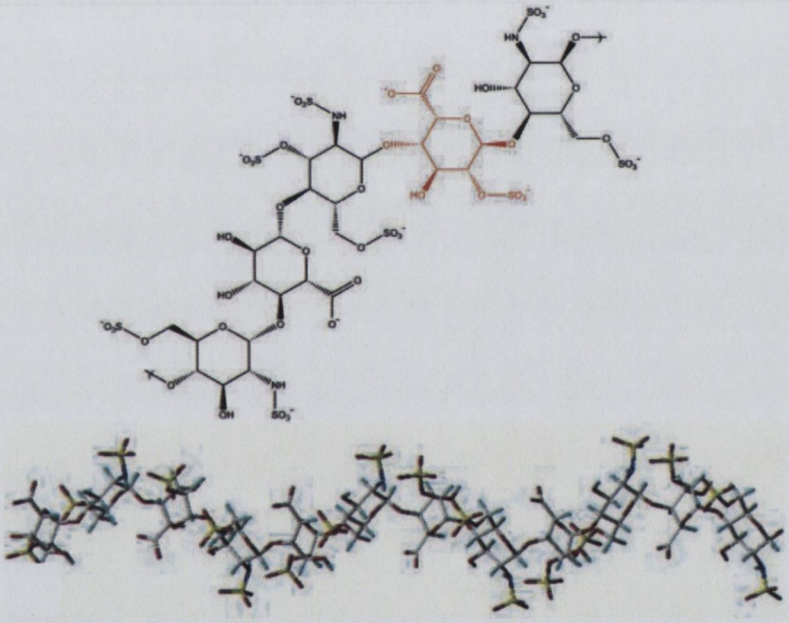

Figure 6.1 Top: Pentasaccharide antithrombin binding site of heparin. A single saccharide unit is shown in red.[1] 3D representation of the structure of a small heparin chain.[2]

Following the procedure developed for the preparation of FA-QD conjugates,[6] heparin -QD (Hep-QD) conjugates were synthesised. The presence of heparin was expected to increase the uptake of QDs by macrophages such as THP-1 cells. Table 6.1 gathers the characterisation details for the resulting Hep-QD as well as TGA and TGA-gel QDs which were synthesised simultaneously. They were produced with similar optical properties, namely UV-visible absorption and PL emission spectra as well as QY. This also

implied that they had the same core diameter. DLS measurements however highlighted a significant increase in hydrodynamic diameter from TGA-QD to TGA-gel QD and Hep-QD which could be attributed in the latter case to the presence of heparin. Zeta potential measurements also supported that conclusion with an increase in the negative charge associated with heparin.

Table 6.1 Characteristics of selected TGA, TGA-gel and Heparin conjugated CdTe QDs

QD type	Max Absorption	Max Emission	QY	Core diameter	Hydrodynamic diameter	Zeta potential
TGA	558 nm	587 nm	35 %	3.3 nm	10 nm	-37.4 mV
TGA-gel	569 nm	594 nm	36 %	3.4 nm	16 nm	-39.1 mV
TGA-gel-Heparin	556 nm	593 nm	32 %	3.3 nm	25 nm	-49.5 mV

These three selected types of QDs were subsequently tested in cell cultures: THP-1 macrophages, A549 epithelial cells and Caco-2 adenocarcinoma cells.

In the case of the live THP-1 cells the uptake of TGA-gel QDs was the lowest of all three. Sample images are presented in Figure 6.2. It was previously observed that TGA QDs yielded a greater uptake than TGA-gel in Caco-2 and HT-1080 cells (Chapter 4). Hep-QDs were better internalised than TGA-gel QDs, although to a slightly smaller extent than TGA-QDs. A major difference however lies in the location of the QDs. TGA-QDs were only found in the cytoplasm, as previously reported,[7-11] whereas Hep-QDs were observed both in the cytoplasm and inside of the nucleus. This suggested that the mode of internalisation was different for TGA- and Hep-QDs. The involvement of Mac-1 receptors allowed Hep-QDs to penetrate the nucleus whereas non-specific phagocytosis restricted TGA-QDs to vesicles, lysosomes or endosomes in the cytoplasm. It was previously demonstrated that only small CdTe QDs (< 2.5 nm) were able to penetrate the nucleus.[11-12] Functionalisation with heparin enabled particles as large as 3.3 nm to enter the nucleus.

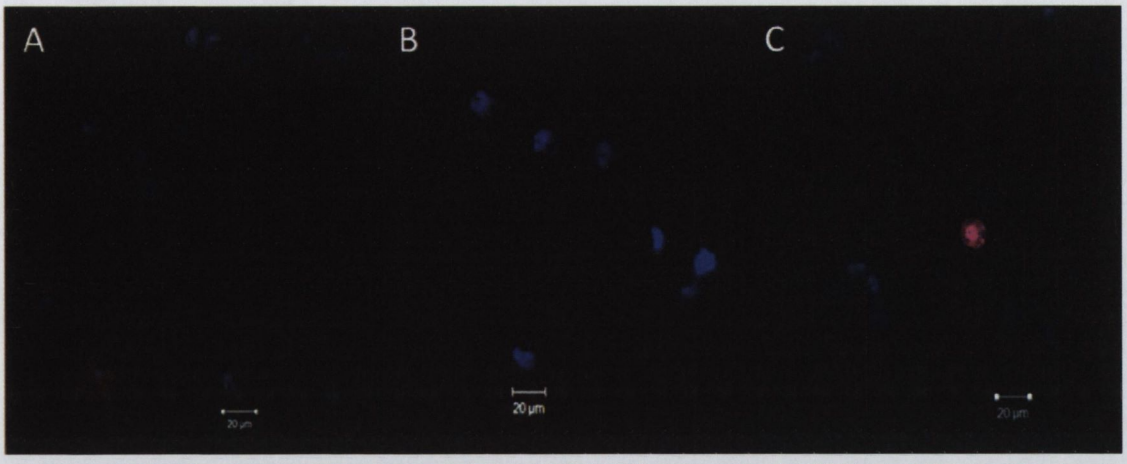

Figure 6.2 Confocal microscopy images of live THP-1 cells treated with (A) TGA-QDs, (B), TGA-gel QDs and (C) Hep-QDs. Nuclei are stained with Hoechst (blue)

A549 cells are an adherent adenocarcinoma human alveolar basal epithelial cell line and are commonly used as a reference cell line in the biological testing of nanomaterials and QDs.[6, 13] They are not phagocytic, and therefore this mode of internalisation was mostly excluded. Confocal imaging (Figure 6.3) revealed that TGA-gel QDs showed the highest uptake by this cell line compared to TGA and Hep-QDs. Since A549 cells have restricted phagocytic capabilities and no Mac-1 receptors, the uptake of all types of QDs was very limited and their location only in the cytoplasm. Heparin had little effect on the uptake of QDs by this cell line. Similar results were observed with Caco-2 cells, with even lower levels of internalisation of all three types.

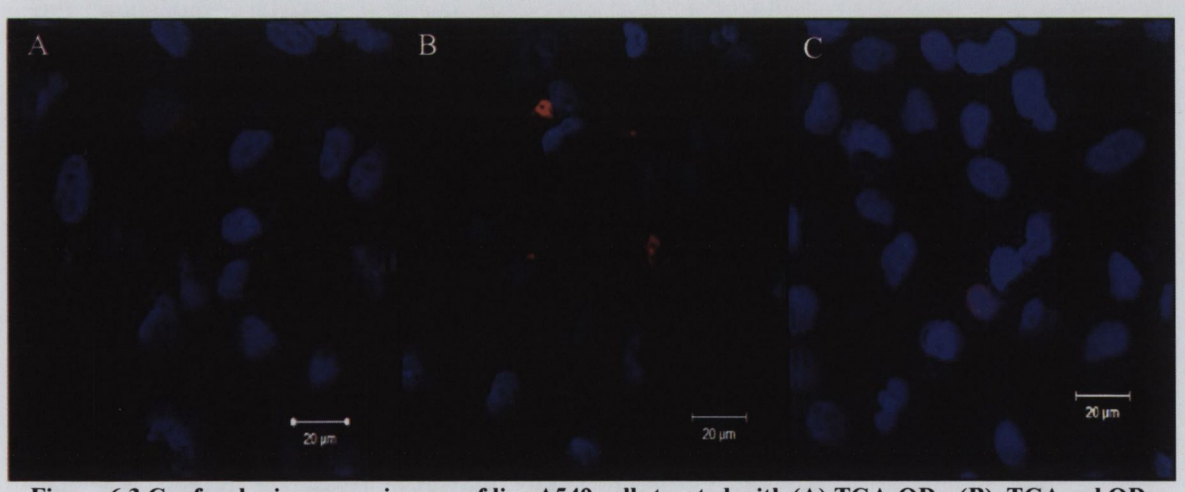

Figure 6.3 Confocal microscopy images of live A549 cells treated with (A) TGA-QDs, (B), TGA-gel QDs and (C) Hep-QDs. Nuclei are stained with Hoechst (blue)

Permeabilising and fixing the cells usually increase the uptake of nanoparticles considerably. This was observed here, and Hep-QD provided excellent visualisation of the

cytoplasms, nuclei and nucleoli of all the cell lines (Figure 6.4), with a better resolution than TGA- or TGA-gel QDs.

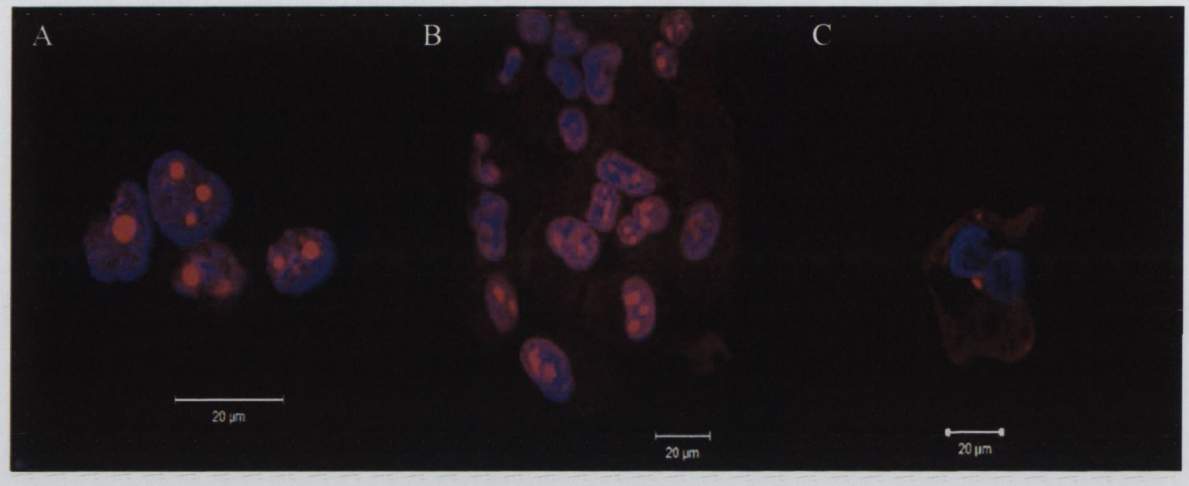

Figure 6.4 Confocal microscopy images of fixed permeabilised (A) THP-1, (B) A549 and (C) Caco-2 cells treated with Hep-QDs. Nuclei are stained with Hoechst (blue)

It was thus demonstrated that heparin was successfully bound to TGA-gel QDs to form a new nanocomposite which was selectively internalised by macrophages. They may be employed for flow cytometry applications. The Hep-QD conjugates also readily illuminated the cell interior and allowed the differentiation between the cytoplasm, nucleus and nucleolus which could be useful for biological imaging. Further investigations are required to optimise the loading of heparin onto QDs as well as to fully understand the mechanism of uptake of the composites.

6.2.3 Biological testing of chiral CdS nanotetrapods

Nanotetrapods are a particular type of quantum-confined, luminescent nanostructures. The synthesis of chiral CdS nanotetrapods has previously been developed in our group.[14] They consist in CdS nanocrystals with four arms, and stabilised with L-Penicillamine (L-Pen), D-Penicillamine (D-Pen), or the racemate (Rac-Pen). Figure 6.5 gathers their spectral characteristics as well as morphology as elucidated by TEM.

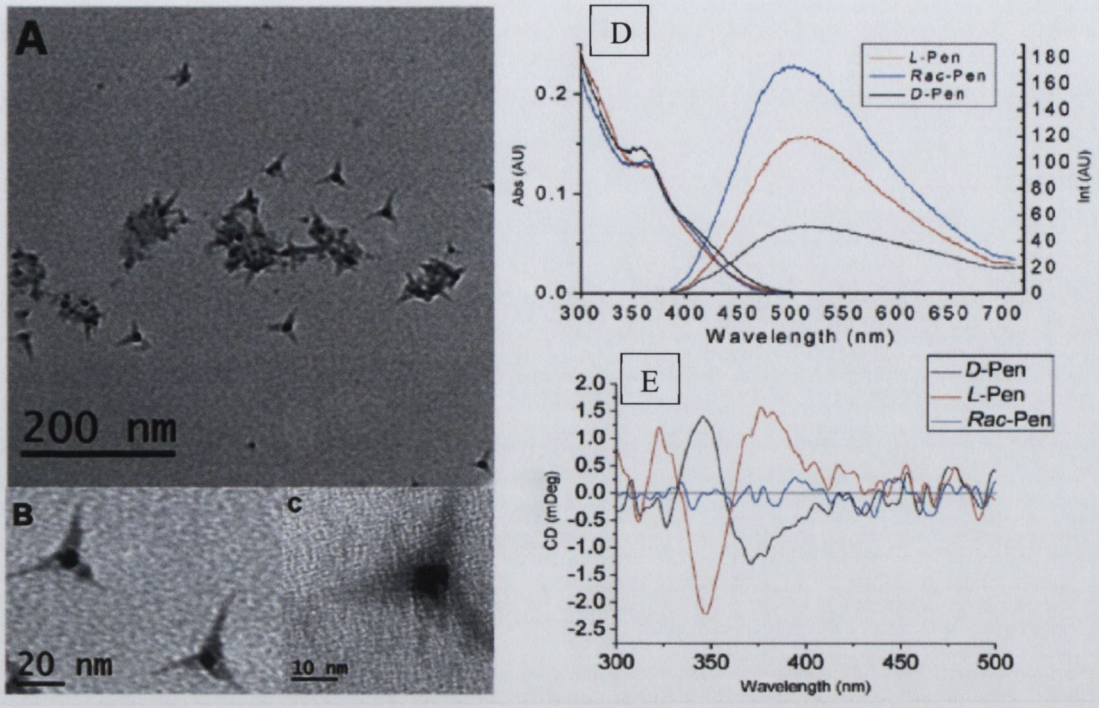

Figure 6.5 A wide field TEM images of D-Pen nano-tetrapods showing a number of tetrapods (A), a closer look of two tetrapods (B) and a high-resolution image of a single tetrapod (C). UV-VIS, PL (D) and CD (E) spectra of Pen stabilised CdS.[14]

Their peculiar shape raised the question of interactions with live cells. Additionally, chirality should also influence the cellular uptake. For these reasons, HT-1080 cells were treated with L-, D- and Rac-Pen stabilised CdS nanotetrapods and analysed by confocal microscopy.

The confocal images (Figure 6.6) clearly showed a very high uptake of the D-Pen stabilized nanoparticles which illuminated the cytoplasm of a number of cells. On the other hand, only a few isolated aggregates of L-Pen stabilized particles were visible. In the case of the Rac-Pen particles, a higher number of spots were visible inside the cells than with L-Pen, but no cell exhibited a cytoplasm filled of particles like in the case of D-Pen.

Integrating the luminescence intensity on each image, and averaging over the various fields, provided confirmation of the higher uptake of D-Pen over L-Pen nanotetrapods, with Rac-Pen falling somewhere in between. This information is plotted in Figure 6.7.

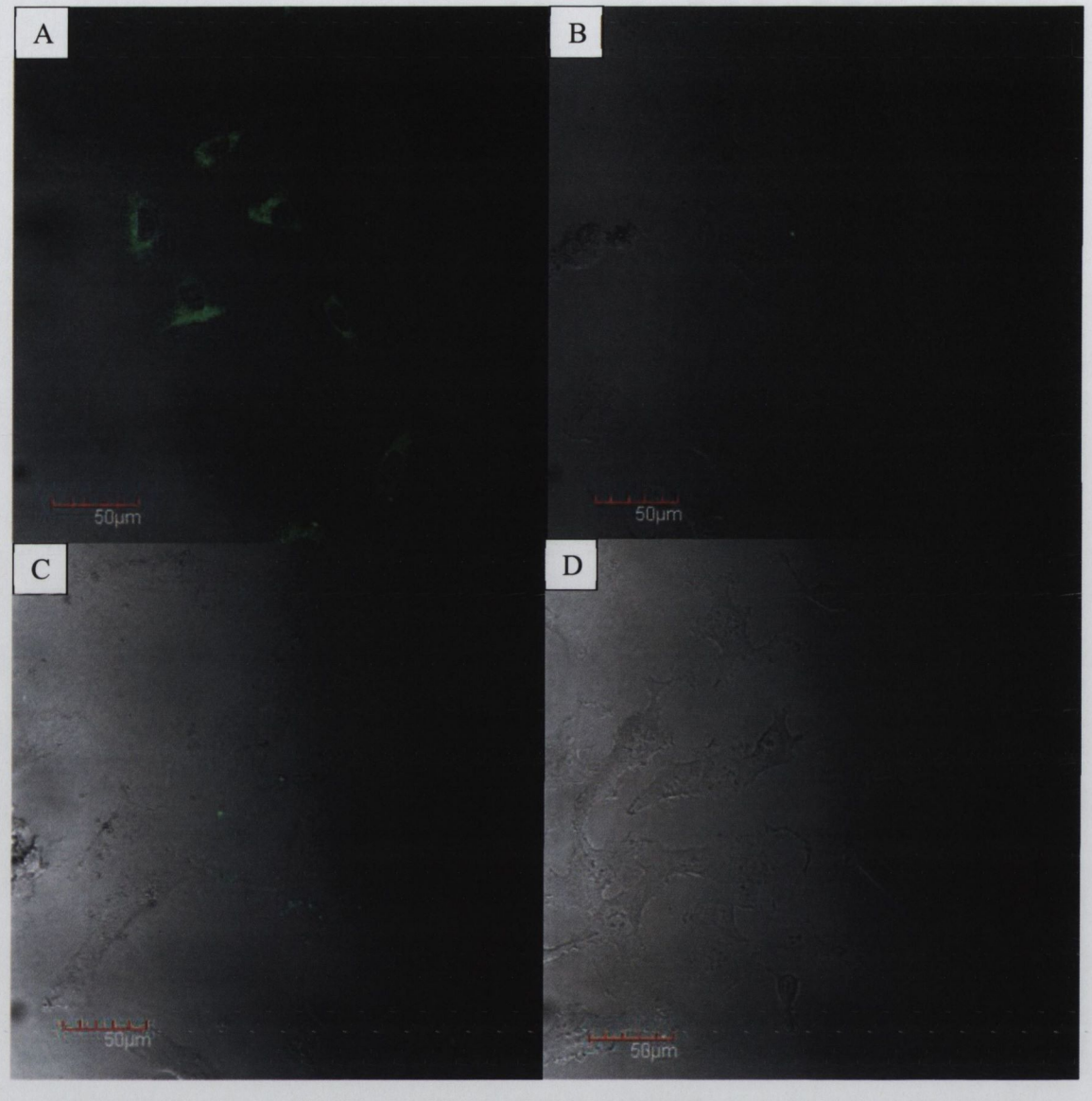

Figure 6.6 Confocal images of HT-1080 cells treated with D-Pen (A), L-Pen (B) and Rac-Pen (C). Control, untreated HT-1080 cells (D). Bright field and green luminescence channels were merged.

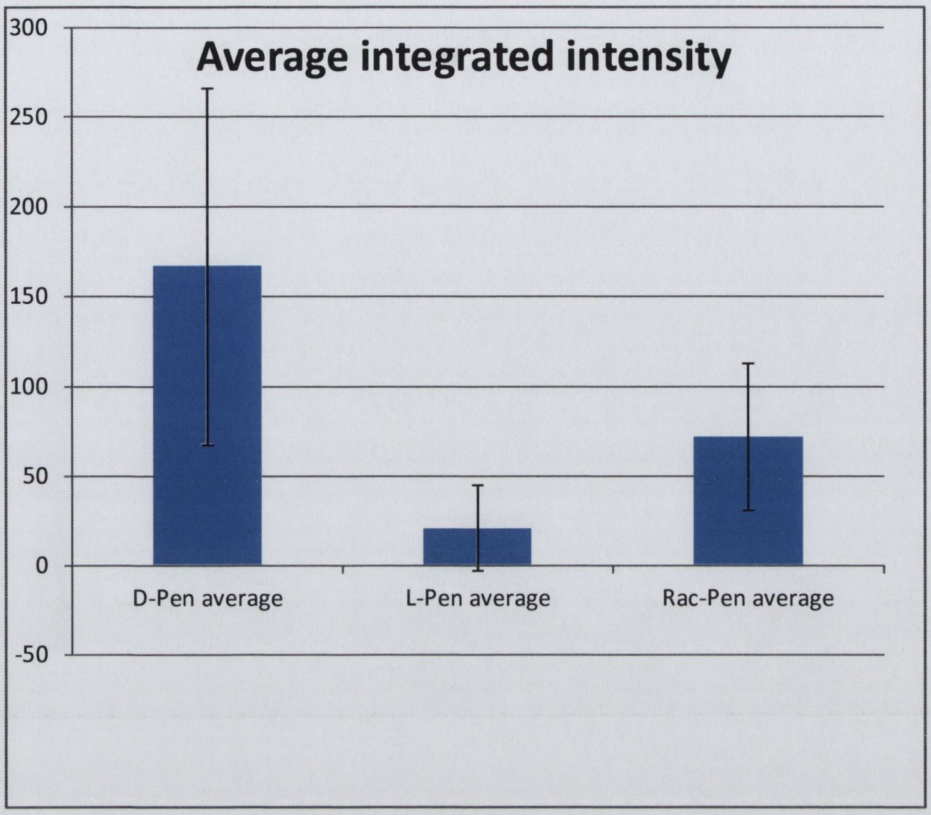

Figure 6.7 Average integrated intensity generated by QDs in cells

These results may seem counter-intuitive at first, knowing that L-Pen is the enantiomer that is naturally internalised through the amino acid endocytosis pathway. It was therefore postulated that nanotetrapod uptake in this case was not driven by the amino-acid recognition. It was previously reported that the stabilisation of CdS QDs with penicillamine lead to local distortions of the semiconductor crystal with a chirality opposite to that of the stabiliser enantiomer.[15] It is possible that cells preferentially uptake (D-Pen stabilised) nanotetrapods having opposite *L*-chirality.

To obtain further information on the mode of interaction between tetrapods and cells, free D-Pen, which was expected to bind to the CdS surface, was added to the culture medium jointly with each type of nanotetrapods. The different degrees of uptake obtained are presented in Figure 6.8. In all cases, the uptake was reduced to about half of its value for nanotetrapods only. D-Pen is known to chelate metal ions and prevent them for entering the cells.[16] This mechanism is likely to be involved here. The action of additional D-Pen binding to the surface does not induce further chiral distortion, which would increase the uptake. Further detailed investigations are required to fully understand both

the interaction of D-Pen with preformed nanotetrapods and the chiral selectivity endocytosis. In particular, the nanotetrapods will be tested in other cell lines.

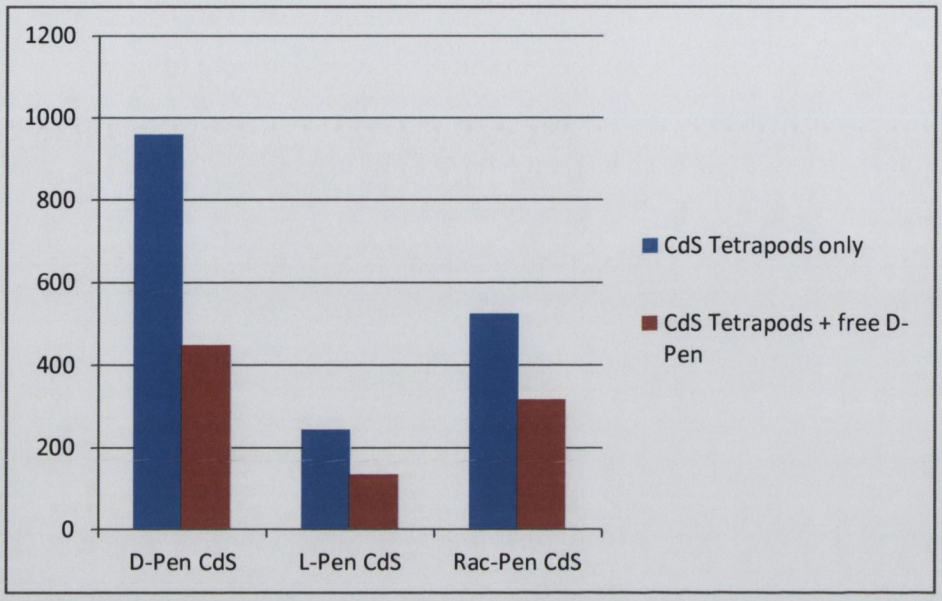

Figure 6.8 Internalisation of D-, L- and Rac-Pen CdS tetrapods in absence and presence of free D-Pen in the cell culture medium

6.2.4 Solid-state CD

In Chapter 5, we demonstrating the generation of plasmon-induced CD highlighted the importance of aggregation (after centrifugation) in the phenomenon. It was postulated that some mechanical action was involved in the process, and that CD enhancement could potentially be pressure dependent.

In order to test that hypothesis, various samples of chiral and achiral nanomaterials and molecules were deposited and dried on glass slides. This allowed recording their solid-state CD. A second glass slide was applied and tied increasingly closely to induce more pressure. Figure 6.9 illustrates the effects observed on some systems composed of metal nanoparticles and a chiral species.

D-Penicillamine stabilised gold nanoparticles (D-Pen AuNP) exhibited, in solid-state, similar spectral features to those in solution. The light path was much smaller in the case of solid state due to the reduced thickness of a deposited film. Consequently, the penicillamine CD signature in the UV which was saturated in solution disappeared in solid-state with no pressure. Comparatively the signal generated by AuNPs was strongly

enhanced. When sufficient pressure was applied all features including that in the UV region were enhanced.

None of this was observed for metal nanoparticles on their own, or chiral molecules without nanoparticles. Similar effects, were observed with silver nanoprisms (AgNP) interacting with DNA. Plasmon-induced CD in this case is very weak in solution and easily hindered by the strong signal of DNA. In solid state however, CD in the plasmon region was in the same order of magnitude than that of DNA.

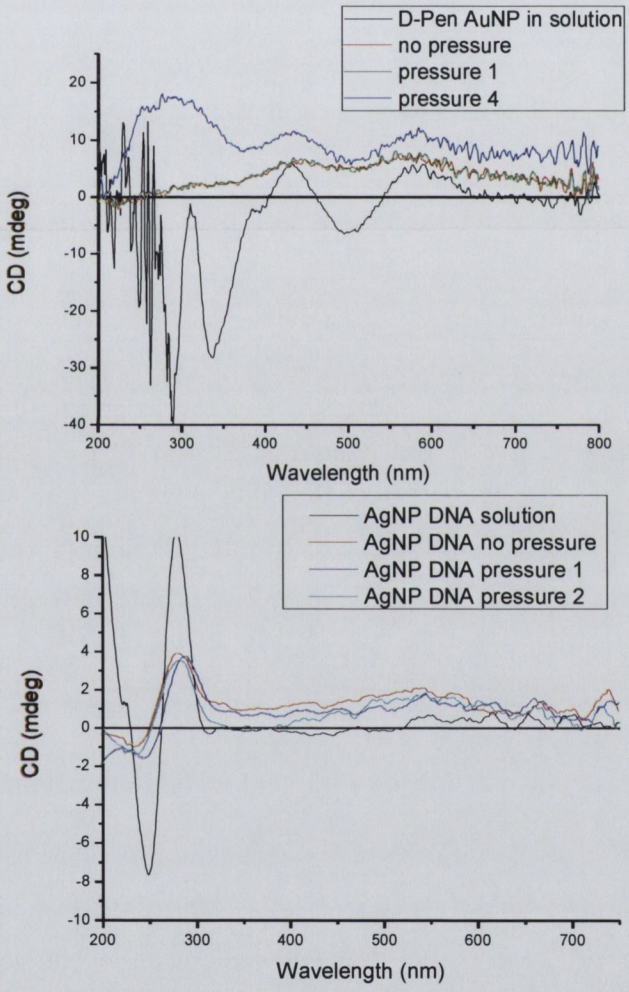

Figure 6.9 Solid-state CD spectra of (top) D-Pen AuNP and (bottom) Ag Nanoprisms in presence of DNA, and comparison with the same in solution.

Controlled pressure dependence proved difficult to achieve especially when dealing with weak signals. However, silver nanowires exhibited very strong signals in solutions (Chapter 3). Figure 6.10 shows that their solid-state CD could be enhanced by gradual pressure increase.

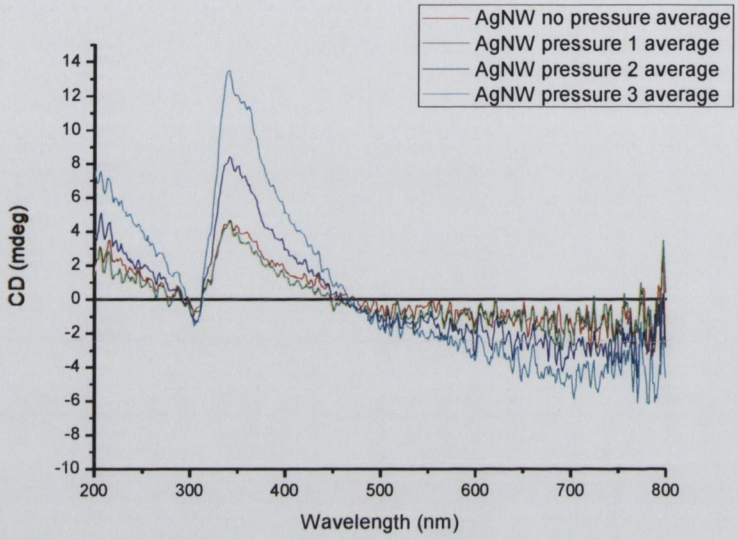

Figure 6.10 Solid-state CD spectra of silver nanowires showing the pressure dependence

The origin of CD effects observed in solid state as well as their pressure dependence still remains unclear. Further detailed investigation and theoretical modelling are required to elucidate the mechanisms involved. A whole new set-up allowing to accurately controlling the pressure applied must also be developed.

6.2.5 Infiltration of polymer tubing with gold metal nanoparticles

Percutaneaous coronary angioplasty is a therapeutic procedure used to reduce the narrowing of artery sections caused by artherosclerosis. Untreated, this condition can lead to ischemia, infarction, stroke, and death.[17] The procedure consists in inserting a deflated balloon in the artery up to the blocked section, and to inflate the balloon in order to dilate the artery, as illustrated in Figure 6.11. The balloon is then removed.

The device currently commercialised by Medtronic Inc. is composed of a Poly(amide-6-*b*-ethylene oxide) (Pebax®) 6333 SA 01 Med polymer catheter supporting the balloon. Positioning the balloon precisely at the correct section of the artery is of outmost importance. This is currently done by X-ray imaging monitoring of two platinum

rings on the catheter, at either side of the balloon (Figure 6.12). This remains delicate to visualise as rings must be made small enough not to impede the flexibility of the catheter. There is therefore a need for a better process that would make the balloon bearing segment of the catheter X-ray opaque.

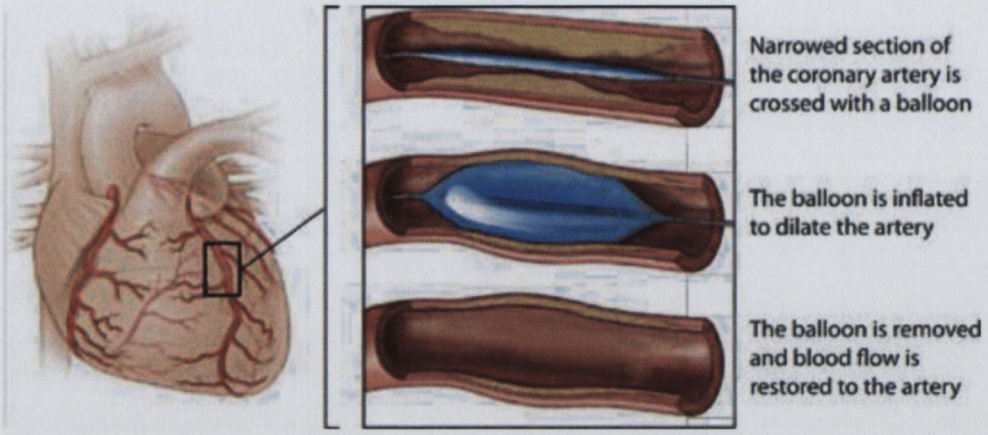

Figure 6.11 Schematic illustration of balloon dilatation catheter application.[18]

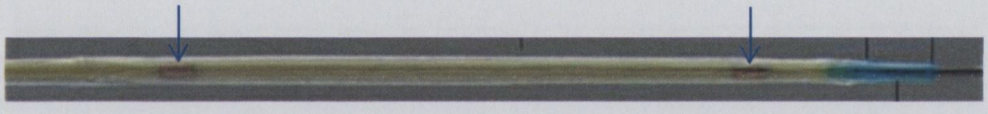

Figure 6.12 Photograph of a catheter bearing the X-ray opaque platinum markers indicated by the arrows

Pebax® is a block-copolymer with the general chemical formula presented in Figure 6.13. It is composed of polyethylene and polyamide blocks which make it very resistant to a variety of solvents.[19]

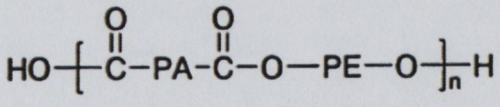

Figure 6.13 Chemical formula of Pebax. PA: polyamide block. PE: polyethylene block.

One proposed method is to infiltrate the catheter with gold nanoparticles. It presents the advantage of altering the catheter itself rather than the starting polymer which would shorten the clinical trials if it was to be commercialised. Infiltration was intended through polymer swelling, according to a method developed in our group.[20-21] A series of

solvents were investigated to optimise the swelling of the polymer tube, and maximise the loading with gold nanoparticles.

Dichloromethane (DCM) showed the best results, with a coloration of the tube visible to the naked eye. The tube was soaked in solvent for an hour before concentrated nanoparticles were added, and the sample was placed in an ultrasonic bath for 1h, 2h, or 4h. SEM examination provided some appreciation of the degree of loading as seen in Figure 6.14. The main difficulty was to image a clean cross-section in order to evaluate the depth of penetration. After 1h of ultrasonic agitation, only few nanoparticles were visible either on the surface or in the section. Two hours appeared to give the best loading, while four hours seemed to damage the polymer without improving infiltration.

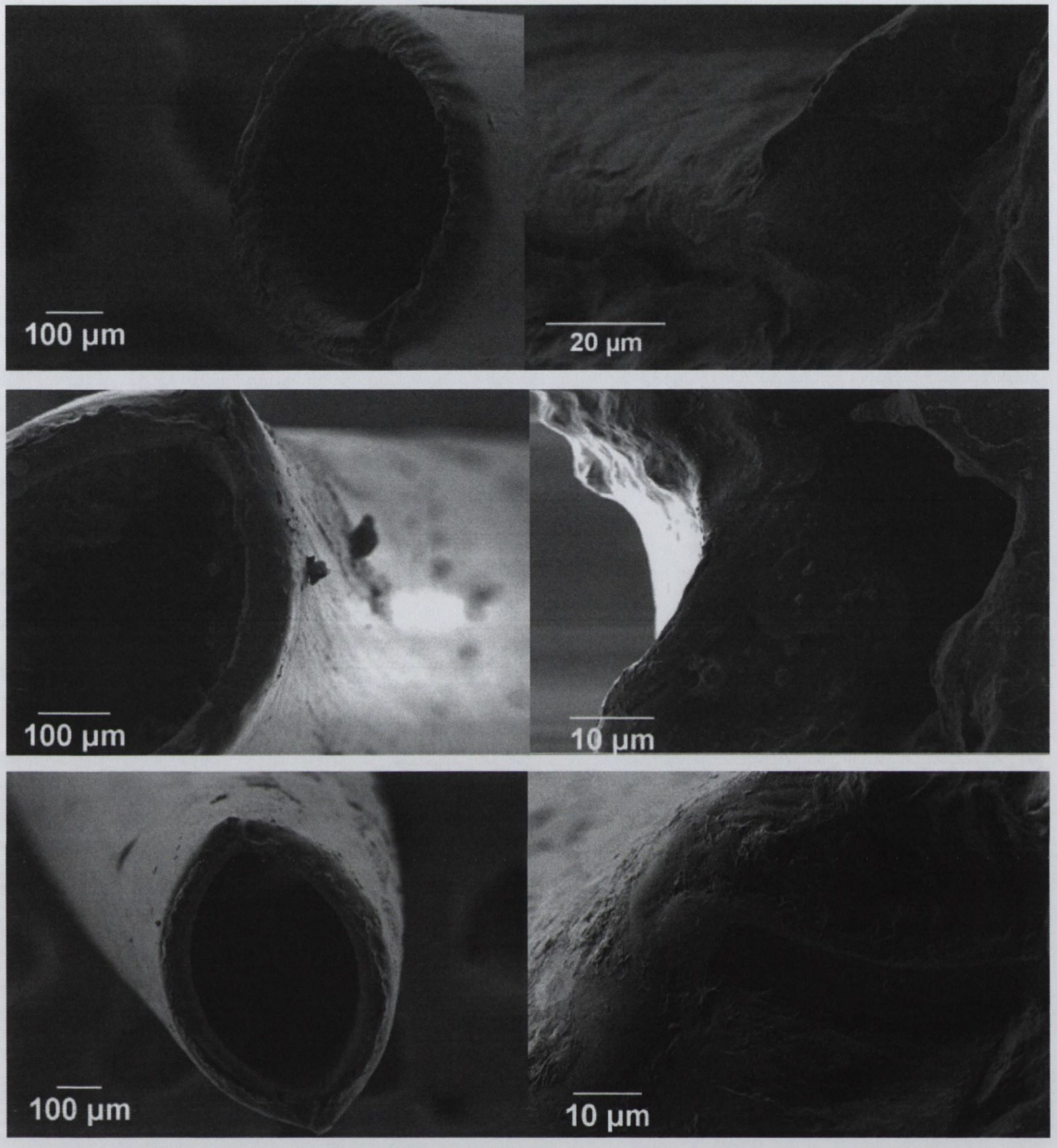

Figure 6.14 SEM images of AuNP-infiltrated polymer tube. Top: 1h ultrasonic agitation; Middle: 2h ultrasonic agitation; Bottom: 4h ultrasonic agitation.

These observations were confirmed by thermogravimetric analysis (TGA), the results of which are presented in Figure 6.15. The sample reacted for 2h exhibited 85% maximum weight loss above 600°C, implying that it was loaded with 15% AuNP by weight. The sample reacted for 4h however had only 3% weight remaining at the end of the combustion, thus confirming the suspected lower loading due to partial dissolvation of the polymer. It was thus concluded that 2h was the optimal swelling time. Unfortunately such loading failed to make the tube X-ray opaque as shown in Figure 6.16.

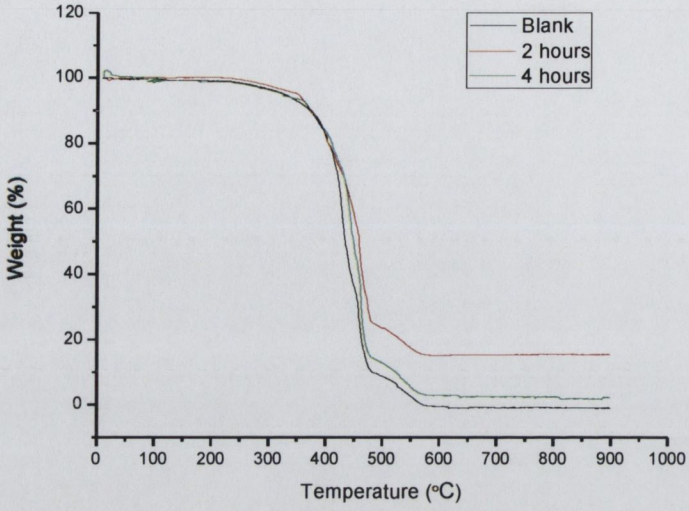

Figure 6.15 TGA of pure polymer and AuNP-infiltrated polymer with 2h and 4 h reaction times.

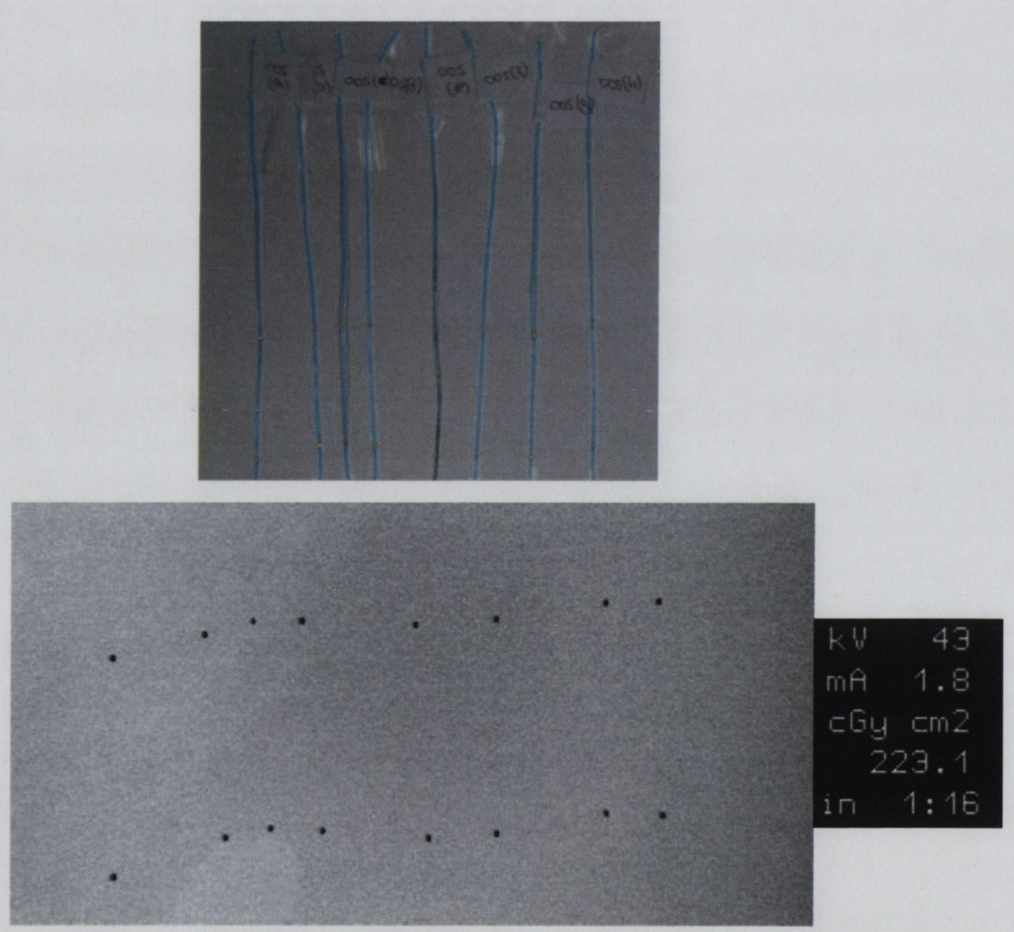

Figure 6.16 Samples of AuNP-infiltrated tubes lined up (top) and X-Ray taken simultaneously (bottom). The black dots visible on X-ray are the gold markers on the catheters.

Since 15% constitutes a reasonably high loading which nevertheless did not provide any X-ray contrast, it was concluded that an extremely high weight percentage of gold nanoparticles would be required for this application. This could only be potentially achieved through the swelling method by submitting the catheter to prolonged immersion into solvents with ultrasonic agitation, which would certainly cause serious damage to its mechanical and chemical properties. Further studies are required in order to develop this techniques and new polymer composite materials. We believe that this swelling under ultrasound technique could be very promising for incorporation of various metal and quantum dot nanostructures. This research is expected to result in new polymer composite materials with unique properties and a range of potential applications.

References

[1] C. M. Lehman, E. L. Frank, *Lab Medicine* **2009**, *40*, 47-51.

[2] R. J. Linhardt, *Chemistry & Biology* **2004**, *11*, 420-422.

[3] P. W. Park, O. Reizes, M. Bernfield, *Journal of Biological Chemistry* **2000**, *275*, 29923-29926.

[4] M. S. Diamond, R. Alon, C. A. Parkos, M. T. Quinn, T. A. Springer, *The Journal of Cell Biology* **1995**, *130*, 1473-1482.

[5] R. S. Stephens, F. S. Fawaz, K. A. Kennedy, K. Koshiyama, B. Nichols, C. van Ooij, J. N. Engel, *Infection and Immunity* **2000**, *68*, 1080-1085.

[6] V. Gérard, C. Maguire, D. Bazou, Y. Gun'ko, *Journal of Nanobiotechnology* **2011**, *9*, 50.

[7] N. Chestnoy, T. D. Harris, R. Hull, L. E. Brus, *The Journal of Physical Chemistry* **1986**, *90*, 3393-3399.

[8] W. C. W. Chan, D. J. Maxwell, X. Gao, R. E. Bailey, M. Han, S. Nie, *Current Opinion in Biotechnology* **2002**, *13*, 40-46.

[9] H. S. Mansur, *Wiley Interdisciplinary Reviews: Nanomedicine and Nanobiotechnology* **2010**, *2*, 113-129.

[10] S. Byrne, Y. Williams, A. Davies, S. Corr, A. Rakovich, Y. Gun'ko, Y. Rakovich, J. Donegan, Y. Volkov, *Small* **2007**, *3*, 1152 - 1156.

[11] I. Nabiev, S. Mitchell, A. Davies, Y. Williams, D. Kelleher, R. Moore, Y. Gun'ko, S. Byrne, Y. Rakovich, J. Donegan, *Nano Letters* **2007**, *7*, 3452 - 3461.

[12] B. Prasad, N. Nikolskaya, D. Connolly, T. Smith, S. Byrne, V. Gerard, Y. Gun'ko, Y. Rochev, *Journal of Nanobiotechnology* **2010**, *8*, 7.

[13] X. Wu, H. Liu, J. Liu, K. Haley, J. Treadway, J. Larson, N. Ge, F. Peale, M. Bruchez, *Nat Biotech* **2003**, *21*, 41 - 46.

[14] J. E. Govan, E. Jan, A. Querejeta, N. A. Kotov, Y. K. Gun'ko, *Chemical Communications* **2010**, *46*, 6072-6074.

[15] M. P. Moloney, Y. K. Gun'ko, J. M. Kelly, *Chemical Communications* **2007**, 3900-3902.

[16] M. Shannon, J. Graef, F. H. Lovejoy Jr, *The Journal of Pediatrics* **1988**, *112*, 799-804.

[17] C. L. Grines, D. A. Cox, G. W. Stone, E. Garcia, L. A. Mattos, A. Giambartolomei, B. R. Brodie, O. Madonna, M. Eijgelshoven, A. J. Lansky, W. W. O'Neill, M.-C. Morice, *New England Journal of Medicine* **1999**, *341*, 1949-1956.

[18] Medtronic, Inc., **2012**, http://www.medtronic.com/for-healthcare-professionals/products-therapies/cardiovascular/catheters/balloon-dilatation-catheters/sprinter-otw-semicompliant-over-the-wire-balloon-dilatation-catheter/index.htm, Accessed 16/08/2012

[19] J. H. Kim, S. Y. Ha, Y. M. Lee, *J. Membr. Sci.* **2001**, *190*, 179-193.

[20] I. O'Connor, H. Hayden, J. N. Coleman, Y. K. Gun'ko, *Small* **2009**, *5*, 466-469.

[21] **I. O'Connor, S. De, J. N. Coleman, Y. K. Gun'ko,** *Carbon* **2009**, *47*, 1983-1988.

Appendices

Appendix 1: HRTEM sizing data for CdTe QDs correlated to UV-visible absorption maxima (provided by Dr Yury Rakovich)

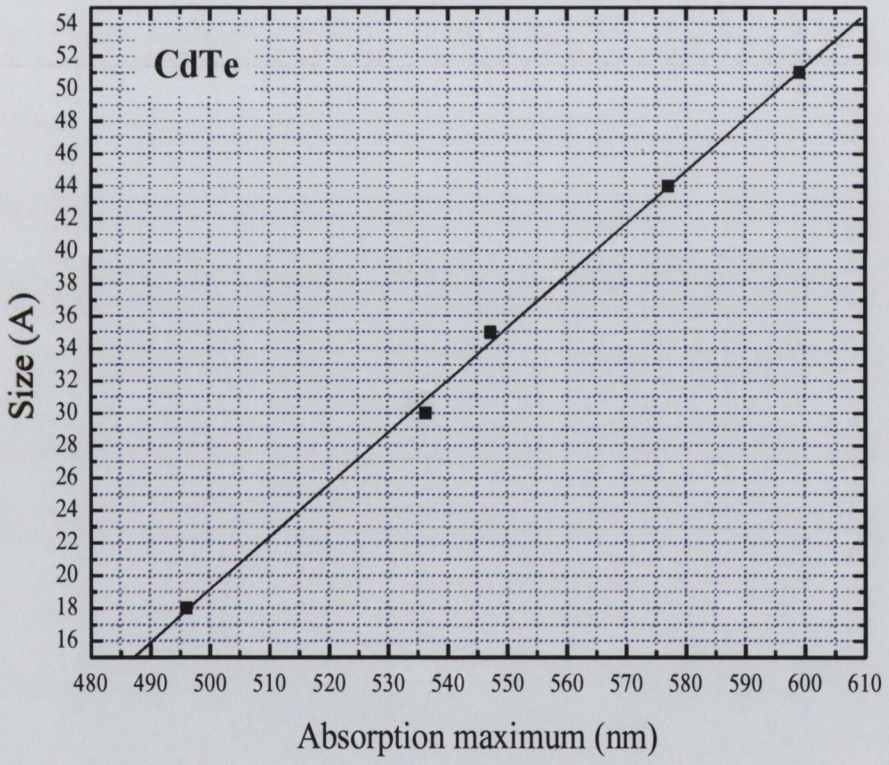

Figure A.1 Experimental plot of CdTe QD core size against UV-Visible absorption maximum

Appendix 2: Three plane projections of cells internalising QDs

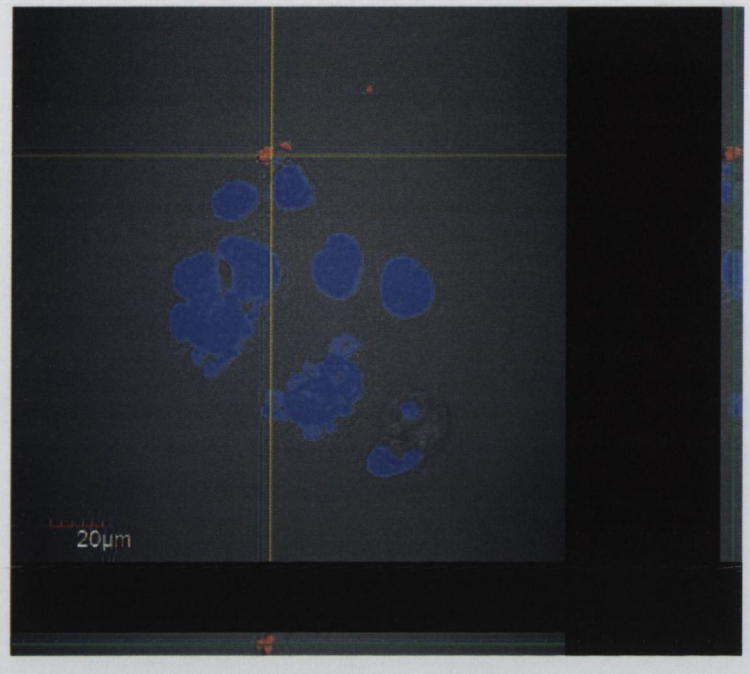

Figure A.1 Three-plane projection of Caco-2 cells treated with red-emitting TGA-gel QDs (excitation 543 nm) and counter-stained with DAPI (excitation 405 nm)

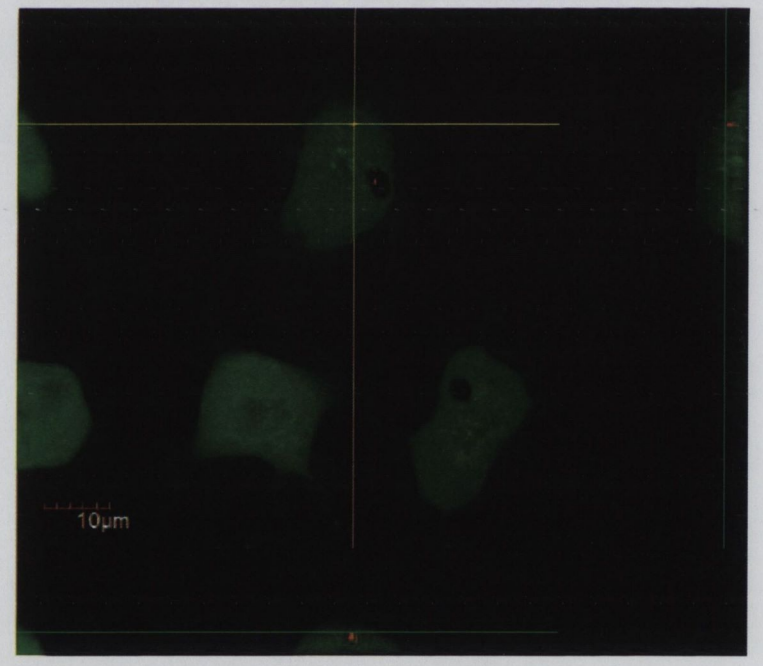

Figure A.2 Three-plane projection of HT-1080 cells treated with red-emitting TGA-gel QDs (excitation 543 nm) and counter-stained with Calcein AM (excitation 488 nm)

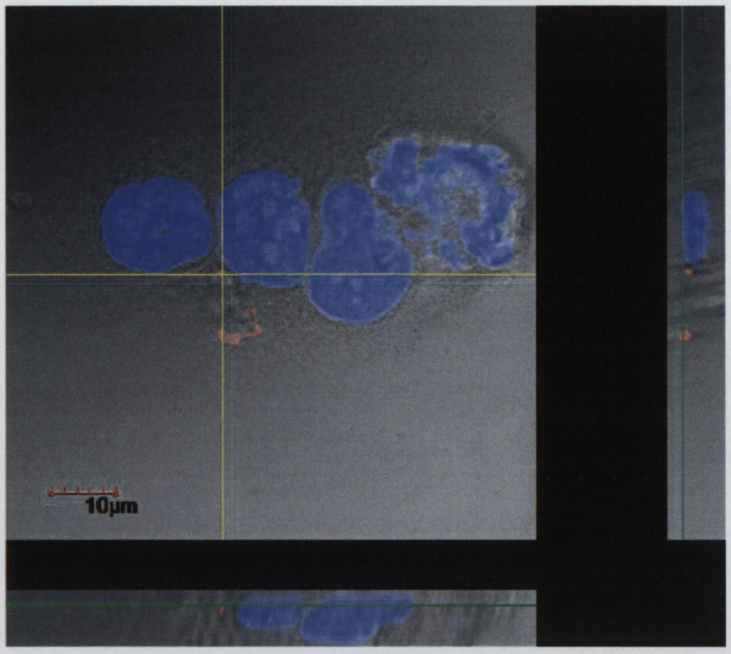

Figure A.3 Three-plane projection of Caco-2 cells treated with red-emitting QD (B), FA incorporated into the gelatin shell, (excitation 543 nm) and counter-stained with DAPI (excitation 405 nm)

Figure A.4 Three-plane projection of Caco-2 cells treated with red-emitting QD (c), FA covalently bound, (excitation 543 nm) and counter-stained with DAPI (excitation 405 nm)

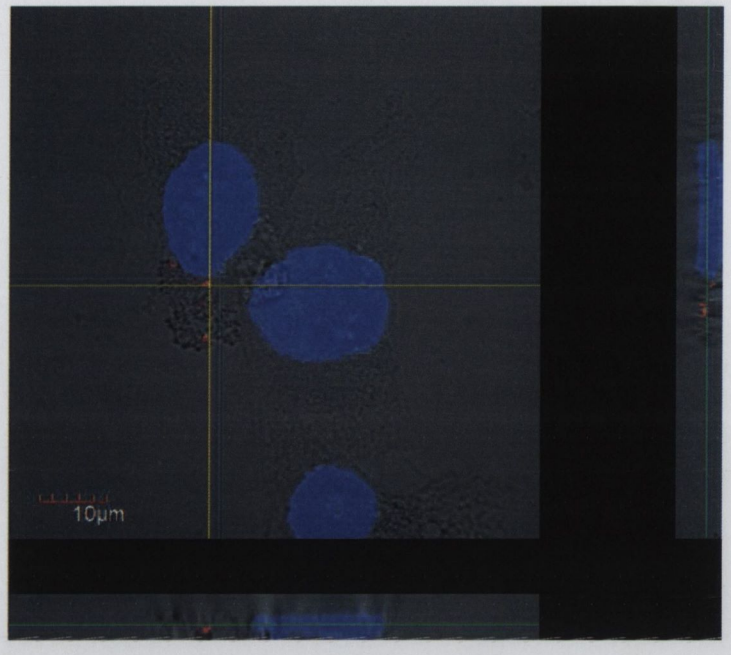

Figure A.5 Three-plane projection of HT-1080 cells treated with red-emitting QD (B), FA incorporated into the gelatin shell, (excitation 543 nm) and counter-stained with DAPI (excitation 405 nm)

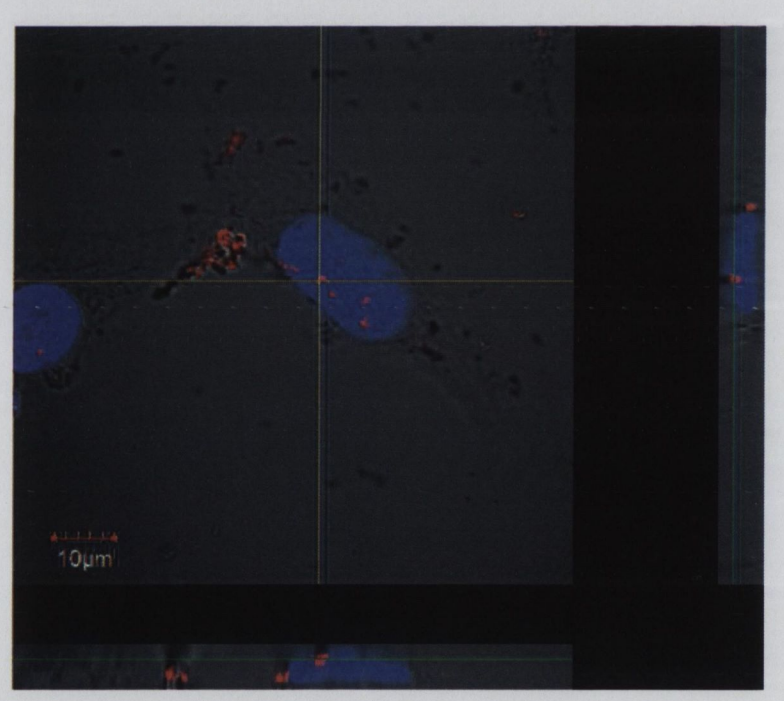

Figure A.6 Three-plane projection of HT-1080 cells treated with red-emitting QD (c), FA covalently bound, (excitation 543 nm) and counter-stained with DAPI (excitation 405 nm)

Figure A.7 Three-plane projection of HT-1080 cells treated with QD-oligo donor (a) (excitation 488 nm, emission 520 nm)

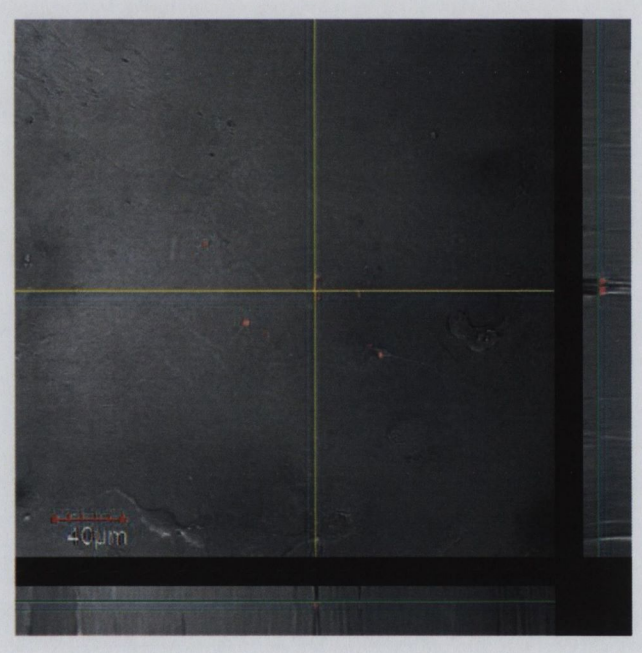

Figure A.8 Three-plane projection of HT-1080 cells treated with QD-oligo acceptor (a) (excitation 543 nm, emission 612 nm)

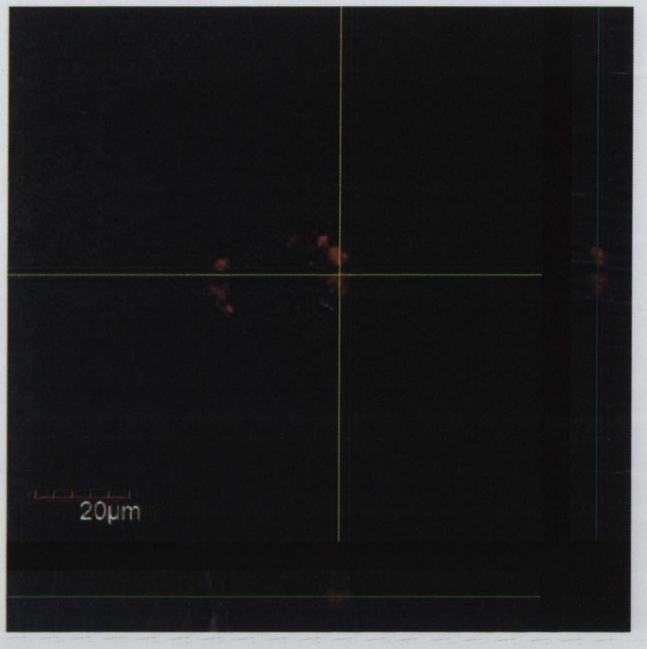

Figure A.9 Three-plane projection of HT-1080 cells treated with QD-oligo donor and acceptor (a) (excitation 488 and 543 nm, emission 520 and 612 nm)

Figure A.10 Three-plane projection of HT-1080 cells treated with pre-mixed QD-oligo donor and acceptor (a) (excitation 488 and 543 nm, emission 520 and 612 nm)

Appendix 3: Localisation of internalised QDs and Golgi apparatus in live *in vitro* cell cultures

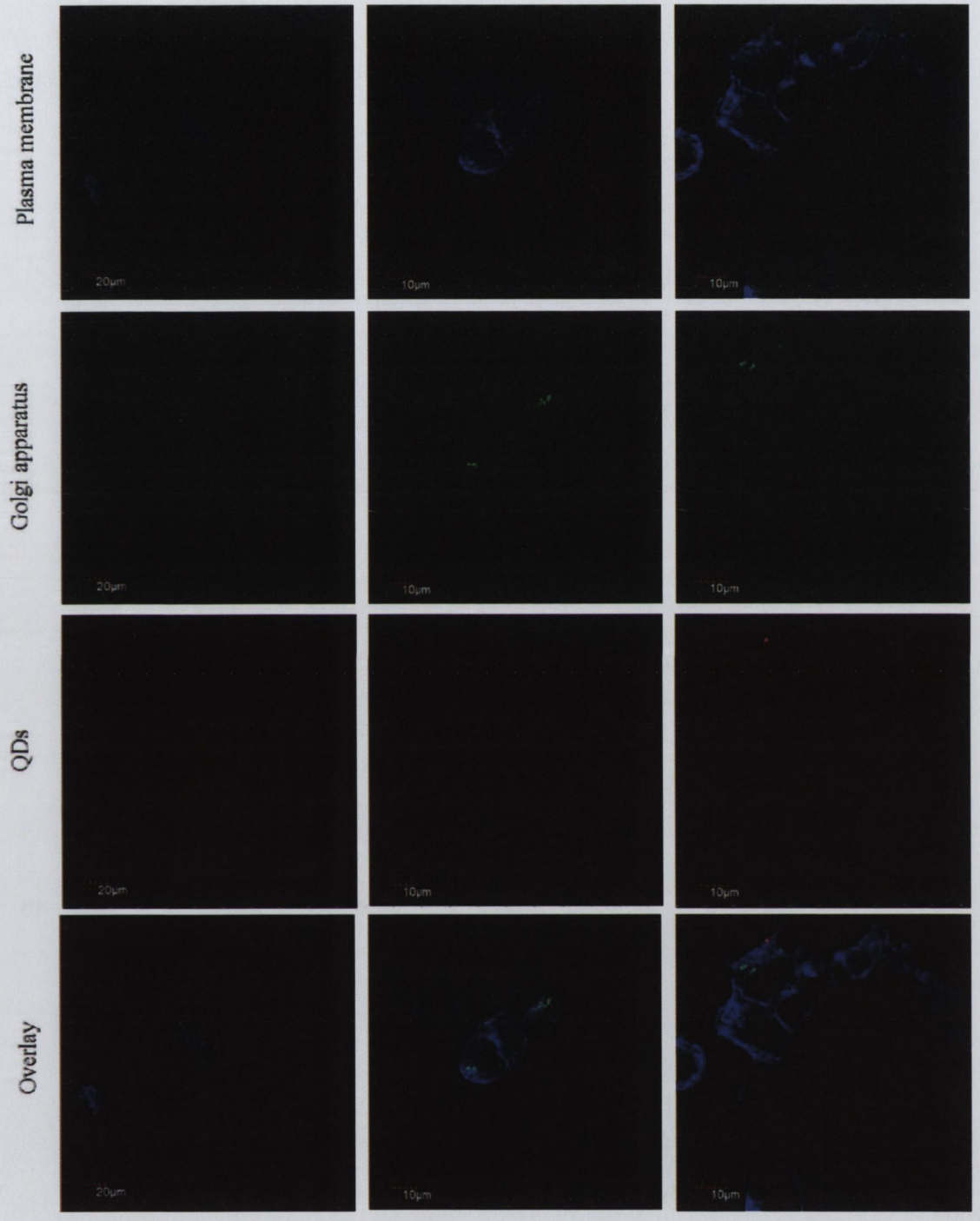

Figure A.11 Confocal microscope images of Caco-2 cells treated with TGA-capped QDs and counter-stained with Organelle Lights CPF-PM and GPF-Golgi. Top row: Plasma membrane stained in blue (excitation 405 nm); Second row: Golgi apparatus stained in green (excitation 488 nm); Third row: red luminescent QDs (excitation 543 nm); Bottom row: overlay of the first three rows showing no co-localisation of QDs and Golgi apparati.

It was demonstrated in chapter 4 that TGA-capped CdTe QDs were readily internalised into Caco-2 cells and appeared as sporadic spots in the cytoplasm. It was postulated that they might be located in the Golgi apparatus. In order to investigate this hypothesis, Caco-2 cells were treated with QDs and stained with a Golgi-specific dye. Confocal images in Figure A.11 and plot of the intensities emerging from the channels corresponding to the QDs and the Golgi apparatus in Figure A.12 showed no co-localisation. QDs are therefore not internalised into the Golgi apparatus.

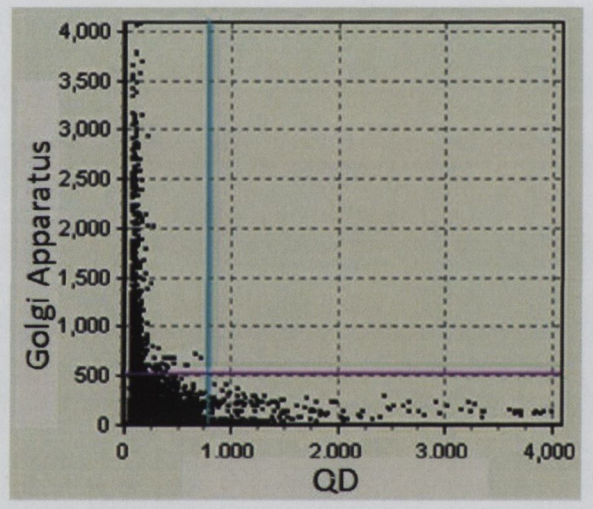

Figure A.12 Co-localisation plot of QDs and Golgi apparatus computed from confocal microscopy images

Publications

Book Chapters

- **Synthesis of Biocompatible Gelatinated Thioglycolic Acid-Capped CdTe Quantum Dots ("Jelly Dots")**
  Valérie A. Gérard, Yurii K. Gun'ko, Babu R. Prasad and Yury Rochev

- **Evaluating the Potential of Quantum Dots for In Vitro Biological Studies: Effects on Gene Expression Using Microarray Analysis**
  Babu R. Prasad, Enda O'Connell, Terry J. Smith, Valérie A. Gérard, Yurii K. Gun'ko and Yury Rochev

  Book: **Nanoparticles in Biology and Medicine,** 978-1-61779-953-2, Published by Humana Press, **2012**

Journal Articles

- **Effect of Metal Nanoparticle Concentration on Localized Surface Plasmon Mediated Forster Resonant Energy Transfer**
  Manuela Lunz, Xia Zhang, Valérie A. Gérard, Yurii K. Gun'ko, Vladimir Lesnyak, Nikolai Gaponik, Andrei S. Susha, Andrey L. Rogach, A. Louise Bradley
  Journal of Physical Chemistry C **2012,** *116* (50): 26529-26534.

- **Wavelength, Concentration and Distance Dependence of Non-Radiative Energy Transfer to a Plane of Gold Nanoparticles**
  Xia Zhang, Crisitan Marocico, Manuela Lunz, Valérie Gérard, Yurii Gun'Ko, Vladimir Lesnyak, Nikolai Gaponik, Andrei Susha, Andrey Rogach and Louise A. Bradley
  ACS Nano, **2012**, *6* (10): 9283-9290

- **Multifactorial Determinants that Govern Nanoparticle Uptake by Human Endothelial Cells under Flow**

  Stephen P. Samuel, Namrata Jain, Frank O'Dowd, Toby Paul, Dmitry Kashanin, Valérie A. Gérard, Yurii K. Gun'ko, Adriele Prina-Mello and Yuri Volkov

  Int J Nanomedicine, **2012**, 7: 2943-56.

- **Effects of Long-term Exposure of Gelatinated and Non-Gelatinated Cadmium Telluride Quantum Dots on Differentiated PC12 Cells**

  Babu R. Prasad, Gillian Mullins, Natalia Nikolskaya, David Connolly, Terry J. Smith, Valérie A. Gérard, Stephen J. Byrne, Gemma-Louise Davies, Yurii K. Gun'ko and Yury Rochev

  Journal of Nanobiotechnology, **2012**, 10: 4.

- **Folic acid modified gelatine coated quantum dots as potential reagents for in vitro cancer diagnostics**

  Valérie Gérard, Ciaran Maguire, Despina Bazou and Yurii Gun'ko

  Journal of Nanobiotechnology, **2011**, 9 (1): 50.

- **Surface plasmon enhanced energy transfer between donor and acceptor CdTe nanocrystal quantum dot monolayers**

  Manuela Lunz, Valérie A. Gérard, Yurii Gun'Ko, Vladimir Lesnyak, Nikolai Gaponik, Andrei Susha, Andrey L. Rogach and A. Louise Bradley

  Nano Letters, **2011**, 11 (8): 3341-5.

- **Plasmon-induced CD response of oligonucleotide-conjugated metal nanoparticles**

  Valérie A. Gérard, Yurii K. Gun'ko, Eric Defrancq and Alexander O. Govorov

  Chemical Communications, **2011**, 47 (26): 7383-7385.

- **Energy transfer in colloidal CdTe quantum dot nanoclusters**
  Clare Higgins, Manuela Lunz, A. Louise Bradley, Valérie A. Gérard, Stephen Byrne, Yurii K. Gun'ko, Vladimir Lesnyak and Nikolai Gaponik
  Opt. Express, **2010**, 18 (24): 24486-24494.

- **Influence of quantum dot concentration on Forster resonant energy transfer in monodispersed nanocrystal quantum dot monolayers**
  Manuela Lunz, A. Louise Bradley, Wu Y. Chen, Valérie A. Gérard, Stephen J. Byrne, Yurii K. Gun'ko, Vladimir Lesnyak and Nikolai Gaponik
  Physical Review B, **2010**, 81 (20): 205316-26.

- **Long-term exposure of CdTe quantum dots on PC12 cellular activity and the determination of optimum non-toxic concentrations for biological use**
  Babu Prasad, Natalia Nikolskaya, David Connolly, Terry Smith, Stephen Byrne, Valérie Gérard, Yurii Gun'ko and Yury Rochev
  Journal of Nanobiotechnology, **2010**, 8 (1): 7.

Review Article

- **Chiral nanoparticle assemblies: circular dichroism, plasmonic interactions, and exciton effects**
  Alexander O. Govorov, Yurii K. Gun'ko, Joseph M. Slocik, Valérie A. Gerard, Zhiyuan Fan and Rajesh R. Naik
  Journal of Materials Chemistry, **2011**, 21 (42): 16806-16818.

Presentations

Oral Presentations

- **New Quantum Dot and Metal Nanoparticle based Materials and their Applications**, Dublin Chemistry Graduate Seminar, Trinity College Dublin, Ireland, *31st May 2012.*

- **Folic Acid-modified Quantum Dots for Cancer Diagnostics**, International Conference on Nanoscience and Nanotechnology (ICONN), Perth, Australia, *5-9th February 2012.*

- **Oligonucleotide-Nanoparticle Conjugates**, COST Meeting, Brussels, Belgium, *13-14th January 2011.*

Poster Presentations

- **Nanoparticle-based Materials for Biomedical Applications**, Brian Dorgan Prize Poster Competition, Trinity College Dublin, Ireland, *17th November 2011.*

- **Oligonucleotide – Metal Nanoparticles conjugates**, Materials Research Society (MRS) Fall Meeting, Boston, USA, *29th November-2nd December 2010.*